UNIVERSIDAD POLITÉCNICA DE MADRID

ESCUELA TÉCNICA SUPERIOR DE INGENIERÍA AGRONÓMICA,

ALIMENTARIA Y DE BIOSISTEMAS

REMOTE SENSING ASSESSMENT OF LAND USE AND CROP PARAMETERS IN IRRIGATED SYSTEMS

TESIS DOCTORAL

JOSE LUIS PANCORBO DE OÑATE

Ingeniero de Montes

2023

DEPARTAMENTO DE PRODUCCIÓN AGRARIA

ESCUELA TÉCNICA SUPERIOR DE INGENIERÍA AGRONÓMICA, ALIMENTARIA Y DE BIOSISTEMAS

REMOTE SENSING ASSESSMENT OF LAND USE AND CROP PARAMETERS IN IRRIGATED SYSTEMS

Memoria presentada por:

Jose Luis Pancorbo de Oñate

Ingeniero de Montes

Directores:

Dr. Miguel Quemada Sáenz-Badillos

Doctor Ingeniero Agrónomo

Dr. Íñigo Molina Sánchez

Doctor por Universidad Politécnica de Madrid

Madrid, 2023

POLITÉCNICA

Tribunal nombrado por el Sr. Rector Magfco. de la Universidad Politécnica de Madrid, el día.....de.....de 20....

Presidente: _____

Vocal: _____

Vocal: _____

Vocal: _____

Secretario: _____

Suplente: _____

Suplente: _____

Realizado el acto de defensa y lectura de la Tesis el día.....de.....de 20 ... en la E.T.S.I. /Facultad.....

Calificación.....

EL PRESIDENTE LOS VOCALES

EL SECRETARIO

Table of contents

List of figures

List of tables

“Man must rise above the earth–to the top of the atmosphere and beyond– for only thus will he fully understand the world in which he lives.”

Socrates, fifth century B.C.E.

Acknowledgements

I would like to express my deepest gratitude to my supervisors for their invaluable time and support. I could not have pursued this thesis without the guidance and motivation provided by Dr. Miguel Quemada and Dr. Iñigo Molina. They have always demonstrated their absolute commitment to my training and well-being. I especially appreciate the meticulousness of their reviews, the encouragement provided, and the time expended helping me to surmount the numerous bureaucratic, personal and analytical difficulties found through these years. I consider myself privileged to have the opportunity of learning from their expertise and work, that have allowed me to do high quality research studies. In addition, they have been a great source of inspiration for me in many ways.

Throughout these years I had the pleasure of working with and learning from great experts and people. Particularly, I would like to express my special thanks to my lab mates María, María Dolores, Luis, Nacho, Maritza, Renato, Miguel, Raúl, Andrés and Giorgia, who have helped and supported me both personally and professionally. I want to thank to all the people from CEIGRAM for creating such a good atmosphere every day. I appreciate how generously they have helped me meet my goals and confront unfamiliar situations and problems. I also want to thank to Carlos Camino for his great contribution to my thesis in innumerable aspects and for sharing his extensive knowledge. I had the chance to work in the VIPER Lab at University of California Santa Barbara, where I met the very talented Dr. Dar Roberts. I gratefully acknowledge him for welcoming me at his lab and sharing his great expertise and knowledge. I want to thank all the work made by the people from La Chimenea, who made this thesis possible.

I gratefully acknowledge the funding provided by Ministerio de Economía y Competitividad (Spain; AGL2017-83283-C2-1-R; PRE2018-084215), Ministerio de Educación (Spain; FPU17/01251), Comunidad de Madrid, Spain (AGRISOST-CM S2018/BAA-4330 project) and Structural Funds 2014-2020 (ERDF and ESF).

Finally, but most importantly, I sincerely thank Teresa, my family, and friends, for their encouragement, patience, and generous support throughout my studies

Abstract

Remote sensing is a valuable tool that could contribute to reduce the environmental impact of agricultural systems by measuring crop parameters to inform management decisions at field and regional scales. At the field scale, it could allow assessing the spatial variation of crop status to adjust water and nitrogen (N) applications and predict harvest parameters. At the regional scale, remote sensing could allow monitoring crop land use and field abandonment to support government management decisions related to water distribution or rural development. This thesis analyzes the performance of different remote sensing systems and modeling techniques to monitor crop parameters at field and regional scale, with a focus on modern satellite imagery.

For field-scale monitoring, we compared remote sensing information with ground-truth measurements at different growth stages (GS) to improve the adjustment of N fertilization and irrigation rates and the prediction of winter wheat traits (yield, grain protein concentration (GPC) and N output). For this purpose, we compared the performance of spectral vegetation indices (VIs), planar-domain indicators, ensemble modeling approaches combining information from different sensors and a hybrid artificial neural network-PROSAIL-PRO method. The suitability of the sensors was determined with acquisitions collected at field level with a spectroradiometer, at 300 m with a hyperspectral and a thermal sensor and with different satellite platforms. Additionally, the accuracy of atmospherically corrected reflectance values acquired by two satellites were validated with the field-level acquisitions. These analyses were conducted in a winter wheat (*Triticum aestivum* L.) field experiment combining four N and two water levels in central Spain over 2 years.

At the regional scale, we used remote sensing data to determine the trends in field abandonment associated to different farming strategies during a multi-year drought. For this purpose, crop land use maps were created following a multiple endmember spectral mixture analysis (MESMA) applied to a time series of hyperspectral AVIRIS imagery (350 – 2500 nm). MESMA classifies images by decomposing each pixel into subpixel fractional covers of land use classes. The area of abandoned fields was estimated from the change in bare soil area given by these maps over the years. The performance of the crop land use maps was assessed by comparing them with official crop reports. These analyses were conducted over 2334 km^2 in the Central Valley of California from 2013 to 2018.

This thesis showed that analyzing together spectral and thermal information enables simultaneous adjustment of N and water application to match crop demand. Combining a VI related to chlorophyll content with another related to biomass improved N status assessment by reducing soil background noise at early GS and minimizing the effect of the water status that was evident in most VIs. The temperature-based indicators were a reliable method for adjusting irrigation because they were only affected by the water and not by the N levels. The water status assessment improved when the soil background noise was compensated with a VI. For the prediction of winter wheat traits, it was found that combining indicators related to different crop parameters with ensemble modeling approaches improved the prediction. The yield was the best estimated trait, achieving similar results with the hyperspectral sensor and with the open-access multispectral satellite Sentinel-2. The GPC prediction was the most challenging, and the results revealed the importance of using hyperspectral short-wave infrared (SWIR) bands. The SWIR bands that cover the protein absorption region improved the prediction of the N-related traits (GPC and grain N output) with both sensors. The hybrid method that estimates crop parameters using the entire spectra presented better results than the VIs based on few bands. This thesis confirmed the suitability of the hybrid method applied to Sentinel-2 for estimating the N status in all GSs and for predicting traits. The reflectance values of Sentinel-2 atmospherically corrected with Sen2Cor, MODTRAN and FLAASH models matched the on-ground spectral data. However, the WorldView-3 satellite displayed significant differences that were attributed to acquisitions under steep off-nadir view angles (24.5º and 39.1º). This thesis proposed and validated an empirical signal normalization procedure that allowed compensating the angular-induced effects and coupling Sentinel-2 and WorldView-3 imagery.

The performance of crop monitoring at regional scale was validated with the good agreement between the MESMA results and the official crop reports. Additionally, the MESMA results revealed an increase in non-cultivated area during the drought. This was achieved thanks to the narrow SWIR bands of the AVIRIS sensor that allow distinguishing between soil and crop residue. AVIRIS is currently used as part of the NASA Surface Biology and Geology Mission (SBG) preparatory campaigns that aims to acquire sub-monthly global imagery with a satellite carrying AVIRIS and a thermal sensor. The results of this thesis confirmed the suitability of this mission for adjusting N and irrigation rates due to the simultaneous acquisition of thermal and spectral data, and to provide accurate prediction of yield, GPC and grain N output, and identification of non-cultivated fields due to the narrow SWIR bands.

Resumen

La teledetección permite estimar parámetros de los cultivos para ayudar en la toma de decisiones y así reducir el impacto ambiental de los sistemas agrícolas. A escala de cultivo, podría evaluar la variación espacial del estado de los cultivos para ajustar las dosis de agua y nitrógeno (N) y para predecir parámetros de la cosecha. A escala regional, la teledetección puede permitir hacer el seguimiento del uso de suelo de los campos de cultivo y detectar los cultivos abandonados para apoyar las políticas relacionadas con la distribución del agua o el desarrollo rural. Esta tesis analiza la capacidad de diferentes sistemas de teledetección y técnicas de modelización para monitorizar parámetros del cultivo a escala de cultivo y regional, centrándose en las imágenes de satélite más modernas.

Para estudiar la monitorización a escala de cultivo, se comparó la información obtenida con teledetección con las muestras tomadas en campo en diferentes estadios de crecimiento (GS) para mejorar el ajuste de la fertilización N y del riego y la predicción de la cosecha del trigo (rendimiento, concentración de proteína en grano (GPC) y cantidad de N exportado). Para ello, se comparó la precisión de índices espectrales de vegetación (VIs), indicadores biplanares, modelos que combinan información de diferentes sensores y un método híbrido de redes neuronales artificiales-PROSAIL-PRO. La idoneidad de los sensores se determinó con adquisiciones recogidas con un espectrorradiómetro a nivel de terreno, a 300 m con un sensor hiperespectral y térmico y con diferentes satélites. La reflectancia adquirida por dos satélites corregida atmosféricamente se validó con las medidas a nivel de terreno. Los análisis se llevaron a cabo en un experimento de campo con trigo de invierno (*Triticum aestivum* L.) que combinaba cuatro niveles de N y dos de agua en el centro de España durante 2 años.

A escala regional, utilizamos la teledetección para determinar las tendencias en el abandono de campos de cultivo asociadas a estrategias agrícolas durante una sequía. Para ello, se crearon mapas de uso del suelo usando un multiple endmember spectral mixture analysis (MESMA) aplicado a una serie temporal de imágenes hiperespectrales AVIRIS (350 – 2500 nm). MESMA clasifica las imágenes descomponiendo cada píxel en fracciones de cobertura de las clases de uso del suelo. La superficie de los cultivos abandonados se estimó midiendo la superficie de suelo desnudo ofrecida por los mapas obtenidos con MESMA de los distintos años. La información de estos mapas se comparó con informes oficiales de los cultivos. Estos análisis se realizaron sobre 2334 km^2 del Central Valley de California desde 2013 hasta 2018.

Esta tesis demuestra que analizar información espectral y térmica permite ajustar simultáneamente las dosis de N y agua. La combinación de un VI relacionado con el contenido de clorofila y otro relacionado con la biomasa mejoró la estimación del estado de N al reducir el ruido del suelo en GSs tempranos y minimizar el efecto del agua que era evidente en la mayoría de los VIs. Los indicadores térmicos fueron fiables para ajustar el riego porque sólo estaban afectados por el agua y no por los niveles de N. La estimación del estado hídrico mejoró al compensar el ruido del suelo con un VI. La combinación de indicadores relacionados con distintos parámetros del cultivo mejoró la predicción de la cosecha. El rendimiento fue la característica de la cosecha mejor estimada, obteniéndose resultados similares con el sensor hiperespectral y con el satélite multiespectral de libre acceso Sentinel-2. La predicción del GPC fue la más difícil, y los resultados revelaron la importancia de utilizar bandas hiperespectrales de la región infrarroja de onda corta (SWIR). Las bandas SWIR que cubren la región de absorción de la proteína mejoraron la predicción de las características de la cosecha relacionadas con el N (GPC y N exportado). El método híbrido que estima parámetros del cultivo utilizando el espectro completo presentó mejores resultados que los VIs que utilizan pocas bandas. Esta tesis confirma la idoneidad del método híbrido aplicado a Sentinel-2 para estimar el estado de N en todos los GSs y para predecir la cosecha. Los valores de reflectancia de Sentinel-2 corregidos atmosféricamente con Sen2Cor, MODTRAN y FLAASH coincidieron con los datos adquiridos a nivel de terreno. Sin embargo, el satélite WorldView-3 mostró diferencias que se atribuyeron a los ángulos de adquisición pronunciados (24.5º and 39.1º). Esta tesis propuso y validó un procedimiento empírico de normalización de la señal que permitió compensar los efectos angulares y acoplar las imágenes Sentinel-2 y WorldView-3.

El seguimiento de los cultivos a escala regional fue validado con la concordancia entre los resultados de MESMA y los informes oficiales. Los resultados de MESMA además revelaron un aumento de la superficie no cultivada durante la sequía. Esto se consiguió gracias a las estrechas bandas SWIR del sensor AVIRIS que permiten distinguir entre suelo y residuo del cultivo. AVIRIS se utiliza actualmente en las campañas preparatorias de la Surface Biology and Geology Mission de la NASA, cuyo objetivo es adquirir imágenes globales con un satélite portando AVIRIS y un sensor térmico. Esta tesis confirman la idoneidad de esta misión para ajustar las dosis de N y de riego gracias a los datos térmicos y espectrales simultáneos, y para proporcionar una predicción precisa del rendimiento, la GPC y el N exportado, así como la identificación de campos no cultivados gracias a las bandas SWIR

Chapter 1: Introduction

1.1. Precision agriculture

The "Green Revolution" comprises a technological development that enhanced the agricultural production during the last century (Patel, 2013), and is based on synthetic fertilizers, new irrigation systems, pesticides and new crop varieties (Pingali, 2012). The new technologies led to an increase in the cultivated area by one third that were able to meet the tripling food demand since the 1960s (Wik et al., 2008; Balogh and Jámbor, 2020). Although, the new goal of the Food and Agriculture Organization (FAO) to ensure food security for the growing population is to increase agricultural production by at least 70% by 2050 (Grainger, 2010). Given the limited cultivated land, the increase in food production will be carried out through sustainable agricultural intensification, by increasing the efficiency of fertilizers, water, pesticides and other inputs in parallel with mitigation of environmental degradation (Sishodia et al., 2020). Therefore, the development of new technologies that allow the efficiency of inputs to increase is key for an economically and environmentally sustainable agricultural system (Manfreda et al., 2018). The agricultural practices based on technology that aim to increase profitability and reduce the environmental impact of the cropping systems by applying site-specific input rates that match crop demand are called precision agriculture (Basso and Antle, 2020; Sishodia et al., 2020).

Among the environmental factors that farmers can modify to increase plant growth and productivity, water and Nitrogen (N) are the main ones (Gonzalez-Dugo et al., 2009). The climate change trend is causing more frequent droughts worldwide that limit the global crop production (Lobell et al., 2011; Cook et al., 2015). Agriculture consumes ~ 70% of the total fresh water used worldwide (Campbell et al., 2017), therefore, adjusting irrigation to crop demand is important to optimize water use in a scenario of climate change (Lesk et al., 2016). Water is the major transport agent of N, so the crop N uptake is regulated by the water availability in different crops (Garwood and Williams, 1967) including wheat (Sadras et al., 2004). However, excessive water increases N losses to the environment that are not assimilated by the crop (Quemada and Gabriel, 2016). Overfertilization has been a common practice in the last decades, with only about half of the N applied being assimilated by the crops (Ladha et al., 2005; Lassaletta et al., 2014). Excessive N application enhances N losses that contribute to water contamination by NO_3–N leaching, soil pollution (Arregui et al.,

2006), greenhouse gas emissions and worsen air quality (Snyder et al., 2009; Aguilera et al., 2013). Additionally, ammonia deposition in natural ecosystems is a threat for biodiversity, and the N_2O emissions enhance stratospheric ozone depletion (Eickhout et al., 2006; Ottman et al., 2000). Finally, overfertilization entails an economic loss for farmers; therefore, technologies that allow determining the crop N and water status to adjust input application rates to crop requirements are crucial for enhancing resource use efficiency (Quemada and Gabriel, 2016; Basso and Antle, 2020).

Crop growth is function of water, nutrients, CO_2 and radiation, so growth can be limited by the scarcity of one resource; however, interaction when a resource is limited has often a larger effect (Cossani and Sadras, 2018). Due to the importance and complexity of the effects that water deficit has on crop N status, their interaction has been the focus of many research studies (Gonzalez-Dugo et al., 2005; Mistele and Schmidhalter, 2008; Cossani et al., 2012; Sadras and Lemaire, 2014). Water deficit has a direct effect on plant N demand because it reduces growth and affects the partitioning between structural and metabolic tissues, in addition to limit crop N uptake (Sandras and Lemaire, 2014). In this aspect, under water scarcity, the crop N demand is reduced because the growth rate decrease. This reduction in N uptake also implies a reduction in plant growth in addition to the reduction produced by the water scarcity (Gonzalez-Dugo et al., 2009). This is because the optimal N concentration (%N) in plants changes with crop growth (Sadras and Lemaire, 2014). This interaction between resources is known as colimitation, and due to the large effect that N, water and their interaction have on crop production, the availability of both resources must be considered together (Sadras, 2004; Quemada and Gabriel, 2016). This implies that N fertilization and irrigation increase production only when the applied resource is limited in the soil (Gonzalez-Dugo et al., 2009). In well-managed crops, with correct N and water availability, the crop produces adequate levels of chlorophyll, which allows increasing photosynthesis rate, sunlight interception and therefore, biomass production that would result in higher grain yields (Marti et al., 2007). The linear correlation between dry biomass and yield is well defined by the harvest index (Singh and Stoskopf, 1971). This index indicates the percentage of crop dry matter that is converted into harvest product. Under water stress, plants reduce some physiological functions, such as transpiration, leading to a decrease in photosynthesis rate and final yield (Tanner and Sinclair, 1983; Sandras and Lemaire, 2014; Hoogmoed and Sadras, 2018).

Many efforts have been attempted to develop accurate techniques to determine crop status and adjust fertilization and irrigation to crop demand (Tilling et al., 2007; Longmire et al., 2022). Due to the negative allometric relationship between optimal %N and biomass, evaluating %N in leaves and shoots alone is not adequate to identify the crop N status because it requires information about the biomass (Lemaire et al., 2008; Sadras and Lemaire, 2014). This concept is well integrated in the nitrogen nutrition index (NNI), which is a well-known indicator of crop N status proposed by Greenwood et al. (1990). The NNI compares %N in leaves and shoots with the critical %N at a given biomass. The critical %N is the minimum %N that produces the maximum growth rate of biomass, and decreases with biomass production following the N critical dilution curve (CDC). For a given biomass, if the actual NNI value is below the minimum threshold, N is limiting crop growth. Because the CDC was originally developed for non-water stressed crops, efforts have been made to develop an alternative CDC for water deficit regimes (Hoogmoed and Sadras, 2018; Neuhaus et al., 2017). Consequently, the assessment of crop N demand can be monitored by determining the %N in a sample of known aerial biomass (Mistele and Schmidhalter, 2008). However, this procedure is expensive, slow and hard to apply to large fields (Haboudane et al., 2002; Min and Lee, 2005). Furthermore, by the time the %N results are available, in many cases the phenological stage of the crop has changed and it is of little support for making decisions related to fertilization.

The N use efficiency (NUE) is defined as the ratio between the total N content in the harvested product and the sum of all N input (Quemada and Gabriel, 2016; Lassaletta et al., 2014). Analogously, the water use efficiency (WUE) is defined as the ratio between crop biomass and evapotranspiration (ET), or as the ratio between yield (WUEy) and ET (Sadras, 2004). Due to the co-limitation effect, sustainable agricultural systems should rely on improving NUE and WUE simultaneously for reducing environmental pollution and maintaining economic profitability (Arregui et al., 2006). Each crop requires a specific strategy to adjust the application of N fertilizer as the N demand changes with crop development (Sticksel et al., 1999). Along these lines, monitoring temporal variations of crop N status could allow adapting N application to crop requirements (Quemada et al., 2014). as the ratio between

Sustainable intensification of agriculture should rely on non-destructive and real-time management strategies. These techniques should assess the N and water status of the crop

prior to N application to distinguish the sites that will respond to N fertilization and those that will not (Lemaire and Gastal, 1997; Quemada and Gabriel, 2016). This purpose can be achieved with remote sensing techniques that allow mapping the spatial and temporal variability of the crop status within a field using non-destructive methods (Raya-Sereno et al., 2021a). Even though its use is still limited (Weiss et al., 2020), this approach provides potential for valuable insights into improving NUE and WUE in large areas (Hatfield et al., 2008; Tsouros et al., 2019).

In addition to enabling site-specific input application, remote sensing techniques allow spatial and temporal assessment of agricultural practices at regional levels by monitoring land use (Shivers et al., 2018). These methods allow assessing the sustainability of agricultural practices and the effect of policy regulations at a regional or national scale (Sishodia et al., 2020). Field abandonment is a global common practice (Yang et al., 2020) and has multiple impacts on the environment, such as a reduction in nutrient, carbon or water storage (Yang et al., 2020; Khorchani et al., 2021), an increase in wildfire risk (Lloret et al., 2002) or changes in wildlife movements and habitat availability (Goicolea and Mateo-Sánchez, 2022). As a consequence, it is important to identify the crop fields covered by plant residues, senescence vegetation or soil when mapping crop land use (Hively et al., 2019). Quantification of the fallow or abandoned cropland can be useful to guide management decisions related to water distribution (Otero et al., 2011), planting abandoned cropland (Schierhorn et al., 2014), reforestation efforts (Yang et al., 2020), bioenergy production (Campbell et al., 2008), rural development or awarding subsidies (Milenov et al., 2014). For this reason, remote sensing imagery with global or broad-scale coverage has the potential to mitigate environmental and social damage.

1.2. Spectral features of crop components

Recent innovations in computer science, electronics and sensor technologies have promoted the development of accurate plant biochemical and physical parameters characterization that allows enhancing resource use efficiency (Qui et al., 2018). The technique most extensively used in precision agriculture for plant status monitoring is radiometry, i.e., measurement of radiation using physical devices (Wolfe, 1998). This technique combined with innovations in remote sensing offers new opportunities in the field of precision agriculture (Cawse-Nicholson et al., 2021). The American Society for Photogrammetry and Remote Sensing defined remote sensing as “the art, science and technology of obtaining reliable information

about physical objects and the environment, through the process of recording, measuring and interpreting imagery and digital representations of energy patterns derived from non-contact sensor systems" (Gogoi et al., 2018).

The term radiation refers to the energy that is transported as photons/electromagnetic waves. Each photon has a specific amount of energy that is a function of its frequency and wavelength (Wolfe, 1998). The Sun emits radiation in the 0.3 – 3.0 µm range that reaches the Earth surface with different intensity depending on the wavelength. The Sun radiation received by a surface is reflected, absorbed or transmitted with different relative intensities according to the wavelength and the surface (Ferguson and Rundquist, 2018). The relative proportion of light reflected, transmitted or absorbed is characteristic of the surface properties and therefore it can be used to analyze the surface structure and composition. Due to the different properties of the plant constituents, the sensors that measure the light reflected by the crop have received much attention as an accurate, fast and non-destructive tool to retrieve crop traits (Gabriel et al., 2017).

During the photosynthesis process, under the correct levels of N and water availability, plants generate organic matter using electromagnetic energy from the Sun together with atmospheric CO_2, water and other molecules such as adenosine triphosphate (ATP) and nicotinamide adenine dinucleotide phosphate (NADPH) (Gonzalez-Dugo et al., 2009). The photosynthesis process is composed by light-dependent and light-independent biochemical reactions that take place in the photosystems I and II of the leaves. This process starts with the light-dependent reactions when chloroplasts absorb the energy from the photosynthetically active radiation (PAR; 400 – 700 nm) that reaches the leaves. The PAR is the portion of the solar irradiance that belongs to the visible region and can be absorbed by photosynthetic pigments (Gueymard, 1989). Approximately 75% of incident PAR is absorbed by leaves; however, most of this energy is dissipated and only ~ 3 % is used to generate organic matter (Tremblay et al., 2012).

During the photosynthesis light-process, ATP and NDPH molecules are generated in the thylakoid membranes of the chloroplasts. This process is regulated by the maximum rate of electron transport in the thylakoid (Jmax) (Yamori and Shikanai, 2016). The electron transport is originated when the chlorophyll molecules are excited by the incoming PAR. This process, as well as the electron gradient derived from water molecules, is used to generate ATP and NDPH (Kramer et al., 2004). The ATP and NADPH molecules are used by

Ribulose-1,5-biphosphate carboxylase/oxygenase (RuBisCO) to synthesize ribulose bisphosphate (RuBP), which reacts with CO_2 to reduce phosphoglycerid acid into glucose. This reaction is constrained by the maximum carboxylation capacity (Vcmax). As proposed in the photosynthesis model by Farquhar et al., 1980, the photosynthesis assimilation rate can be defined with Jmax and Vcmax, which are highly correlated between them, and their estimation can be used to assess plant production (Walker et al., 2017). However, they cannot be directly measured and must be inferred based on photosynthesis rate assessment (Kattge et al., 2009). Most of the leaf-N in plants is invested in chloroplasts (~ 75%), especially in RuBisCO protein, which accounts for 15 to 30% of the total leaf-N content (Makino and Osmond, 1991). Therefore, chlorophyll content can be used as a proxy of photosynthesis rate or N availability (Makino, 2003).

Most of the PAR intercepted by leaves is absorbed in the chloroplasts during the photosynthesis process. Consequently, the photosynthetic pigments located in leaf tissue, such as chlorophyll a + b, greatly reduce the light reflected by plants in the visible region of the spectrum (450 – 680 nm). The reflectance in the visible region is also affected by other leaf pigments, such as anthocyanin or carotenoid. They avoid damage in the photosynthetic system by dissipating the excess incident energy in the visible or ultra-violet (UV) region (Tanaka et al., 2008). Chlorophyll strongly absorbs radiation in the PAR region, but has absorbance peaks in the red (~ 670 nm) and blue (~ 445 nm) wavelengths. The blue band overlap with the absorbance of carotenoids, and the green band overlaps with the anthocyanin absorption region (Fig 1). The signal of these pigments is weaker than the chlorophyll signal due to the stronger absorbance of chlorophyll in the overlapping wavelengths and the usually higher concentration of chlorophyll in the leaves (Sims and Gamon, 2002). Chlorophyll degradation usually occurs under nutrient or water deficiencies or at senescence. During this process, the chlorophyll absorbance is strongly reduced, and consequently the reflectance in the visible region increases, especially in the red and green bands (Gitelson et al., 1996).

In addition to regulate the leaf pigments content, the plants have developed other strategies to prevent damage in the photosynthetic apparatus. During the photosynthesis process, the excess amount of light can be dissipated by the leaves as chlorophyll fluorescence or heat emission. The relative proportion of energy that is absorbed by the chlorophyll for the photosynthesis process, that is emitted as chlorophyll fluorescence or that is emitted as heat, change with plant N and water status (Zarco-Tejada et al., 2012; Camino et al., 2018). The

solar induced chlorophyll fluorescence (SIF) takes place when the incoming Sun light is absorbed by the chlorophyll and it is excited. During the de-excitation process this energy is emitted at a longer wavelength within a very short time period. This process produces two subtle peaks in the visible- near-infrared region of the emitted signal added to the spectral radiation reflected (Damm et al., 2011). The 685-nm peak is produced by the photosystem II, and the peak at 740 nm is emitted by the photosystem I and II (Baker, 2008; Palombi et al., 2011). The proportion of light emitted as fluorescence usually is ~ 1 % of the total received light (Tremblay et al., 2012).

At longer wavelengths, such as the near-infrared (NIR; 780 – 1100 nm) and short-wave infrared (SWIR; 1100 – 2500 nm) regions, light penetrates deeper into leaves, and reflectance in these regions is also influenced by internal leaf structure and composition (Serrano et al., 2002). Well-watered plants expand intercellular air space in the spongy mesophyll, increasing the gas exchange rate with the atmosphere, the photosynthesis capacity and the reflectance in the NIR region. Bigger air space in the spongy mesophyll increases scattering of NIR radiation within the leaf, which increases NIR reflectance, and therefore the internal leave structure can be monitored using the reflectance in the NIR region (Heithold et al., 1991; Zhao and Nakano, 2018). As a result, the characteristic spectrum reflectance of healthy vegetation is characterized by combining low reflectance in the visible wavelengths with high reflectance in the NIR wavelengths (Fig 1). On the other hand, the characteristic soil spectrum is characterized by higher reflectance than green vegetation in the visible and lower in the NIR regions (Daughtry et al., 2000) (Fig 1). However, different soil parameters can affect the reflectance values, such as soil type, composition, water content and organic matter, being the reflectance in the visible-NIR (VNIR) region reduced with higher values of organic matter and water content (Bartholomeus et al., 2008; Ben-Dor et al., 2002).

The region between the strong chlorophyll absorption peak in the red and the within-leaf scattering in the NIR wavelengths is called “red edge” (680 – 780 nm). An increase in chlorophyll content produces a broadening of the chlorophyll absorption feature in the red region, increasing the absorption boundary to longer wavelengths (Munden et al., 1994). Consequently, the reflectance in the red edge changes with chlorophyll content (Cho and Skidmore, 2006) or N content due to the link between both plant components (Inoue et al., 2016). The spectral variation found in the red edge under varying chlorophyll content was also found in the region comprised between the red and green wavelengths. However, the red

edge region is only affected by chlorophyll a + b, whereas the red-green region is sensitive to chlorophyll a + b and carotenoids (Gitelson et al., 1996).

Longer wavelengths located in the SWIR region can be used to estimate different plant components. For example, plant protein content, such as those contained in the chlorophyll, can be assessed with the SWIR region using the absorption feature of N=H bonds around 1510 nm and 2180 nm (Curran, 1989; Fig 1). Identification of non-photosynthetic vegetation or plant residue relies on the narrow absorption band of lignin and cellulose in the SWIR region around 2100 nm (Daughtry, 2001; Fig 1). However, this region is also highly affected by the water content, which can mask the effect of the protein and lignin content in the narrow absorption band of the reflectance spectrum (Sims and Gamon, 2003).

In other part of the electromagnetic spectrum; in the microwave region (1 m – 1 mm) the radiation reflected is function of the dielectric and structural properties of the surface. In crop fields, the radiation reflected in this region is dominated by the bounces and scattering of the radiation within the canopy structure or the soil that defines the intensity of the reflected signal (McNairn and Shang, 2016). Because the penetration capacity of a radiation increases with wavelength, the radiation in the microwave region can penetrate in the surface and, therefore, it is also affected by internal leaf structure, soil structure or soil roughness among other parameters (McNairn and Shang, 2016). The radiation backscattering in this region is sensitive to the dielectric constant, and typically increases with water content due to the high dielectric constant (~ 80) of the water relative to the dry soil (~ 4) or air (~ 1) (Fawwaz et al., 1996; Mandal et al., 2020; Salarieh et al., 2020). Because the microwave radiation reflected by a crop field is driven by the canopy and soil structure, and water content, the radiation reflected in this region is sensitive to biomass, plant growth dynamics, and soil and vegetation water content, among other parameters (McNairn and Shang, 2016; Mandal et al., 2020).

Plants experience water stress when the evaporative demand exceeds water availability over a period of time (Chaves et al., 2002). The plants respond to water stress by closing the leaf stomata to reduce water loss, which reduces plant transpiration and CO_2 assimilation. These induced responses, together with the reduction in RuBP synthesis due to water scarcity, constrain the photosynthesis activity (Medrano et al., 1997; Jackson et al., 1981). Consequently, water stress produces changes in the SIF because the proportion of incident light that is used in the photosynthesis process or is dissipated as SIF or heat change due to a

reduction in photosynthesis activity (Zarco-Tejada et al., 2012). Stomata closure limits plant transpiration, which is a major cooling mechanism for plants. Therefore, plant temperature increases with stomatal closure (Rud et al., 2014). Ehrler, 1973 found that in addition to water availability, other environmental factors such as the vapour pressure deficit (VPD) affect plant temperature.

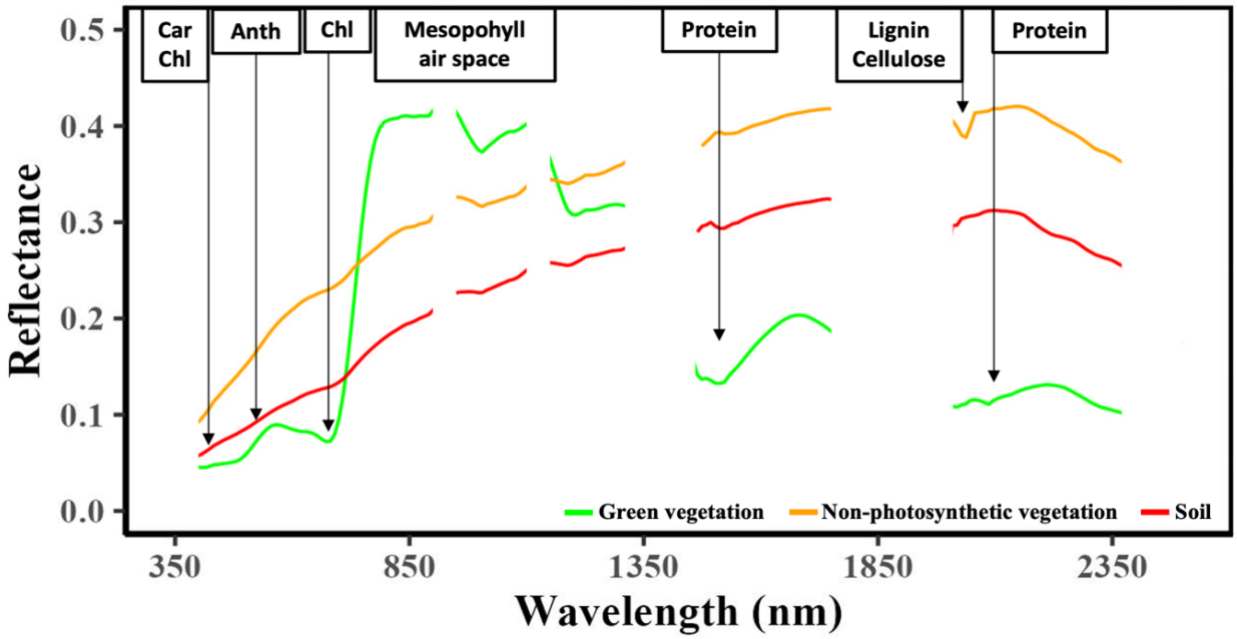

Fig 1. Reflectance spectrum (350 – 2350 nm) of green vegetation, non-photosynthetic vegetation and bare soil extracted from the AVIRIS image on the "Soda-straw" flight line. Arrows indicate the absorption peaks of some important plant components according to Curran et al. (1989); Daughtry (2001) and Sims and Gamon (2002). Car, Anth and Chl mean carotenoid, anthocyanin and chlorophyll, respectively.

1.3. Sensing systems used in precision agriculture

Sensing systems used in precision agriculture can be characterized by the platform and the sensor used. Regarding the platform used, the sensing systems can be classified as remote sensing; which obtains the information from the surface without physical contact, or leaf clip systems that ensure full contact with the leaf tissue (Arregui et al., 2006). In remote sensing, one of the most common platforms used to carry the sensor are satellites that collect the information from space at hundreds of kilometers from the Earth surface (Fig 2a, b). Aerial platforms, such as unmanned aerial vehicles (UAVs) and aircrafts, are platforms commonly used to collect images at several meters away from the target surface (Fig 2e, f). Field-level

platforms that include farm machinery or humans collects measurements at < 10 m from the surface (Fig 2g).; this technique is also known as proximal sensing due to their close proximity to the sensed surface (Sishodia et al., 2020).

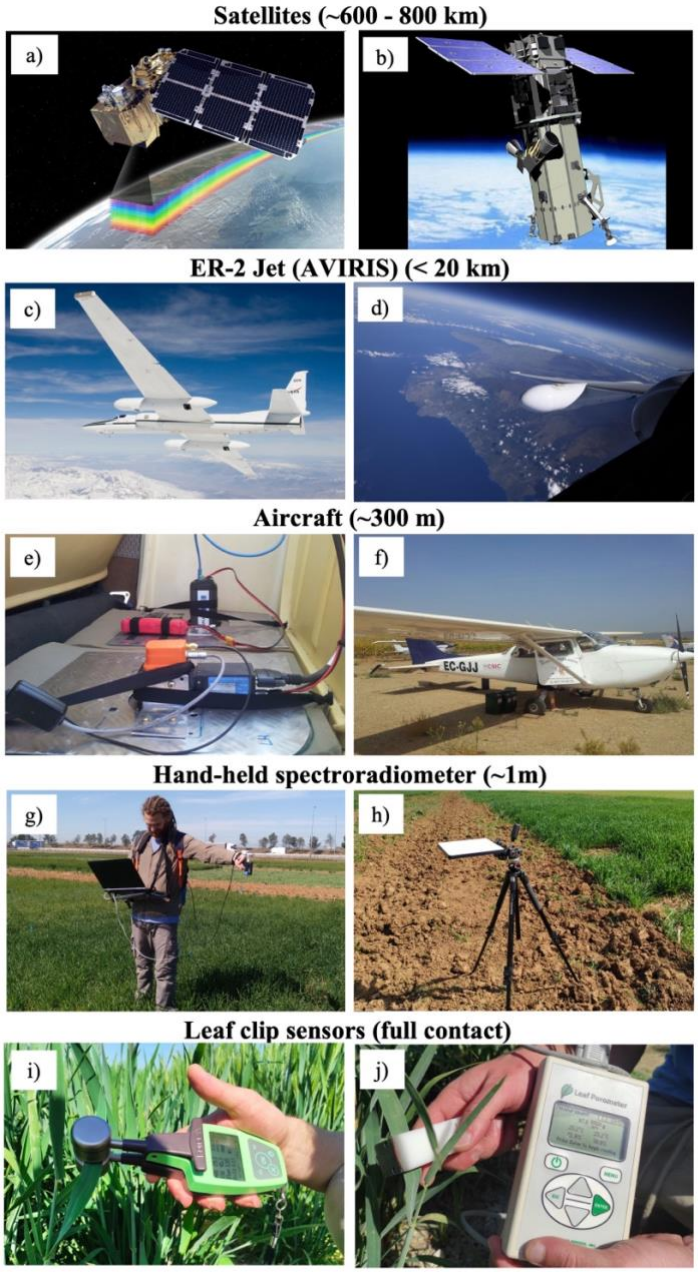

Fig 2. Some sensors and platforms used in this study: a) Sentinel-2 (ESA, 2023a), b) WorldView-3 (ESA, 2023b), c) ER-2 Jet (NASA, 2023a), d) picture taken from the window of the ER-2 (JPL, 2023a) e) spectroradiometer and thermal sensors installed onboard the Cessna aircraft, f) Cessna aircraft, g) hand-held spectroradiometer FieldSpec, h) white reference panel spectralon i) Dualex and j) leaf porometer.

The sensors used in remote sensing can be active or passive, while the leaf clip sensors are always active. Active sensors provide information about the target surface based on the light emitted by the sensor that is captured back after being reflected or transmitted by the target surface. This characteristic allows the sensor to take measurements that are not affected by the sunlight conditions (Gabriel et al., 2019). On the other hand, the information provided by the passive sensors is based on a portion of the solar spectral radiation reflected by the observed surface (Peddle et al., 2001), or the radiation emitted by the observed surface at specific wavelengths (Tremblay et al., 2012). One of the most common sensor types used in precision agriculture are spectroradiometers. They are passive sensors that measure the solar spectral radiation reflected from a surface in a particular range of the electromagnetic spectrum to generate a radiance spectrum ($W \cdot m^{-2} \cdot sr^{-1} \cdot \mu m^{-1}$). In addition to the surface properties, the value of the collected spectral radiance is dependent on the amount of incoming solar spectral radiation (irradiance; $W \cdot m^{-2} \cdot sr^{-1} \cdot \mu m^{-1}$) that changes with time and location. For this reason, the spectral radiance is usually converted into reflectance values by compensating the spectral radiance measured with the sensor by the incoming spectral irradiance. Therefore, reflectance values indicate the relative portion of the spectral irradiance that is reflected by the target surface (Peddle et al., 2001). The reflectance spectrum is characteristic of the properties of the observed surface, so it does not vary with illumination conditions and can be compared with a collection of spectral libraries or used for studying the composition of different land uses, such as mineral, vegetation or water (Milton et al., 2009; Schodlok et al., 2022). If the spectroradiometer acquires both spectral and spatial information of the scene covered by the field of view (FOVº) of the instrument, this information processed with modern imaging systems allows extracting the reflectance spectrum of a georeferenced image in a pixel-base (Qian, 2021). The characteristics of the derived image depend on the distance between the sensor and the observed surface, as well as on the specific characteristics of the sensor.

The characteristics of the remote sensing sensors differ in spatial, spectral and temporal resolution (Katkani et al., 2022). Spatial resolution refers to the minimum region of the ground where the information is measured and extracted; this value corresponds to the pixel size (m) in the derived images. The spatial resolution of the product varies with the distance between the sensor and the target surface. The spatial coverage, or footprint, is the total surface that is covered by an image derived from remote sensing techniques and depends on the FOVº and altitude of the acquisitions. Sensors providing a wide footprint allow broad-

scale monitoring; however, they usually have a low spatial resolution (big pixel size), such as most of the current satellite images (Rossi et al., 2022). Spatial resolution is important in crop monitoring because the information extracted from the pixel can be affected only by the plant, or by a combination of crop components contained within the pixel, such as a soil-plant mix (Moran et al., 1994).

The spectral resolution is determined by the region of the electromagnetic spectrum that each band captures (bandwidth) and plays an important role in spectroradiometer acquisitions. Nowadays, the most advanced spectroradiometers are the hyperspectral sensors that measure reflectance over a large number of wavelengths with bandwidths < 10 nm. Therefore, these sensors provide a quasi-continuous spectrum that offers more information than broader band multispectral sensors with coarser spectral resolution (Li et al., 2021). High spectral resolution (narrow bandwidth) is important for analyzing specific crop components that have a narrow absorption band, such as lignin or protein, by separating the effect of other components that affect neighboring bands and can mask the influence of these component in the signal, such as water content or other canopy components (Kokaly, 2001; Yan et al., 2021; Li et al., 2018). In addition, other measurements such as the excess energy dissipated as chlorophyll fluorescence require a high-resolution hyperspectral sensor to measure the energy emitted by the chlorophyll at 685 or 740 nm. Usually, SIF is calculated using sensors that provide a spectral resolution of < 0.5 nm, however, Damm et al. (2011) found that hyperspectral sensors with 5- or 6-nm spectral resolution can successfully estimate SIF using the Fraunhofer line discrimination (FLD) method.

The number of bands measured in a particular region of the electromagnetic spectrum, as well as the total region of the electromagnetic spectrum covered by the sensor are also a limiting factor (Segarra et al., 2020). The response of some plant components to incident spectral radiation can only be detected in some regions of the electromagnetic spectrum, such as the protein and lignin absorption feature located in a portion of the SWIR region (Curran, 1989). For this reason, a hyperspectral sensor covering the SWIR region is recommended for protein or lignin content characterization, however, the price of these instruments limits their widespread use (Milton et al., 2009). To solve limitations related to the spectral region covered, a common practice is to install various sensors on tandem in the platform to collect information simultaneously from sensors with different characteristics, such as the portion of the electromagnetic spectrum covered. However, this method requires solving preprocessing

issues such as the co-registration between non-aligned detectors (Zarco-Tejada et al., 2012; Camino et al., 2018). The temporal resolution of the sensing system depends on the platform and refers to the time between acquisitions taken at the same location. In the case of orbiting satellites, it refers to the time needed to complete an orbit (Liang and Wang, 2019).

Sensors that operate within the visible-SWIR (VSWIR) region of the electromagnetic spectrum are called optical sensors. On the other hand, radar sensors are active sensors that operate in the microwave region. Synthetic aperture radar (SAR) systems are commonly used for this purpose and consists of a side-looking radar imager that sequentially generates electromagnetic radiation in the microwave region and measures the intensity of the energy backscattered from the observed surface as decibels (db) with the antenna. The platforms of the SAR systems are satellites or aircrafts in motion. The spatial coverage of a radar sensor depends on the length of the sensor antenna. For this reason, to increase the spatial resolution, a virtual aperture longer than the antenna length is placed in the platform to allow receiving more signal. This mechanism gives the name “synthetic aperture” to the remote sensing technique. Because they are active sensors that operate in the microwave region, they can take accurate measurements independently from sunlight conditions and with the presence of cloud and haze (Moreira et al., 2013).

The SAR sensors characteristics depend on the operating wavelengths, incident angle and polarization. The incident angle is defined as the angle between the sensor beam and the line perpendicular to the observed surface. The SAR operational radiation can penetrates into the surface to retrieve information from internal structural and composition parameters (Moreira et al., 2013). The depth of penetration into the observed surface increases with wavelength but decreases with incident angle (McNairn and Shang, 2016). Some of the most commonly used bands are X (2.5 – 4 cm), C (4 – 8 cm) and L (2 – 1 cm), being the penetration capacity of the L band the highest. The polarization of the SAR sensors is the orientation of the beam in the transmitted and received path. The polarization is important to understand the structure of the target. Depending on the sensor, they can emit and collect information in different polarization combinations of horizontal (H) and vertical (V) channels (HH, VV, HV and/or VH).

Due to the link between crop water status and plant thermal emissivity, plant temperature can be used to detect plant water stress (Tanner, 1963; Constable and Rawson, 1980; Zarco-Tejada et al., 2012). Before infrared thermometry became available in the 1960s, most plant

temperature measurements were conducted with leaf clip sensors (Tanner, 1963). The development of infrared thermometry allows acquiring measurements of canopy temperature with remote sensing techniques and mapping its spatial variability (Coates et al., 2015). Thermal sensors calculate the surface temperature by measuring the peak of radiation emitted in the thermal infrared region (TIR; 8 – 14 µm). The radiation measured is converted to temperature units based on the Stefan-Boltzmann law, which states that the amount of energy emitted by a body is related to its temperature following Eq. 1 where σ is the Stefan-Boltzmann constant ($5.67 \cdot 10^{-8}$ W · m^{-2} · K^{-4}) and ε the emissivity factor. Infrared thermal sensors operate in the TIR because most Earth objects have high emissivity in this region with ε = 0.94 – 0.98 (Bal et al., 2018).

$$Emittance = \varepsilon \cdot \sigma \cdot T^4 \qquad \text{(Eq. 1)}$$

Non-destructive and accurate assessment of the water status at field level can be achieved with a leaf porometer (Möller et al., 2007; Masseroni et al., 2017). These leaf clip sensors measure stomatal conductance (mmol · m^{-2} · s^{-1}), which depends on the stomatal aperture and regulates transpiration and gas exchange through the leaf stomata (Pietragalla and Pask, 2019). Leaf porometers take measurements by placing two known conductance elements in series with the leaf. The difference in humidity between both conductance elements is measured, and when the flux gradient reaches a steady state, the sensor calculates the leaf stomatal conductance (as reciprocal of resistance) (Toro et al., 2019). A leaf with a more open stomata allows greater conductance. Because the stomatal aperture varies during the daytime, it is recommended to take porometer and thermal measurements close to solar noon (Pietragalla and Pask, 2019).

Leaf clip optical sensors have been long used for non-destructive assessment of plant status at ground level (Yadava, 1986). The clip system allows collecting information of both the light transmitted and reflected by a plant leaf when the active sensor provides illumination in a small dark chamber (Gabriel et al., 2019). This system ensures full contact with leaf tissue and provides measurements independent to external light conditions (Arregui et al., 2006). These sensors present some limitations, such as the time consuming of the measurements and the non-uniform distribution of leaf and plant constituents that could lead to inconsistent results (Monje and Bugbee, 1992). The leaf clip sensors known as chlorophyll-meters are commonly used to measure leaf chlorophyll content, such as the Dualex® Scientific (Force-A,

Orsay, France). This sensor measures leaf chlorophyll content as the ratio between the light transmitted at two different wavelengths: one in the red edge (710 nm) absorbed by chlorophyll and another in the NIR (850 nm) as reference (Tremblay et al., 2012). Assessment of some epidermal polyphenol content, such as flavonols or anthocyanins, is also performed by this sensor. Polyphenols are secondary metabolites present in the leaf epidermis that avoid leaf damage by absorbing UV spectral radiation. Polyphenol production and accumulation increases under different stress conditions and particularly under N deficiency (Kandil et al., 2004). Dualex assessment of polyphenol content is based on the epidermis absorbance as the screening effect of polyphenols on chlorophyll fluorescence. For the assessment of polyphenols content, the Dualex sensor compares the NIR-induced chlorophyll fluorescence not absorbed by polyphenols and a light absorbed by polyphenols in the ultra-violet (UV; 375 nm) for flavonols or in the green (528 nm) domain for anthocyanin content assessment (Goulas et al., 2004). The ratio between chlorophyll and polyphenol content measured with Duakex is called the nitrogen balance index (NBI) and has been used to assess the N status of different crops, such as maize (Tremblay et al., 2007; Quemada et al., 2014) or wheat (Cartelat et al., 2005; Tremblay et al., 2010).

1.4. Crop monitoring with remote sensing

Canopy reflectance is affected by different crop characteristics such as vegetation structure, photosynthetic pigments content, nutritional status (Gabriel et al., 2017) or water content (Chen et al., 2005). For these reasons, remote sensing is a valuable tool for reducing the environmental impact of agricultural practices by estimating crop parameters such as chlorophyll and N content or aboveground biomass. A common technique for assessing crop parameters is to calculate and analyze spectral vegetation indices (VI) obtained from the reflectance spectrum. The VIs are calculated by combining the value of the reflectance at different wavelengths (Daughtry et al., 2000). Usually, the VIs are calculated with two to four wavelengths, and they are sensitive to different crop parameters depending on the regions of the spectrum used (Gabriel et al., 2017). Therefore, the identification of the most sensitive spectral region, as well as the most suitable and affordable sensor is important to optimize crop management strategies (Prey and Schmidhalter, 2019a).

Due to the strong absorbance of leaf pigments in the visible region, there are several VIs based on this region to retrieve pigment content, such as the ratio between reflectance at green and red (peak of chlorophyll absorbance), to retrieve chlorophyll content (Gamon et al.,

1992). Because the blue peak of chlorophyll absorbance overlaps the absorbance region of carotenoids, this peak is not usually used for chlorophyll estimation. Due to the strong influence of chlorophyll on the reflectance in the visible region, the estimation of other leaf pigments is more challenging (Sims and Gamon, 2002). The VIs based on the peak absorbance of chlorophyll at 660 – 680 nm have showed good correlation with chlorophyll content, however, this region tends to saturate with relatively low values of chlorophyll content (Gitelson et al., 1996). Consequently, different studies proposed VIs based on slightly longer wavelengths in the red edge region to estimate chlorophyll content, which saturates latter than the red region and it is also sensitive to chlorophyll activity (Sims and Gamon, 2002; Chen et al., 2010).

The spectrum of healthy vegetation is characterized by a low reflectance in the visible region and a high reflectance in the NIR region. On the other hand, the characteristic soil spectrum displays higher reflectance in the visible region than green vegetation and lower reflectance in the NIR (Daughtry et al., 2000). For this reason, VIs based on the red and NIR region have shown robust performance for biomass estimation, such as the well-known normalized difference vegetation index (NDVI; Rouse et al., 1974). Due to the reduction in sensitivity of the red band due to saturation, the VIs based on green and NIR bands showed promising results in biomass estimation (Gitelson et al., 1996).

Because most leaf N is contained in chlorophyll, remote sensing assessment of chlorophyll content during the growing seasons based on the VNIR region is used to predict crop N content (Wang et al., 2004; Mistele and Schmidhalter, 2008) and final grain N content (Zhao et al., 2005; Reyniers and Vrindts, 2006; Wang et al., 2004). However, their relationship varies with different factors such as crop development, genetic, environmental variables or due to the presence of N invested in proteins or other components different from chlorophyll that can lead to inconsistent results (Wood et al., 1993; Houlès et al., 2006; Berger et al., 2020). Direct measurement of crop %N with remote sensing platforms is challenging because it relies on the narrow range of the protein or N=H bond absorption feature located in the SWIR region (Curran, 1989). Therefore, high-resolution hyperspectral sensors that cover the SWIR region are the recommended method to directly estimate the N content (Berger et al., 2020).

Distinction between plant residue and bare soil in crop fields is important due to the negative impact of bare soil on soil quality and the benefits of conservation tillage practice (Delgado et

al., 2010; Mitchel et al., 2016; Hively et al., 2019). However, this distinction is challenging because it relies on the narrow absorption band of lignin and cellulose in the SWIR region (Daughtry, 2001; Fig 1). Although some studies demonstrated the ability of multispectral sensors to distinguish between crop residue and soil (Quemada and Daughtry, 2016; Dai et al., 2018), hyperspectral sensors are able to improve the performance by measuring reflectance in the narrow absorption band of lignin and cellulose (Daughtry and Hunt, 2008).

Furthermore, several challenges arise when using VIs to estimate the crop N status; for example, most VIs have been developed to estimate the chlorophyll content or aboveground biomass without considering the N dilution effect (Mistele and Schmidhalter, 2008). The optimal %N depends on the biomass and changes with crop development; therefore, accurate crop N status assessment requires information about both crop parameters (Lemaire et al., 2008; Sadras and Lemaire, 2014). Also, when determining crop N status at early growth stages (GS), before achieving full canopy cover, the soil background affects the reflectance (Fig 3), making it difficult to distinguish between the soil and plant spectral components (Chen et al., 2019). This is a critical issue because decisions based on N fertilization rates are usually made at early GSs (Basso et al., 2009). Therefore, reliable estimation of crop N status with remote sensing at early GS has been the focus of different research studies (Rodrigues et al., 2018; He et al., 2016). In this aspect, the “canopy N status indices” comprise VIs that compensate for the soil background effect by combining a structural and a photosynthetic pigment index, such as in the transformed chlorophyll absorption reflectance index (TCARI) normalized by the optimized soil adjusted vegetation index (OSAVI), forming the TCARI/OSAVI index (Haboudane et al., 2002), or in other cases by estimating the two components of the CDC using a planar domain approach (Clarke et al., 2001). The canopy chlorophyll content index (CCCI) is the most common planar domain index and uses a structural VI as a proxy for crop biomass and a chlorophyll-related VI as a proxy for crop N concentration (Barnes et al., 2000; Fitzgerald et al., 2006; 2010).

Fig 3. Red-Green-Blue (RGB) orthophoto of winter wheat at the beginning of stem elongation showing the soil background.

Solar-induced fluorescence (SIF) emission is a proxy of photosynthetic capacity and has been widely used to detect plant stress during the past few decades (Mohammed et al., 2019). The proportion of the emitted SIF and photosynthesis rates varies with the plant status; therefore, chlorophyll fluorescence has been used for the diagnosis of crop N (Camino et al., 2018) or water status (Zarco-Tejada et al., 2012). The SIF can be retrieved with passive spectroradiometers using the Fraunhofer Line Discrimination (FLD) approach. This method requires measurements of solar irradiance, reflectance (at least in the 650 – 800 nm range) and atmospheric O_2 absorption band, which is the band where solar spectral irradiance is attenuated due to atmospheric O_2 absorption. Despite several absorption bands can be found in the solar spectral irradiance, the O_2 absorption bands located at 687 and 760.6 nm are typically used to estimate SIF. This method calculates SIF by comparing radiance and irradiance at a wavelength inside and outside the O_2 absorption bands (Moya et al., 2004; Meroni and Colombo, 2006; Damm et al., 2011).

Both crop N and water status affect the spectral radiance reflected by the crop and may produce confounding effects on the acquired spectral reflectance, making difficult the identification of the crop deficiencies (Barnes et al., 2000; Osborne et al., 2002; Tilling et al., 2007; Cossani and Sadras, 2018). For this reason, it is necessary to identify spectral indicators that are sensitive to crop N status but are not affected by the water status and vice versa. In addition, the ability to estimate crop parameters through VIs is reduced when the crop is experiencing water stress (Schepers et al., 1996; Kusnierek and Korsaeth, 2015). Combining spectral and thermal information can be a solution to distinguish between the N and water status of the crop (Tilling et al., 2007). The leaf and air temperature difference was

proposed as a reliable method to detect plant water stress (Idso et al., 1977). However, information of plant and air temperatures are not enough because other environmental factors different from the water supply influence the plant temperature (Heitholt et al., 1991). To overcome this limitation, Idso et al. (1981) developed the crop water stress index (CWSI) by normalizing the leaf-air temperature difference with the vapour pressure deficit (VPD), allowing comparison between vegetation at different environmental conditions and dates. The CWSI is based on the ratio between actual and potential transpiration, calculated as the relationship between the distance to the minimum and maximum water stress baselines. One limitation arises when applying the CWSI with remote thermal sensors under partially vegetated canopies: the information is taken from soil-plant mixed pixels, and soil and plant thermal emission can be drastically different (Jackson et al., 1981; Rodriguez et al., 2005; Shivers et al., 2019). To solve this problem, Moran et al. (1994) proposed the water deficit index (WDI) based on the concept of the vegetation index-temperature (VIT) trapezoid, which is calculated by plotting in a two-dimensional space the canopy-air temperature difference and the ground cover simulated by a spectral VI.

Due to the sensitivity of the backscattering signal measured by SAR sensors to canopy structure and water content, different indicators have been developed for crop monitoring (Mandal et al., 2020). The signal from the cross-polarized channels (HV and VH) is sensitive to the structural parameters, being the intensity of the reflected light strong when multiple scattering dominates, or low with a single bounce scattering (i.e., bare soil). On the other hand, co-polarized channels (HH or VV) are more sensitive to water content or soil roughness (Moreira et al., 2013). The radar vegetation index (RVI) was proposed to identify vegetated areas using HV, HH, HV and VV SAR-channels (Kim and Van Zyl, 2009), and has shown accurate results for biomass assessment (Shang et al., 2013; Wiseman et al., 2014). The index value is close to zero for bare soils and increases with biomass production until its maximum value of one. Alternative formulations were proposed for dual-polarized SAR sensors using the VH and VV channels (Trudel et al., 2012), or the VV and VH channels (Mandal et al., 2020), like those provided by the satellite Sentinel-1 dual-polarized SAR.

Because the final harvest depends on different crop parameters in the earlier stages, the combination of different remote sensing indicators showed potential to predict the final crop traits in advance (Quemada et al., 2014; Rahman et al., 2018). Approaches based on remote sensing offer extensive information on the in-season crop parameters that affect crop

productivity, but it is necessary to identify the best remote sensing indicator for an accurate harvest prediction and to quantify the improvement in the prediction when combining indicators related to different crop parameters. Due to the variety of crop parameters that affect the final harvest, parametric statistical models that combine several remote sensing indicators are a common technique to estimate final crop traits and have provided reliable results for many crops, including wheat (Prey and Schmidhalter, 2019a; Zhao et al., 2019; Raya-Sereno et al., 2021a), maize (Quemada et al., 2014; Leroux et al., 2019), or rice (Liu and Sun, 2016). However, the error committed in the prediction is still high for many crop traits (Raun et al., 2005; Colaço and Bramley, 2018; Quemada et al., 2014), and particularly for those related to grain N concentration or grain quality (Rodrigues et al., 2018; Raya-Sereno et al., 2021a). Non-parametric models, such as random forest (RF) (Breiman, 2001) or artificial neural network (ANN) (Rumelhart et al., 1986), are expected to improve crop trait prediction thanks to their ability to find patterns, extract information, and build high-performance predictive models from large datasets (van Klompenburg et al., 2020). Because of this, the number of studies that combine remote sensing data with machine learning (ML) algorithms to estimate yield is increasing each year (Ma et al., 2019; Van Klompenburg et al., 2020). However, more studies using ML to estimate N-related traits are needed, particularly grain quality (Prey and Schmidhalter, 2019a; Aranguren et al., 2020; Raya-Sereno et al., 2021b).

The most widely used remote sensing approach to retrieve crop status is based on the link between VIs and plant constituents. However, this empirical technique relies only on the relationship between a few spectral bands, ignoring information from other wavelengths of the spectra and therefore, can lack of transferability (Camino et al., 2022). In addition, the values of the VIs can be affected by external factors, such as viewing geometry, background effect or structural composition (Zarco-Tejada et al., 2005). Because analyzing the entire spectrum allows retrieving more detailed information about specific crop parameters, the development of radiative transfer models (RTM) has gained importance in recent years (Berger et al., 2020). These models can overcome the limitations of the VIs by modeling the entire spectrum in a physic-based approach (Upreti et al., 2019; Féret et al., 2021). The RTMs simulate the absorption and scattering of electromagnetic radiation within the vegetation canopies while accounting for plant biochemical composition and canopy structure (Jacquemoud et al., 2009; Verhoef and Bach, 2007).

Several RTMs have been developed to retrieve plant biochemical and physical parameters at the leaf and canopy levels. One of the most widely used RTM for retrieving plant parameters at leaf level is the PRoperties Optique SPECTrales des feuilles (PROSPECT; Jacquemoud and Baret, 1990). This RTM simulates leaf hemispherical reflectance and transmittance over 400 – 2500 nm to estimate different leaf parameters: chlorophyll content (Cab), carotenoid content (Car), water content (EWT) and the leaf structure (N) (Atzberger et al., 2003). In the last years different versions of PROSPECT have been released to improve the accuracy of the estimations (Féret et al., 2017). The latest version is PROSPECT-PRO (Féret et al., 2021), which includes the monitoring of the three main leaf pigments: chlorophyll, carotenoids and anthocyanins. The RTMs that retrieve crop parameters at the canopy level perform by coupling leaf properties with canopy structure and composition. One of the first RTMs that performed at canopy level was the scattering by arbitrary inclined leaves (SAIL; Verhoef, 1984, 1985). The variables that are considered in the SAIL model are the leaf area index (LAI), leaf inclination distribution function (LIDF), soil reflectance, hot spot parameter and viewing and illumination angles. The PROSAIL model integrates the leaf (PROSPECT) and canopy (SAIL) optical properties to retrieve the biochemical and physical parameters of the crop (Jacquemoud et al., 2009). The recently released PROSAIL-PRO (Camino et al., 2022) couples the PROSPECT-PRO (Féret et al., 2021) and the 4SAIL (Verhoef and Bach, 2007) models.

Inversion methods that couple an RTM with machine learning regression algorithm (such as artificial neural network (ANN)) for retrieving crop biochemical and physical parameters of an observed spectrum are called hybrid methods and have shown promising results in the last years (Camino et al., 2022; Verrelts et al., 2019). This method relies on a spectrum dataset generated by the RTM simulating different combinations of plant biochemical and physical parameters, which is called “look-up table” (LUT). The machine learning algorithm identifies the crop parameters that best define the observed spectrum based on the link between the spectral properties and the crop parameters extracted from the training LUT (Verrelts et al., 2019). Hybrid methods applied with the PROSAIL model and remote sensing hyperspectral sensors showed promising results in winter wheat Cab and LAI (Danner et al., 2021) or N content assessment (Berger et al., 2020). However, the suitability of the hybrid RTM inversion method for retrieving winter wheat parameters using freely available multispectral satellite images requires further validation (Bossung et al., 2022).

When mapping crop land use at broad scale, the typical land use classes used to categorize the pixels in agricultural settings are green vegetation (GV), non-photosynthetic vegetation (NPV) and soil. However, various land use classes can be captured in a single pixel when using coarse spatial resolution imagery (Roberts et al., 2015; Almeida-Ñauñay et al., 2022). Assessment of cropland use can be performed with spectral mixture analysis (SMA) applications that model each pixel as fractions of different land cover classes based on pure spectra of each class, called endmembers (Adams et al., 1986). However, this technique can lead to fraction errors because traditional SMA does not consider endmember variability caused by varying chemical and physical conditions of the land use classes through the image (Somers et al., 2009). For these reasons, Roberts et al. (1998) developed multiple endmember spectral mixture analysis (MESMA) that "unmixes" images by decomposing each pixel into subpixel fractional covers allowing the number and types of endmembers to vary on a per pixel basis. Different studies have used MESMA for vegetation monitoring purposes; such as assessing crop fractional cover (Dennison et al., 2019), estimating water status as a function of fractional covers and thermal signature (Shivers et al., 2019), monitoring changes of urban and natural vegetation during drought (Tane et al., 2018a; Miller et al., 2022), mapping fire severity (Tane et al., 2018b) or improving the assessment of vegetation stress and aboveground biomass (Swatantran et al., 2011).

1.5. Satellite missions for land use and vegetation monitoring

The process towards sustainable agriculture should rely on technology economically viable for large-scale industrial cropping systems, as well as for smaller-scale systems (Basso et al., 2020). Aerial or proximal sensors usually provide better spectral resolution than satellite images. However, these sensors are less affordable and have spatial coverage limitations (Dian et al., 2021). In this aspect, the satellite imagery available with global coverage provides crop management support for all types of agricultural systems and land use monitoring at a regional, national or global scale. For these reasons, freely accessible satellite images for crop monitoring are receiving increasing attention (Zhao et al., 2019; Gómez et al., 2019).

The first aerial mission designed to map the Earth began in the 1930-1940s (Michaelsen, 2013). The first satellite launched for Earth observation that was suitable for precision agriculture purposes was Landsat 1 or Earth Resources Technology Satellite (ERTS) with two instruments: the Radio Corporation of America (RCA) and the Multispectral Scanner

(MSS). The Landsat 1 was launched by the National Aeronautics and Space Administration (NASA) on July 1972. Currently, the Landsat program is managed jointly by the NASA and the United States Geological Survey (USGS). Since then, a series of Landsat and other satellites have been launched to monitor the Earth's surface.

According to Sishodia et al., 2020; Segarra et al., 2020 and McAllister et al., 2022 there are 25 multispectral satellite missions operating for Earth observation (Table 1). The suitability of the products for crop monitoring can be analyzed on the basis of their spatial resolution, spectral region covered, time resolution and economic cost. The best spatial resolution of the multispectral sensors and the lowest revisit time are provided by the commercial satellites Skysat (1 m spatial resolution, < 1 day time resolution) and WorldView-3 (1.24 m in VNIR spatial resolution and 3.7 m in SWIR, < 1 day time resolution). One advantage of WorldView-3 (Fig 2b) images is the number and ranges of the spectral bands; while the multispectral Skysat sensor provides four spectral bands (blue, green, red and NIR), the WorldView-3 collects one panchromatic band, eight visible-NIR bands, and eight short-wave infrared (SWIR) bands, along with 12 Clouds, Aerosols, Vapors, Ice, and Snow (CAVIS) bands. The WorldView-3 allows extracting information at broad-scale, since it can measure 1200000 km^2 of the Earth surface in a day (DigitalGlobe, 2023). The sensing instrument of WorldView-3 has similar characteristics than the previously launched WorldView-2, but with an important addition of 8 SWIR bands that showed accurate results in mineral mapping (Kruse et al., 2015), identification of bare soil and crop residue (Quemada et al., 2018), in crop monitoring (Sagan et al., 2021) and in assessing water content (Hunt et al., 2016). The WorldView-3 was launched on August 2014 to operate in a nearly circular and sun-synchronous orbit at an altitude of approximately 617 km.

Regarding the open-access satellite imagery, the launch of the Sentinel-2 constellation allowed improvements in spectral bands, revisit time and spatial resolution in comparison with previously launched open-access multispectral satellite missions (Segarra et al., 2020; Table 1). The Sentinel-2 constellation (Fig 2a) is managed by the European Space Agency (ESA) as part of the European Union Copernicus Program, and is composed of two platforms: Sentinel-2A and Sentinel-2B that were launched in 2015 and 2017, respectively. The Sentinel-2 satellites are identical and operate in a Sun-synchronous orbit at a mean altitude of 786 km. Combining both Sentinel-2 platforms, this mission provides a revisit time of two to five days between -58º to +83º latitude, supporting near-continuous monitoring of

vegetation processes (Schulz et al., 2021a). The spatial resolution of Sentinel-2 upgraded the resolution of Landsat 8 OLI instrument from 30 to 10 m in the VNIR bands, and from 30 to 20 m in the SWIR bands. In addition, Sentinel-2 provides three spectral bands covering the red edge regions, which are useful for assessing chlorophyll content (Xie et al., 2019). Sentinel-2 has been extensively used for land use and vegetation monitoring (Cisneros-Araujo et al., 2021; Immitzer et al., 2016; Clevers et al., 2017). Moreover, convolution of Sentinel-2 bands with ground-truth hyperspectral information confirmed the high accuracy of reflectance acquired by the satellite sensor and, therefore, the potential for crop trait estimation (Prey and Schmidhalter, 2019a). In September 2021, Landsat-9 EO satellite was launched with instruments onboard very similar to those in Landsat 8, but with an improvement in radiometric and geometric characteristics. Landsat 8 and 9 satellites provide a revisit time of 8 days. An advantage of recent Landsat satellites is that they carry a sensor to measure two bands in the TIR (USGS, 2023a).

Table 1. Characteristics of the multispectral satellites currently orbiting Earth according to Sishodia et al., 2020; Segarra et al., 2020; McAllister et al., 2022 and ESA 2023c.

Satellite	**Year launched**	**Spatial resolution**	**Temporal resolution**	**Comercial/ Open access**
Landsat 9	2021	> 30 m	8 days (with Landsat 8)	Open access
PlanetScope	2016	3 m	1 day	Commercial
Sentinel-2	2015	10, 20 m	2-5 days	Open access
KOMPSAT-3A	2015	2.2, 5.5 m	1.4 days	Commercial
TripleSat	2015	3.2 m	1 day	Commercial
Spot-7	2014	6 m	1 day	Commercial
WorldView-3	2014	1.24 m VNIR y 3.4 m SWIR	< 1 day	Commercial
Landsat 8	2013	> 30 m	17 days	Open access
SkySat constellation	2013	1 m	< 1 day	Commercial
Pleiades-1B	2012	2 m	1 day	Commercial
KOMPSAT-3	2012	2.8 m	1.4 days	Commercial
Spot-6	2012	6 m	1 day	Commercial
Pleiades-1A	2011	2 m	1 day	Commercial
WorldView-2	2009	1.4 m	1.1 days	Commercial
RadidEye	2008	6.5 m	1 - 5.5 days	Commercial
GeoEye-1	2008	1 m	1.7 days	Commercial
KOMPSAT-2	2006	4 m	5.5 days	Commercial
Terra-ASTER	2000	15, 30 m	16 days	Open access
MODIS	1999	> 250 m	1 – 2 days	Open access

Satellite imagery covering the SWIR region with a wide footprint is an effective solution for crop land use monitoring because it can identify not cultivated crop fields and tillage practices (Goga et al., 2019). The spectral resolution of WorldView-3 (Quemada et al., 2018; Hively et al., 2019) and Sentinel-2 (Dai et al., 2018) in the SWIR region was demonstrated to be useful for monitoring crop residue in agricultural settings. However, hyperspectral sensors can improve the performance by measuring reflectance in the narrow absorption band of lignin and cellulose (Daughtry and Hunt, 2008). A new generation of hyperspectral satellites begun at the beginning of this century. According to Qian (2021), a total of 21 spaceborne hyperspectral sensors have been deployed into space to orbit the Earth. Currently, there are seven hyperspectral sensors onboard satellites that cover the SWIR region: The Advanced Hyperspectral Imager onboard the Chinesse GaoFen-5 satellite (AHSI), the Hyperspectral Imager onboard the Indian Mini Satellite-1 (HySI), the Italian PRecursore IperSpettrale della Missione Applicativa (PRISMA), the Hyperspectral Image Suite onboard the Japan Experiment Module on the International Space Station (HISUI), the HyperSpectral Imager of the LEWIS mission developed by NASA and TRW (HSI/Gisat-1), the Environmental Mapping and Analysis Program of the German Hyperspectral satellite mission (EnMAP), and the NASA's Earth Surface Mineral Dust Source Investigation on the International Space Station (EMIT). To our knowledge, the ability of these missions to monitor NPV was tested in AHSI (Tian et al., 2021) and PRISMA (Loredana et al., 2021). New opportunities for land use monitoring will arise with the upcoming spaceborne hyperspectral missions such as the Surface Biology and Geology Mission (SBG; Cawse-Nicholson et al., 2021), Copernicus Hyperspectral Imaging Mission for the Environment (CHIME; Berger et al., 2021) and Landsat Next (Hively et al., 2021). The SBG is a NASA mission that the 2017 – 2027 National Academies' Decadal Survey, *Thriving on Our Changing Planet* recommended as a "Designated Targeted Observable" due to the need to acquire high-resolution images coupling a hyperspectral VSWIR and thermal infrared data in a sub-monthly temporal resolution at global scale (National Academy of Sciences, Engineering and Medicine, 2018). The Decadal Survey recommends for the VSWIR sensor a 30 – 45 m spatial resolution, < 16 days temporal resolution and 10 nm spectral resolution. The suggested characteristics for the thermal instrument are more than five bands in the TIR, one band at 4 µm, ≤ 60 m spatial resolution and ≤ 3 days of temporal resolution. The final characteristics will be determined in the last phases of the project. For this purpose, the Airborne Visible/Infrared Imaging-Spectrometer (AVIRIS; 350 – 2500 nm spatial resolution; ~ 10 nm spectral resolution; Green et al., 1998) sensor is currently being used in the SBG preparatory airborne campaigns to

demonstrate the importance and applications of the spaceborne VSWIR sensor, showing valuable performance in crop monitoring (Dennison et al., 2019; Shivers et al., 2019). AVIRIS has been flown in four aircrafts; however, the most common is the NASA ER-2 jet (Fig 2c, d), which flies at higher altitude than the aircraft commonly used in remote sensing due to its characteristic combustion method (~ 20 km above sea level) (JPL, 2023b). AVIRIS was developed by the Jet Propulsion Laboratory (JPL) in 1984, and was the first operational airborne hyperspectral sensor when the flight took place in 1986 on board the NASA ER-2 at a 20 km altitude (Qian, 2021). Many modifications and upgrades have been applied to AVIRIS since 1984 (Eastwood et al., 1991; Green et al., 1993; 1998; Cawse-Nicholson et al., 2021). Spectrum reflectance of green vegetation, non-photosynthetic vegetation and soil extracted from an AVIRIS image can be found in Fig 1.

Although spaceborne spectroradiometers have been successfully used for crop monitoring, they are sensitive or restricted by atmospheric conditions (Mandal et al., 2020). The SAR information has proven to be a reliable data source in all weather conditions despite the interaction between microwave radiation and canopy is complex (McNairn et al., 2016) and requires many radiometric corrections and processing, such as speckle correction (Liu et al., 2021). The first SAR satellite launched was the Seasat dedicated to analyze the oceans. An important improvement in Earth monitoring with SAR technology took place with the European Remote Sensing 1 and 2 (ERS-1/2) launched in 1991, and the Japanese Earth Resources Satellite 1 (JERS-1) launched in 1992. However, these sensors transmitted and received microwave radiation only in a single linear polarization (VV and HH, respectively) (Dobson et al., 1996; Kerbaol et al., 1998). The next generation of SAR satellites was able to collect different channels in the linear polarized and in the cross-polarized channels (HV and VH) at different frequencies (mainly at X, C and L) (Paek et al., 2020).

The Copernicus Sentinel-1 Synthetic Aperture Radar (SAR) mission was an unprecedented opportunity for intense radar mapping of the Earth due to the improvements in time resolution and spatial coverage, combined with the free availability (Lanari et al., 2020). The Sentinel-1 constellation consists of two satellites, Sentinel-1A and Sentinel-1B that were launched in 2014 and 2016, respectively, and were positioned to have the same ground track coverage, allowing a revisit time of 6 days due to the orbital separation of 180º (Liu et al., 2019a). The acquisition mode of the Sentinel-1 sensor is based in the interferometric wide (IW) swath; this method integrates three subpaths of terrain observed by the progressive

scans (TOPS) technique to generate a wider final product (footprint = 250 km; De Zan and Guarnieri, 2006). The final product consists of cross-orbit images of dual-polarized (VV-VH) backscatter in the C band in the ascending and descending orbits. Despite dual-polarized sensors provide less polarimetric information than quad-polarized sensors, they allow larger width swath acquisition with less volume of data that reduce processing time (Ainsworth et al., 2009).

Due to the variety of spaceborne sensors available, different studies proposed the combination of sensors with different spectral, spatial or temporal resolution (Knipper et al., 2019; Dian et al., 2021; Zhu et al., 2018). Coupling information can be valuable for improving time series monitoring, such as changes in land use or in vegetation status, and for validating the information acquired with other sensors at different resolutions (Peddle et al., 2001). When coupling images obtained with different sensors at different dates, discrepancies can be found due to differences in viewing and illumination angles (Fig 4). These angles are an important issue that must be addressed since they may lead to spectral differences when compared to nadir-looking acquired spectra due to bidirectional reflectance distribution function (BRDF) effects of non-lambertian surfaces (Pacifici et al., 2014; Cross et al., 2018). Thus, the spectral intercomparison between images obtained with different platforms is challenging. Under a given off-nadir view angle, each spectral region is affected differently; therefore, it is necessary to evaluate how each spectral band performs under different viewing and illumination conditions for a given surface. Convolution of satellite bands from ground-truth nadir-looking hyperspectral data collected during field surveys is a reliable method for validating satellite-acquired measurements (Milton et al., 2009).

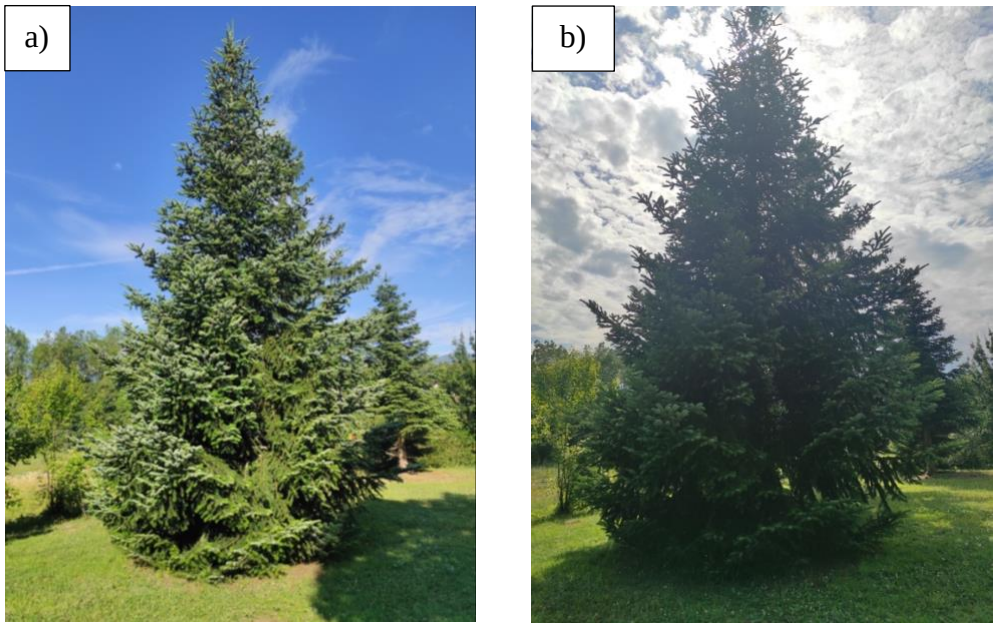

Fig 4. Red-green-blue photography of the same tree a) showing the sun-illuminated side with brighter colors than b) the unilluminated side.

In addition to irradiance, viewing and illumination conditions, Earth land surface imagery registered by passive spaceborne sensors requires compensating by the radiometric disturbances that take place in the overlying atmosphere (Liang and Wang, 2019). The main disturbances are due to absorption and scattering phenomena in the atmosphere that result from aerosols, water vapor, and other gaseous constituents (Gilabert et al., 1994). These disturbance effects must be compensated or corrected for accurate crop status monitoring, time series analysis or inter-sensor comparisons (Ariza et al., 2018). This correction is particularly important for biochemical and physical parameters extracted from multispectral or hyperspectral images based on surface reflectance (Liang et al., 2002). The surface reflectance values acquired by a satellite image can be quantitatively validated with ground-truth spectral reflectance collected by field surveys using a hand-held spectroradiometer at a particular location and time (Milton et al., 2009). This validation method can be applied in different types of land use, including vegetation (Cross et al., 2018; Sola et al., 2018) or inland water bodies (Martins et al., 2017; Warren et al., 2019; Wang et al., 2019a).

There are two main approaches for performing atmospheric corrections of satellite imagery, referred to as empirical and model-based methods (Martins et al., 2017). Empirical methodologies, such as Dark Object Subtraction (Chavez, 1988) or others described in Gao et al. (2009) are mainly scene-based and require reflectance measurements that are either in situ

or image derived (Gilabert et al., 1994). In contrast to empirical atmospheric correction procedures, physical-based atmospheric-RTMs can convert image radiance into image surface reflectance while compensating atmospheric disturbances. The corrections of the atmospheric-RTM are based on physical models of atmospheric absorption and scattering by the different atmospheric constituents such as gases and aerosols (Griffin and Burke, 2003; Liang and Wang, 2019). These physic-based models requires the atmospheric constituents measured at the time of the image acquisition to derive their contributions to the remotely measured signal. Thus, they require input values for the modeled atmospheric constituents, such as water vapor, aerosol or O_3 concentration, for accounting for the effects of both absorption and scattering in the different spectral regions.

Atmospheric constituents at the time of satellite acquisition can be accurately measured with other spaceborne sensors designed for this purpose. In this regard, the open-access MODerate resolution Imaging Spectroradiometer (MODIS) instrument on board the twin Terra and Aqua satellites launched in 1999 and 2002, respectively, is one of the most commonly used sensors for this purpose (NASA, 2023b; Vermote et al., 2016; Martins et al., 2017). The Level 2 MODIS atmosphere product provides six different atmospheric characteristic measurements: aerosol (such as type and aerosol optical thickness (AOT)), atmospheric water vapour, physical and radiative properties of clouds, atmosphere profile (such as temperature and moisture) and cloud mask (NASA, 2023c). Due to the synchronous orbiting path of the twin satellites, these products are available for a specific location every one or two days.

Commonly used atmospheric-RTM tools include MODTRAN (MODerate resolution atmospheric TRANsmission; Berk et al., 1987), 6S (Second Simulation of a Satellite Signal in the Solar Spectrum; Vermote et al., 1997), FLAASH (Fast Line-of-sight Atmospheric Analysis of Hypercubes; Adler-Golden et al., 1999), and ATCOR (Richter, 1996; Liang and Wang, 2019). An important feature of MODTRAN and FLAASH is their ability to compensate for atmospheric effects recorded at the Top of Atmosphere (TOA) for a wide range of space-borne optical sensors. These packages convert TOA radiances into bottom-of-atmosphere (BOA) reflectance or surface reflectance while accounting for the sensor view and illumination geometry. In recent years, new system-based algorithms of atmospheric-RTMs have been released for atmospheric corrections. This is the case of the atmospheric correction package Sen2Cor, developed in the framework of the Copernicus Program for Earth Observation and embedded in the Sentinel Application Platform (SNAP) released by

the European Space Agency (ESA, 2023d). Sen2Cor corrects multispectral Sentinel-2 Level-1C TOA products for atmospheric scattering and absorbance, delivering a Level-2A surface reflectance product (Main-Knorn et al., 2017), but does not allow correcting for other types of satellite imagery.

1.6. Assessment of wheat nitrogen and water status. Application to wheat management

According to FAOstat, in 2018, 15% of the total area harvested in the world by primary crops was wheat, which received 17% of the total N fertilizer consumption; the highest percentage of any crop (FAO, 2023). Wheat is one of the crops that contribute the most to dietary calories and proteins worldwide (20%) (Shiferaw et al., 2013). Therefore, improving assessment of wheat yield and grain protein concentration is key for global food security, and optimizing the N applied to wheat in terms of quantity and timing must be studied to ensure food security while maintaining environmental sustainability (Arregui et al., 2006; Tester and Langridge, 2010). Wheat grain quality is established according to the grain protein concentration, which is the conversion of grain N concentration (McMullan et al., 1988; Mariotti et al., 2008). Therefore, grain N concentration determines its price in the market and the profitability for the farmers (Wang et al., 2019b). An important source of grain N is the N located in the vegetative organs that is translocated to the grain. The efficacy of this translocation determines the final grain quality (Kichey et al., 2007). Yield and grain quality maps over different years can be used as a surrogate for soil testing to define management zones (Taylor et al., 2005; Yuzugullu 2020). Site-specific identification of grain protein content would allow selective harvesting to segregate grains according to their quality to obtain the highest benefits on the market (Long et al., 2008; Rodrigues et al., 2018).

According to Meier (2001), there are 10 different phenological growth stages (GS) during the winter wheat life cycle (Fig 5): germination (GS0), leaf development (GS10), tillering (GS20), stem elongation (when nodes in the stem can be detected; GS30), booting (GS40), heading or spike emergence (GS50), flowering (GS60), fruit development (GS70), ripening (GS80), and senescence (GS90). Between leaf development and the beginning of flowering, the winter wheat canopy is developed and is characterized by a fast growth. Stems developed in these stages have a great contribution to biomass in terms of weight, therefore, according to the harvest index, a correct stem development is important for increasing yield. In winter wheat, the harvest index was found to vary between 28 and 46 % (Singh and Stoskopf, 1971).

There are two main sources of N that are translocated to the grain: The N accumulated in vegetative organs before flowering and the N uptake from soil during flowering (Gaju et al., 2014). The N stored in vegetative organs represents approximately 50 – 95 % of the final grain protein, and therefore translocation of N from vegetative organs to the grain plays an important role in grain quality (Kichey et al., 2007). Synchronizing the timing of fertilizer application with winter wheat demand is important to increase NUE, yield and grain protein content (YARA, 2023). The winter wheat maximum nutrient demand is reached during the fast canopy development period (~ 6 months after sowing), so a common strategy is to split into two topdressing N fertilizer applications: one at the beginning of tillering and the rest during stem elongation (Arregui et al., 2006). Additionally, N foliar application around flowering may be applied to increase grain protein content (Arregui et al., 2006). Consequently, it is crucial to determine crop N status at early GSs to adjust N fertilizer rates (Raun et al., 2005; Ravier et al. 2017). The N and water availability between late boot stage and early grain filling determine N translocation to the grain (Ottman et al., 2000), so wheat status information is also crucial for guiding management strategies during these GSs (Zhao et al., 2005; Diacono et al., 2013).

A common strategy to identify the wheat N status is to calculate the NNI using the CDC proposed for winter wheat (Justes et al., 1994). However, some studies found that this dilution model overestimates N deficiency in wheat under water stress. For this reason, efforts have been made to develop an alternative CDC for winter wheat under water deficit regimes (Hoogmoed and Sadras, 2018; Neuhaus et al., 2017) or for spring wheat, often exposed to limited water availability (Ziadi et al., 2010).

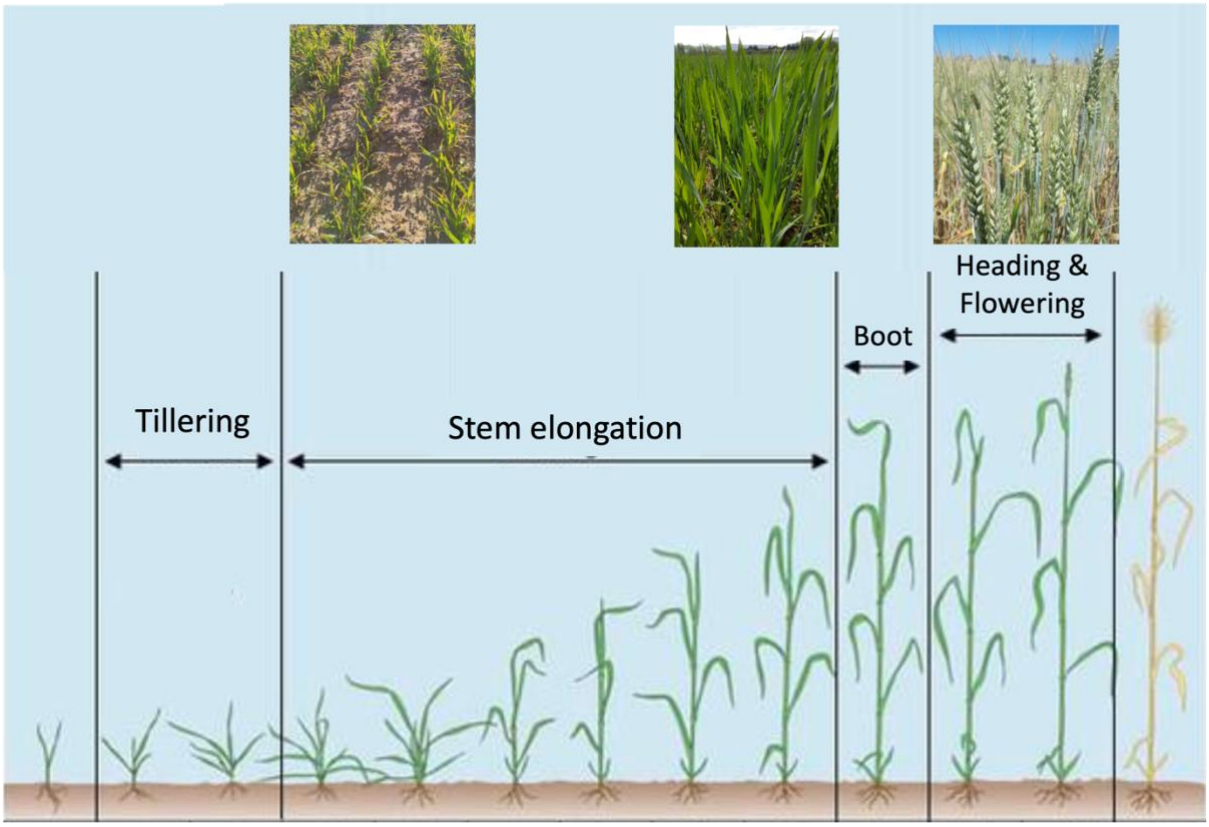

Fig 5. Winter wheat growth stages. Scheme downloaded from University of Illinois Extension.

Chapter 2: Research objectives

The main objective of this Ph.D. thesis is to enhance the sustainability of cropping systems by improving the performance of different remote sensing techniques for crop monitoring at field and regional scale. A field experiment was conducted in Aranjuez (central Spain) to achieve the specific objectives related to field-scale monitoring (Objectives 1, 2, 3, 4). A dataset from California was used to fulfill the objective related to regional-scale monitoring (Objective 5). For a better understanding of the workflow followed in this thesis, see Fig 6.

The specific objectives pursued to address the main objective of the thesis are as follows:

Objective 1: simultaneous estimation of winter wheat N and water status for adjustment of N fertilizer and irrigation.

a) find a remote sensing indicator able to assess winter wheat N status at early growth stages by reducing soil background noise.

b) assess the ability of different spectral and thermal indicators to detect the crop N and water status with minimum confounding effects.

Objective 2: improve the prediction of winter wheat traits (yield, grain protein concentration and grain N output).

a) quantify the improvement in the prediction of winter wheat traits when combining indicators related to different crop parameters.

b) compare the feasibility when using indicators derived from airborne hyperspectral and thermal sensors, and from the freely available Sentinel-1 and Sentinel-2 satellites.

Objective 3: compare the performance of vegetation indices and a hybrid artificial neural network-PROSAIL-PRO method for winter wheat N status estimation and traits prediction.

a) evaluate the feasibility of applying a hybrid artificial neural network-PROSAIL-PRO method to Sentinel-2 imagery for retrieving winter wheat crop parameters at different growth stages.

b) analyze the performance of estimating winter wheat N status and traits by combining the retrieved variables.

Objective 4: analyze the accuracy of the Sentinel-2 and WorldView-3 signal in winter wheat monitoring.

a) assess the reliability of the surface reflectance measured by Sentinel-2 and WorldView-3 satellites for winter wheat monitoring after applying different atmospheric correction approaches.

b) propose and validate an empirical signal normalization procedure for compensating for the off-nadir view angle-induced effects on the surface reflectance of WorldView-3.

Objective 5: validate the application of remote sensing imagery for landscape planning at regional scale.

a) assess the reliability of the AVIRIS imagery processed with multiple endmember spectral mixture analysis (MESMA) for cropland use change monitoring by comparing it with official crop reports.

b) determine the agricultural trends and quantify the non-cultivated areas during a multi-year drought period and post-drought period in the Central Valley, California.

The results of this thesis are showed in Chapter 4, which is structured in six sections that achieve the above-mentioned objectives:

Chapter 4.1: Agronomical variables obtained in the Aranjuez field experiment.

- Objective 1
- Objective 2
- Objective 3

Chapter 4.2: Simultaneous assessment of nitrogen and water status in winter wheat through planar-domain vegetation indices using hyperspectral and thermal sensors.

- Objective 1

Chapter 4.3: Winter wheat traits prediction through ensemble modeling approaches using aerial and satellite imagery.

- Objective 2

Chapter 4.4: Quantification of winter wheat nitrogen status and traits through radiative transfer models using Sentinel-2 imagery.

- Objective 3

Chapter 4.5: Sentinel-2 and WorldView-3 atmospheric correction and signal normalization based on ground-truth spectroradiometric measurements.

- Objective 4

Chapter 4.6: Drought impact on cropland use monitored through multiple endmember spectral mixture analysis using AVIRIS imagery.

- Objective 5

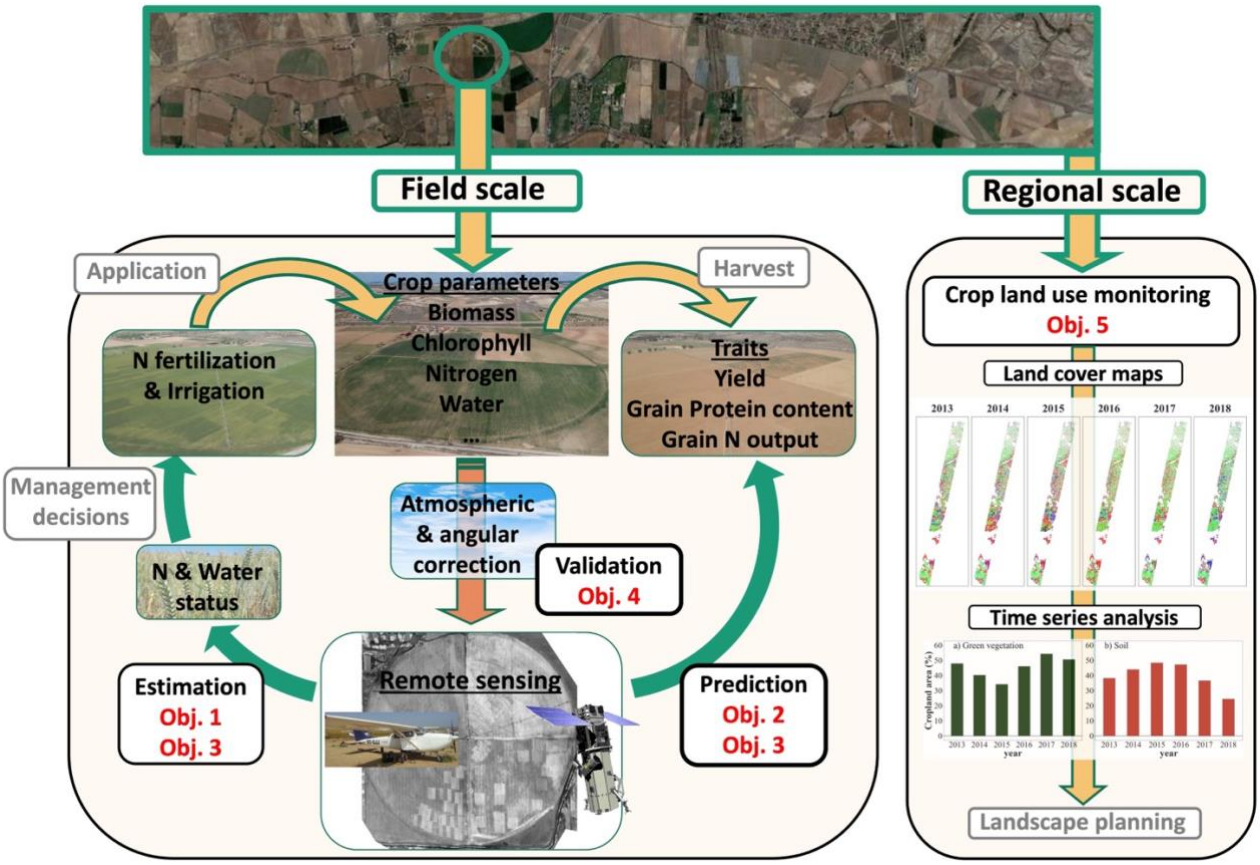

Fig 6. The general workflow followed in this thesis to fulfill the specific objectives (Obj).

Chapter 3: Materials and methods

3.1. Study sites

3.1.1. Aranjuez, Spain

A field experiment with winter wheat (*Triticum aestivum* L.) was carried out at La Chimenea Research Station near Aranjuez (Madrid, Spain; Fig 7) during two consecutive growing seasons: 2017/2018 and 2018/2019 (hereinafter referred to as 2018 and 2019, respectively). The experimental site is bounded by the geodetical coordinates of the upper right {φ = 40° 04' 4.97" N, λ = 3° 32' 24.89" W} and lower left {φ = 40° 03' 47.73" N, λ = 3° 32' 0.45" W} corners of the study area. These coordinates are given in the European Terrestrial Reference System 1989 (ETRS89) geodetic system. The study site is flat (slope < 1%) and the soil, representative of the medium Tajo River terraces, is mapped as *Haplic Calcisol* (World Reference Base for Soil Resources, 2014) with a pH ≈ 8.1, medium organic matter content (topsoil organic C 1.01 g kg^{-1}), and a silty clay loam texture with low stone content throughout the soil profile. The climate of the area is classified as cold semi-arid (Bsk) according to the Köppen classification (World maps of Köppen-Geiger climate classification, 2023). Usually, spring and summer are characterized by a substantial water deficit that is compensated by irrigation since April. High interannual variability is characteristic of the region; therefore, relevant climate variables were recorded hourly throughout the experimental period with a weather station located at the farm. The mean annual temperature is 14.8 °C and the rainfall is 360 mm (Fig 8). However, the 2018 experimental year was unusually wet (342 mm from 1 November 2017 to 20 July 2018).

Fig 7. Field experiment at La Chimenea Research Station, Comunidad de Madrid, Spain

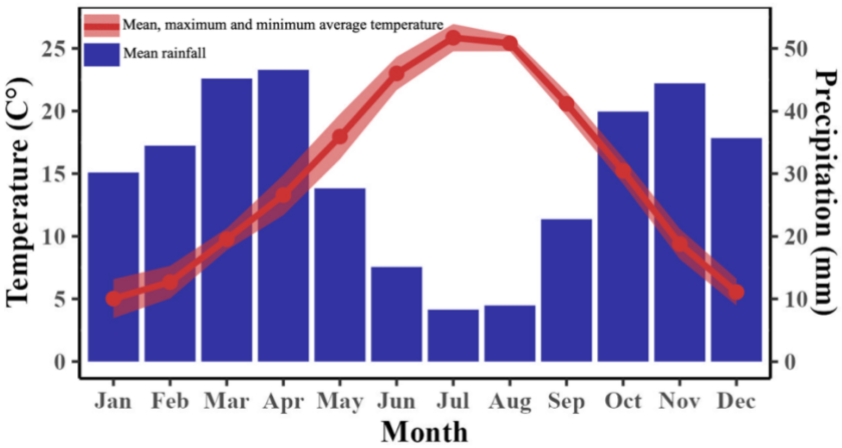

Fig 8. Average monthly precipitation (mm), mean, maximum and minimum temperature (ºC) in Aranjuez from 2009 to 2019 downloaded from MAPA, 2023

Each year, the study site was a different quarter of a field irrigated by a circular pivot (220 m radius) that enables an adjustable and uniform water delivery (Fig 7). At the beginning of each growing season (02/11/2017; 17/11/2018) a different quarter of the field was sown with winter wheat (*Triticum aestivum* L, cv. Nogal) at a seeding rate of 220 kg seeds ha^{-1}. The soil uniformity and low levels of soil N inorganic content were ensured by establishing a maize crop (*Zea mays* L.), that did not receive N fertilizer, before both wheat experiments. In addition, no organic amendments were applied during the 4 years before the experiments.

A factorial experiment was established in 32 plots (22 × 22 m in 2018 and 25 × 25 m in 2019) randomly assigned into four N and two water levels, with four replications (Fig 9). The plots were georeferenced with real-time kinematic (RTK) through the National Geodetic Network of Reference Stations GNSS (ERGNSS) technique, using the permanent station of Sonseca (Toledo) and Aranjuez (Madrid) due to their proximity, with a Topcon HiPer Pro receptor® (Topcon Singapore Holdings Pte. Ltd, Singapore) (Fig 11b).

The plots were randomly assigned to four N levels and two water levels, with four replications (Fig 9). The four N levels were established by applying N fertilizer (calcium ammonium nitrate, CAN) from 0 to no limiting rates for crop growth, in 50 kg N ha^{-1} increments. The wheat N requirements were calculated as the product of the expected grain yield (6.5 Mg ha^{-1}) times an extraction coefficient of 30 kg N Mg^{-1} (Arregui et al., 2006). Before the first fertilizer application each year, soil samples from 0 – 0.6 m in 0.2 m depth intervals were taken from each plot to determine the soil mineral N content (kg N ha^{-1}) and to adjust the amount of N fertilization accordingly (Fig 11a). Soil subsamples were extracted

with 1 M KCl, and soil extracts were analyzed for N-NH_4^+ and N-NO_3^- (Keeney and Nelson, 1982). Soil mineral N was calculated as the addition of N-NH_4^+ and N-NO_3^- content in the 0.60 m, and was 36 kg N ha^{-1} in 2018 and 57 kg N ha^{-1} in 2019. The N available in each treatment was calculated by adding the N applied with the fertilizer to the soil mineral N content before fertilizer application. Prior to sowing wheat, phosphorus (50 kg P ha^{-1}) and potassium (70 kg K ha^{-1}) were applied to the field to warrant no limitations. The fertilizer rates applied to each N level were 0, 50, 100 and 150 kg N ha^{-1} for N0, N1, N2 and N3, respectively, in 2018; and 0, 42, 92 and 142 kg N ha^{-1} in 2019. N fertilizer was hand-broadcasted to plots in two growth stage (GS; Meier, 2001): two thirds at tillering (GS22; 25/01/2018 and 30/01/2019) and one third at stem elongation (GS35; 22/03/2018) or booting (GS43; 15/04/2019).

To evaluate the effect of water availability on crop status, half of the plots were irrigated at the beginning of flowering (GS63) in both experimental years (Fig 11e). In 2018, half of the plots received 25 mm of water on May 8th. An accumulated rainfall of 46 mm between May 24th and 29th 2018 replenished soil water storage mitigating crop water stress. In 2019, half of the plots were irrigated in two events (30 mm on May 7th and 9 mm on May 10th). Additionally, due to the scarcity of winter rainfall in 2019 all plots were irrigated twice with 25 mm at GS32 (13/03/2019) and GS39 (15/04/2019). In the text, the plots that did not receive irrigation at flowering are referred to as W1, while the others as W2.

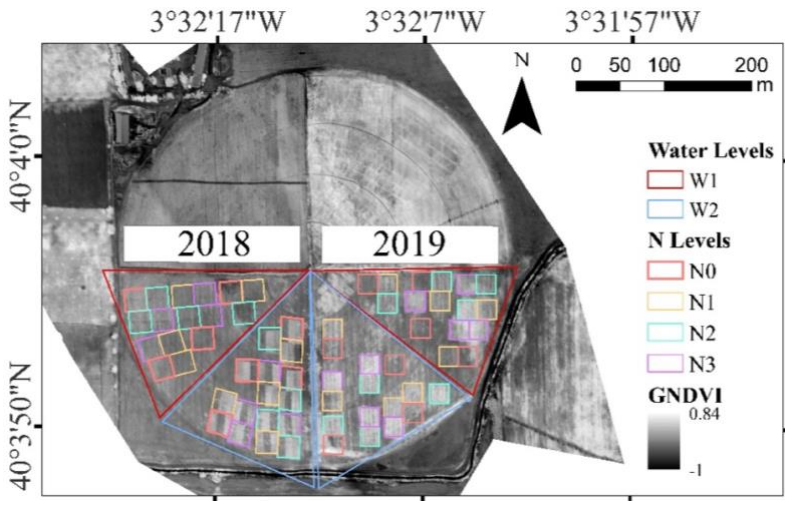

Fig 9. Green normalized difference vegetation index (GNDVI) calculated over the Aranjuez study site with the airborne hyperspectral imager at flowering 2019. The 32 plots of each year separated by nitrogen rates (N0, N1, N2, N3) and water levels (W1, W2) are shown.

3.1.2. Central Valley, California

This thesis analyzed the agricultural patterns in a region of the Southern Central Valley (California, USA) with high abundance of crop fields (Fig 10). The Central Valley (52000 km^2) is one of the most productive regions in the world; growing more than 250 different crops that comprise one-sixth of the USA irrigated land (Faunt, 2009). The study area is located at the Tulare Lake Hydrologic region, which is one of the driest regions of the Central Valley and includes some of the most important agricultural producing counties in California (California Department of Food and Agriculture, 2016): Kern (26% of the study area), Kings (28%), Tulare (33%) and Fresno (13%). The climate is characterized as Mediterranean with warm and dry summers, and mild and wet winters. The mean annual temperature was 13 ^{o}C and the mean annual precipitation 533 mm in the 2000 – 2010 period (Climatic data in Tulare, 2022).

The agricultural patterns were analyzed in the 2013 – 2018 period because it includes the historical drought experienced in California during 2012 – 2016 (Warter et al., 2021). One of the sectors that suffered most from the drought was agriculture, particularly in the southern portions of the Central Valley of California (Lund et al., 2018). The drought intensity was analyzed using the weekly climatic conditions reported by the United States Drought Monitor (2022a) for Kern, Kings and Tulare counties. These reports provide the relative area of the selected county that is experiencing each drought severity level (abnormally dry, moderate drought, severe drought, extreme drought and exceptional drought). The classification of the drought intensity levels is based on several indicators including soil moisture, precipitation, streamflow, or impact reports, among others. More detailed information about the drought severity levels can be found in Supplementary Material S6.

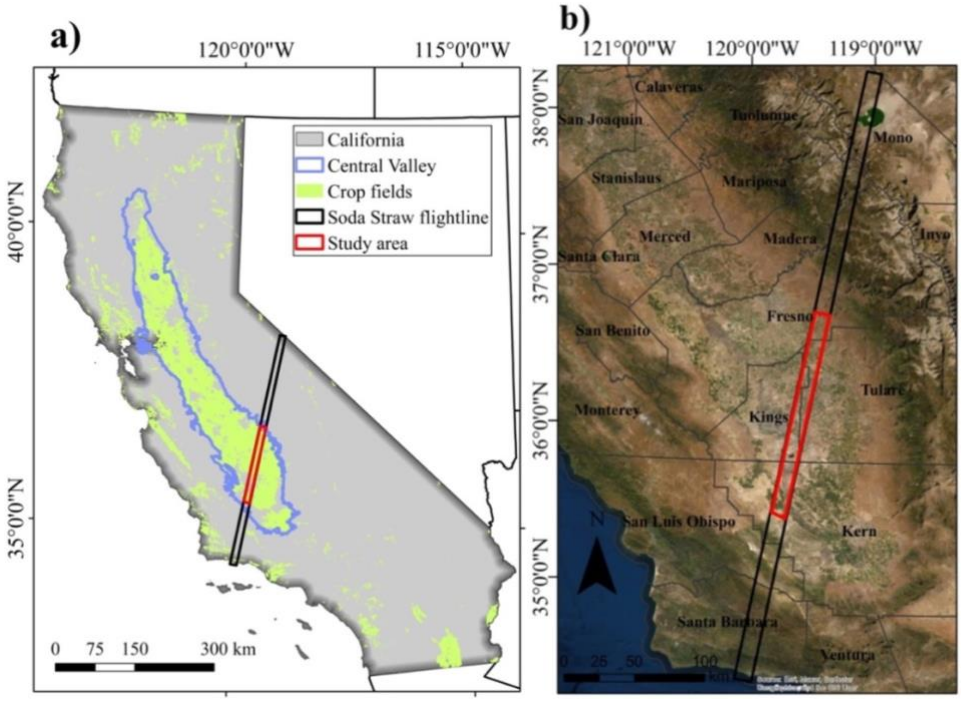

Fig 10. a) Map of California showing the location of the crop fields and the study area within the "Soda straw" flightline that crosses a Southern part of the Central Valley, and b) more details of the study area showing the counties. Crop fields shapefiles were downloaded from California Department of Water Resources (2022), and the boundaries of the Central Valley from United States Geological Survey (2022a). Source basemap: Esri, Maxar, Earthstar Geographics.

3.2. Agronomical variables

3.2.1. Aranjuez, Spain

The effect of N and water levels on winter wheat was determined by analyzing two samples (0.5 x 0.5 m) of aerial biomass per plot collected three times each experimental year at mid stem elongation (GS34, 22/03/2018 and GS32, 11/03/2019), final stem elongation (GS37, 17/04/2018 and GS39, 12/04/2019), and flowering (GS65 both years, 11/05/2018 and 13/05/2019, respectively) (Fig 11c; Table 2). The samples were dried at 65 ºC during 48 h and weighed to determine aerial biomass (shoot + leaves; kg ha^{-1}). A subsample was analyzed for calculating N concentration (%N) using the Dumas combustion method (LECO FP-428 analyzer, St. Joseph, MI, USA). At flowering, the spikes and the rest of the aerial biomass were analyzed separately. The first sampling campaign was conducted between the first and

second N fertilizer application, as it might be important for adjusting the second N application. The second campaign corresponded to maximum ground cover, reached just before flowering, and crop N status could indicate if foliar N application increases grain protein concentration (Angus and Fisher, 1991). The third sampling campaign was carried out at full flowering, when N translocation to spikes had already started and the experiment was split into two water levels. This campaign was conducted 3 and 4 days after the last W2 irrigation event in both years to determine the water status while avoiding superficial water that could affect the measurements.

To determine crop N status, the nitrogen nutrition index (NNI) was calculated by using the CDC for winter wheat proposed by Justes et al. (1994) (Eq. 2):

$$\%N_{critical} = 5.35 * Biomass^{-0.442} \qquad \text{(Eq. 2)}$$

where $\%N_{critical}$ is the minimum %N that produces the maximum growth at a given *Biomass*.

The actual ratio of %N and aerial biomass determined in the samples collected from the experimental plots was used to calculate the NNI following the Eq. 3:

$$NNI = \frac{\%N}{\%N_{critical}} \qquad \text{(Eq. 3)}$$

Therefore, values of NNI close to 1 represent vegetation with N fertilization adjusted to crop requirement, while values above 1 represent vegetation over-fertilized and below 1, vegetation with N deficiencies. At flowering, the NNI was calculated with shoots and leaves, excluding spikes, to account for N dilution.

To measure the yield, all plots were harvested on 20 July 2018 and 3 July 2019 with a 1.4-m-wide combiner (Fig 11d, f). A 1-m buffer was left at both ends of the plots to avoid edges. Simultaneously, a grain sample of each plot was saved for analysis. As performed with the biomass samples, the grain samples were dried at 65 ºC for 48 h and weighed to determine the moisture content and yield (kg grain ha^{-1}). The subsamples of grain samples were analyzed in the laboratory to determine the grain N concentration by using the Dumas combustion method (LECO FP-428 analyzer, St. Joseph, MI, USA). The grain protein

concentration (GPC; %) of each plot was calculated from the grain N concentration, and the N output (kg N ha^{-1}) was calculated by multiplying yield by grain N concentration.

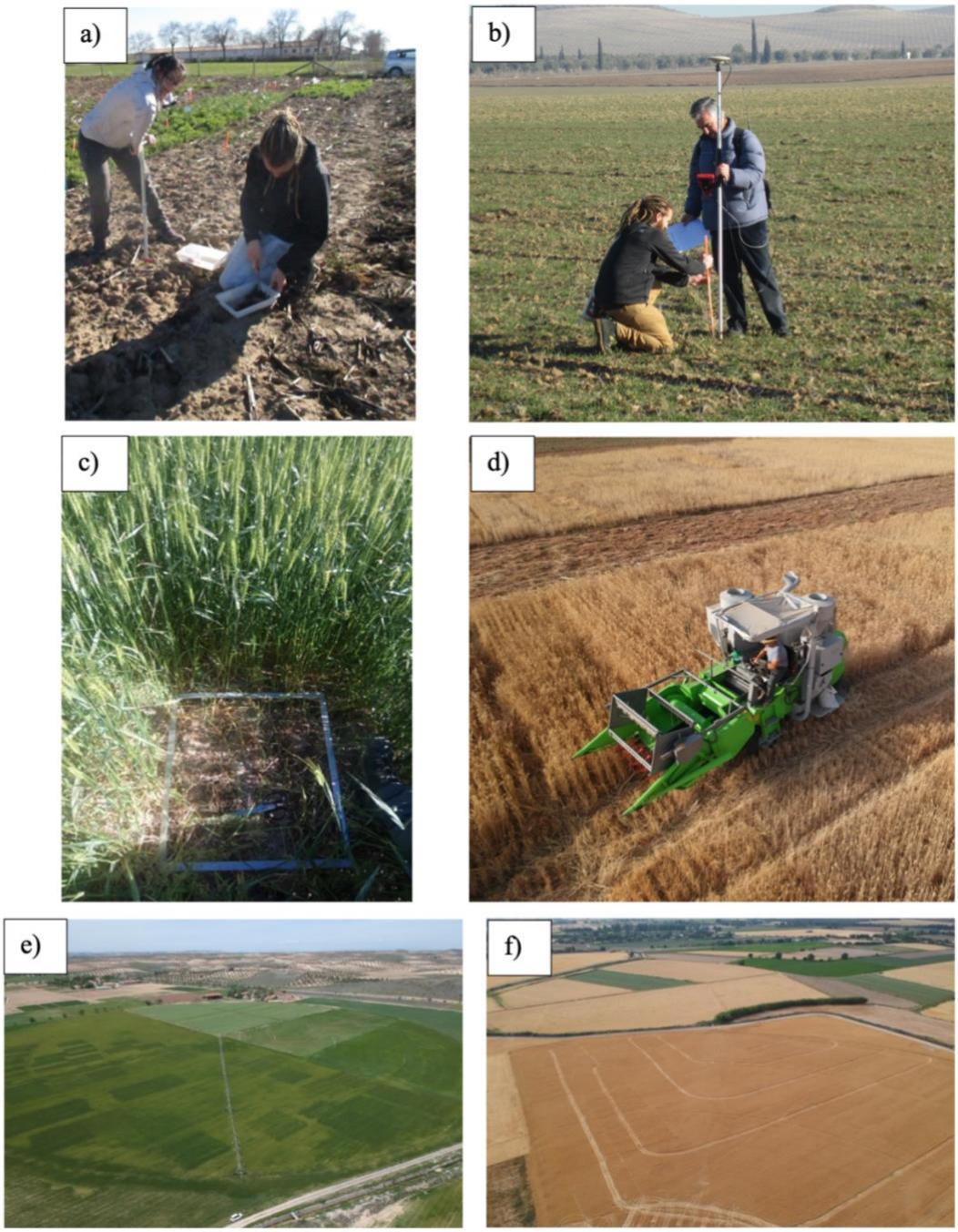

Fig 11. a) Soil samples collection for mineral soil N determination, b) georreferencing plots with real-time kinematic, c) 0.5 x 0.5 winter wheat biomass sample at flowering stage, d) experimental combiner, e) two water levels (W1 and W2) plots of the field experiment separated by the irrigation pivot before irrigating W2 plots and f) track of the experimental combiner after harvesting the experiment.

3.2.2. Central Valley, California

Yearly official crop reports providing the harvested area by species were used to determine the cropland use trends between 2013 and 2018. This dataset was downloaded for the counties that lay inside the study area through Kern County Department of Agriculture and Measurement Standards (2022a); Kings County Department of Agriculture and Measurement Standards (2022); and Tulare County Agricultural Commissioner/Sealer (2022). Fresno 2013 crop reports were not available, therefore this county crop reports were not included. The crop reports were used to calculate the cropland area covered by green vegetation (GV) and non-photosynthetic vegetation (NPV) in the studied counties in June each year. June was chosen because it is the peak growth of the summer crops and the vegetation status this month is closely dependent on water availability (Shivers et al., 2018; University of California Division of Agriculture and Natural Resources, 2022). One limitation of the crop reports is that they do not provide the area of non-cultivated crop fields or the physiological stage of the crops. To calculate the GV and NPV area, the species harvested each year were classified according to their physiological status in June as GV or NPV. To ensure that crops fell into either GV or NPV, the physiological status in June was confirmed based on the planting and harvesting dates provided by Kern County Department of Agriculture and Measurement Standards (2022b) and by Meier, 2001. The GV area was calculated by summing the harvested area of the crops that are photosynthetically active in June. This category includes summer crops, orchards and irrigated pasture. The summer crops included in the GV category are alfalfa, blueberries, broccoli, cantaloupe, cherries, corn, cotton, cucumbers, garlic, lettuce, onions, peppers, spring potatoes, sorghum, tomatoes, triticale, watermelons and some crops that the crop reports enclose in a group called “others” that includes carrots, cilantro, eggplants, beets or zucchini among others. The orchards found in the crop reports are almonds, apples, apricots, grapes, kiwifruit, lemons, nectarines, olives, oranges, peaches, pears, pecans, persimmons, pistachios, plums, pomegranates, prunes, quince, tangerines, walnuts and other citrus. Despite the fact that the area between rows can be covered by soil or senesced vegetation, it is included when calculating the GV area because the crop reports do not separate it. Similarly, the area covered by NPV in June was calculated by summing the harvested area of the crops that would be senesced by that month. This category includes safflowers, winter cereals (barley, wheat and oat), beans and non-irrigated pasture.

3.3. Sensors campaigns

3.3.1. Aranjuez, Spain

- Leaf clip sensors

Optical determination of leaf chlorophyll content (Cab-D), leaf anthocyanin content (Anth-D) and N status (NBI) at field level was performed with the leaf clip sensor Dualex® Scientific (Force-A, Orsay, France) the same dates as the biomass sampling campaigns (Table 2; Fig 2i). The Cab-D is calculated as the ratio between the light transmitted at the red edge (710 nm) and the NIR (850 nm) wavelengths. The leaf epidermal polyphenols content assessment is based on its screening effect on chlorophyll fluorescence, and it is calculated as the ratio between the transmitted light of the NIR-induced chlorophyll fluorescence not absorbed by polyphenols and a light absorbed by polyphenols in the ultra-violet (UV; 375 nm) for flavonols or in the green (528 nm) for Anth-D assessment (Goulas et al., 2004). The readings provided by the instrument are calculated by comparing the ratio of the light transmitted at these wavelengths when measuring a leaf and in the absence of a sample (Tremblay et al., 2012). The Dualex campaigns were conducted by taking 15 measurements per plot at the uppermost fully developed leaf, on the upper side on representative plants avoiding midribs. The representative value of each plot was calculated as the average of the 15 measurements. Because the clip system ensures full contact with the leaf tissue and independence of the measurements from external conditions (Arregui et al., 2006), Dualex readings were used as ground-truth measurements to validate remote sensing assessment in Chapter 4.4. The ratio between chlorophyll and polyphenols (flavonols) content is called the nitrogen balance index (NBI), and it is used in this Chapter as on-ground optical determinations of crop N status of each plot.

To build a ground-truth dataset of water status, the leaf stomata aperture was determined by measuring the leaf conductance ($mmol \cdot m^{-2} \cdot s^{-1}$) of three representative plants per plot with a clip leaf porometer (Decagon Leaf Porometer, Decagon Devices, Inc. Pullman) on 13 May 13 2019 (Table 2; Fig 2j). The leaf porometer measures stomatal conductance by placing the conductance of a leaf in series with two known conductance elements and comparing the humidity measurements between them. The leaf porometer calculates the stomatal conductance resistance between the inside and outside of the leaf based on the resistance between the leaf and the first humidity sensor and the first and second sensor (Sanad et al.,

2019). As performed by Idso et al., 1981, the porometer measurements were collected within one hour of solar noon. These values were used in Chapter 4.2 to validate the remote sensing measurements for water status monitoring.

- Hand-held spectroradiometer

Ground-based reflectance spectra were acquired with a FieldSpec® Hand-Held VNIR (Analytical Spectral Devices, Boulder, CO, USA) positioned 1 m above the winter wheat canopy in a nadir orientation with a 25º FOV provided by fiber optics (Table 2; Fig 2g). A bubble level fixed into the pistol grip of the Fieldspec probe ensured a pointing direction near the vertical. The spectrum that characterized each plot was the average of 15 representative spectra randomly acquired inside each plot; each of the 15 spectra was obtained as the average of 10 consecutive scans recorded at the same location. The number of spectra collected per area is considered adequate to provide a representative spectrum of the vegetation studied (Zhao et al., 2005; Cui et al., 2019). Each scan had a spectral resolution of 3 nm over 325 – 1075 nm wavelengths, and was trimmed to 400 – 900 nm to reduce noisy portions of the data. The readings were continuously calibrated and optimized by recording the black and baseline reflectance with a Spectralon reference panel (Labsphere, Inc., North Sutton, NH, USA) placed in the Fieldspec field of view at 15-min intervals (Fig 2h). These acquisitions were used to convert the measurements to percent surface reflectance values (Quemada and Daughtry, 2016). In each experimental year, three ground-level acquisition campaigns were conducted at the same GS as the crop sampling collection ensuring cloud-free sky conditions: at mid stem elongation (GS34, 22/03/2018), final stem elongation (GS37, 17/04/2018), and flowering (GS65, 11/05/2018) in 2018 and at mid stem elongation (GS32, 08/03/2019), final stem elongation (GS39, 12/04/2019) and flowering (GS65, 14/05/2019) in 2019 (Table 2). All spectra were acquired within 2 h of local solar noon under clear sky conditions. In addition to validate the performance of the Fieldspec measurements for determining winter wheat N status in Chapter 4.2, these acquisitions were used to validate the atmospherically corrected surface reflectance acquired by Sentinel-2 and WorldView-3 in Chapter 4.5.

- Airborne sensors

The Laboratory for Research Methods in Quantitative Remote Sensing of the Consejo Superior de Investigaciones Científicas (QuantaLab, IAS-CSIC, Spain) carried out five

airborne campaigns as close as possible to biomass sampling campaigns ensuring cloud-free sky conditions (Table 2; Fig 2e, f). The flights were conducted at midday to minimize the effects produced by different Sun illumination angles at 75 km h^{-1} ground speed, heading on the solar plane in all campaigns. Two hyperspectral sensors covering the VNIR and a portion of the NIR–SWIR region, together with a thermal sensor, were installed in tandem on a Cessna aircraft that flew 300 m above the experiment site.

The hyperspectral sensors carried by the aircraft were a VNIR imager (Micro-Hyperspec VNIR model, Headwall Photonics, Fitchburg, MA, USA) that collected reflectance in the 400 – 850 nm region with a spectral resolution of 6.5 nm and a spatial resolution of 0.2 m, and a SWIR Hyperspec linear-array imager (NIR-100 model, Headwall Photonics, Fitchburg, MA, USA) capturing in the 950 – 1750 nm region with 165 spectral bands at 6.05 nm FWHM and 16-bit resolution, yielding 0.6 m spatial resolution. The radiometric calibrations of both hyperspectral sensors were conducted with an integrating sphere (CSTM-USS-2000C LabSphere, North Sutton, NH, USA) using four levels of illumination and six integration times. Hyperspectral imagery was atmospherically corrected through empirical line methods using incoming irradiance measured with a field spectrometer and simulated by the SMARTS model (Gueymard, 1995; Gueymard et al., 2002). Spectral smoothing of the airborne spectra was performed using the Savitzky Golay method with a filter length of 9 and interpolated to 1 nm. Wavelengths between 1320 – 1500 and 1085 – 1185 nm were removed due to atmospheric water vapor absorption (Gao et al., 2009).

The aircraft recorded canopy temperature with a thermal infrared sensor (SC655 model, FLIR Systems, Wilsonville, OR, USA) with a spatial resolution of 0.25 m, 16-bit radiometric resolution, 13.1 mm focal length and 45 x 33.7° FOVº. The thermal imagery was calibrated using ground temperature data collected with a handheld infrared thermometer (LaserSight, Optris, Germany) on each flight date.

Two airborne spectral campaigns were conducted in 2018: at final stem elongation (GS37, 19/04/2018) with the VNIR sensor and at flowering (GS65, 15/05/2018) with the VNIR and the SWIR sensors. Three campaigns were conducted in 2019: at mid stem elongation (GS32, 11/03/2019) with the VNIR sensor, and at final stem elongation (GS39, 12/04/2019) and flowering (GS65, 16/05/2019) with the VNIR and SWIR sensors. The canopy temperature was recorded during the flowering campaigns of both years (Table 2). The RTK coordinates were used to extract from the hyperspectral and thermal imagery the mean canopy spectrum

and temperature per plot using a 2-m buffer on each side to ensure treatment representativeness. The airborne hyperspectral and thermal images were used in Chapter 4.2 to assess their capability to estimate N and water status, and in Chapter 4.3 to predict winter wheat traits.

- Satellite imagery

The accuracy of satellite imagery for crop parameters monitoring was tested using Sentinel-2 and Sentinel-1 products downloaded from the European Space Agency (ESA) DataHUB server (ESA, 2023e) in Chapter 4.3 and Chapter 4.4. The Sentinel-2 payload is the Multi-Spectral Instrument (MSI), which is a push-broom sensor with a swath width of 290 km that registers the spectral radiation reflected from the Earth in 13 spectral bands: four bands at 10-m, six bands at 20-m and three bands at 60-m spatial resolution (Table 4). The visible and NIR bands at 10- and 20-m spatial resolution are useful for the retrieval of biophysical surface parameters, especially vegetation characterization. Meanwhile, the 60-m resolution bands are used for atmospheric aerosols and water vapor retrieval in atmospheric correction approaches. The range and spectral distribution of these bands can be accessed at ESA (2023f) and are summarized in Table 4 and Fig 14. In the study area of Aranjuez, located in an area of swath overlap, the revisit frequency of Sentinel-2 constellation is four to five days with an 11º forward-looking view angle. The products selected were those with the overpass closest to the biomass collection campaigns, ensuring cloud-free sky conditions over the experimental site in both years (Table 2). The products downloaded for retrieving the crop parameters in Chapter 4.3 and Chapter 4.4 were the Sentinel-2 Level 2A, which indicates that the atmospheric corrections were automatically made by the payload data ground segment (PDGS) with the Sen2Cor procedure using atmospheric constituents derived from in-scene spectral bands. Validation of geometric alignment of the images was conducted using the airborne images as reference.

Two Sentinel-1 Single Look Complex (SLC)-products collected at flowering of both years were used in Chapter 4.3 (Table 2). Sentinel-1 provides images of dual-polarized (VV-VH) backscatter in the C band. A preprocessing process was applied to obtain images with co- and cross-polarized backscatter (σVVº and σVHº (db)) at 10-m spatial resolution using the Sentinel Application Platform (SNAP) (Mandal et al., 2020). The correction process followed includes the conversion of the SLC product (the individual sub-swath of the IW and the burst) to ground range detected (GRD), a terrain correction using the shuttle radar topography

mission (SRTM) product as digital elevation model (DEM), a co-registration process, a speckle correction using the “Gamma Map” filter, and a conversion of digital numbers to db values. The final 10-m spatial resolution product allowed extracting information of one to four pure pixels per plot. The value of the SAR channels for each plot was calculated as the average of the pixels that completely lay inside the plot.

In addition to testing the accuracy for crop monitoring of the above-described satellite images, another set of multispectral satellite imagery was used to validate the accuracy of the acquired surface reflectance after applying different atmospheric correction procedures, and to test and validate an empirical signal normalization procedure for compensating the off-nadir viewing angle effects in Chapter 4.5. The images used for these purposes were acquired by Sentinel-2 and WorldView-3 at final stem elongation both years (Table 2 and Table 3). For the validation of the atmospheric correction approaches in Sentinel-2 imagery, in addition to the above-mentioned Sentinel-2 Level 2A (atmospherically corrected with Sen2Cor using atmospheric parameters derived from the Sentinel-2 bands) products acquired at stem elongation both years, Sentinel-2 Top of Atmosphere (TOA) reflectance products without being atmospherically corrected were downloaded as Level 1C to test the performance of the different atmospheric correction approaches.

The WorldView-3 imagery acquisition was supported by the USGS Land Resources Mission Area, Land Change Science Program. This satellite simultaneously collects one panchromatic band, eight VNIR bands, and eight SWIR bands, along with 12 Clouds, Aerosols, Vapors, Ice, and Snow (CAVIS) bands. The sensor provides a spatial resolution of 0.31 m in the panchromatic mode, 1.24-m in the multispectral mode for the VNIR bands, 3.4 m in the SWIR bands, and the CAVIS sensor provides a spatial resolution of 30 m (Table 4). The WorldView-3 instrument is pointable, and thus has the ability to acquire images at a variety of viewing angles, which enables a revisit time of less than one day due to its orbital and altitude maneuvering capabilities, which enables image acquisition at varying off-nadir angles (Satellite Image Corporation, 2017). The WorldView-3 satellite usually observes with ≈ 20º off-nadir viewing and has geolocation accuracy (CE90) performance better than 3.5 m without ground control. The preprocessing operations of the WorldView-3 images included radiometric calibration consisting of converting WorldView-3 image Digital Numbers (DN) into physical meaning values, such as TOA spectral radiances (LTOA, $W \cdot m^{-2} \cdot sr^{-1} \cdot \mu m^{-1}$), and rectification of geometric misalignments in which the upper left datum coordinate of

each WorldView-3 image was altered by up to 40 m to shift the imagery into alignment with the Sentinel-2 imagery through visual comparison of clear geometric features within each image. Subsequent to the geometric correction, the various imagery datasets were clipped to the bounds of the study area. At this point, it was verified that all the datasets were geometrically consistent and presented georegistration disparities below their spatial resolution. This is equivalent to an error under one pixel, which ensures geometric fidelity during the spectral extraction and comparison process. All the imagery datasets were geodetically referenced to the ERTS89 system and projected to the Universal Transverse Mercator (UTM) coordinates cartographic system (Zone 30).

Regarding the acquisition schedule for these datasets, Sentinel-2 and WorldView-3 products were selected with the minimum possible time difference. In 2019, both types of imagery were acquired almost simultaneously on April 12th. In 2018, the Sentinel-2 and WorldView-3 products were acquired with a one-day difference on April 17th and 18th, respectively, which is expected to produce a low and affordable difference in surface reflectance (Qiu et al., 2019; Shang et al., 2019). The satellite imagery product identifiers and acquisition times are summarized in Table 3. In the Aranjuez study site, the WorldView-3 acquisitions for 2018 and 2019 were acquired with 24.6^{o} and 39.1^{o} satellite off-nadir viewing angles with backward and forward solar illumination geometries, respectively. Sentinel-2 was acquired with a consistent 11° forward view angle. The aim was to ensure similar illumination and atmospheric conditions, which ideally allows more consistent comparison of surface reflectance values from both satellite images.

Table 2. Growth stages (GS) and dates of sensors and biomass campaigns in the Aranjuez field experiment.

	Mid stem elongation		Final stem elongation		Flowering	
	Dates	GS	Dates	GS	Dates	GS
Biomass	22/03/2018	GS34	17/04/2018	GS37	11/05/2018	GS65
	11/03/2019	GS32	12/04/2019	GS39	13/05/2019	GS65
Dualex	22/03/2018	GS34	17/04/2018	GS37	11/05/2018	GS65
	11/03/2019	GS32	12/04/2019	GS39	13/05/2019	GS65
Porometer	-	GS34	-	GS37	-	GS65
	-	GS32	-	GS39	13/05/2019	GS65
FieldSpec	22/03/2018	GS34	17/04/2018	GS37	11/05/2018	GS65
	08/03/2019	GS32	12/04/2019	GS39	14/05/2019	GS65
Aircraft	-	GS34	19/04/2018	GS37	15/05/2018	GS65
	11/03/2019	GS32	12/04/2019	GS39	16/05/2019	GS65
Sentinel-2	28/03/2018	GS34	17/04/2018	GS37	12/05/2018	GS65
	10/03/2019	GS32	12/04/2019	GS39	12/05/2019	GS65
Sentinel-1	-	GS34	-	GS37	11/05/2018	GS65
	-	GS32	-	GS39	18/05/2019	GS65
WorldView-3	-	GS34	18/04/2018	GS37	-	GS65
	-	GS32	12/04/2019	GS39	-	GS65

Table 3. Sentinel-2 and WorldView-3 products used in this thesis for atmospheric correction and signal normalization analysis.

Acquisition day/time (dd-mm-yyyy)	Mission	Product Identifier
17-04-2018 11:06:51	Sentinel-2	S2A_MSIL1C_20180417T110651_N0206_R137_T30TVK_20180417T150806 S2A_MSIL2A_20180417T110651_N0207_R137_T30TVK_20180417T150806
18-04-2018 11:22:32	WorldView-3	VNIR: WV320180418112232M01
12-04-2019 11:06:21	Sentinel-2	S2A_MSIL1C_20190412T110621_N0207_R137_T30TVK_20190412T115548 S2A_MSIL2A_20190412T110621_N0211_R137_T30TVK_20190412T123858
12-04-2019 11:40:08	WorldView-3	VNIR: WV320190412114009M00

Table 4. Spectral and spatial resolution of the Sentinel-2 and WorldView-3 satellites. The bands used in the assessment of atmospheric correction are shaded.

Sentinel-2				**WorldView-3**			
Name	**Center (nm)**	**Spectral resolution (nm)**	**Spatial resolution (m)**	**Name**	**Center (nm)**	**Spectral resolution (nm)**	**Spatial resolution (m)**
B1	443	20	60	Coastal	425	50	1.24
B2	490	65	10	Blue	480	60	1.24
B3	560	35	10	Green	545	70	1.24
				Yellow	605	40	1.24
B4	665	30	10	Red	660	60	1.24
B5	705	15	20				
B6	740	15	20	Red Edge	725	40	1.24
B7	783	20	20				
B8	842	115	10	NIR 1	832.5	125	1.24
B8A	865	20	20				
B9	940	20	60	NIR 2	950	180	1.24
				SWIR 1	1210	30	3.7
B10	1375	30	60				
				SWIR 2	1570	40	3.7
B11	1610	90	20				
				SWIR 3	1660	40	3.7
				SWIR 4	1730	40	3.7
B12	2190	180	20	SWIR 5	2165	40	3.7
				SWIR 6	2205	40	3.7
				SWIR 7	2260	50	3.7
				SWIR 8	2330	70	3.7

3.3.2. Central Valley, California

The surface reflectance of the study area collected with AVIRIS-classic was downloaded from the Jet Propulsion Laboratory (2023c) and analyzed to obtain the cropland use between 2013 and 2018 (Fig 10). The AVIRIS-classic sensor collects 224 narrow bands from the visible to the SWIR region (350 – 2500 nm) at 10 nm FWHM (Green et al., 1998). It has a FOVº that generates a spatial resolution of 20-m from an aircraft altitude of 20 km; the height often flown by the NASA ER-2 jet. The images used belong to the "Soda Straw" flightline collected on 6 June 2013, 3 June 2014, 2 June 2015, 21 June 2016, 7 June 2017, and 21 June 2018. The flights took place within 2 hours of solar noon. The NASA Jet Propulsion Laboratory (JPL) performed the atmospheric correction to Level 2 surface reflectance using the ATmospheric REMoval (ATREM) algorithm (Thompson et al., 2015), and the orthorectification of the imagery at a spatial resolution of 18 m. The bands that were affected by atmospheric disturbances and those at both ends of the spectrum were removed using ENVI bad band list to reduce noise in the data. The bands removed were those within the 350 – 400 nm, 900 – 950 nm, 1100 – 1150 nm, 1320 – 1430 nm, 1750 – 2000 nm and 2370 – 2500 nm spectral regions. No clouds or cloud shadows were found over the study area.

3.4. Development of vegetation indicators

3.4.1. Spectral Vegetation indices

Various spectral vegetation indices (VIs) described in the literature were calculated using the derived surface reflectance (Table 5). Different sensors and VIs were used in each Chapter to meet the specific objectives. For the hyperspectral sensors, the original equation proposed for narrow bands was used. For the VIs calculated with the Sentinel-2 multispectral bands, the equation with the closest bands was used (Table 4 ;Table 5).

The VIs are linked to different crop parameters depending on the region of the electromagnetic spectrum used. The VIs were classified according to their main sensitivity to i) canopy structure, ii) chlorophyll a + b and other photosynthetic pigments, iii) canopy N status and iv) water status (Table 5). The structural indices are based on the relationship between bands in the NIR and visible regions. The photosynthetic pigments VIs are based on bands from visible and red edge regions, sometimes normalized by the NIR reflectance. Two VIs based on the reflectance in the SWIR region were selected as water VIs due to the sensitivity of this region to water content (Gao et al., 2015). Among the canopy N status

indices, the canopy chlorophyll content index (CCCI) is a planar domain VI that estimates plant N status in a mixed soil/plant pixel by analyzing the relationship between one biomass- and one chlorophyll -related VI plotted in a two-dimensional space (Clarke et al., 2001). The CCCI value of each plot was calculated in a two-dimensional space by representing the NDVI on the X-axis, and the NDRE on the Y-axis. Consequently, the value of CCCI was calculated by comparing the distance of each point to the upper and bottom lines that involve the cloud of points from the coordinate origin. N-sufficient plots will be located in the graph close to the upper line, whereas N-deficient plots will approach the bottom line. The TCARI/OSAVI estimates crop N status and compensates the soil effect by combining a structural (OSAVI) and a photosynthetic pigment (TCARI) index (Haboudane et al., 2002).

3.4.2. Solar-induced chlorophyll fluorescence

The hyperspectral canopy reflectance acquired by the airborne sensors was used to calculate the solar-induced chlorophyll fluorescence (SIF) emission for each plot at the time of the flights. The SIF was calculated by the Fraunhofer line-depth (FLD) approach using the solar irradiance and the radiance reflected from the canopy in the atmospheric O_2 absorption band at 760.5 nm (Plascyk and Gabriel et al., 1975; Meroni et al., 2010). The FLD method used two spectral bands “in” and “out” the O_2 absorption band. The radiance used was L_{in} (L_{762} nm) and L_{out} (L_{750} nm) as well as the irradiance E_{in} (E_{762} nm) and E_{out} (E_{750} nm) from the irradiance spectra concurrently measured at the time of the flights. The incoming irradiance was simulated using the SMART model (Gueymard, 1995; Gueymard et al., 2002) based on the aerosol properties and weather condition at the time of the corresponding flight. The atmospheric aerosol properties were characterized using the aerosol optical thickness (AOT), Ångström exponent and air the mass measured by the closest AErosol RObotic NETwork (AERONET; NASA, 2023d). The simulated spectral irradiance was interpolated and convolved to fit the bandwidth of the hyperspectral senor.

Table 5. The original equation and the equation adapted to the multispectral Sentinel-2 bands of the spectral vegetation indices used in this thesis.

Index	Equation	Equation Sentinel-2	Reference
	Structural indices		
Normalized Difference Vegetation Index (NDVI)	(R800 - R670)/(R800 + R670)	(B8 - B4) / (B8 + B4)	Rouse et al., 1974
Green NDVI (GNDVI)	(R800 - R550)/(R800 + R550)	(B8 - B3) / (B8 + B3)	Gitelson et al., 1996
Optimized soil-adjusted vegetation index (OSAVI)	(1 + 0.16) * (R800 - R670)/(R800 + R670 + 0.16)	(1 + 0.16) * (B8 - B4) / (B8 + B4 + 0.16)	Rondeaux et al., 1996
Enhanced Vegetation Index (EVI)	2.5 * (R800 - R670) / (R800 + 6 * R670 - 7.5 * R400 + 1)	2.5*(B8 - B4) / (B8 + 6 * B4 - 7.5 *B2+1)	Huete et al., 2002
	Photosynthetic pigment indices		
Photochemical Reflectance Index (PRI)	(R531 - R570)/(R531 + R570)	(B2 – B3) / (B2 + B3)	Gamon et al., 1992
Red Edge Chlorophyll Index (CI)	R750/R710	B6 / B5	Zarco-Tejada et al., 2001
Transformed Chlorophyll Absorption in Reflectance Index (TCARI)	3 ((R700 - R670) - 0.2* (R700 - R550)*(R700/R670))	3 * ((B5 - B4) - 0.2 * (B5 - B3) * (B5 / B4))	Haboudane et al., 2002
Double-Peak Canopy Nitrogen Index (DCNI)	(R720 - R700)/(R700 - R760))/(R720 - R670 + 0.03)	(B6 - B5) / (B5 - B4)/ (B6 - B4 + 0.03)	Chen et al., 2010
Modified Normalized Difference 705 (mND_{705})	(R750 – R445)/(R705 – R445)	(B6 - B5) / (B6 - B5 - 2*B2)	Sims and Gamon, 2002
Modified Simple Ratio 705 (mSR_{705})	(R750 – R705)/(R750 + R705 – 2*R445)	(B6 - B2) / (B5 - B2)	Sims and Gamon, 2002
Normalized Difference Red Edge (NDRE)	(R790-R720)/(R790+R720)	(B8 - B6) / (B8 + B6)	Barnes et al., 2000
N850,1510	(R850-R1510)/(R850+R1510)	(B8 - B11) / (B8 + B11)	Camino et al., 2018
Cellulose Absorption Index (CAI)	0.5*(R2000+R2200)-R2100	-	Daughtry, 2001
	Water indices		
Normalized Difference Water Index 1240 (NDWI 1240)	(R860 – R1240)/(R860 + R1240)	-	Gao 1996
Normalized Difference Water Index 1640 (NDWI 1640)	(R860 – R1640)/(R860 + R1640)	(B8A – B11) / (B8A – B11)	Jackson et al., 2004
WET	-	0.1509*B2+0.1973*B3+0.3279*B4+0.3406*B 8A-0.7112*B11-0.4572*B12	Schulz et al., 2021b
	Canopy indices		
TCARI/OSAVI	TCARI/OSAVI		Haboudane et al., 2002
Canopy Chlorophyll Content Index	CCCI = *f*(NDVI, NDRE)		Barnes et al., 2000

3.4.3. Microwave-based indicator

In addition to the spectral VIs based on the VSWIR region, the radar vegetation index (RVI) was calculated with the information of the backscattering intensity in the microwave region collected with the satellite Sentinel-1 SAR. The modification of the quad-pol RVI (Kim and Van Zyl, 2009) for dual-pol SAR (Mandal et al., 2020) data was calculated for each plot following Eq. 3.

$$RVI = \frac{4\sigma VH}{(\sigma VV + \sigma VH)} \qquad \text{(Eq. 3)}$$

3.4.4. Temperature-based indicators

In this thesis, the performance of canopy temperature-based indicators was tested to assess water status. The temperature-based indicators were the canopy-air temperature difference (T_c-T_{air}; Idso et al., 1977) and the water deficit index (WDI; Moran et al., 1994). The WDI is an indicator of crop water status that adapts the T_c-T_{air} to partially vegetated fields. To calculate the WDI, the vegetation index-temperature (VIT) trapezoid was plotted in a two-dimensional space created by the surface-air temperature differential on the X-axis, and a fractional vegetation cover VI on the Y-axis. As proposed by Moran et al. (1994), the soil-adjusted vegetation index (SAVI; Huete 1988) was used as a surrogate for fractional vegetation cover. The VIT trapezoid was defined by two horizontal lines at full ground cover and at bare soil. The value of the full ground cover was the maximum SAVI obtained in all airborne spectral images. The bare soil value was the minimum SAVI extracted from 30 pixels randomly located at the pivot-track, half at each water level. The dry and wet bare soil vertices were determined using the image mean temperature of the dry and wet pixels located on the pivot-track of the W1 and W2 zones, respectively. The maximum and minimum water stress vertices at full canopy cover were derived based on the baselines proposed for post-heading winter wheat by Idso (1982). The air vapor water pressure was calculated from the relative humidity and air temperature recorded at the time of image acquisition by the weather station located at the experimental farm. The minimum water stress line of the VIT connects the vertices of wet bare soil and minimum water stress at full canopy cover. Vegetation points close to this line experience minimum water stress. The maximum water stress line links the dry soil vertex with the maximum water stress at full canopy cover. The

WDI was calculated for each plot as the ratio between the horizontal distance to maximum and minimum water stress lines.

3.5. Statistical analysis for crop parameters retrieval

3.5.1. Simultaneous assessment of crop N and water status

Statistical analyses were carried out to assess the potential of the different indicators for estimating N and water status using the information extracted from the FieldSpec and from the hyperspectral and thermal airborne sensors in Aranjuez field experiment. The results are shown in Chapter 4.2.

In the first step, a set of structural, photosynthetic pigment and canopy VIs were tested as proxy of the N status (Table 5), and the water VIs and the thermal indicators as proxy of the water status. The crop parameter used to define the N status was the NNI calculated from biomass measurements. The crop parameter that described the water status was the leaf stomatal conductance (mmol · m^{-2} · s^{-1}) measured with the leaf porometer. The different water levels were established at flowering stage both years, therefore, the water status was determined only at this GS. The predictive ability of the indicators to estimate crop status in each sampling campaign was evaluated by calculating the coefficient of determination (R^2) and the root mean square error (RMSE) from the linear relationships. In the second step, the remote sensing indicators that best described the N and water status were combined using a multiple lineal regression model fitted to the NNI to develop a new index for N status assessment that consider the water status.

The ability of VIs to distinguish between N levels without confounding effects was evaluated at flowering using least squares means contrasted with the Tukey test ($P \leq 0.05$) with the N level as the factor. The same methodology was applied to validate the performance for water status but using the water level as the factor for each N level. In addition, a two-way ANOVA was conducted to analyze the effect of N, water and N × water in the indicators.

3.5.2. Assessment of winter wheat traits with ensemble models

The capacity of the VIs to estimate winter wheat traits (yield (kg ha^{-1}), grain protein concentration (%; GPC) and grain N output (kg N ha^{-1})) was compared against combining different indicators with ensemble models. For each trait, the indicators included in the

ensemble models were selected according to their link with the traits and with specific crop biochemical and physical parameters that affect crop traits. To identify the most suitable sensor, the indicators were grouped according to the sensor required to calculate them. Each group of indicators was added one at a time to the ensemble models to quantify the potential improvement in the estimation. This thesis compared the performance when using airborne and Sentinel information. The results obtained from these analyses conducted in the Aranjuez field experiment are shown in Chapter 4.3.

3.5.2.1. Selection of indices as proxy of crop parameters

The mean airborne spectrum of each plot was used to construct a R^2 contour map for each winter wheat trait. The contour maps represent the R^2 value from the linear regression between each trait and each normalized difference spectral index [NDSI (λ_1, λ_2) = (λ_1-λ_2)/(λ_1+λ_2)] calculated with a combination of all possible hyperspectral bands (λ) when $\lambda_1 > \lambda_2$ and $\lambda \in$ [400, 1750 nm]. From each contour map, the NDSI with the highest R^2 value was selected as proxy of the trait and used as benchmark to test the potential improvement when combining several indicators. The first sensor tested with the ensemble models was the hyperspectral VNIR. For this, a canopy structure-related NDSI and a chlorophyll-related NDSI were selected from this region. The structural NDSI was selected among those based on an NIR and a visible band (Rondeaux et al., 1996). The chlorophyll-related indices were selected among the NDSIs based on an NIR and a red edge band, two bands in the red edge, or two bands in the visible region (Prey and Schmidhalter, 2019b). The links between the selected NDSIs with the canopy structure, and chlorophyll content were verified by analyzing their linear relationship with aboveground biomass and plant %N, respectively. The second sensor included was a hyperspectral sensor that covers the SWIR region. To this end, an NDSI based on one or two SWIR bands was selected and included in the ensemble models. Collinearity between the selected NDSIs was avoided by ensuring a Pearson's correlation coefficient $\leq$ 0.75. The third analysis tested the performance when a high-resolution VNIR hyperspectral imager and radiance information are available. For this purpose, the SIF emission was calculated by the FLD principle. The last sensor included in the analysis was a thermal camera because of its capacity to determine the crop water status. The water deficit index (WDI) was calculated based on the vegetation index–temperature trapezoid (VIT) using the soil adjusted vegetation index (SAVI; Huete et al., 1988) as a proxy of ground cover (Moran et al., 1994).

The estimation capacity using satellite information was tested by applying the methodology described but using the indicators calculated with Sentinel-1 and Sentinel-2. The structural, chlorophyll and SWIR indices used as input variables for estimating wheat traits with the airborne hyperspectral sensor were calculated using the closest Sentinel-2 convolved bands. The B8A band was not used because its spectral region (855 – 875 nm) was in the gap between the regions covered by the VNIR (400 – 850 nm) and the SWIR (950 – 1750 nm) sensors installed on the aircraft. The B11 band was used as the SWIR band in all SWIR-based indices because the region of the B12 band was not covered by the aircraft spectral range (Table 4). The RVI calculated with Sentinel-1 was included in the analysis to quantify the potential improvement when using the combination of Sentinel-1 and Sentinel-2 for winter wheat trait estimation. The SIF and the WDI cannot be calculated with the Sentinel dataset and, therefore, were not included in the Sentinel analysis.

3.5.2.2. Sentinel-2 bands convolved validation

Because no pure pixels of the Sentinel-2 20-m bands were available for all plots, the Sentinel-2 bands were convolved using the reflectance spectra collected with the VNIR and SWIR sensors onboard the aircraft. To validate the convolved bands, first, the 10-m Sentinel-2 bands were resampled to 20 m, which resulted in 59 pixels per year in the study site. For each Sentinel-2 pixel, the average spectrum of the airborne imagery was extracted and convolved using the spectral response function (ESA, 2023f; Fig 14). The coefficients of the regression line of the linear relationship between the Sentinel-2 and the convolved bands were applied to each convolved band to increase similarities between the real Sentinel-2 and the convolved bands. The resulting bands were used to calculate the Sentinel-2 spectral indices applied in this study. Finally, the validation process was performed by analyzing the linear relationship between the NDSIs calculated with Sentinel-2 and with the convolved bands (n = 118).

3.5.2.3. Ensemble models for winter wheat traits estimation

The ensemble models used to quantify the potential improvement in the estimation when combining different sensors/indicators were i) multiple linear regression (MLR), ii) artificial neural network (ANN) and iii) random forest (RF). The 10-fold cross-validation resampling technique was used with a random subset of 70% of the plots for training and the remaining 30% for testing. The training dataset was used to calibrate and optimize the models. The

testing dataset was used to evaluate the learning capacity of model transfer by calculating R^2 and RMSE between the measured traits and the estimated values at each fold.

The performance of the MLR model was evaluated by first fitting the training dataset to the crop trait analyzed. Second, the equation of the linear regression was used with the testing dataset. Finally, the linear relationship between the predicted and observed crop trait was analyzed.

The ANN model was built using the back-propagation algorithm. This model consists of a network composed of one input layer, one or more hidden layers, and one output layer connected by neuron-like units where each connection has a weighting factor. During the training process, the back-propagation algorithm repeatedly adjusts the weighting factors to minimize the mean square error (MSE) between the output and the estimated parameter (Rumelhart et al., 1986). In this study, the ANN was run by setting the number of hidden layers to 2 and the number of neurons in the hidden layer equal to the number of input variables. The ANN model was executed using the "neuralnet" package implemented in the R software (version 4.0.5; R Core Team, 2021).

The RF is an machine learning model based on multiple decision trees (Breiman, 2001). The training dataset was used to optimize the model by selecting the optimal number of regression trees (ntree) and the number of variables included in each node (mtry). The most suitable value of ntree was calculated by varying it from 50 to 1000 with 50 intervals while fixing mtry as default (500). The selected mtry value was optimized by varying mtry from 1 to the number of input variables minus 1 with a single interval, while setting ntree as the optimized value. For the optimization process, the ntree and mtry variables selected were those that obtained the minimum MSE using the training dataset. The RF model also quantified the importance of each input variable in the estimation as the increase in node purity (IncNodePurity; Dube et al., 2019). This index measures the increase in MSE when permuting the out-of-bag (OOB) portion of the data (Liaw and Wiener, 2002). The most important variables have a higher IncNodePurity value; therefore, this value was used to rank the input variables according to their importance in the estimation to identify the most suitable sensor. The RF regression was conducted using the "randomForest" R package (Liaw and Wiener, 2002).

3.5.3. Hybrid artificial neural network-PROSAIL-PRO method for crop N status and traits monitoring

A hybrid machine learning method was applied to the Sentinel-2 imagery collected in the Aranjuez experiment to retrieve the chlorophyll content (Cab), the anthocyanin content (Anth), the leaf area index (LAI) and the equivalent water thickness (EWT) of each plot at mid stem elongation, final stem elongation and flowering each year. The retrieved crop parameters were combined accordingly to estimate the winter wheat N status and to predict traits. The hybrid method was implemented by following several steps: i) applying the PROSAIL-PRO radiative transfer model to generate a dataset of simulated Sentinel-2 spectra corresponding to different combinations of crop parameters, ii) selection of the simulated spectra that match the range of the observed 10- and 20-m Sentinel-2 bands, iii) identification of the most suitable VIs for estimating the crop parameters based on the simulated spectra, iv) retrieval of the crop parameters corresponding to the observed Sentinel-2 spectra by feeding an ANN regression algorithm with the simulated spectra dataset, the selected VIs and the Sentinel-2 bands, and v) to combine the retrieved crop parameters to estimate winter wheat N status and to predict traits. These results were compared when using spectral VIs from literature to estimate N status and to predict traits.

The dataset used in this process comprises the three Sentinel-2 images downloaded at mid stem elongation, final stem elongation and flowering each year (Table 2). It was selected 16 plots each year, ensuring that > 60% of the 20-m Sentinel-2 bands pixels lay inside the corresponding plot (Fig 12). The 10-m Sentinel-2 bands were extracted from the pure pixels that were completely inside the plots. This process allowed acquiring between 1 to 4 pure 10-m pixels per plot. The characteristic spectrum of each plot was calculated as the average of the spectral bands. The results of these analyses are shown in Chapter 4.4.

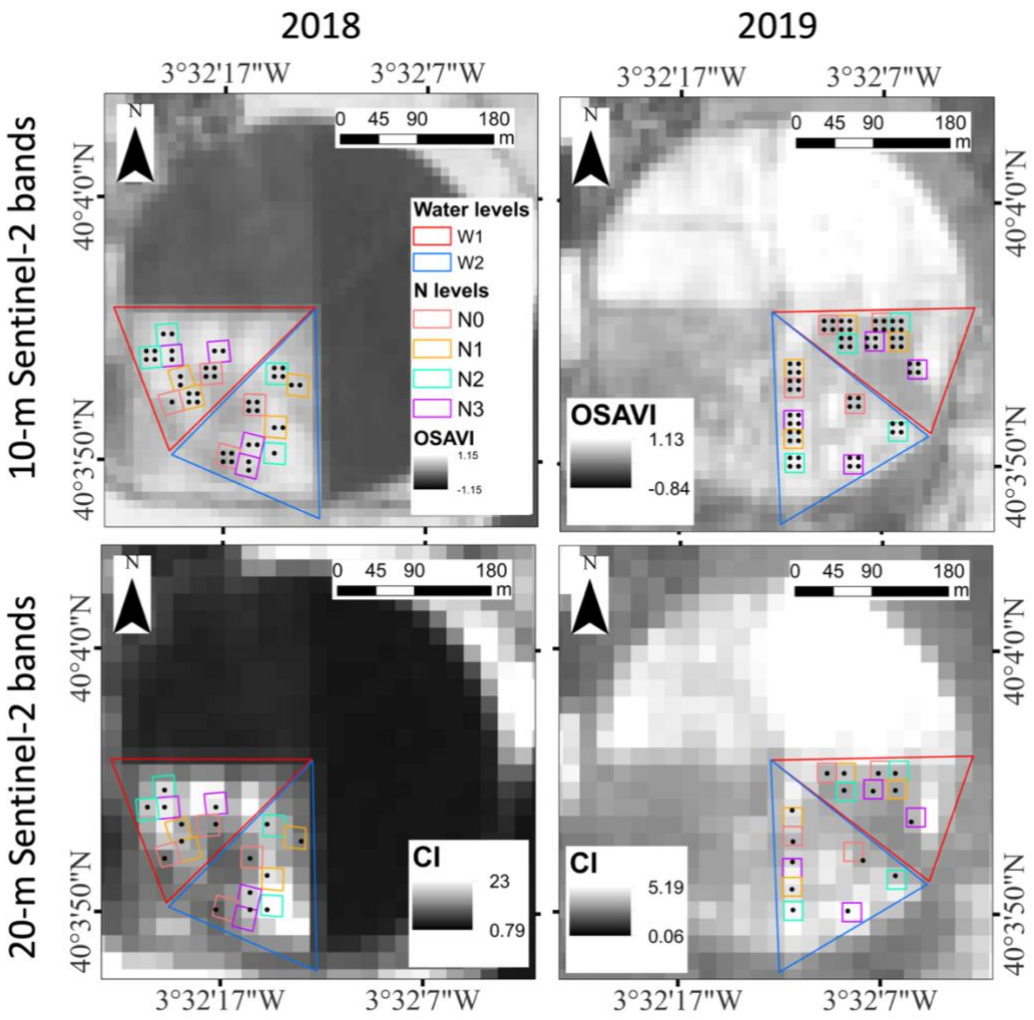

Fig 12. Maps of a) the optical soil vegetation index (OSAVI) and b) the red edge chlorophyll index (CI) calculated with the 10-m and 20-m Sentinel-2 bands, respectively, over the Aranjuez experimental site both years at flowering. Plots display different colors according to the N level (N0, N1, N2 and N3). The triangles with different colors indicate the two water levels (W1 and W2). The points indicate the pixels selected for the study.

3.5.3.1. Development of Look-up tables with PROSAIL-PRO radiative transfer model

The PROSAIL-PRO model couples the PROSPECT-PRO leaf reflectance model (Féret et al., 2021) and the 4SAIL turbid medium canopy radiative transfer model (Verhoef and Bach, 2007) to generate simulated spectra (LUT). The LUTs used in this study are datasets containing several spectra simulated with PROSAIL-PRO where each spectrum corresponds to a different combination of crop parameters, view and illumination angles and soil spectra. More detailed information and the range of the parameters considered in the PROSAIL-PRO

is shown in Table 6. A LUT with 30000 spectra convolved to the Sentinel-2 spectral bands was generated for each date by matching the simulated spectra with the corresponding Sentinel-2 bands. The LUTs were generated by constraining the ranges of the crop parameters used by PROSAIL-PRO until a similar mean value and standard deviation were obtained between the simulated and observed Sentinel-2 bands of each date. The ranges of the crop parameters used in this study were based on field measurements, preliminary simulations and previous studies conducted with winter wheat (Camino et al., 2022; Raya-Sereno et al., 2022; Longmire et al., 2022) (Table 6). The values of the crop parameters were randomly generated using a uniform distribution between the minimum and maximum values. PROSPECT-PRO identifies the leaf dry matter content (LMA) as the sum of its components: N-based (proteins) and carbon-based constituents (CBC; cellulose, lignin, hemicellulose, starch and sugars). To generate the LUTs, the protein and CBC values were fixed, and LMA varied (Table 6). The soil spectra used by PROSAIL-PRO were extracted from six pixels of bare soil located near or within the Aranjuez experimental field in each Sentinel-2 image. The viewing and illumination geometry were retrieved from the Sentinel-2 metadata and added an extra ± 5º to the final range. The soil spectra and the viewing and illumination angles extracted from each image were used to generate the LUT of the corresponding image. The LUTs were generated in R (version 4.1.1; R Core Team, 2021) using the “hsdar” R package (Lehnert et al., 2019).

The number of spectra in the LUT corresponding to each Sentinel-2 date was later reduced by eliminating the simulated spectra that differ from the observed spectra. For this purpose, the minimum and maximum values of each Sentinel-2 observed band were calculated, and the simulated spectra that were not within these ranges in all bands were excluded. A difference of surface reflectance in 20% was allowed in the visible and red edge bands, and a difference of 10% was allowed in the NIR and SWIR bands. After the spectra selection, the six LUTs corresponding to each date were merged in a common LUT, which would allow testing the transferability capacity of the method.

3.5.3.2. Selection of vegetation indices

The five VIs that best describe each of the crop parameters (Cab, Anth, LAI and EWT) were selected to be included in the machine learning algorithm described below, together with the ten 10- and 20-m multispectral Sentinel-2 bands from the final LUT. To select the VIs included in the method, the VIs from the literature (Table 5) were calculated for each

spectrum of the LUT using the equations adapted to the multispectral Sentinel-2 bands. In addition, another set of VIs was selected from the R^2 contour maps calculated for each crop parameter with all normalized difference spectral indices [NDSI (λ_1, λ_2) = (λ_1-λ_2)/(λ_1+λ_2)] calculated with all possible Sentinel-2 multispectral bands (λ) combination when $\lambda_1 > \lambda_2$. The five VIs that obtained the highest R^2 with each crop parameter in the LUT were selected to be included in the hybrid method as input variable in the learning process for the corresponding agronomical variable. The selected VIs were also calculated with the observed Sentinel-2 reflectance spectra and included as input variable in the prediction process. The VIs calculated with the observed spectra were extracted for each plot using the mean value of the spectral bands in each date.

3.5.3.3. Retrieval of crop parameters with artificial neural network

For implementing the hybrid method, the LUT with the corresponding spectra, the selected VIs and the corresponding crop parameters was used to train a machine learning ANN algorithm with four hidden layers. This approach was trained using the LUT to find the link of the input variables with Cab, Anth, LAI and EWT. This learning process allowed retrieving the crop parameters corresponding to each observed Sentinel-2 spectrum. In the simulated training process, the spectra were split into a training (80%) and testing (20%) part. In the training part, a 10-fold cross-validation procedure was implemented to select the best variables and to avoid overfitting using the stepwise variance inflation factors (VIF). Later, the spectra of the LUT were scaled to provide a faster and more stable convergence during the learning process. Six different transformations were used for the spectral scaling: i) normalization ii) minimum-maximum iii) standardization, iv) robust scaling based on the Interquartile Range (IQR), v) quantile transformer and vi) YeoJohnson. The dependent variable was also scaled by normalizing the values between 0 and 1 to ensure that the predicted and observed variables have a similar range. For each observed Sentinel-2 spectrum, the ANN regressor model applied a mean squared error cost function to identify the most similar spectrum of the LUT to retrieve the corresponding crop parameters. The hybrid ANN-PROSAIL-PRO method was executed in Python (version 3.10; Python Software Foundation, 2021) using the “keras” Python library (Chollet, 2015).

3.5.3.4. Performance of the hybrid method for retrieving crop parameters, winter wheat N status and traits

The suitability of the hybrid method applied to Sentinel-2 for retrieving Cab, Anth and LAI was tested by analyzing the linear correlation between the retrieved values and the corresponding crop parameters measured at ground level in each plot. The crop parameter used to validate Cab retrieved with the hybrid method was the chlorophyll content measured with the leaf clip sensor Dualex (Cab-D). Similarly, the crop parameter measured at ground level used to validate Anth was the anthocyanin content measured with Dualex (Anth-D). Aboveground biomass measured with the crop samples of each plot was used to validate the LAI retrieved values. These relationships were analyzed for the measurements obtained in the six sampling days (n = 16 each date), the same GS of both years (n = 32 for mid stem elongation, final stem elongation and flowering) and for all dates together (n = 96).

The suitability of EWT to identify the water content was analyzed by testing its performance when distinguishing between the two water levels at flowering both years. For this purpose, the EWT values were analyzed with a least squares means contrasted with the Tukey test ($P \leq 0.05$) using the water level of each year as factor to find significant differences. The same method was applied to the water indices calculated with the Sentinel-2 bands (Table 5) of each plot to compare the accuracy of the water content estimated with the hybrid method and the with the spectral VIs.

The potential of the hybrid method applied to Sentinel-2 to determine the winter wheat N status was tested by analyzing the capacity of the crop parameters to estimate the NBI calculated with the Dualex and the NNI calculated with the biomass samples. The crop parameters retrieved were combined using a multiple lineal regression (MLR) model fitted to the NBI and to the NNI to develop new indicators for N status assessment. Because NBI is calculated as the ratio between Cab-D and a polyphenol (flavonol) content measured with Dualex, the MLR model was fitted to Cab and Anth retrieved with the hybrid method to estimate NBI. Similarly, the MLR model used to estimate NNI was fitted to the two components of the CDC: Cab (as a proxy of %N) and LAI (as a proxy of biomass). The ability of Sentinel-2 to estimate the crop N status combining different crop parameters retrieved with the hybrid method was compared with the performance of using one VI from the literature (Table 5). The VIs were calculated for each plot using the mean value of the spectral bands in each date.

A similar method using MLR was applied to predict winter wheat traits. The traits that were measured with the grain samples at harvest and predicted with the hybrid method were yield (kg ha^{-1}), GPC (%) and N output (kg N ha^{-1}). For each trait, it was selected the best combination of Cab, LAI, Anth and EWT to be included in an MLR to test their potential as traits indicators. Because the value of the crop parameters changes with crop growth and development, only the flowering dataset was used to estimate the winter wheat traits. The statistical analyses were conducted using R (version 4.1.1; R Core Team, 2021).

Table 6. The input parameters and their total ranges used to generate the look-up tables (LUT) with the PROSAIL-PRO model.

	Description	Ranges	Units
PROSPECT-PRO			
N	Internal leaf structure parameter	1.5 - 3	[-]
Cab	Chlorophyll a+b content	0 - 60	µg/cm^2
Car	Carotenoid content	0 - 25	µg/cm^2
Anth	Anthocyanin content	0 - 7	µg/cm^2
Cbrown	Brown pigments content	0 - 1	[-]
EWT	Equivalent water thickness	0.001 - 0.035	g/cm^2
LMA	Leaf dry matter content	0.001 - 0.035	g/cm^2
SAILH-5B			
LAI	Leaf area index	0.5 - 7	[-]
LIDFa	Leaf angle distribution	20 - 90	deg
hspot	Hotspot parameter	0 - 1	deg
tts	Solar zenith angle	19º - 72º	deg
tto	Observer zenith angle	0º - 16 º	deg
psi	Relative azimuth angle	139º - 161 º	deg

3.5.4. Multiple Endmember Spectral Mixture Analysis for land use monitoring

The validation of remote sensing information to monitor crop land use change at regional scale was performed using the AVIRIS imagery collected in the California study area. The results are shown in Chapter 4.6. For this purpose, maps of subpixel fractional covers of GV, NPV and soil were produced using MESMA (Roberts et al., 1998) in Viper Tools 2.1 (Roberts et al., 2019) for each AVIRIS image (Fig 10). Therefore, the models used to calculate the subpixel fractional covers were constructed with 1, 2 or 3 endmembers plus shade fraction for brightness normalization. MESMA was run using spectral libraries constructed with endmembers from in-scene pixels that belonged to a single class in each image. Spectral libraries were constructed for each year because libraries built from the same image produce more accurate land use maps (Meerdink et al., 2019). Spectral endmembers were extracted from shapefile polygons uniformly distributed throughout the study area.

MESMA identifies the fractional covers of each pixel as the combination of endmembers that produces the smallest RMSE. Fraction limits were restricted to between 0 and 1 with a maximum shade fraction of 0.80 and a RMSE ≤ 2.5%. All unmixed pixels were shade normalized by dividing each non-shade class by the sum of all non-shade classes to obtain a sum of subpixels fraction of one (Dennison and Roberts, 2003).

The NDVI (Table 5) and natural color maps developed with the AVIRIS images were used to identify the GV areas within the study site. The cellulose absorption index (CAI; Table 5), together with natural color maps were used to identify the NPV and soil endmembers by selecting the areas with extreme values of CAI. Yearly spatial data of Kern County crops available as ESRI format shapefiles (Kern County Department of Agriculture and Measurement Standards, 2022c) were used to validate the selected in-scene endmembers in this county.

Iterative endmember selection (IES; Schaaf et al., 2011; Roth et al., 2012) was used to select the optimal and representative endmembers used in each image classification. IES relies on a square array that calculates the performance of each endmember of the training library when it is used to model the other spectra of the library (Roberts et al., 1997). Viper Tools 2.1 creates the square arrays as standard ENVI images constituted by several *n* by *n* matrix, being *n* the number of spectra in the library. The different matrices show the performance as RMSE, spectral angle, endmember fraction, shade fraction and a band indicating if the model fits the constraints previously set. Based on the square arrays, IES identifies the best single spectra as the one that produces the highest kappa coefficient (Cohen, 1960); usually belongs to the most represented class. Next, IES adds a second endmember, which in combination with the first endmember produces the largest increase in kappa. As more endmembers are added, it systematically removes endmembers to test whether an endmember selected earlier in the process generates a suboptimal solution; if kappa improves or does not change the endmember is removed, but if kappa decreases it is added back to the library. IES continues this process until the kappa coefficient no longer improves, generating an endmember library that is a subset of the original library. This process was repeated using 10 subsets of the original spectral library, selecting the subset dataset that obtained the highest kappa coefficient with the minimum number of endmembers as described in Roberts et al., 2017. Each of the 10 subsets was calculated by randomly selecting a maximum of 20 pixels from

each polygon, or at most 50% of the pixels for smaller polygons. The initial number of endmembers used to model GV, NPV and soil fractional covers was between 777 and 2686.

The shapefiles developed by the California Department of Water Resources (2022) that enclose each crop field individually were used to mask the MESMA results. The MESMA results statistics were computed from the area that lies inside the polygons that enclose the crop fields. An inner 40 m-buffer was previously applied in each polygon to minimize the edge effect and to avoid other cover classes such as impervious surface. The total number of polygons (crop fields) analyzed was 7405, covering 608 km^2. The GV, NPV and soil areas in each image were calculated as the sum of all subpixel fractional covers of each class in the masked area and then normalized by the total number of pixels to obtain the percentage of the area covered by each class.

3.6. Atmospheric correction and signal normalization of satellite imagery

The accuracy of the surface reflectance measured with two spaceborne sensors after Sen2Cor, FLAASH and MODTRAN atmospheric correction was validated for winter wheat monitoring in Chapter 4.5. For this purpose, it was i) retrieved the atmospheric constituents at the time and location of the satellite acquisition, ii) conducted a sensitivity analysis to determine the effect of different atmospheric constituents on the atmospheric correction of Sentinel-2 and WorldView-3 spectral bands, iii) hypothesized that the atmospherically corrected Sentinel-2 and WorldView-3 surface reflectance values were comparable to nadir field spectral measurements, and iv) proposed and validated an empirical signal normalization procedure for compensating for the off-nadir view angle induced effects on surface reflectance that allowed coupling Sentinel-2 and WorldView-3 images.

3.6.1. Atmospheric constituents retrieval

As part of atmospheric correction, it is critical to consider the scattering and absorbing impacts of three components of the atmosphere: aerosol optical thickness (AOT) impact on visibility, the water vapor column (WVC), and the ozone atmospheric concentration (O_3) (Liang and Wang, 2019). For this purpose, the atmospheric constituents should be measured at the time and location of the satellite spectral acquisition. In this thesis, the values of these constituents in the Aranjuez study area were obtained from different types of Moderate Resolution Imaging Spectrometer (MODIS) Level-1 Atmosphere and Land products, as used by Vermote et al. (2016) in the Landsat 8 LaSRC atmospheric correction scheme. The WVC

and O_3 values were retrieved from MOD/MOD07 products with an approximate 5-km spatial resolution (NASA, 2023e). The AOT and WVC were retrieved from MCD19A2 products with an approximate 1-km spatial resolution (NASA, 2023f). The algorithm to calculate visibility from AOT was originally acquired from the Second Simulation of a Satellite Signal in the Solar Spectrum (6S) source code (Vermote et al., 1997) and was further referenced and validated in González et al. (2005). The AOT-visibility equation is shown in Eq.3. The land surface temperature was retrieved from MOD/MYD11C1 A1 products (1-km resolution). Other studies used atmospheric constituent values delivered from the Aerosol Robotic Network (AERONET) (Xu et al., 2020; Doxani et al., 2018). However, we decided to use MODIS retrieved values, which have already been successfully used for atmospheric correction assessment (Martins et al., 2017; Sola et al., 2018), and follow the approach proposed by the Landsat 8 Program for estimating Land Surface Reflectance (USGS, 2023b).

$$Visibility = \exp\left(\frac{-\ln\left(\frac{AOT}{2.7628}\right)}{0.79902}\right) \qquad \text{(Eq. 3)}$$

3.6.2. Atmospheric corrections

The atmospheric correction in satellite images of three atmospheric-RTMs were compared: ESA Sen2Cor algorithm (Main-Knorn et al., 2017), MODTRAN5 (Berk et al., 1987; Berk et al., 2008), and FLAASH (Adler-Golden et al., 1999). The Sen2Cor only processes Sentinel-2 Level 1C products, whereas MODTRAN5 and FLAASH were used to process both Sentinel-2 Level 1C (after conversion to TOA radiance) and WorldView-3 products. For MODTRAN and FLAASH, the bands SRF of WorldView-3 and Sentinel-2 (Fig 14) were generated prior to the atmospheric correction process; this step was not needed for Sentinel-2 imagery in Sen2Cor. Additionally, while both Sen2Cor and FLAASH generate surface reflectance images at the end of the atmospheric correction process, corrections with MODTRAN are more complex. For each WorldView-3 and Sentinel-2 image, MODTRAN was run for three separate surface albedo iterations (0.0, 0.5, 1.0). For each surface albedo iteration, MODTRAN generates corresponding upwelling radiance values which are used as scaling factors for deriving surface reflectance transform coefficients. These transform coefficients were then band-wise applied to the radiance images to derive surface reflectance images. The three-albedo MODTRAN procedure is commonly used when using MODTRAN to estimate

surface radiance and to correct image radiance to surface reflectance (Matthew et al., 2000; Berk et al., 2008; Mousivand et al., 2015).

The scattering and absorbing impact of AOT, WVC and O_3 atmospheric constituents have different treatment in Sen2Cor than in MODTRAN and FLAASH. In Sen2Cor, AOT at 550 nm and WVC values are calculated from in-scene spectral band combinations and cannot be modified; however, O_3 concentration and visibility can be changed. The Sen2Cor WVC algorithm derives a water vapor product based on Sentinel-2 band B9 (945 nm, 60-m spatial resolution) in conjunction with B8A (865 nm, 20 m), both in the NIR region of the spectrum. A value for AOT is derived from Sentinel-2 L1C products using the dense dark vegetation (DDV) algorithm (Kaufman et al., 1997), based on information from B2 (490 nm, 10 m), B4 (665 nm, 10 m) and B12 (2190 nm, 20 m). The derived WVC and AOT products with Sen2Cor contain sets of spatial values of these variables, instead of a single value for the whole scene. By default, visibility is extracted pixel by pixel from the generated AOT product, but a constant value for the entire image can be defined by the user. The relationship between AOT and visibility is defined in Eq 3. These new Sen2Cor processed products comprise a new set of Sentinel-2 atmospherically corrected images, in addition to the downloaded Sentinel-2 L2A products specified in Table 3. Conversely, in MODTRAN and FLAASH, the values of these atmospheric constituents are user specified. Moreover, spatial and temporal variation in atmospheric constituents must be considered for each Sentinel-2 Level 1C and WorldView-3 scene, which requires that the atmospheric constituent values be queried at the time and location where satellite products were acquired. The O_3 value retrieved from MODIS was used in Sen2Cor to process Sentinel-2 L1C imagery together with a visibility value calculated from the actual MODIS AOT, and the new product generated was named Sentinel-2 L2A_O3V.

To summarize, the set of satellite imagery used in Chapter 4.5 consisted of 16, half in each year at final stem elongation. The Sentinel-2 dataset was as follows: Sentinel-2 Level 1C (i.e. TOA image downloaded from the ESA DataHUB server; (ESA, 2023e) as Level 1C); Sentinel-2 L2A that displayed surface reflectance values and had been atmospherically corrected by the Payload Data Ground Segment using in-scene information (downloaded from the ESA DataHUB server (ESA, 2023e) as Level 2A); Sentinel-2 L2A_O3V was the Sentinel-2 L1C image atmospherically corrected with Sen2Cor using the ancillary data (O_3 and Visibility) retrieved from MODIS, after calculating Visibility with Eq. 3; Sentinel-2 -

MODTRAN and Sentinel-2 -FLAASH were the Sentinel-2 imagery atmospherically corrected with MODTRAN or FLAASH packages. The WorldView-3 dataset used in this study was: WorldView-3-TOA (i.e. the image before atmospheric correction); WorldView-3-MODTRAN and WorldView-3 -FLAASH, were the WorldView-3 images corrected with MODTRAN or FLAASH using the atmospheric constituents retrieved from MODIS.

3.6.3. Sensitivity analysis

A sensitivity analysis combining two years of satellite imagery was conducted to evaluate the impact of atmospheric constituent variability on the surface reflectance corrections. For the Sen2Cor atmospheric corrections of the Sentinel-2 L1C images, modified corrections were made for the minimum and the maximum ranges of visibility (5 and 120 km) and O_3 concentration (250 and 450 Dobson units (DU)) commonly found in the atmosphere (World Meteorological Organization, 2018). A sensitivity analysis for the MODTRAN atmospheric correction of WorldView-3 imagery was conducted for AOT and O_3 atmospheric constituents varying in the same range as the Sen2Cor sensitivity analysis. Additionally, WVC was included in this analysis ranging from 0.22 to 1.22 g cm^{-1}. High and low variations in each of the three atmospheric parameters were applied individually, while the original settings for the remaining values were kept to clearly observe the differences resulting from the minimum and maximum values. The modified corrections were also compared to the original imagery corrected with the current atmospheric constituents retrieved from MODIS by computing the relative reflectance difference for each band expressed as a percentage.

3.6.4. Atmospheric correction assessment

A statistical analysis was conducted to compare the ground-truth reflectance data collected with the hand-held spectroradiometer and the resulting surface reflectance values derived from the various atmospherically corrected satellite images. For this purpose, a statistical single-sample t-test was performed using information from four dense and four sparse vegetation plots identified in the Aranjuez experiment each year (Fig 13; Table 7). The single-sample t-test was carried out using the spectroradiometer measurements in the dense vegetation (DV) and sparse vegetation (SV) plots as the representative population value for comparison, while surface reflectance values from Sentinel-2 and WorldView-3 derived by the corresponding atmospheric correction approaches were taken as the tested samples. This allowed determining which of the atmospheric procedures was better suited for this kind of

environment and verifying whether the values observed from the WorldView-3 and Sentinel-2 sensors were significantly different from the field spectra (Cross et al., 2018). In this study, the approach stated in Manakos et al. (2011) was followed, i.e., the lack of differences between Sentinel-2 or WorldView-3 surface reflectance and the spectroradiometer reflectance constitutes the null hypothesis. It was tested with a 95% confidence level; therefore *P*-values > 0.05 confirm the null hypothesis and denote no differences between ground-truth spectra and satellite-derived surface reflectance. In the validation procedure of the proposed empirical approach, linear least squares regression and parameters defining the goodness of fit (R^2 and RMSE) between the reference and the transformed dataset were calculated (Cross et al., 2018).

To validate Sentinel-2 and WorldView-3 surface reflectance values of each band using ground-truth measurements, the characteristic field spectra acquired with the FieldSpec were convolved over Sentinel-2 and WorldView-3 bands using the corresponding satellite SRFs, after resampling from 3 to 1 nm (Milton et al., 2009). The spectral response functions (Fig 14) were obtained from DigitalGlobe (Kuester, 2016) for WorldView3 and from the ESA Sentinel-2 Spectral Response Functions Document Library for Sentinel-2 (ESA, 2023f). Due to the effective spectral range of the FieldScpec (400 – 900 nm), only the bands within the VNIR region were analyzed (Table 4).

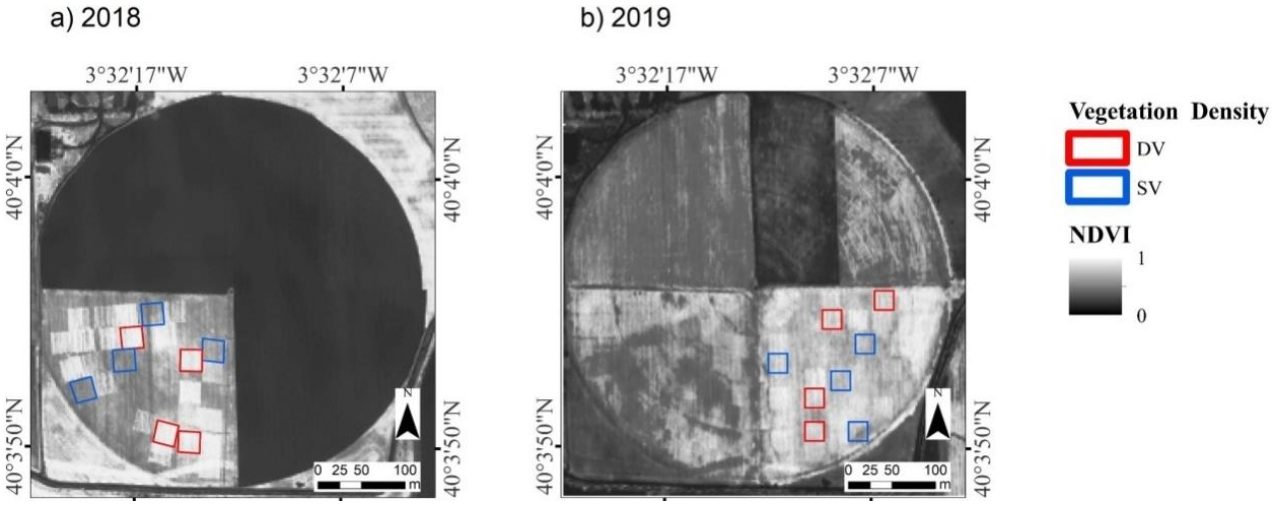

Fig 13. Plots with different vegetation density (dense vegetation (DV) and sparse vegetation (SV)) selected both years delimited over the Normalized Difference Vegetation Index (NDVI) map generated from the WorldView-3 image on a) 18 April 2018 and b) 12 April 2019.

Table 7. Center coordinates of the plots with different vegetation density selected from both years, and the mean value of the normalized difference vegetation index (NDVI) calculated with the field spectra acquisition.

Vegetation density	Area Center coordinates (lat (φ), lon (λ))	NDVI
	17 April 2018	
Dense Vegetation (DV1)	3°32'14,394"W 40°3'50,288"N	0.958
Dense Vegetation (DV2)	3°32'17,189"W 40°3'54,137"N	0.966
Dense Vegetation (DV3)	3°32'14,367"W 40°3'53,275"N	0.964
Dense Vegetation (DV4)	3°32'15,586"W 40°3'50,592"N	0.956
Sparse Vegetation (SV1)	3°32'13,275"W 40°3'53,762"N	0.816
Sparse Vegetation (SV2)	3°32'19,569"W 40°3'52,182"N	0.581
Sparse Vegetation (SV3)	3°32'17,601"W 40°3'53,298"N	0.684
Sparse Vegetation (SV4)	3°32'16,258"W 40°3'55,042"N	0.764
	12 April 2019	
Dense Vegetation (DV1)	3°32'6,27"W 40°3'55,384"N	0.894
Dense Vegetation (DV2)	3°32'9,561"W 40°3'50,563"N	0.827
Dense Vegetation (DV3)	3°32'9,584"W 40°3'51,741"N	0.894
Dense Vegetation (DV4)	3°32'8,79"W 40°3'54,737"N	0.857
Sparse Vegetation (SV1)	3°32'7,35"W 40°3'50,573"N	0.700
Sparse Vegetation (SV2)	3°32'8,347"W 40°3'52,457"N	0.716
Sparse Vegetation (SV3)	3°32'7,152"W 40°3'53,784"N	0.696
Sparse Vegetation (SV4)	3°32'11,345"W 40°3'52,958"N	0.703

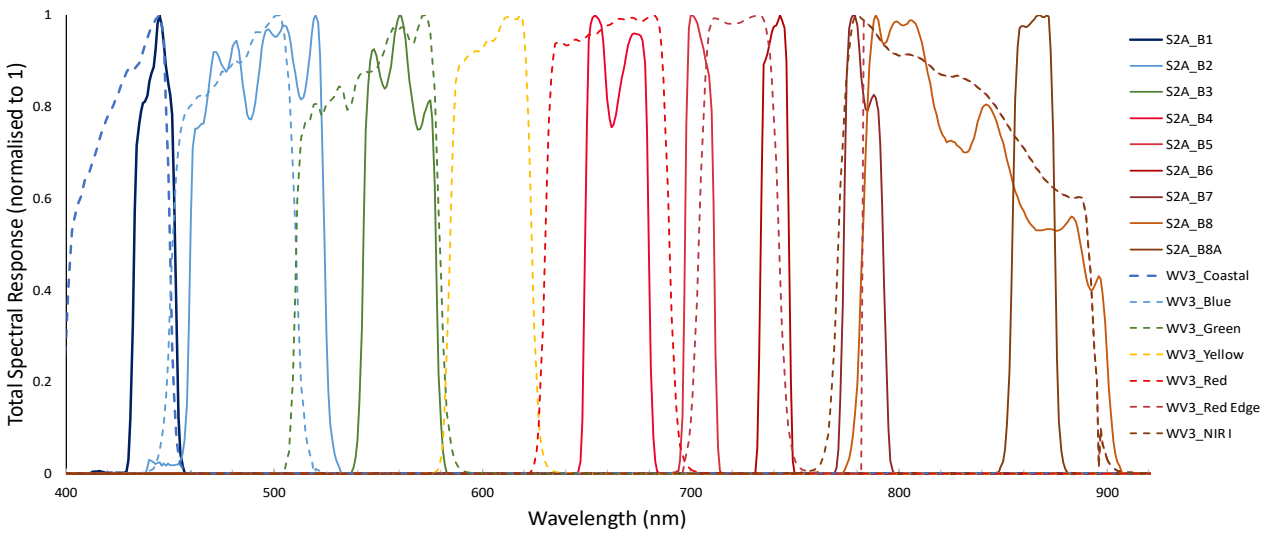

Fig 14. Spectral response functions of the Sentinel-2 (S2) and WorldView-3 (WV3) bands used for atmospheric correction assessment and signal normalization.

3.6.5. WorldView-3 signal normalization

While little effect from solar-surface-sensor geometric variability was expected in Sentinel-2 surface reflectance due to its constant 11º forward view angle and its Sun synchronous orbit, heavy surface anisotropy effects are envisaged in WorldView-3 surface reflectance due to the large (24.6º and 39.1º) off-nadir view angles (Pacifici et al., 2014). Furthermore, these off-nadir angles lengthen the atmospheric paths of the upwelling radiance signals observed by the WorldView-3 sensor. In addition, the different relative position of the satellite with the Sun produced different illumination conditions in the two images: a backward scattering acquisition in 2018, and a forward scattering in 2019. Accurate surface reflectance estimation requires correction for both surface anisotropy and lengthened atmospheric path, which can be challenging as both signals are integrated into a single radiance value. In a preliminary evaluation of these effects, FLAASH and MODTRAN corrections were performed with the azimuth and zenith (off-nadir) angles specified in the WorldView-3 product metadata in addition to nadir view calculations. Due to combined effects of surface anisotropy and lengthened atmospheric paths, corrections of the 2018 WorldView-3 (backscattering) imagery tended to overestimate reflectance, while corrections of the 2019 WorldView-3 (forward scattering) imagery tended to underestimate reflectance (Pacifici et al., 2014; Fig 4). In contrast, the nadir corrections for both years produced more accurate reflectance estimates and were selected for all final atmospheric corrections. However, further corrections of surface anisotropy effects are required, as described below.

To best account for surface anisotropy effects, a normalization or harmonization of the atmospherically corrected WorldView-3 reflectance to nadir BRDF-adjusted reflectance was required (Roy et al., 2017). For this purpose, two approaches were used: i) the semi-empirical Rahman-Pinty-Verstraete (RPV) model was applied using values for ρ_0 (surface cover reflectance intensity), k (surface anisotropy) and Θ (relative amount of forward/backward scattering) proposed for wheat surfaces by Rahman et al. (1993), and ii) the kernel-driven Ross-Li method applied by deriving the MODIS MCD43A1 BRDF/albedo product (Wanner et al., 1995). In the second approach for the MODIS/WorldView-3 spectrally equivalent bands, two sets of isotropic, volumetric, and geometric kernel parameters were used to apply the c-factor approach (Lucht and Roujean, 2000). For this purpose, first, the values provided by Roy et al. (2017) were applied to MODTRAN/FLAASH atmospherically corrected WorldView-3 imagery to compensate for BRDF effects. Then, the values for the same

parameters were extracted from MCD43A1 products downloaded using the NASA Level-1 and Atmosphere Archive and Distribution System (LAADS) Distributed Active Archive Center (DAAC) service (NASA, 2023g) for the two WorldView-3 overpasses. The required spatial orientation parameters, i.e., azimuth and elevation angles, were available in the WorldView-3 product metadata files.

The empirical approach for normalization of WorldView-3 data based on field spectral measurements was proposed in the framework of this study to ensure a reliable coupling of WorldView-3 and Sentinel-2 information. Only the blue, green, red and NIR bands were used for this normalization strategy, as their SRF of both satellite bands overlap (Fig 14) and are within the spectroradiometer effective spectral range. The red edge bands were excluded because of the high variations along this region in the spectrum of vegetated surfaces (Horler et al., 1983) and the fact that small differences in the SRF would lead to large surface reflectance discrepancies between the Sentinel-2 and WorldView-3 imagery when coupling the products. The basic steps for this procedure are summarized as follows:

a. In a first stage, the atmospherically corrected values of WorldView-3 derived with FLAASH were calibrated against field survey spectra, obtaining the corresponding calibration coefficients for each WorldView-3 spectral band, which were then applied to transform each band. The calibration or normalization coefficient of each band was calculated by dividing the averaged WorldView-3 surface reflectance by the convolved reflectance measured at ground level. The calibration procedure was conducted for each date (and therefore, unique viewing geometry) to construct a database with the calibration coefficients of each band.

b. For the validation procedure, it was selected the pixels of the Sentinel-2 images within the study area avoiding edges in the images of both years; this resulted in a total of 454 Sentinel-2 10-m pixels (Fig 15). For each Sentinel-2 pixel, the spectral bands of the WorldView-3 pure pixels were extracted and transformed by the corresponding coefficient. To validate the coefficients, the Sentinel-2 bands were compared to the band average of the pure WorldView-3 pixels that lay inside each Sentinel-2 pixel after leaving 1-m buffer on each side of the Sentinel-2 pixels. A regression analysis was performed per spectral band between the reference (Sentinel-2 L2A) and the transformed WorlView-3 bands. The performance was verified by means of agreement analysis statistics.

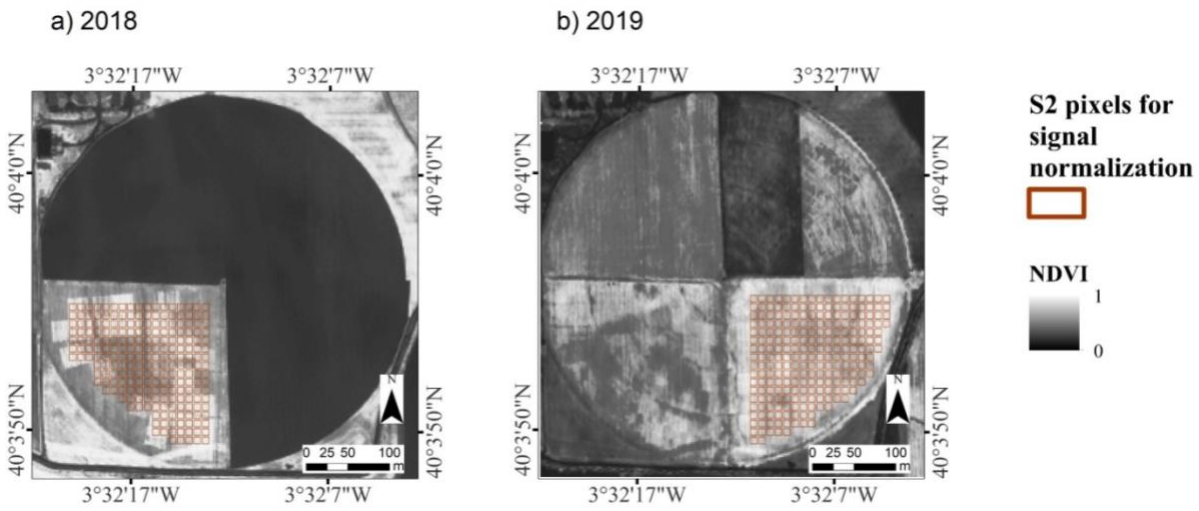

Fig 15. Normalized Difference Vegetation Index (NDVI) map generated from the WorldView-3 image of April 18, 2018 (a) and April 12, 2019 (b). Brown squares (8 x 8 m) are located in the center of the 10-m Sentinel-2 pixels used to validate the suitability of the empirical signal normalization procedure for coupling Sentinel-2 and WorldView-3 images.

Chapter 4:
Results

Chapter 4.1:
Agronomical variables obtained in the Aranjuez field experiment

4.1.1. Crop response to water and nitrogen supply

Different climatic conditions between experimental years, particularly the rainfall distribution, had a large effect on crop growth. The total amount of water received by W2 plots until biomass collection at flowering stage was 304 mm in 2018 and 216 mm in 2019. Differences in water availability between experimental years were also observed at tillering and stem elongation (Fig 16). Since no water was available for irrigation for several weeks of the 2019 growing season, the wheat suffered severe water stress, which later limited the crop response to N supply. Biomass accumulation and %N (Table 8) were greatly affected by the different climatic conditions, widening the range in the crop variables investigated and creating a suitable dataset for testing the relationships between crop performance and spectral measurements.

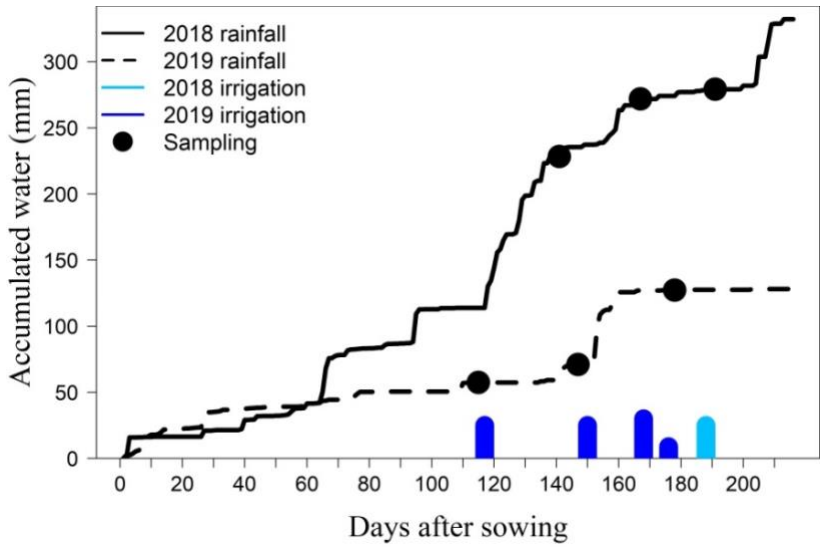

Fig 16. Total amount of accumulated rainfall (mm) and irrigation during the two experimental years. Only half of the experiment was irrigated at flowering. The dots indicate the dates of biomass sampling.

The biomass increased with GS and %N decreased (Table 8). This N dilution effect was also observed when comparing the crop parameters between years; the biomass accumulation tended to be higher in 2018, with significant differences between years at mid stem elongation and flowering ($P \leq 0.05$). In contrast, the %N was higher in 2019 with significant differences between years in the same dates as biomass. The effect of the different N fertilization rates was observed in the relative position with the CDC: data from low N levels

remained below the critical requirements, whereas high N levels tended to approach or surpass the $\%N_c$ (Fig 17a).

Increasing N levels had a positive effect on biomass, %N and NNI in the two experimental years (Table 8). The NNI distinguished between N-deficit plots (N0 and N1), plots with the recommended rate (N2), and the overfertilized plots (N3) in all the 2018 GSs. The NNI distinguished between the non-fertilized plots and the overfertilized plots in all the 2019 GSs, but the discriminatory capacity of intermediate N levels varied with the GS. Treatments N1 and N2 had a similar NNI at mid stem elongation in 2019, but a different NNI at final stem elongation. At flowering, the NNI differences between N1 and N2 treatments were clearer in the W2 level than in the W1 (Table 8). Differences in the NNI between the water levels established in each N level were only found in the 2019 N2 treatment, yielding higher a NNI in the W2 plots. The effect of water levels was clear in reducing %N in the N2 and N3 treatments but was also accompanied by a reduction in biomass. Increasing water level was associated with an increase in the spikes' N content (kg N ha^{-1}): it was 12% higher in W2 than in W1 in 2018 and 9% higher in N3-W2 plots with respect to N3-W1 in 2019 (data not shown).

A strong crop response to water levels was observed in the leaf conductance measured at flowering in 2019 (Table 8). Treatments with a higher irrigation level showed higher conductance than treatments with lower water application across all the N levels ($P \leq 0.05$). For each water level, no differences in leaf conductance were observed between N levels. The greatest difference between water levels was observed in N0, which obtained the highest leaf stomatal conductance mean value among the W2 plots.

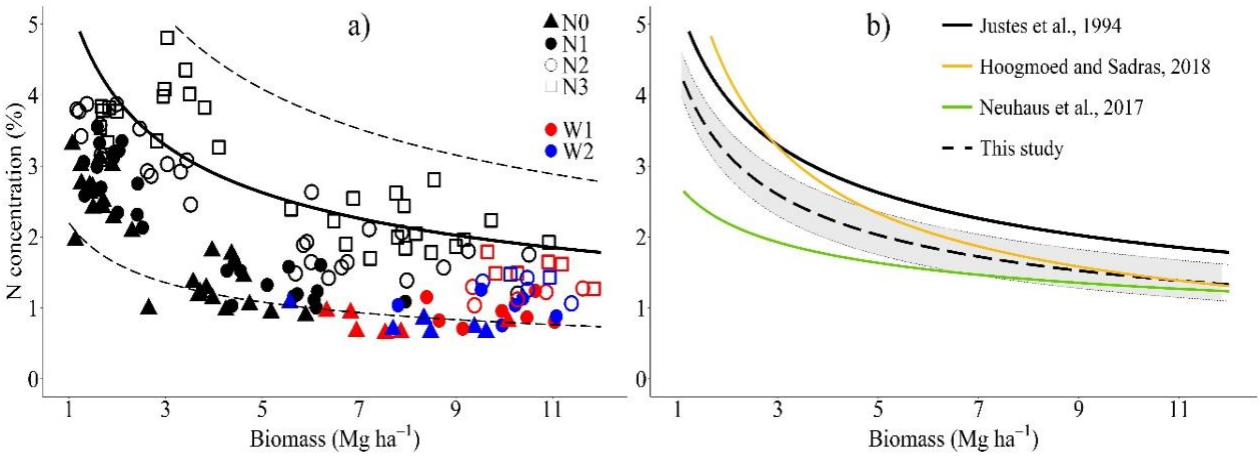

Fig 17. a) Pair values of aerial biomass (Mg ha^{-1}) and N concentration (%) for all N levels (symbols), water levels (colors) and sampling dates of the experiment. The continuous line is the critical N dilution curve (CDC) (%$N_{critical}$= 5.35 x Biomass $^{-0.442}$) for winter wheat, and the dashed lines the envelop curves (N_{max} = 8.3 x Biomass $^{-0.442}$ and N_{min} = 2.2 x Biomass $^{-0.442}$) according to Justes et al. (1994). b) Comparison of the CDC proposed by Justes et al. (1994) (solid black line) with the CDC fitted to the N2 treatments in this study (%N_c= 4.42 x Biomass $^{-0.483}$, R^2 = 0.88) (dashed line); the gray area indicates the envelop curves at 95% confidence intervals (N_{max} = 4.14 x Biomass $^{-0.532}$ and N_{min} = 4.73 x Biomass $^{-0.433}$). The green line is the CDC under water limited conditions proposed by Neuhaus et al. (2017) (%N_c =0.7 x 3.91 x Biomass $^{-0.32}$), and the yellow line is the CDC proposed by Hoogmoed and Sadras (2018) (%N_c =6.75 x Biomass $^{-0.66}$).

Table 8. Biomass (kg · DM · ha^{-1}), plant N concentration (N conc, %), nitrogen nutrition index (NNI) and flag leaf conductance (mmol · m^{-2} · s^{-1}) for the various N and water levels at different growth stages for the two experimental years. Within a year and growth stage, values followed by the same letter are not significantly different according to Tukey's test at $P \leq 0.05$.

Growth stage	Treatment Water	Treatment N	2018 Biomass (kg DM ha^{-1})	2018 N conc. (%)	2018 NNI	2019 Biomass (kg DM ha^{-1})	2019 N conc. (%)	2019 NNI	2019 Conductance (mmol m^{-2} s^{-1})
Mid stem elongation		**N0**	1568 a	2.46 a	0.55 a	1521 a	2.83 a	0.63 a	-
		N1	2091 a	2.63 a	0.68 a	1683 a	3.23 ab	0.74 ab	-
		N2	2843 b	3.00 a	0.88 b	1531 a	3.58 bc	0.8 bc	-
		N3	3322 b	3.96 b	1.25 c	1771 a	3.70 c	0.89 c	-
Final stem elongation		**N0**	4256 a	1.04 a	0.37 a	4068 a	1.48 a	0.53 a	-
		N1	5924 a	1.14 a	0.47 a	5107 ab	1.65 ab	0.58 a	-
		N2	8242 b	1.68 b	0.79 b	6456 bc	1.85 bc	0.78 b	-
		N3	8593 b	2.29 c	1.1 c	7456 c	2.00 c	0.9 b	-
Flowering	**W1**	**N0**	8108 a	0.69 a	0.33 a	6576 a	0.94 a	0.4 a	144 ab
		N1	9830 ab	0.8 ab	0.41 a	9667 ab	1.12 abc	0.57 ab	151 ab
		N2	12965 c	1.06 bc	0.61 b	9970 ab	1.17 abc	0.6 bc	175 abc
		N3	11851 bc	1.51 e	0.84 c	10551 b	1.56 d	0.83 d	141 a
	W2	**N0**	8797 a	0.69 a	0.33 a	7412 a	0.92 a	0.41 a	297 d
		N1	11101 abc	0.8 ab	0.43 a	9487 ab	1.12 ab	0.56 ab	245 cd
		N2	12979 c	1.14 cd	0.66 b	10877 b	1.37 cd	0.74 cd	240 cd
		N3	13713 c	1.40 de	0.83 c	11654 b	1.36 bcd	0.75 d	266 cd

4.1.2. Winter wheat traits

As mentioned, higher levels of N and water led to an increase in biomass and plant %N at the flowering stage, with more noticeable effects in 2018. Biomass showed a correlation with yield (R^2 = 0.48) and with N output (R^2 = 0.53), but not with GPC. On the other hand, plant %N was linked to GPC (R^2 = 0.69) and to N output (R^2 = 0.49), but not to yield.

The yield response to N fertilization was stronger in 2018 than in 2019. All N levels obtained more yield in 2018, and the differences between N levels were larger that year (Fig 18a). Water levels did not affect the yield for any N level and year ($P \geq 0.05$). Yield increased with N application following a quadratic plateau model in both years. This fit resulted in significant differences between all N levels, except for N2 and N3 in 2018 ($P \leq 0.05$). In fact, for 2018, the optimal N fertilizer rate was 213.7 kg N ha^{-1}, indicating that the plateau was not reached by the N3 plots (186 kg N ha^{-1}). In contrast, for 2019, the yield showed differences in

the control treatment (N0), reaching the plateau with a lower N fertilization dose (127.8 kg N ha^{-1}). Therefore, this finding showed that N2 (149 kg N ha^{-1}) and N3 (199 kg N ha^{-1}) plots were over-fertilized.

Contrary to yield, GPC was higher in 2019 than in 2018 for all N levels ($P \geq 0.05$). Significant differences between water levels were only found in the N3 plots of 2018, with higher values in W2 (Fig 18b). Therefore, the GPC of the W1 and W2 levels of 2018 were plotted separately, while the two water levels of 2019 were plotted together. The GPC increased linearly with N fertilization in 2019, and it fitted a quadratic model in 2018 for the two water levels. The different N fertilization rates produced significant differences between N levels in 2018, as well as in 2019, except for the N-stressed plots (N0 and N1).

The N output was higher in 2018 than in 2019 (Fig 18c). Nevertheless, this difference between years was not found in the N-stressed plots (N0 and N1) ($P \geq 0.05$). The effect of the N fertilization in N output was stronger in 2018 than in 2019, as the different N fertilization rates led to differences in N output between all N levels in 2018, whereas the N output of the well-fertilized plots (N2 and N3) was not different in 2019 ($P \geq 0.05$). Consequently, the N output fitted a quadratic plateau model in 2019, with a maximum of 114 kg N ha $^{-1}$ in N output, which was reached with 251 kg of available N per hectare. The effect of water levels in N output, as well as in GPC, was not apparent in 2019 and was only found in the N3 plots of 2018, with a higher value in W2. Therefore, the two water levels were plotted together in 2019 (Fig 18c).

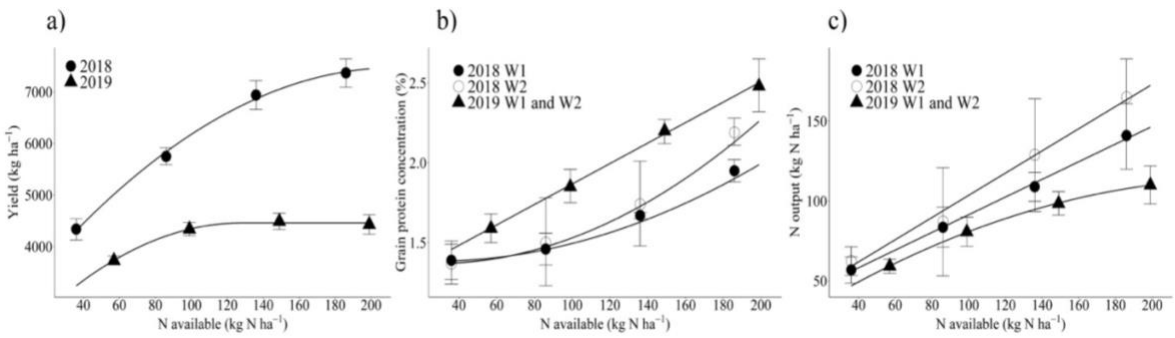

Fig 18. Winter wheat a) yield (kg ha^{-1}), b) grain protein concentration (%), and c) N output (kg N ha^{-1}) response curves to N availability (soil mineral + fertilizer) according to year (2018 and 2019). The variables were separated by water levels (W1 and W2) when significant differences were observed. The symbols are the mean values with standard errors as bars. Lines represent the adjusted model.

Chapter 4.2:
Simultaneous assessment of nitrogen and water status in winter wheat through planar-domain vegetation indices using hyperspectral and thermal sensors

4.2.1 Specific objectives and application of methods

This Chapter follows the analysis described in Chapter 3.5.1 to fulfill the **Objective 1:** simultaneous estimation of winter wheat N and water status for adjustment of N fertilizer and irrigation.

a) find a remote sensing indicator able to assess winter wheat N status at early growth stages by reducing soil background noise.

b) assess the ability of different spectral and thermal indicators to detect the crop N and water status with minimum confounding effects.

Due to the importance of assessing the within-field variability of the crop N and water status prior to N application to distinguish the areas that will respond to N fertilization and those that will not, this Chapter analyze the suitability of remote sensing indicators to accomplish this purpose. To assess the performance of remote sensing indicators for crop N status estimation, the NNI calculated with the biomass samples collected at different GSs was used as the ground-truth measurement of N status. Therefore, the relationship between a set of spectral VIs and NNI was analyzed at several GSs. One limitation is that at early GSs (when N fertilizer is usually applied in winter wheat) the soil background affects the signal measured by the sensor and makes difficult to identify the plant component of the spectrum when aiming to retrieve crop parameters. For this reason, this Chapter analyses the performance of VIs calculated with spectral bands from different regions of the spectrum, and the canopy VIs that combine two VIs to account for the two components of the critical dilution curve (CDC). Because the canopy VIs compensates the value of a chlorophyll index with a VI related to biomass, this index has the capacity to reduce the soil background effect and improve the NNI estimation. It is well known that the canopy and air temperature difference is related to water availability. This Chapter analyzed if the correlation of remote sensing thermal indicators with the leaf stomatal aperture improves when the soil effect in the thermal indicators is compensated with a VI related to biomass or ground cover. The performance of the thermal indicators was compared with the performance of the water VIs from Table 5.

Due to the effect of the water availability on the crop N status, this Chapter analyses if the N status assessment improves when the indicators selected as proxy of N and water status are combined in a new indicator. Finally, the effect of the N and water levels on the indicators

was analyzed to determine their suitability for adjusting N and water application simultaneously.

To reinforce the results, the performance of the spectral VIs was compared when the surface reflectance was measured with hyperspectral sensors at ground level with the FieldSpec and with the airborne sensors at 300 m above the experiment. The SWIR region was not covered by the FieldSpec spectral range (400 – 900 nm), and therefore, the SWIR-based VIs were not calculated with this sensor.

4.2.2 Vegetation indices as a proxy of NNI across growth stages

Most of the VIs based on the red edge region had a significant relationship with the NNI, showing variations in R^2 and RMSE according to the various GSs and sensors (Table 9 and Supplementary material S1). The NDRE index, based on the red edge and the NIR reflectance, yielded $R^2 > 0.5$ with the NNI in most cases, except for mid stem elongation 2019. The suitability of the red edge region as an N status indicator was also supported by the performance of other photosynthetic pigment VIs based on reflectance in red edge and visible regions: the DCNI, mND_{705} and mSR_{705}. Also, the CI, which used two wavelengths to calculate the slope of the red edge region, was related to the NNI and behaved similarly to mSR_{705}: the difference in RMSE between the two VIs was less than 0.006 in all cases (Supplementary material S1). Additionally, the PRI, based only on reflectance in the visible region (or the pigment absorption region), presented a high R^2 value with the NNI, but its performance varied widely between acquisition dates. In this study, the photosynthetic pigment VI based on the NIR-SWIR bands ($N_{850,\ 1510}$) showed a weak correlation with the NNI, as well as the TCARI.

The suitability of the red edge region combined with NIR reflectance to estimate NNI is supported when observing the better performance of NDRE with respect to the structural VIs NDVI and GNDVI in almost all cases. Structural VIs are calculated with an equation similar to NDRE but switching the red edge reflectance by red or green. Among them, the GNDVI performed better than the NDVI at final stem elongation with the two sensors for both years, especially with the FieldSpec. When analyzing the EVI, which was calculated with the same wavelengths as the NDVI but adding blue reflectance, it was observed that the airborne data obtained a higher R^2 and lower RMSE than the FieldSpec in most cases; also, the correlation improved with respect to the NDVI at mid stem elongation 2018 and final stem elongation

both years. Similarly, the OSAVI, which was calculated with the same wavelengths as the NDVI but adding a factor, performed better than the NDVI in the same dates as the EVI.

Overall, the best correlation with the NNI was obtained with the canopy indices, as the R^2 were among the highest in all stages. Particularly, the CCCI was the only index that reached $R^2 > 0.72$ in one of the sampling campaigns (Table 9). The low R^2 of most VIs at mid stem elongation 2019 was attributed to the effects caused by the soil background at low ground cover stages. This effect was compensated with the canopy VIs, especially with the CCCI, supporting the suitability of the planar-domain VIs to remove the soil background influence. At mid stem elongation 2018 most VIs performed similarly ($R^2 \sim 0.5$) and no improvement was achieved with the canopy indices because the amount of biomass was higher than at mid stem elongation 2019 (Table 8). Most structural and photosynthetic pigment VIs performed poorly at flowering 2019, suggesting that they were inaccurate under water stress. This was particularly evident with the PRI with the two sensors.

Table 9. Coefficient of determination (R^2) of the linear relationship between nitrogen nutrition index (NNI) and the different spectral vegetation indices extracted from the airborne imagery (AB) and the ground-level FieldSpec (FS). Bold numbers were significant at $P \leq 0.001$.

	Mid stem elongation			Final stem elongation				Flowering			
	2018	2019		2018		2019		2018		2019	
Vegetation indices	FS	AB	FS	AB	FS	AB	FS	AB	FS	AB	FS
NDVI	**0.51**	0.02	0.10	**0.53**	**0.41**	**0.52**	**0.39**	**0.59**	**0.59**	**0.40**	**0.41**
GNDVI	**0.50**	0	0.20	**0.57**	**0.54**	**0.54**	**0.51**	**0.62**	0.48	**0.52**	**0.49**
OSAVI	**0.53**	0.03	0.11	**0.60**	**0.53**	**0.56**	**0.41**	**0.65**	0.46	**0.39**	**0.41**
EVI	**0.54**	0.03	0.11	**0.65**	**0.59**	**0.57**	**0.43**	**0.68**	0.33	**0.38**	**0.39**
PRI	**0.52**	0.02	0.15	**0.59**	**0.61**	0.28	**0.51**	**0.61**	**0.59**	0.27	0.28
CI	**0.48**	0	0.20	**0.58**	**0.67**	**0.59**	**0.53**	**0.65**	**0.63**	**0.40**	**0.42**
TCARI	**0.30**	0.27	0.10	0.26	**0.48**	0.35	0.44	0.20	0.20	0.16	0.42
DCNI	**0.45**	**0.40**	0.22	0.28	**0.69**	**0.46**	**0.59**	**0.42**	**0.61**	**0.42**	**0.49**
mND_{705}	**0.53**	0.02	0.22	**0.56**	**0.58**	**0.62**	**0.60**	**0.64**	**0.63**	**0.38**	**0.45**
mSR_{705}	**0.48**	0.02	0.22	**0.58**	**0.69**	**0.62**	**0.55**	**0.64**	**0.62**	**0.38**	**0.40**
NDRE	**0.51**	0.07	0.27	**0.57**	**0.64**	**0.58**	**0.64**	**0.65**	**0.66**	**0.50**	**0.51**
$N_{850, 1510}$	-	-	-	-	-	0.31	-	**0.45**	-	0.18	-
TCARI/OSAVI	**0.46**	**0.39**	0.25	**0.46**	**0.57**	**0.53**	**0.64**	**0.56**	0.51	**0.59**	**0.58**
CCCI	**0.50**	**0.56**	**0.44**	**0.54**	**0.67**	**0.53**	**0.73**	**0.64**	**0.65**	**0.62**	**0.59**

The CCCI showed a significant correlation with the NNI when calculated with the aircraft or FieldSpec in all GSs. In this study, the CCCI calculated with the two hyperspectral sensors behaved similarly: they were significantly correlated in all dates ($P \leq 0.001$) with an R^2 = 0.64 ($P \leq 0.001$) when all dates are analyzed together (Fig 20). The equations of the upper ($NDRE_{max}$) and lower ($NDRE_{min}$) lines that involved the data from both campaigns were similar with the two sensors (Fig 19) and with the equations reported by Fitzgerald et al. (2010) for winter wheat in Australia ($NDRE_{max}$ = 0.61 × NDVI; $NDRE_{min}$ = 0.34 × NDVI), who also used a FieldSpec.

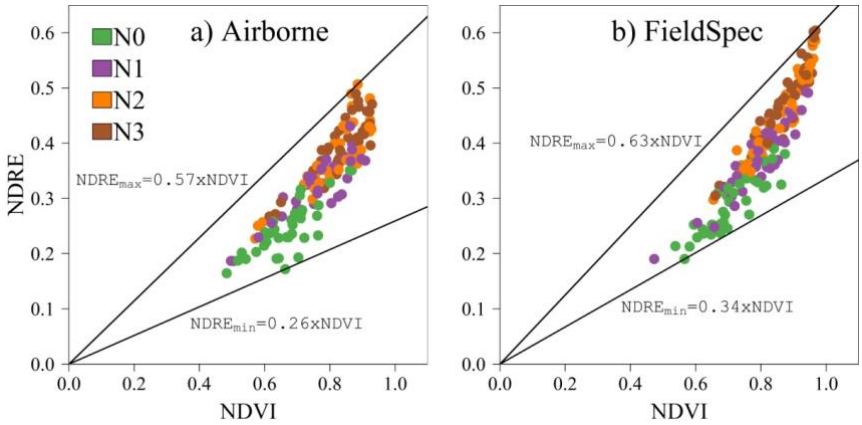

Fig 19. Graphical representation of the canopy chlorophyll content index (CCCI) developed with the mean value of the NDVI and NDRE of each plot extracted from a) the airborne imagery and b) with the FieldSpec in all campaigns. The CCCI value of each plot with a certain NDVI was calculated as CCCI = ($NDRE - NDRE_{min}$)/($NDRE_{max} - NDRE_{min}$).

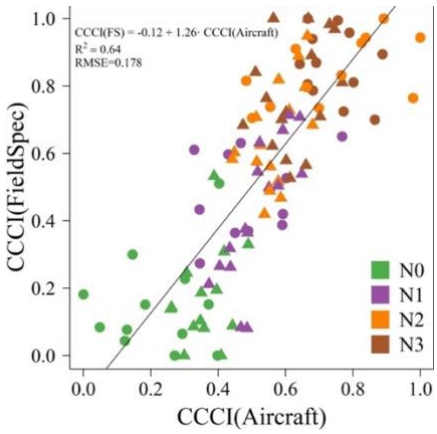

Fig 20. Pair-wise comparison of canopy chlorophyll content index (CCCI) calculated from the spectra acquired with FieldSpec at ground level and from the spectra acquired with the VNIR hyperspectral sensor from the aircraft. Data from mid stem elongation 2019 are not included because the delay between both samplings was longer than three days.

4.2.3 Spectral and thermal analysis at different water levels to assess leaf conductance

The effect of the water levels on the reflectance spectra was consistently detected in the SWIR as a function of different N levels (Fig 21). As expected, low water availability increased the spectral reflectance in the regions centered at 1240 nm and 1640 nm. Smaller differences in the NIR reflectance appeared in most cases. In the visible region, differences in the red region were evident, detected for all N levels in 2019 and for N0 in 2018. For this reason, the normalized difference between the NIR and SWIR proposed by Gao et al. (2015), was tested to detect crop water status.

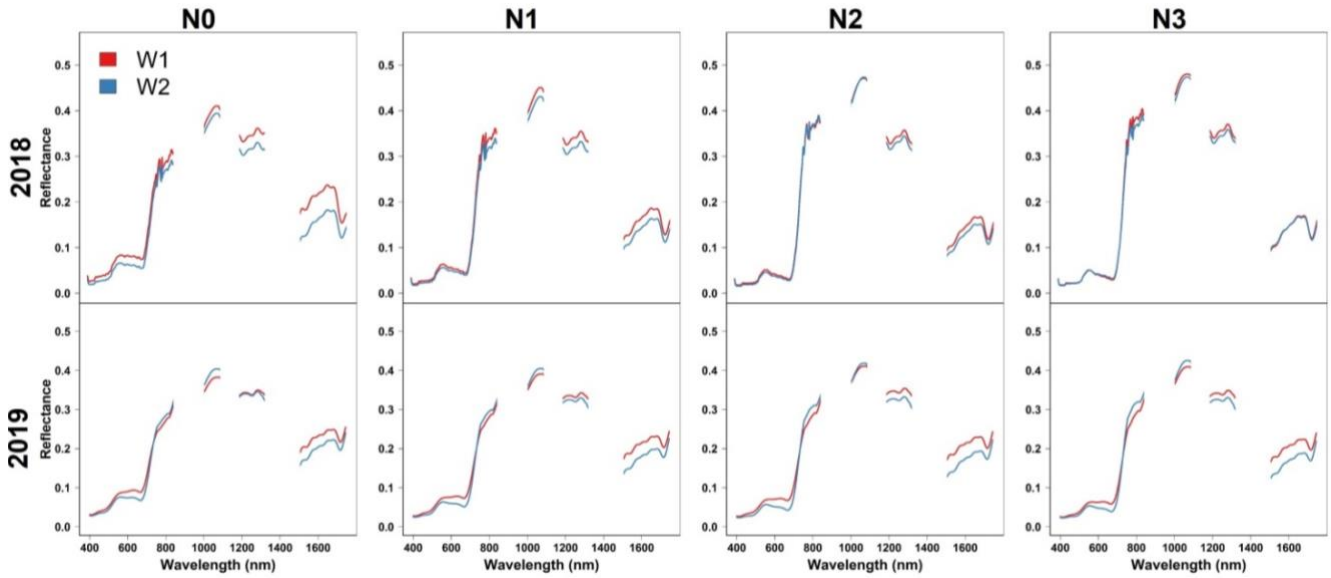

Fig 21. Average canopy reflectance acquired with the airborne hyperspectral sensors in the 400 – 1750 nm region at 300 m above ground level at flowering separated by nitrogen (N0, N1, N2 and N3) and water levels (W1 and W2) both years.

The distribution of all observations at flowering in the VIT plotted in the two-dimensional space formed by the SAVI and the temperature difference obtained from the thermal camera clearly distinguished among data from W1 and W2 water levels in both experimental years (Fig 22). The location in the VIT also stated that the water stress suffered by all plots was lower in 2018 than in 2019, with significant differences in the WDI between years ($P \leq 0.05$), in agreement with the comments in Chapter 4.1 on climate conditions (Fig 16).

Ground-based measurements of leaf stomatal conductance were better correlated with the WDI than with canopy-air temperature differences (Table 10), supporting the improvement in the crop water status estimation when canopy temperature is corrected by the ground cover

(Fig 23). The relationship of VIs based on SWIR reflectance with leaf stomatal conductance was significant only for $NDWI_{1640}$ ($P \leq 0.001$), but the $R^2 < 0.34$ for both indices (Table 10). The trend of the linear relationships between the index related to water stress (WDI) and the indices related to water content ($NDWI_{1240}$, $NDWI_{1640}$) were negative with a $R^2 > 0.55$ when the indices were extracted from the airborne spectra. Between them, the best correlation was obtained with the $NDWI_{1640}$ ($R^2 = 0.63$). Furthermore, the $NDWI_{1640}$ was the only VI based on SWIR bands that found differences in water status between years ($P \leq 0.05$). Therefore, the optical indices involving SWIR bands were able to detect the crop water status, but the best indicator of water status was the WDI.

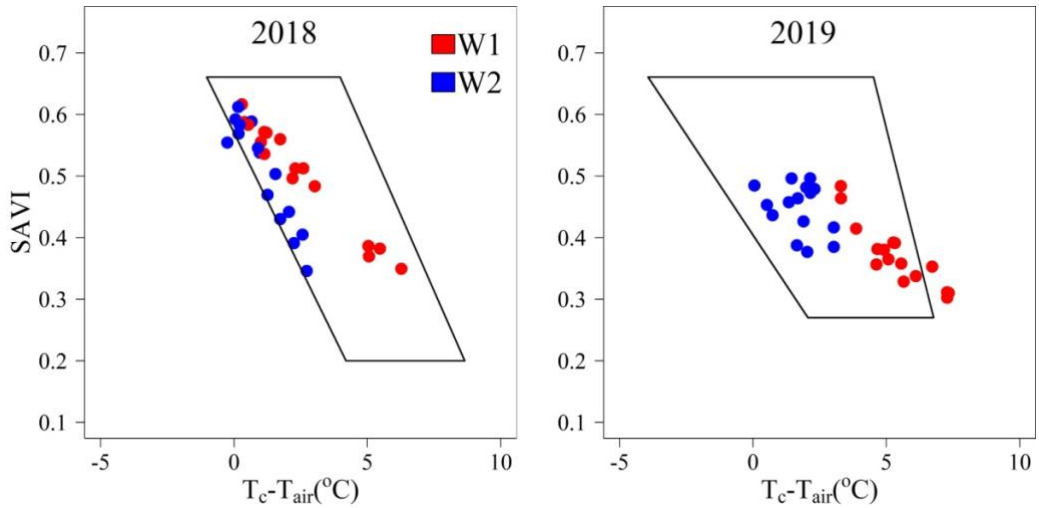

Fig 22. Representation of all observations at flowering in the vegetation index-temperature (VIT) trapezoid plotted in the two-dimensional space formed by the soil adjusted vegetation index (SAVI) and the difference between canopy (T_c) and air temperature (T_{air}) extracted with the aircraft. Symbols represent the mean value for each plot.

Table 10. Coefficient of determination (R^2) and root mean square error (RMSE) of the linear relationship between leaf conductance (mmol · m^{-2} · s^{-1}) and water deficit index (WDI) with different spectral and temperature-based indices extracted from the airborne imagery at flowering 2019. The bold numbers indicate significance level $P \leq 0.001$.

	Conductance		WDI	
	R^2	RMSE (mmol m^{-2} s^{-1})	R^2	RMSE
WDI	**0.66**	**39.56**	-	-
T_c-T_{air}	**0.59**	**43.26**	-	-
$NDWI_{1240}$	0.31	56.20	**0.56**	**0.175**
$NDWI_{1640}$	**0.34**	**54.76**	**0.63**	**0.162**

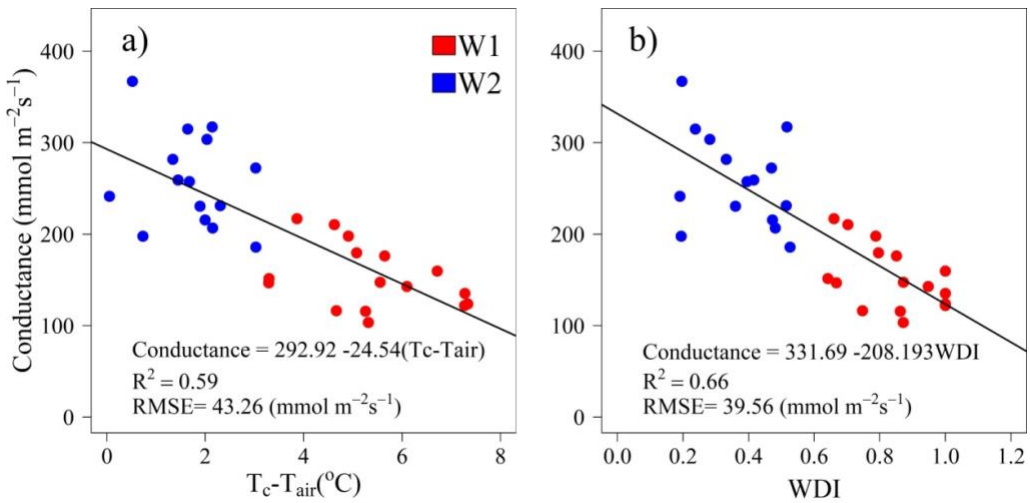

Fig 23. Pair values of leaf stomatal conductance (mmol · m^{-2} · s^{-1}) and a) canopy-air temperature difference (T_c - T_{air}) or b) the water deficit index (WDI) extracted from the airborne imagery at flowering 2019. Blue symbols are the pair values of the plots that were irrigated at flowering (W2) and the red symbols pair values of plots not irrigated at flowering (W1). The solid lines are the linear regression with the corresponding equation, coefficient of determination (R^2) and root mean square error (RMSE).

4.2.4 Development of an N status indicator combining N and water indices

The best hyperspectral VI for the NNI estimation (CCCI), and the temperature-based indicator for water status estimation (WDI) were combined using a multiple lineal regression model fitted to NNI to develop a new indicator for N status monitoring (Fig 24). The assessment capacity was enhanced when the NNI was estimated based on the CCCI and WDI rather than only on the CCCI alone, as the R^2 increased and the RMSE was reduced. When analyzing each year individually, a similar performance in the assessment capacity was obtained at flowering 2018 (RMSE = 0.123 and R^2 = 0.64 for the CCCI versus RMSE = 0.127 and R^2 = 0.62 for *f*(CCCI, WDI)), and a substantial improvement was achieved at flowering 2019, the year that the crop experienced a more severe water stress (RMSE = 0.091 and R^2 = 0.62 for CCCI versus RMSE = 0.081 and R^2 = 0.70 for *f*(CCCI, WDI)).

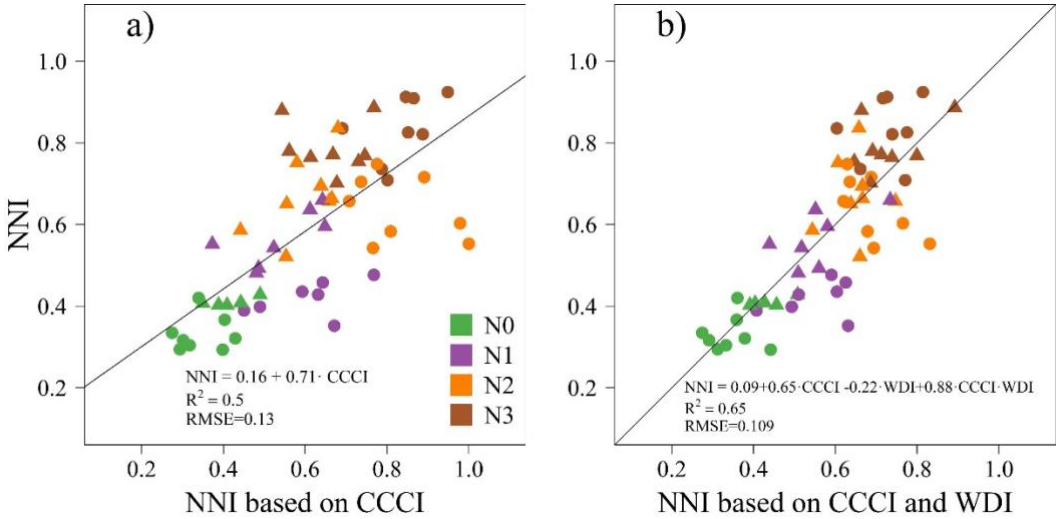

Fig 24. The nitrogen nutrition index (NNI) observed versus the estimated NNI based on a linear relationship based on a) the canopy chlorophyll content index (CCCI) and b) a combination of the CCCI and the water deficit index (WDI). Symbols are the pair values for the various N levels (N0, N1, N2 and N3), circles for 2018 and triangles for 2019. The solid lines are the linear regression with the corresponding equations, coefficient of determination (R^2) and root mean square error (RMSE).

The effect of the N and water levels in the VIs and the temperature-based indicators was tested using the aircraft imagery acquired at flowering for both years (Fig 25 and Supplementary material S2, S3). Most VIs distinguished between N-deficit (N0 and N1) and N-sufficient plots (N2 and N3); nevertheless, the CCCI also distinguished between the nonfertilized plots (N0) and the plots with the reduced dose (N1), as well as between the N1 and N3 plots. The new index based on spectral and thermal information performed similarly to the CCCI when identifying N levels. The ANOVA test indicated that all spectral VIs were highly affected by N fertilization ($P \leq 0.001$), except the TCARI (Supplementary material S2). The ability of NNI and *f*(CCCI,WDI) to distinguish between the N levels within the W2 plots was similar: both indicators distinguished between N1 and N2 plots and identified the N-deficit (N0 and N1) and N-sufficient (N2 and N3) treatments at flowering both years.

As the water availability was similar in W1 and W2 in 2018, the VIs behaved similarly in both water levels; however, differences in the water availability in W1 and W2 caused differences in VI behavior between water levels in 2019 (Supplementary material S2). That year, the structural and photosynthetic pigment VIs at W1 and W2 were different for most N levels, showing that these indices were sensitive to the water effect. However, the canopy VIs

reduced these differences across all N levels; most particularly differences in the CCCI between water levels were significant only for N0 in 2019 (Fig 25b). No differences in *f*(CCCI, WDI) between water levels were found in any N level and year (Fig 25e, f) showing the robustness of the new indicator in estimating crop N status under different water stress conditions. In addition, the ANOVA test indicated that all spectral indices were affected by the water levels at the 0.001 probability level, whereas the CCCI was at 0.05 and *f*(CCCI, WDI) was the only index not affected (Supplementary material S2).

Differences between water levels in 2018 were only detected with information retrieved from thermal imagery (Fig 25; Supplementary material S2, S3). The WDI quantified the water status with a reduced effect of the N levels, showing that for W2 all N levels in the same year suffered a similar water stress, whereas, for W1 the water stress was higher for N0 and decreased with increasing N level, especially in 2018 (Fig 25c, d). Compared to the canopy-air temperature difference, the WDI increased the differences between water levels and mitigated the effect of the N levels. This was particularly evident in the N0 level, in which the high temperature associated with higher soil exposure but not with lower water availability was compensated by the WDI. The two VIs based on SWIR reflectance behaved similarly when identifying water and N levels; they distinguished between the water levels established in each N level in 2019, but in 2018, they displayed differences between N levels but not between water levels. These results emphasize that the WDI was the most reliable indicator to determine crop water stress with a minimum effect of N status.

The robustness of the CCCI for estimating N levels under various water conditions was evident in the CCCI map obtained by the airborne hyperspectral imagery both in 2018 and 2019 (Fig 26). No differences in the CCCI were observed between the W1 and W2 areas with equal N application, whereas the N levels were easily identifiable in both water levels (in agreement with Fig 25a, b). On the other hand, the WDI was particularly sensitive to crop water status, and even in 2018 was able to distinguish between the W1 and W2 sectors of the field experiment. The effect of N on the WDI map was relatively minor compared to the influence of the water level (in agreement with Fig 25c, d).

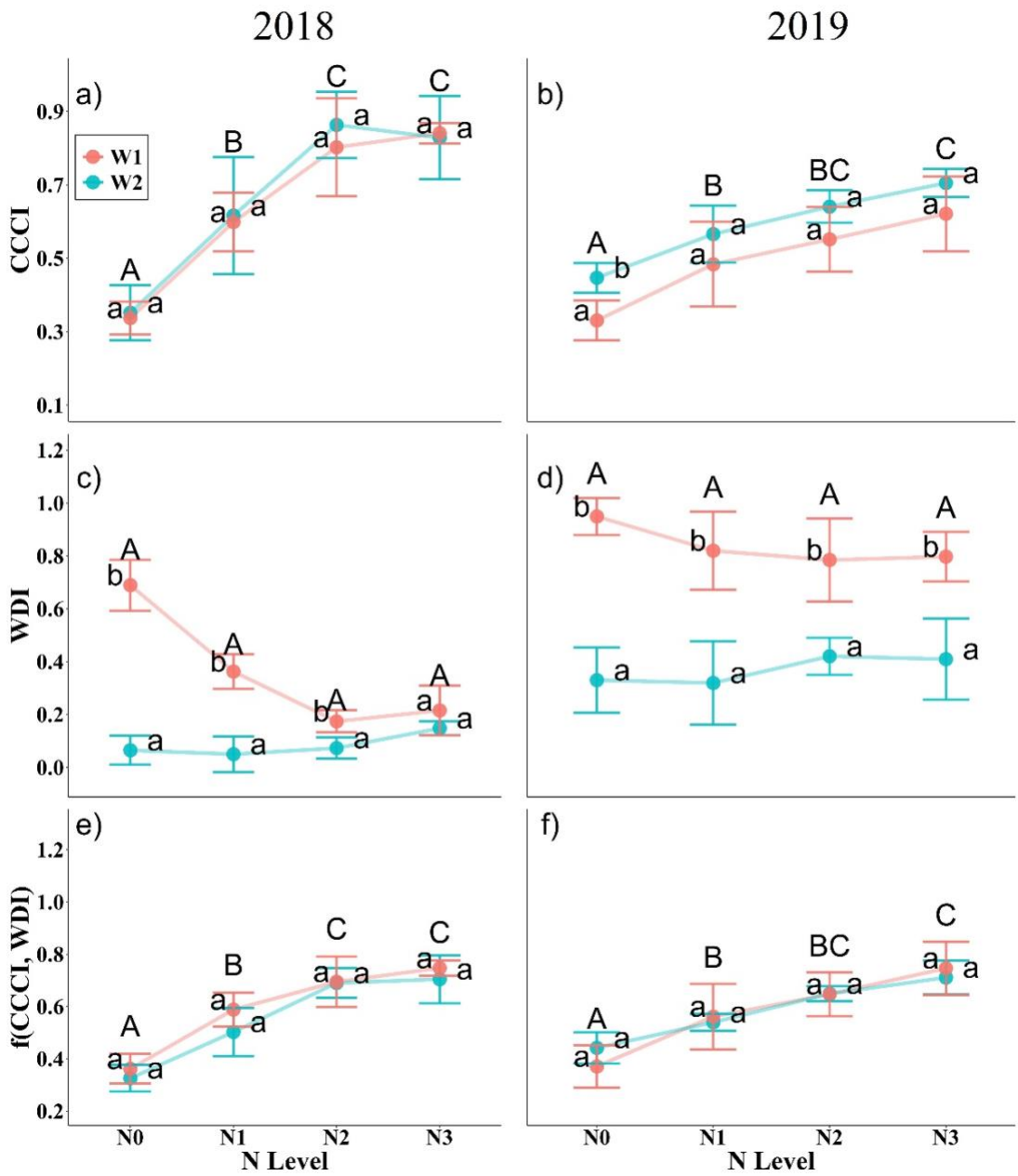

Fig 25. Canopy chlorophyll content index (CCCI), water deficit index (WDI) and the new combined indicator *f*(CCCI,WDI) proposed for nitrogen (N) status assessment retrieved from the aircraft imagery for each N (N0, N1, N2 and N3) and water level (W1 and W2) at flowering in both experimental years. Symbols are the mean values, and bars are the standard errors. Capital letters above the error bars indicate differences among N levels and lower case letters next to the means indicate differences between water levels in each N level according to Tukey test 95%.

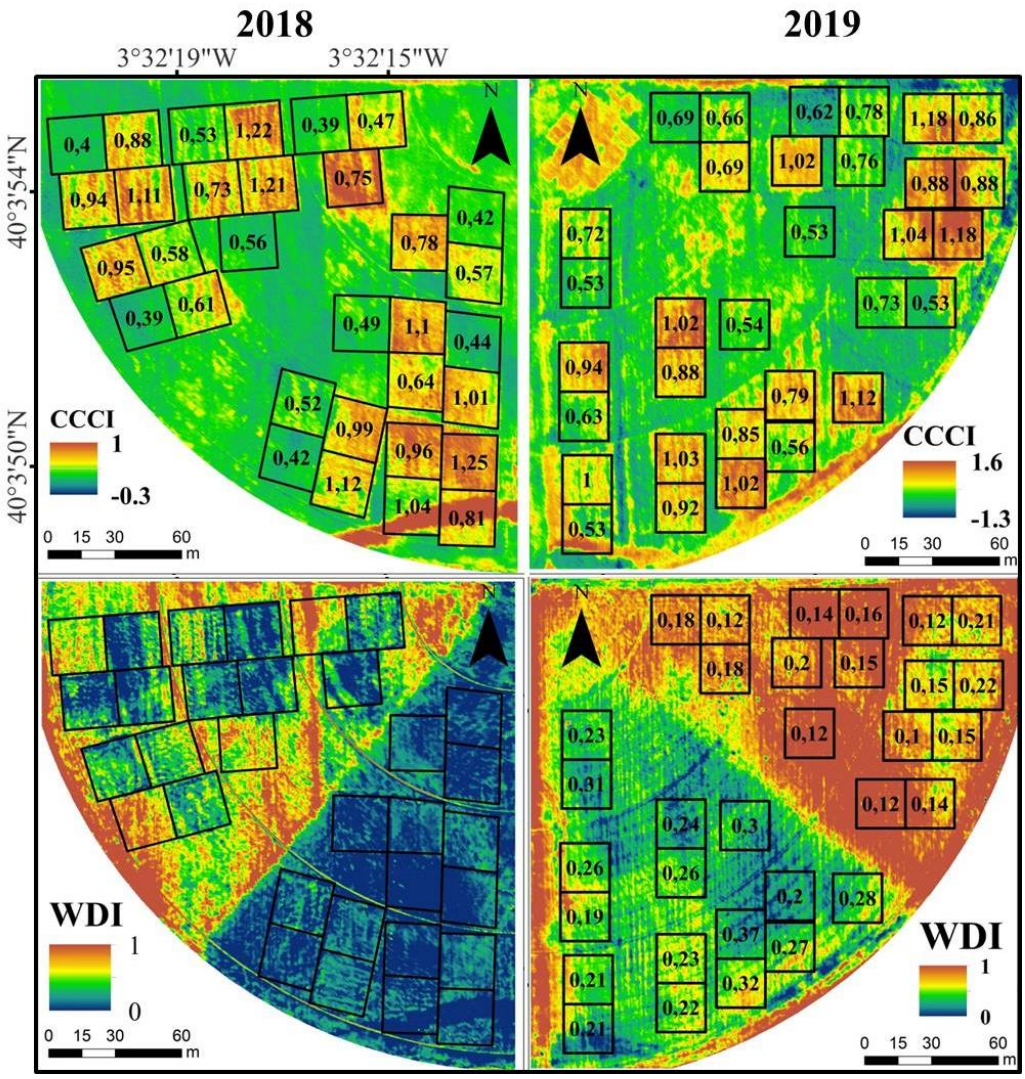

Fig 26. Canopy chlorophyll content index (CCCI) and water deficit index (WDI) maps retrieved from the hyperspectral and thermal imager on-board the aircraft at the flowering stage of both experimental years. Plot values in the CCCI and WDI maps represent the nitrogen nutrition index (NNI) and leaf conductance (mmol · m^{-2} · s^{-1}), respectively (no data available for WDI 2018).

4.2.5 Discussion

This Chapter confirmed the difficulty of disentangling crop N and water status using only spectral information, as the confounding effect was evident in the spectra. Determining the cause of the stress suffered by the crop is a key issue for guiding fertilization and water management (Gonzalez-Dugo et al., 2009). The NNI was a reliable indicator of crop N status and proved to be robust under different water levels, even if %N in shoots decreased in well

fertilized treatments with lower water availability. However, the CDC fitted to the data from this study showed that the $\%N_c$ was lower than the reference values proposed by Justes et al. (1994) for winter wheat under no water limitation (Fig 17b). Because of that, the NNI values were low even for the well fertilized plots (N2 treatments; Table 8). Similar results were reported for the CDC obtained under water-limited conditions in Australia (Neuhaus et al., 2017; Hoogmoed and Sadras, 2018), leading to Hoogmoed and Sadras (2018) to hypothesize that water-limited crops exhibit lower N uptake than well-watered crops and may require specific $\%N_c$ values. The $\%N_c$ proposed by these curves lay within the 95% confidence interval of our CDC when biomass > 4.5 Mg DM ha^{-1} (Fig 17b). Nevertheless, more research is needed to clarify if the lower $\%N_c$ values reported are due to water limited conditions and to solve the discrepancies in the $\%N_c$ at biomass < 4 Mg DM ha^{-1}. This issue is highly relevant, as we hypothesize that using the CDC obtained for winter wheat under no water limitation could lead to overfertilization in water limited environments.

In this Chapter we propose the use of different remote sensing indicators based on spectral and thermal information to determine the N and water status separately and therefore, to adjust N fertilization and irrigation according to crop demands. However, certain limitations were observed when applying most VIs based on spectral information: i) they were highly affected by the soil background signal at early GSs, when decisions related to N fertilization application are made, ii) their performance was reduced when the crop experienced water stress, and iii) the value of the VIs decreased when the crop suffered from N or water stress, making it difficult to identify the reason behind the crop deficiencies. This study demonstrated that these limitations can be overcome by simultaneous analyses of the CCCI and WDI.

In this regard, the CCCI, which relates a structural index and a chlorophyll index, showed a robust and consistent correlation with the NNI within a wide range of ground cover and water status when canopy reflectance was measured at ground level or 300 m above the experiment. These results are in agreement with Fitzgerald et al. (2010), who obtained good CCCI performance in estimating crop N status in winter wheat, and with El-Shikha et al. (2007) and Bronson et al. (2017), who reported the low effect of crop water status on the CCCI. The good match between the lines used to calculate the CCCI in this experiment and in Fitzgerald et al. (2010) provides new insight for the normalization of the equations.

Our study validated the use of the WDI to estimate the crop water status and pointed out the convenience of compensating the canopy temperature by the ground cover to isolate the plant signal. The WDI correction had more effect in the areas with low ground cover, in which the thermal difference between air and dry soil > 8 ºC. It is well known that the amount of water needed to supply crop demand increases with biomass (Tanner and Sinclair, 1983), but in this experiment the WDI suggested that N0 plots were the most water stressed (Fig 25c), even though the amount of water received was the same as the plots with more biomass. Several reasons could explain this apparent contradiction. Seligman et al. (1983) indicated that N-deficit plants increase leaf temperature because the biological processes to maturity are accelerated. This effect was also reported in other studies (Heitholt et al., 1991; Tilling et al., 2007; Fois et al., 2009; Mon et al., 2016). Additionally, in N-deficient cereals of semiarid environments it was reported that a moderate increase in N supply enhances WUE (Cossani et al., 2012). Finally, the proof that it is necessary to correct the effect of N fertilization or biomass in thermal indicators is that the leaf stomatal conductance was better correlated with the WDI than with the thermal difference (T_c-T_{air}). In agreement with these results, field studies showed that variable-rate irrigation based on maps of planar-domain indices such as the WDI could greatly enhance WUE (O'Shaughnessy et al., 2015). In this study, the thermal camera was the only sensor that detected differences between water levels in 2018; the non-limited water scenario.

This study reported that the sensitivity of the CCCI to winter wheat N status increased when it was combined with the temperature-based indicator (WDI), because this combination mitigated the effect of the crop water status. These results led us to propose a new indicator for monitoring N status by combining spectral and thermal information. Similarly, Quemada et al. (2014) reported better grain yield prediction in maize when spectral and thermal information was combined. It is well known that the NNI and grain yield are correlated and affected by N and water availability (Sadras and Lemaire, 2014). To ensure that the crop uptakes the applied N and to mitigate N losses to the environment, the water status of the crop has to be considered before N fertilization (Quemada and Gabriel, 2016). For field application of the proposed method, it is advised to simultaneously measure reflectance in the VNIR region and canopy temperature to provide a map of the CCCI and WDI to calculate the proposed N status-related index as *f*(CCCI,WDI). In irrigated fields with the option of variable water delivery, irrigation should be applied in areas with a high WDI that do not experience N deficit (high CCCI and *f*(CCCI,WDI)) because the possibility of enhancing

crop growth is higher. In contrast, areas with a high WDI in which N is a relevant limiting factor would be less likely to profit from the additional water applied and the risk of diminishing water use efficiency would be higher. The areas in which applied N will be prone to N uptake will be those with a low *f*(CCCI,WDI) and a low WDI, indicating that the area experiences N deficit and has sufficient water availability (Zillman et al., 2006; Tilling et al., 2007). In contrast, N applications should be avoided in water-limited areas (i.e. a low *f*(CCCI,WDI) with a high WDI) as the crop would likely not use the N applied and the risk of increasing losses would be higher. Similarly, areas with high CCCI or *f*(CCCI, WDI) should not receive N fertilization given that the crop N deficit is low. Besides multiple linear regression, the spectral and thermal information could be used by emerging machine learning techniques based on ensemble methods (i.e., random forest, artificial neuronal networks) that already showed potential in obtaining robust outcomes from the combination of multiple variables in agri-environmental studies (Mutanga et al., 2012; Lebourgeois et al., 2017).

Using two different airborne sensors simultaneously (i.e., covering the VNIR + thermal regions) is more complex than when one camera is used (e.g., collecting imagery with a VNIR camera only) due to the different spatial resolutions obtained and co-registration issues between non-aligned detectors. Nevertheless, this study and others clearly demonstrate the need for acquiring images covering the VNIR portion of the electromagnetic spectrum, where photosynthetic pigments can be quantified to understand nutrient status, and the spectral region more directly related with canopy transpiration for its direct connection with water status and water stress detection. New multispectral cameras are becoming available which can be installed on board manned and unmanned vehicles which acquire images with co-registered detectors covering the VNIR and thermal infrared regions, overcoming some of the issues indicated above.

The proposed approach is an application of the N and water co-limitation concept (Sadras, 2004; Cossani and Sadras, 2018). Because of the empirical basis of the proposed indicators, their reliability for improving N fertilization and water management should be tested in different cultivars, soils, and climate conditions.

Chapter 4.3:
Winter wheat traits prediction through ensemble modeling approaches using aerial and satellite imagery

4.3.1 Specific objectives and application of methods

This Chapter follows the analysis described in Chapter 3.5.2 to fulfill the **Objective 2:** improve the prediction of winter wheat traits (yield, grain protein concentration and grain N output).

a) quantify the improvement in the prediction of winter wheat traits when combining indicators related to different crop parameters.

b) compare the feasibility when using indicators derived from airborne hyperspectral and thermal sensors, and from the freely available Sentinel-1 and Sentinel-2 satellites.

Early prediction of crop production by remote sensing systems may help to plan harvest and ensure food security. There are different crop parameters that affect final harvest, such as chlorophyll content, biomass accumulation or water status, and therefore should be considered in the prediction. For this reason, this Chapter determines if combining several remote sensing indicators related to different crop parameters improves the prediction obtained with a single spectral VI, and assesses the importance of the different indicators and spectral regions to identify the most suitable sensor. In addition, this Chapter analyzes the feasibility of the free available Sentinel-1 and Sentinel-2 information for the early prediction of each winter wheat trait by comparing it with the performance obtained with the airborne hyperspectral and thermal sensors.

For this purpose, this Chapter first identifies the most suitable spectral indicators to be included in the ensemble models for the prediction of each trait according to their relationship with agronomical variables using the information extracted with the airborne sensors. The indicators were grouped according to the spectral region covered (or the sensor required to calculate them), and each group of indicators was included in the ensemble models once at a time (Fig 27). The importance of each indicator was measured with the random forest model. Subsequently, the selected spectral indicators were calculated with the Sentinel-2 bands and included in the same models together with the RVI calculated with Sentinel-1 to analyze the feasibility of the free available information for early winter wheat traits prediction.

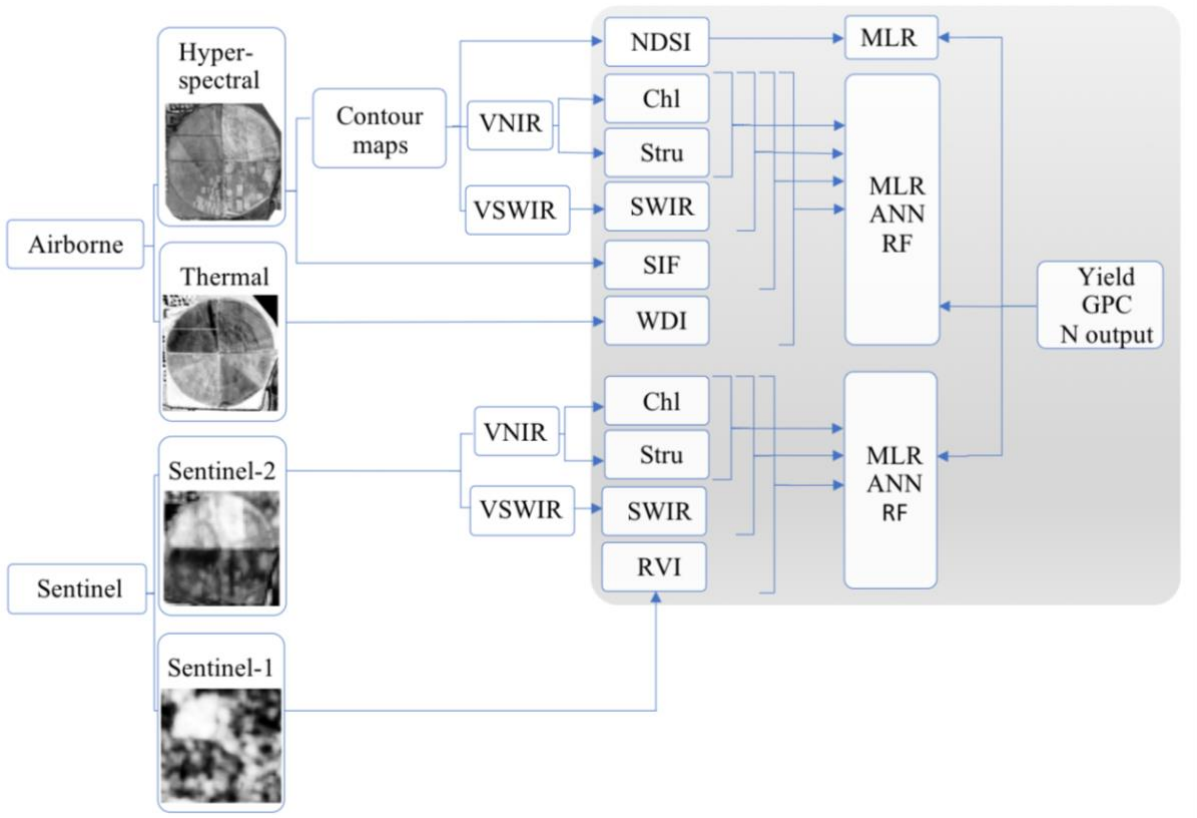

Fig 27. Workflow followed in this Chapter. VNIR refers to a normalized difference spectral index (NDSI) based on the 400 – 1000 nm region. VSWIR indicates an NDSI with at least one band in the 1000 – 1750 nm region. Chl and Stru indicate an NDSI related to chlorophyll content and canopy structure, respectively. SIF, WDI, and RVI indicate solar-induced fluorescence, water deficit index, and radar vegetation index, respectively. MLR, ANN, and RF refer to the ensemble models multiple linear regression, artificial neural network, and random forest. GPC indicates grain protein concentration (%).

4.3.2 Spectral differences due to treatments and selection of indices

The effect of the N levels on the reflectance spectra acquired at flowering by the airborne sensors was detected on the visible, NIR, and SWIR regions, with the differences between N levels being more obvious in 2018 (Fig 28). Low N levels had higher reflectance in the visible region, probably due to a lower photosynthetic pigment absorption, whereas high N levels increased reflectance in the NIR in both years. Within the SWIR region, reflectance in the 1500 – 1700-nm region was particularly sensitive in discriminating between N levels.

This was attributed to the absorption feature of N=H bonds located in this region (Curran, 1989).

Differences in the spectra between water levels were more evident in 2019 and in the N-stressed plots of 2018, which were particularly detectable in the SWIR region (Fig 28). In this region, the plots with less water availability presented higher reflectance. This pattern was also observed in the green and red wavelengths. The reflectance in the NIR region increased in the W2 plots of 2019.

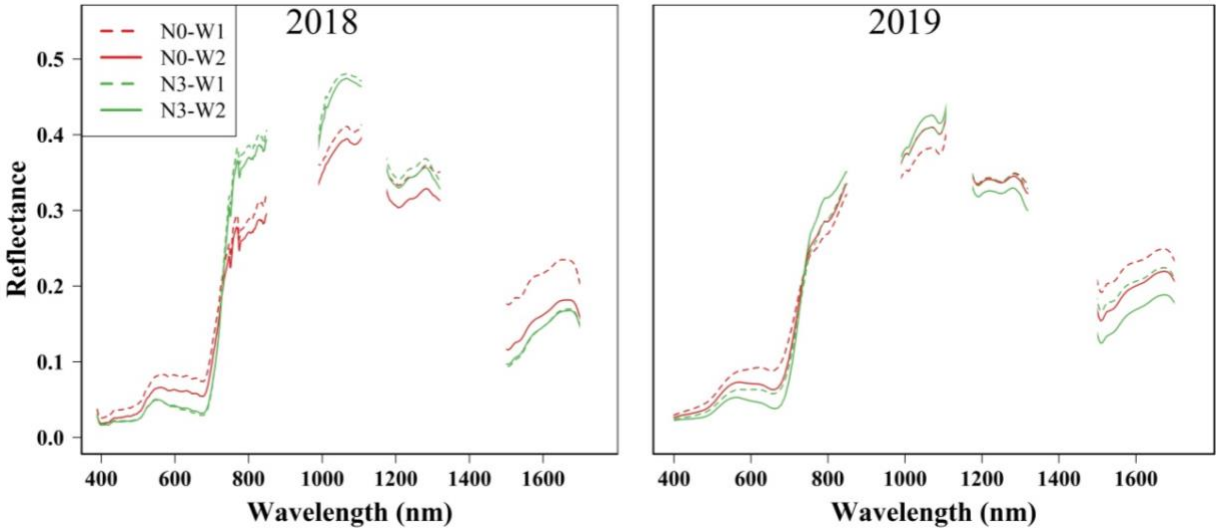

Fig 28. Canopy reflectance spectra acquired with the aerial hyperspectral imager in the two water levels (W1 and W2) of N0 and N3 fertilizer levels at flowering both years.

The R^2 contour maps revealed the importance of using the adequate spectral region for an accurate prediction of each winter wheat trait (Fig 29). Overall, the yield was the wheat trait best predicted by the NDSIs, yielding a value of $R^2 > 0.6$ with most of the NDSIs that used an NIR or SWIR in combination with a visible band (especially green) or an NIR and SWIR band. The highest R^2 value (0.85) in all contour maps was obtained when predicting yield with the NDSIs constructed with different combinations of bands within the red edge and/or NIR regions. On the other hand, the best GPC prediction ($R^2 = 0.72$) was obtained with NDSIs based on reflectance at SWIR between 1600 and 1750 nm and visible region (green), followed by specific wavelengths in the NDSI (NIR, red edge). The best N output prediction ($R^2 = 0.73$) was achieved by NDSIs based on bands in the NIR region (around 790 nm) and red edge (around 750 nm), or two bands within the red edge. Despite the similar maximum R^2 value obtained in predicting the GPC and the N output, N output showed a more robust

correlation with other NDSIs; for example, most of the NDSIs (visible or red edge, NIR or SWIR) presented a value of $R^2 > 0.5$ with the N output, while most of the NDSIs presented a value of $R^2 < 0.3$ with GPC.

The R^2 contour maps showed that NDSI (1650 nm, 550 nm) was highly correlated with GPC, while the yield prediction was more accurate when the 550-nm band was changed by shorter or longer wavelengths (Fig 29). Overall, the R^2 contour map calculated for GPC showed similar patterns to the contour map calculated for plant %N, and the yield contour map was similar to the biomass contour map (Fig 29).

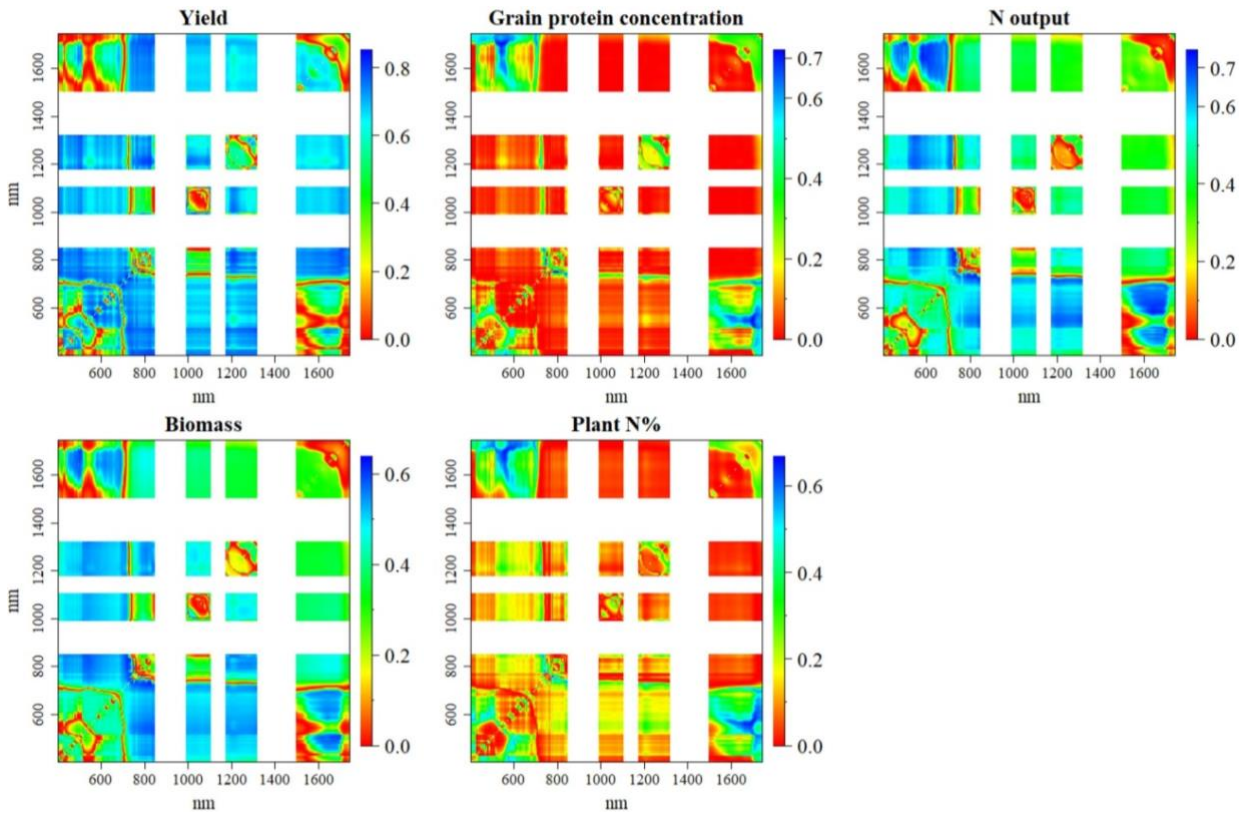

Fig 29. Contour maps representing the coefficient of determination (R^2) from the linear relationship of wheat traits (yield (kg ha^{-1}), grain protein concentration (%) and N output (kg N ha^{-1})) and crop parameters at flowering (biomass and plant %N) against all possible normalized difference spectral indices [NDSI (λ_1, λ_2) = (λ_1-λ_2)/(λ_1+λ_2)] calculated with the airborne hyperspectral imagery acquired at flowering each year. The regions not covered by the sensors (850 – 950 nm) and the water absorption wavelengths are in white.

The VIs used as structural, chlorophyll, and SWIR input variables in the ensemble models were selected based on their performance in the R^2 contour maps (Fig 29) and the lack of correlation between them. To predict yield, the VI selected as a proxy of chlorophyll content was NDSI (799 nm, 755 nm), and the SWIR-based index was NDSI (1106 nm, 1066 nm). They were selected because of their linear correlation with yield (R^2 = 0.76 in both indices) and because there was no collinearity between them (Pearson coefficient ≤ 0.75). Due to the sensitivity of the red edge reflectance to chlorophyll content (Inoue et al., 2016), different studies reported the good performance of NDSI (NIR, red edge) for predicting chlorophyll (Fitzgerald et al., 2006; Zillman et al., 2015) or crop N content (Li et al., 2013a; Inoue et al., 2012). They are crucial components involved in photosynthesis, and therefore their content affects biomass production (Fig 29), and final yield (Quemada and Gabriel, 2016). This explains why this study, in agreement with previous research (Wang et al., 2019b; Raya-Sereno et al., 2021b; Adak et al., 2021), obtained a good correlation between NDSI (NIR, red edge) and wheat yield. The correlation between NDSI (1106 nm, 1066 nm) and yield can be explained because nearby wavelengths are the absorption feature of the structural biochemical components of plants, such as lignin (1120 nm), and the N=H bond absorption wavelength located at 1020 nm (Curran, 1989). Cell structure is affected by the nutritional and water status, which has an effect on plant growth, and therefore these wavelengths are related to yield (Thenkabail et al., 2013). No structural NDSI was found that presented no collinearity with the chlorophyll and SWIR selected indices. This study agrees with previously developed contour maps showing that NDSI (NIR, green) was the most suitable structural index for biomass (Hansen and Schjoerring, 2003) and yield prediction (Raya-Sereno et al. 2021b). For these reasons, the structural index used in the ensemble models for predicting yield was NDSI (800 nm, 550 nm), which corresponds to GNDVI (Gitelson et al., 1996). The chlorophyll strongly absorbs light in the visible region, especially in the blue and red bands (Sims and Gamon, 2002), and thus GNDVI has a lower value than NDVI (NDSI (NIR, red)) and tends to saturate later (Rodrigues et al., 2018).

To predict GPC, the proxy of chlorophyll content was NDSI (795 nm, 750 nm) because it has one of the highest accuracies in GPC prediction (R^2 = 0.70; Fig 29). This NDSI belongs to the small region of the GPC contour map based on the NIR and the red edge reflectance with a high R^2 value. A relationship between NDSI (NIR, red edge) and GPC was also reported by Raya-Sereno et al. (2021b) and Fu et al. (2022). This NDSI presented a Pearson coefficient ≤ 0.75 with NDSI (1650 nm, 545 nm), which is one of the SWIR indices most closely

correlated with GPC (R^2 = 0.64); therefore, it was selected as the SWIR-based NDSI used to predict GPC. The performance of the SWIR index for GPC prediction relies on the protein feature band near this region (Curran, 1989). Similarly, Söderström et al. (2010) successfully used the simple ratio of SWIR (1550 – 1750 nm range) and green reflectance for GPC prediction in barley, and Zhao et al. (2005) reported the suitability of the same SWIR region for GPC prediction in wheat. All structural NDSIs presented a weak correlation with GPC ($R^2 < 0.1$), but the correlation with NDSI (NIR, green) was slightly higher ($P < 0.05$). For this reason, due to the correlation with biomass at flowering and to the lack of collinearity with the other GPC estimators, GNDVI was selected as the proxy of plant structure to predict GPC with the ensemble models.

One of the NDSIs that exhibited the best correlation with N output was NDSI (778 nm, 752 nm) (R^2 = 0.74); therefore, it was used as the chlorophyll index in the N output prediction models. Likewise, Prey and Schmidhalter (2019b) used NDSI (770 nm, 750 nm) for N output prediction. The suitability of this NDSI to assess winter wheat N uptake at the flowering stage was also highlighted in the R^2 contour maps developed by Li et al. (2013). This NDSI presented no collinearity with an SWIR-based NDSI that was correlated with the N output: NDSI (1650 nm, 520 nm) (R^2 = 0.62). The chlorophyll and the SWIR VIs selected to predict N output were correlated with all structural NDSI. The GNDVI was selected as the structural index to predict the N output with the ensemble models because it presented a value of R^2 = 0.65 with the N output and correlated with the biomass at flowering.

4.3.3 Wheat trait prediction with airborne hyperspectral imagery using ensemble models

The performance of predicting wheat traits with a single NDSI was improved when combining different indices with the ensemble models (Fig 30). In this study, the three ensemble models performed similarly when using three or more indices to predict any of the wheat traits. However, significant differences between the accuracy of the models were observed when using only two indices, which resulted in a lower accuracy of the RF model. Overall, the RF showed an improvement in prediction when more indices were used. The good performance of the MLR occurred because a linear regression model (R^2 contour maps) was used to select the explanatory variables (NDSIs) and, therefore, a linear relationship between the response and the explanatory variables exists (Sellam and Poovammal., 2016).

Yield was the wheat trait best predicted when using ensemble models (Fig 30a), as observed in the R^2 contour maps (Fig 29). The most accurate yield prediction was obtained when combining the structural (GNDVI), chlorophyll (NDSI (799 nm, 755 nm)) and SWIR (NDSI (1106 nm, 1066 nm)) indices with ANN (R^2 = 0.86; RMSE = 493.17 kg ha^{-1}; Fig. 6a). In this case, the most important estimator according to the IncNodePurity was the SWIR index. When the SIF was included in the analysis, it obtained the highest or the second highest IncNodePurity value (Fig 31), and was correlated with yield (R^2 = 0.73; data not shown), but no improvement was achieved when included in the models. When using only NDSI (773 nm, 753 nm), which is the best NDSI from the contour maps, to predict yield with 10-fold cross-validation, values of R^2 = 0.84 and RMSE = 521.18 kg ha^{-1} were obtained. This result indicates that the combination of different NDSIs with ANN improved the yield prediction.

The maximum R^2 value obtained when predicting GPC with the NDSIs or with the ensemble models was the lowest among all wheat traits analyzed, indicating that it is the most challenging trait to predict. The most accurate GPC prediction was obtained with MLR using the chlorophyll (NDSI (795 nm, 750 nm)), structural (GNDVI), and SWIR (NDSI (1650 nm, 545 nm)) indices (R^2 = 0.73; RMSE = 0.19 %N; Fig 30b); this was the only model that outperformed the 10-fold cross-validation results obtained with NDSI (1701 nm, 551 nm) (R^2 = 0.72; RMSE = 0.20 %N). When using only VNIR-based NDSIs, the highest R^2 value was 0.68 and the lowest RMSE was 0.21%, which indicates that GPC prediction is the one that improved the most when including SWIR reflectance. According to the IncNodePurity, the most important indices for GPC prediction were chlorophyll and SWIR, which showed important differences with the other indices in IncNodePurity value in all cases. No correlation was found between GPC and the SIF, and there was no improvement when the SIF was included in the GPC prediction models.

The most accurate prediction of N output was obtained with MLR using the chlorophyll (NDSI (778 nm, 752 nm)), structural (GNDVI), and SWIR (NDSI (1650 nm, 520 nm)) indices (R^2 = 0.74; RMSE = 15.47 kg N ha^{-1}; Fig 30c). The IncNodePurity indicated that the most important indices in the prediction were chlorophyll and SWIR; however, the difference with the structural index was smaller than in the GPC prediction. When including only VNIR-based VIs in the ensemble models, the best performance was obtained with the MLR with values of R^2 = 0.72 and RMSE = 16.2 kg N ha^{-1}. Despite a correlation between SIF and

N output was found (R^2 = 0.27; P < 0.001; data not shown), no improvement in the prediction was attained when the SIF was included in the models.

Chapter 4.2 showed that the WDI was able to distinguish between water levels with minimum effect on the N levels; however, the WDI did not improve any trait prediction despite being correlated with yield (R^2 = 0.44; P < 0.001) and with N output (R^2 = 0.18; P < 0.001), but not with GPC (R^2 < 0.1; P > 0.1).

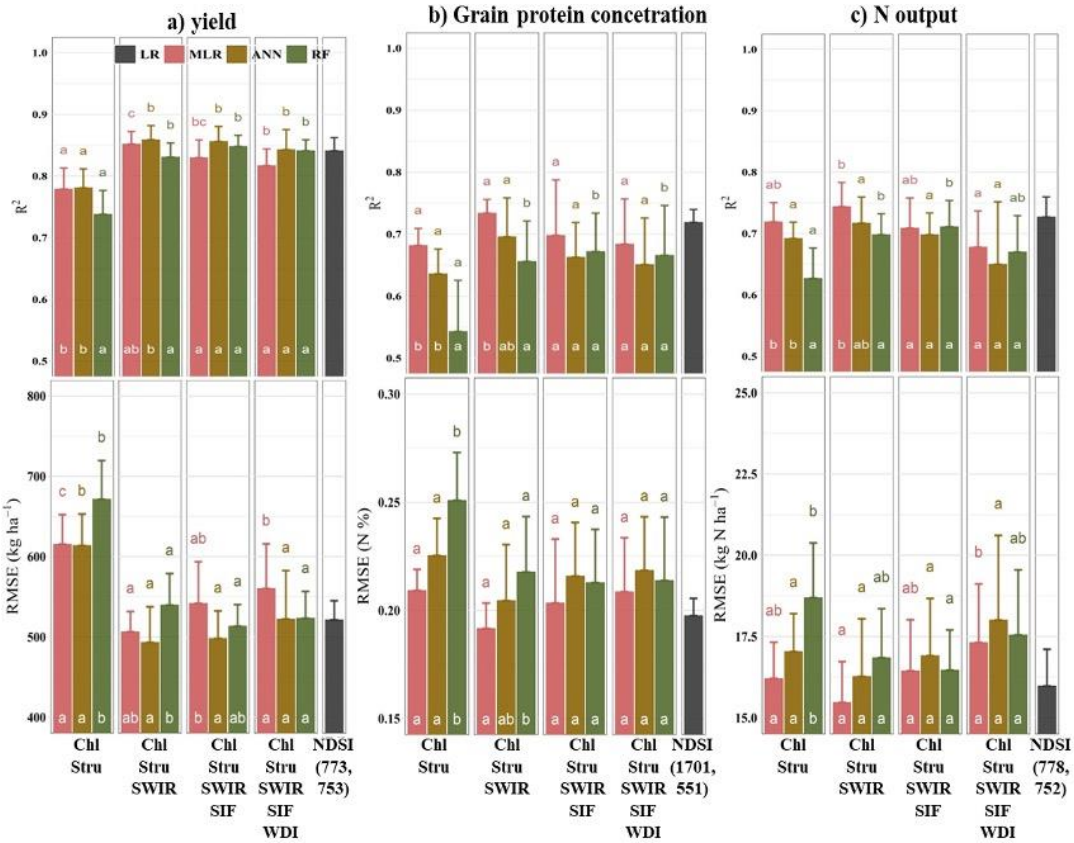

Fig 30. Coefficient of determination (R^2) and root mean square error (RMSE) obtained when using airborne sensors to predict wheat traits: a) yield (kg ha^{-1}), b) grain protein concentration and c) N output with linear regression (LR), multiple linear regression (MLR), artificial neural network (ANN), and random forest (RF). Indices used are on the X-axis: spectral vegetation indices based on visible-near infrared regions related to chlorophyll content (Chl) and plant structure (Stru), a vegetation index that includes a band within the SWIR region (SWIR), solar-induced fluorescence (SIF) and water deficit index (WDI). Different white letters indicate significant differences ($P \geq 0.05$) between ensemble models with the same set of indices. Colored letters indicate differences between the same ensemble models using a different set of indices.

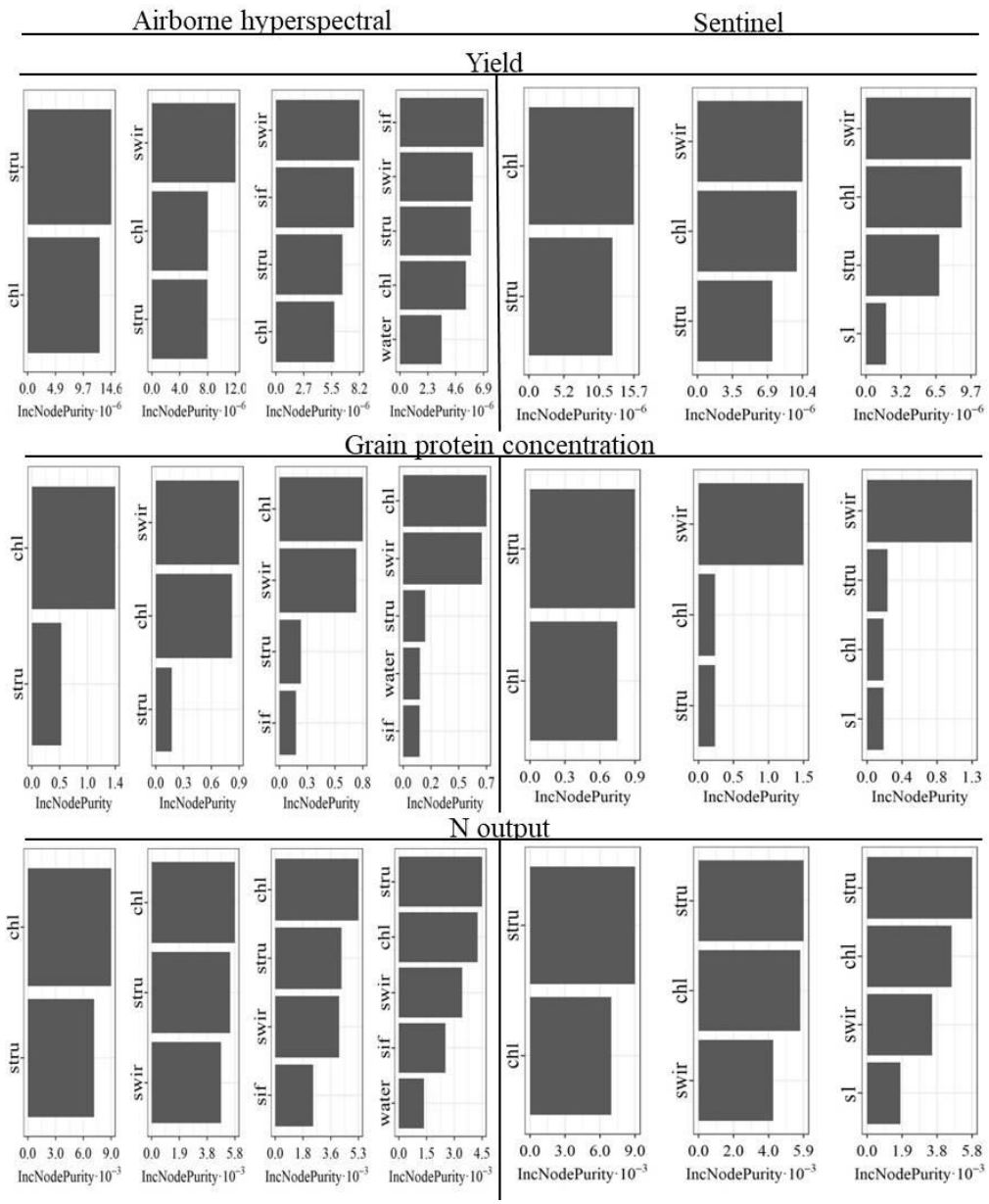

Fig 31. Importance of the input variables according to the increase in node purity (IncNodePurity) when predicting yield, grain protein concentration and N output with the airborne hyperspectral and thermal sensors and Sentinel imagery. Chl and Stru are spectral vegetation indices based on visible-near infrared regions related to chlorophyll content and canopy structure, respectively. SWIR indicates a vegetation index that includes a band within the SWIR region. SIF and WDI stand for solar-induced fluorescence and water deficit index, respectively. S1 indicates the radar vegetation index calculated with Sentinel-1 images.

4.3.4 Winter wheat traits prediction with Sentinel-1 and Sentinel-2 using ensemble models

High similarities were found between the NDSIs extracted from the Sentinel-2 imagery and the NDSIs calculated with the convolved bands ($R^2 > 0.71$, $n = 118$ pixels; Table 11; Fig 32). These strong relationships validate the use of the convolved indices to test the prediction capacity of Sentinel-2.

Table 11. Structural, chlorophyll, and SWIR vegetation indices used as input variables in the ensemble models to predict yield (kg ha^{-1}), grain protein concentration (GPC; %), and N output (kg N ha^{-1}). Equations indicate the reflectance at a specific wavelength (λ; nm) used with the aircraft imagery (Hyperspectral) and the Sentinel-2 band convolved. Normalized difference spectral indices are calculated as NDSI (λ_1, λ_2) = (λ_1-λ_2)/(λ_1+λ_2).

	Yield		**GPC**		**N output**	
	Hyperspectral	**Sentinel-2**	**Hyperspectral**	**Sentinel-2**	**Hyperspectral**	**Sentinel-2**
Structural	NDSI (800,550)	NDSI (B8,B3)	NDSI (800,550)	NDSI (B8,B3)	NDSI (800,550)	NDSI (B8,B3)
Chlorophyll	NDSI (795,755)	NDSI (B8,B6)	NDSI (795,750)	NDSI (B8,B6)	NDSI (778,752)	NDSI (B7,B6)
SWIR	NDSI (1106,1066)	NDSI (B11,B8)	NDSI (1650,545)	NDSI (B11,B3)	NDSI (1650,520)	NDSI (B11,B2)

The accuracy was similar when yield was predicted from the aircraft imagery or the Sentinel-2 bands-derived NDSIs (Fig 30a and Fig 33a). The best yield prediction when using the Sentinel dataset was obtained with the ANN model using the structural (GNDVI), chlorophyll (NDSI (B8,B6)), and SWIR (NDSI (B11,B8)) indices ($R^2 = 0.85$; RMSE = 507.08 kg ha^{-1}; Table 11; Fig 33a). The same model and variables produced the best prediction when indices were calculated with the hyperspectral airborne imagery, but with a slightly more accurate prediction ($R^2 = 0.86$; RMSE = 493.17 kg ha^{-1}; Fig 30a). According to the IncNodePurity, the most important indices to predict yield with Sentinel were the chlorophyll and the SWIR indices in all cases (Fig 31). With the aircraft imagery, the SWIR index also reached the highest IncNodePurity value in most cases. When using only the VNIR Sentinel-2 bands, the combination of the structural and chlorophyll indices ($R^2 = 0.84$; RMSE = 519.67 kg ha^{-1}) outperformed the NDSI with the highest R^2 value in the contour maps but calculated with the Sentinel-2 bands (NDSI (B7, B6); $R^2 = 0.80$; RMSE = 582.13 kg ha^{-1}), highlighting the importance of combining different indices with ensemble models.

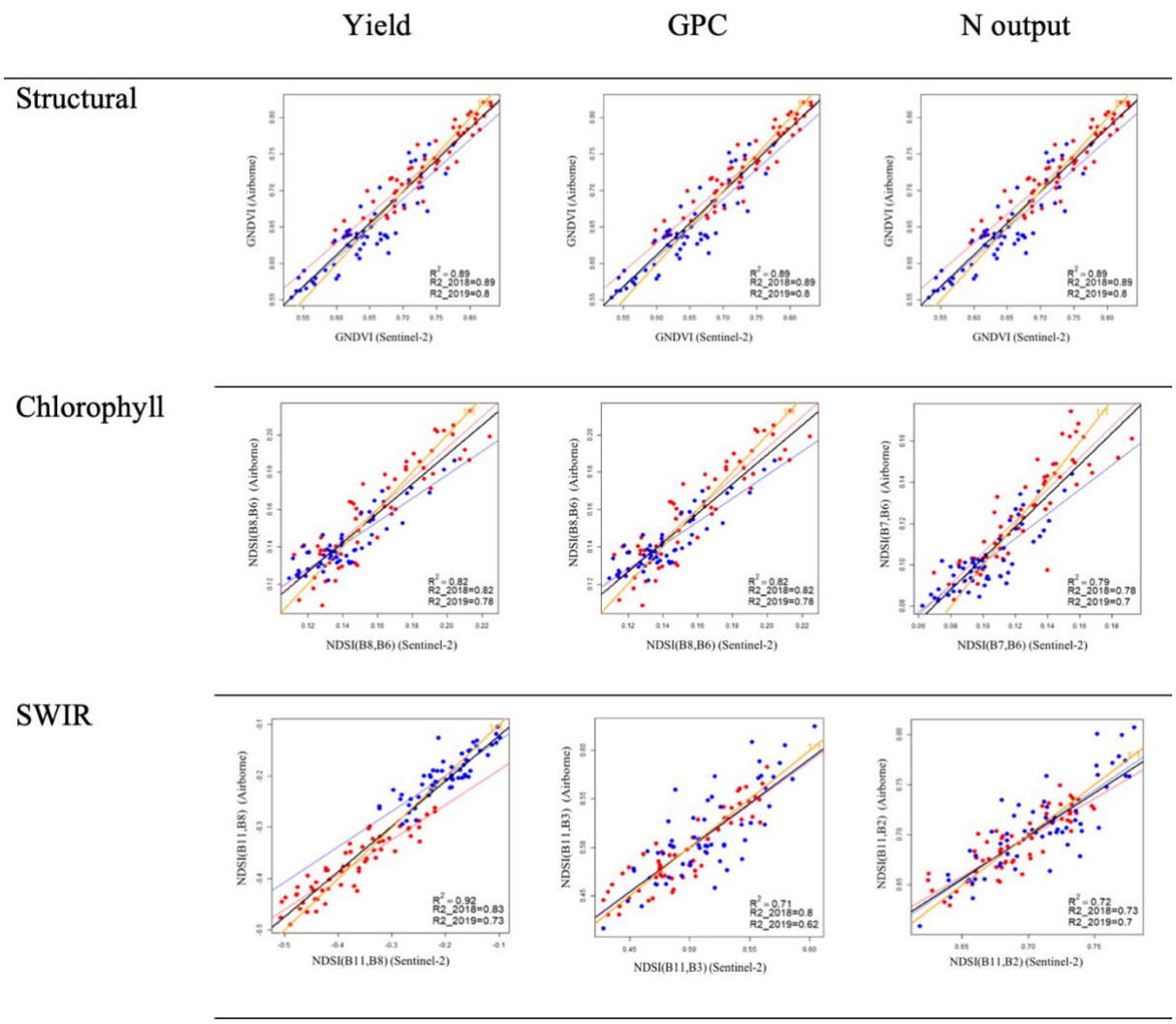

Fig 32. Linear correlation and coefficient of determination (R^2) between the vegetation indices extracted from the Sentinel-2 imagery and from the aircraft imagery using the Sentinel-2 bands convolved. Each point represents a Sentinel-2 pixel resampled to 20 m and the mean value of the aircraft imagery pixels that lay inside (n = 118).

The best prediction of GPC with the Sentinel dataset was obtained with the MLR model using the structural (GNDVI), chlorophyll (NDSI (B8, B6)), and SWIR (NDSI (B11, B3)) indices (R^2 = 0.69, RMSE = 0.19 %N; Table 11; Fig 33b). The same indices gave the best result with the aircraft imagery (Fig 30b). The GPC was the wheat trait that presented the highest improvement in the prediction when the SWIR bands were included in the model, compared to using only the VNIR bands (R^2 < 0.15, RMSE > 0.34 %N). According to the IncNodePurity, the most important estimator was the SWIR index, showing an important difference with the other indices (Fig 31). The performance of using only the SWIR index

was tested (R^2 = 0.65, RMSE = 0.20 %N), but a better result was achieved when it was combined with the VNIR indices.

The most accurate prediction of N output with the Sentinel dataset was obtained with the MLR model using the structural (GNDVI), chlorophyll (NDSI (B7, B8)), and SWIR (NDSI (B11, B2)) indices (R^2 = 0.71; RMSE = 16.46 kg N ha^{-1}; Table 11; Fig 33c), as obtained with the aircraft imagery when predicting N output (Fig 30c). The Sentinel results are in agreement with the aircraft imagery showing that N output prediction is more accurate than GPC prediction but less than yield prediction. The structural index obtained the highest IncNodePurity value in all cases, but it was similar to the value obtained by the chlorophyll index (Fig 31). These indices also obtained the highest IncNodePurity value in all models with the aircraft imagery. The N output prediction was more accurate when using only one index based on the red edge bands (NDSI (B7, B6)) than when combining the chlorophyll and the structural indices (R^2 = 0.59; RMSE = 19.47 kg N ha^{-1}), but including SWIR bands for N output prediction when using Sentinel information, improved the performance compared with the best result obtained using only VNIR bands (R^2 = 0.62; RMSE = 18.95 kg N ha^{-1}).

Differences in RVI between water levels were found in 2018 ($P < 0.05$; data not shown); however, no improvement was achieved when it was included in the analysis of any trait prediction.

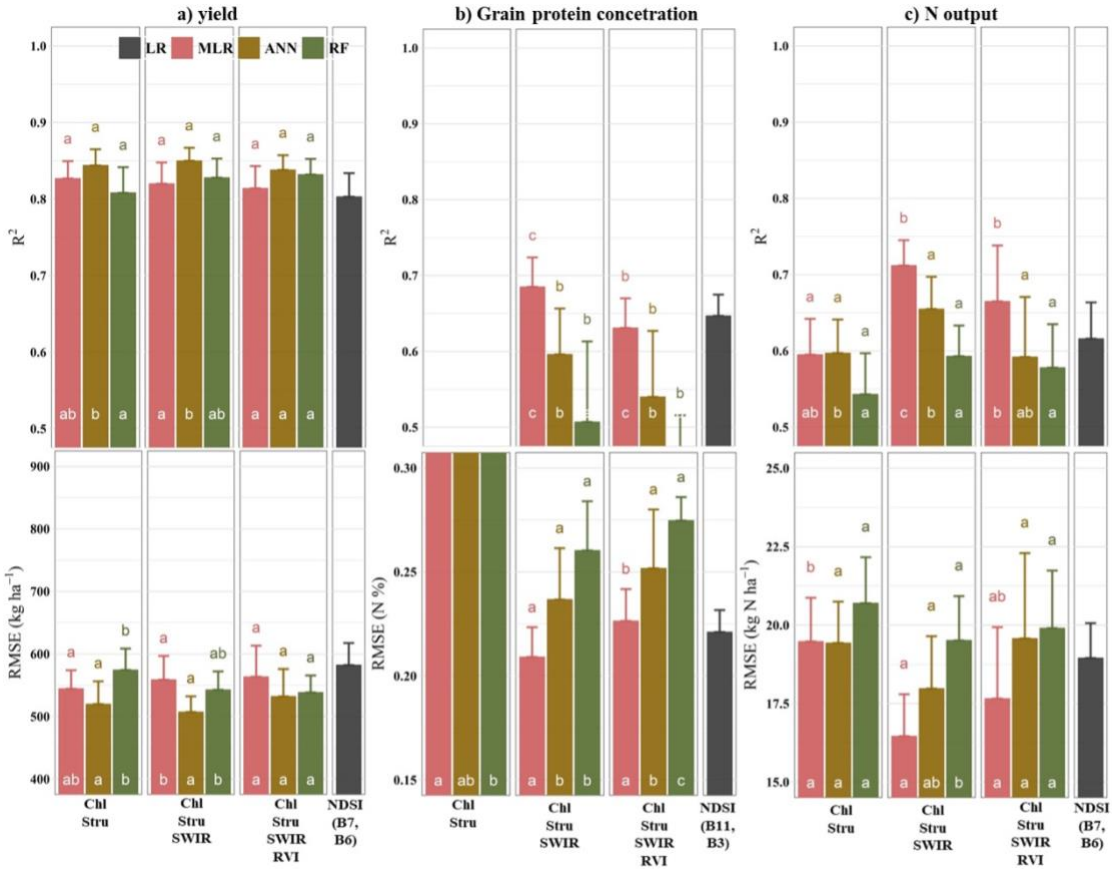

Fig 33. Coefficient of determination (R^2) and root mean square error (RMSE) obtained when using Sentinel imagery to predict wheat traits: a) yield (kg ha^{-1}), b) grain protein concentration and c) N output with linear regression (LR), multiple linear regression (MLR), artificial neural network (ANN), and random forest (RF). Indices used are on the X-axis: spectral vegetation indices based on visible-near infrared regions related to chlorophyll content (Chl) and plant structure (Stru), vegetation index that includes a band within the SWIR region (SWIR), and radar vegetation index (RVI). Different white letters indicate significant differences ($P \geq 0.05$) between ensemble models with the same set of indices. Colored letters indicate differences between the same ensemble models using a different set of indices.

4.3.5 Discussion

The present Chapter analyzed whether the prediction of different winter wheat traits improved by combining indices related to different crop biochemical and physical parameters. In all cases, an improvement was achieved when combining different indices rather than using one index alone. Overall, the results indicated that a visible-SWIR sensor

was the most suitable for all winter wheat traits; however, the spectral resolution and range were important factors when predicting some traits.

Predicting yield based on hyperspectral VSWIR reduced the RMSE by 3% compared with the Sentinel-2 prediction. When only the VNIR region was used, the RMSE difference between hyperspectral and multispectral sensor prediction was < 0.3%. Due to this small reduction in RMSE, the adequate spatial and temporal coverage, and its free availability, Sentinel-2 imagery is suitable for accurately predicting yield in large areas; moreover, including the SWIR bands reduced uncertainty. The most important index for yield prediction was the SWIR index (NDSI (1106 nm, 1066 nm)), which is affected by lignin content and therefore by biomass, that is related to final yield (Marti et al., 2007). When SIF was included in the analysis, it obtained the highest importance; this can be explained by the link between SIF and photosynthesis rate, which is affected by N (Camino et al., 2018) and water availability (Zarco-Tejada et al., 2012). Other studies also reported the suitability of Sentinel-2 for predicting wheat yield using different techniques: Skakun et al. (2017) used Sentinel-2 and Landsat-8 time series for the peak-NDVI approach and obtained an RMSE of 310 kg ha^{-1}. Mehdaoui and Anane (2020) reduced the RMSE to 380 kg·ha^{-1} using the red edge bands. Segarra et al. (2022) combined multidate Sentinel-2 information with ensemble models to achieve an RMSE of 740 kg ha^{-1}. Cavalaris et al. (2021) used EVI and NMDI for durum wheat yield prediction and obtained an RMSE of 538 kg ha^{-1}. Hunt et al. (2019) reduced the RMSE in the prediction of winter wheat yield from 660 kg ha^{-1} when using only Sentinel-2 information to 610 kg ha^{-1} when it was combined with environmental data. For this reason, our study encourages further research to include environmental data when aiming to predict crop traits.

The GPC prediction was less accurate than the prediction of the other traits, and its accuracy depended greatly on the spectral region and resolution used. The Sentinel-2 VNIR bands were not suitable for GPC prediction in this study, as the RMSE was 39% higher than the RMSE obtained with the hyperspectral VNIR or with the VSWIR Sentinel-2 bands. The difference in RMSE between hyperspectral and multispectral VSWIR sensors was 8.1%, the same as between a hyperspectral VNIR and VSWIR sensor. Therefore, it is recommended to use a hyperspectral VSWIR sensor for GPC prediction. Raya-Sereno et al. (2021b) also reported that broad bands were reliable for yield prediction; however, accurate GPC and N output prediction required narrow bands. The need for a SWIR narrow band is attributed to

the N=H bond absorption feature in the SWIR region (Curran, 1989), and because the N stored in vegetative organs is an important source of the final GPC (Kichey et al., 2007). In addition, different factors affect reflectance in the SWIR region that can mask the influence of N in this region (Yan et al., 2021). A review study (Bastos et al., 2021) indicated that VIs based on the absorption and reflectance peak of chlorophyll (blue and green, respectively) are commonly used to predict GPC near anthesis (GS60) because most leaf N is contained in chlorophyll (Wang et al., 2004). In the current study, a relationship ($R^2 \sim 0.5$) between NDSI (green, blue) with GPC and with plant %N was obtained. Zhao et al. (2019) applied multiple linear regression using crop parameters together with Sentinel-2 information and obtained a maximum value of $R^2 = 0.47$ when predicting GPC.

The most accurate N output prediction was achieved with the hyperspectral VSWIR sensor; however, the differences in RMSE with the hyperspectral VNIR was only 3.1%. The RMSE obtained with the hyperspectral VNIR sensor was 15.7% lower than with the multispectral VNIR Sentinel-2 bands, but this difference was reduced to 2.7% if the multispectral SWIR bands were included. Therefore, if a hyperspectral VSWIR sensor is not available, similar accuracies in predicting N output can be achieved with a hyperspectral VNIR. Despite the fact that the Sentinel-2 ($R^2 = 0.71$) and the hyperspectral ($R^2 = 0.74$) VSWIR bands showed potential for N output prediction, the hyperspectral sensor reduced the RMSE by 6%. The hyperspectral sensor was found to be important because the most important index in the N output prediction was constructed with two bands in the red edge, which are difficult to adapt to multispectral sensors. Similar results were reported by Prey and Schmidhalter (2019a), who highlighted the importance of the Sentinel-2 red edge bands for the prediction of winter wheat N-related traits.

Chapter 4.4:
Quantification of winter wheat N status and traits through radiative transfer models using Sentinel-2 imagery

4.4.1 Specific objectives and application of methods

This Chapter follows the analysis described in Chapter 3.5.3 to meet the **Objective 3**: compare the performance of vegetation indices and a hybrid artificial neural network-PROSAIL-PRO method for winter wheat N status estimation and traits prediction.

a) evaluate the feasibility of applying a hybrid artificial neural network-PROSAIL-PRO method to Sentinel-2 imagery for retrieving winter wheat crop parameters at different growth stages.

b) analyze the performance of estimating winter wheat N status and traits by combining the retrieved variables.

Recently developed RTMs that are based on the entire reflectance spectrum to retrieve crop parameters are receiving increasing attention. These models can provide more accurate estimation than a single VI because they are able to analyze more spectral information, and therefore increase the transferability capacity. These models are commonly developed for hyperspectral information, but due to the benefits of the modern satellite images, it is important to validate the feasibility of the RTMs applied to free available multispectral satellite imagery that provides less spectral information than hyperspectral sensors.

This Chapter analyzes the performance of a hybrid artificial neural network-PROSAIL-PRO method applied to the multispectral Sentinel-2 imagery to retrieve different winter wheat parameters: Cab, LAI, Anth and EWT. The accuracy of different VIs from the literature (Table 5) for assessing winter wheat N status and traits is compared with the performance when combining the crop parameters retrieved with the hybrid method. The N status was determined at ground level with the NBI provided by the Dualex leaf clip sensor, and with the NNI calculated with the biomass samples (Fig 34). The winter wheat traits measured at harvest were yield, GPC and N output.

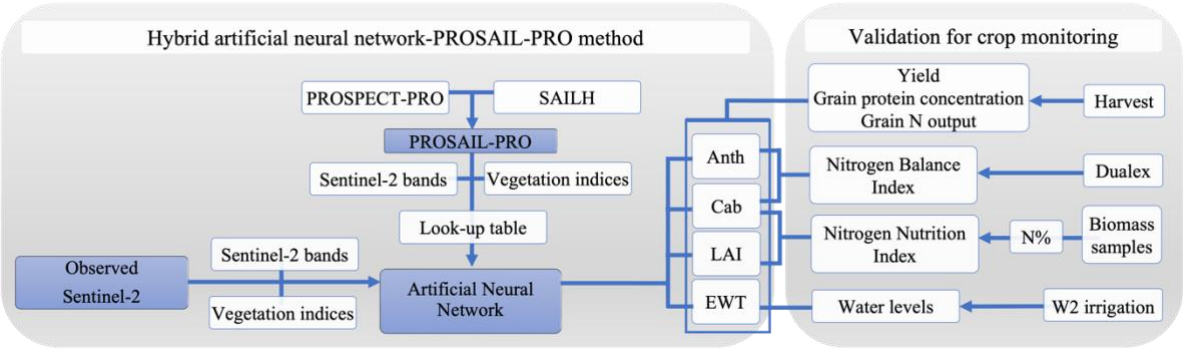

Fig 34. Workflow followed in this study for implementing the hybrid artificial neural network-PROSAIL-PRO method to the Sentinel-2 imagery, and the validation of the method for assessing winter wheat N status and traits. Anth, Cab, LAI and EWT indicate the anthocyanin content, chlorophyll content, leaf area index and equivalent water content retrieved with the hybrid method.

4.4.2 Performance of crop parameters retrieved with hybrid method

The LUTs generated with PROSAIL-PRO displayed an important number of spectra that did not fit the observed spectral range of the Sentinel-2 bands in each date. Therefore, using the observed spectra for the dimensional reduction of the LUT enabled reducing the number of spectra in the final LUT from 180000 to 7235 (Fig 35).

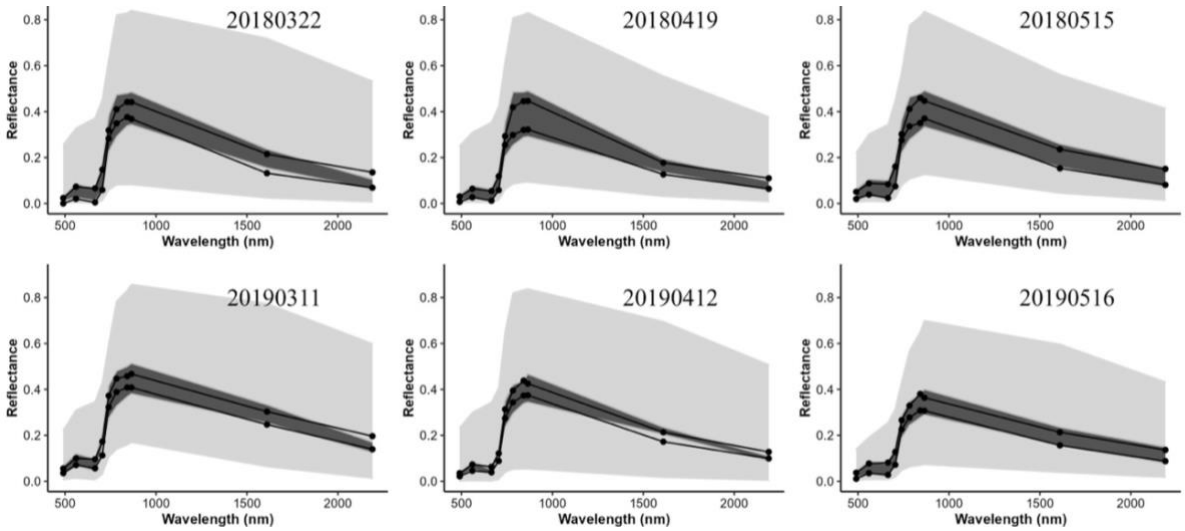

Fig 35. Spectral range of each Sentinel-2 band generated with the original look-up table (LUT; clear grey) and the reduced spectral range of the LUT (dark grey) when using the observed range of each band (lines and circles in black) for each date.

The R^2 contour maps developed with the LUT using the simulated Sentinel-2 bands and the corresponding crop parameters showed different regions or NDSIs sensitive to crop parameters (Fig 36). Among the crop parameters studied, Cab was the most accurate assessed. The red edge band B5 and the green band B3 of Sentinel-2 showed to be important for Cab, Anth and LAI estimation. High correlation between NDSIs and EWT was only obtained when the Sentinel-2 SWIR B11 and B12 were used. The five VIs and NDSIs calculated with the LUT that best described the simulated Cab, and therefore were included in the hybrid method for retrieving Cab, were NDSI (B7, B5), NDSI (B6, B5), CI, NDSI (B8, B5), NDSI (B8A, B5). Similarly, the indices included in the model for estimating LAI were NR, NDSI (B6, B3), NG, NDSI (B7, B3) and NDSI (B7, B5). The VIs included for estimating Anth were NDSI (B7, B3), NDSI (B6, B3), NG, GNDVI and GNDVI(B8A). The VIs used in the hybrid method to retrieve EWT were WET, TCARI (1510), TCARI/OSAVI-1510, NDSI (B12, B2) and NDSI (B11, B8A).

The hybrid method applied to Sentinel-2 enabled an accurate estimation of Cab and LAI (Fig 37). The most accurate estimation was Cab because it was significantly correlated ($P < 0.001$) (Fig 37a) with Cab-D when analyzing each date separated or all dates together ($R^2 = 0.37$). When analyzing each date separated, the R^2 values ranged between 0.56 and 0.8. Overall, the year 2018 obtained stronger relationship than the 2019 in all dates, probably because the water scarcity of 2019 reduced crop growth and produced a lower range of the crop parameters (such as %N or biomass) in all dates in 2019, as explained in Chapter 4.1. The estimated and observed Cab values were close to the 1:1 line, however, it was overestimated in some dates, especially at final stem elongation 2018. The strongest correlation between the Cab retrieved with the hybrid method and the Cab-D was achieved with the YeoJohnson transformation.

A significant correlation was observed between the LAI values retrieved with the hybrid method and the biomass measured in all GS using both years dataset ($R^2 > 0.45$; $P < 0.001$; Fig 37b). Better prediction capacity was observed in 2018 than in 2019, as observed when analyzing Cab. The lowest R^2 was obtained at flowering (GS65), and the highest R^2 at final stem elongation (GS37) both years. The R^2 obtained at GS32 was greatly reduced from 2018 to 2019, as it did the range of the observed biomass. The values of the retrieved LAI presented similar range in all GSs, and therefore, LAI retrieval with the hybrid method was less robust than the Cab retrieval because no significant relationship was obtained when

analyzing all dates together. The best result for LAI retrieval was obtained with the minimum-maximum transformation.

The hybrid method applied to Sentinel-2 was unable to accurately retrieve Anth because the retrieved values did not correlate with the Dualex measurement (data not shown).

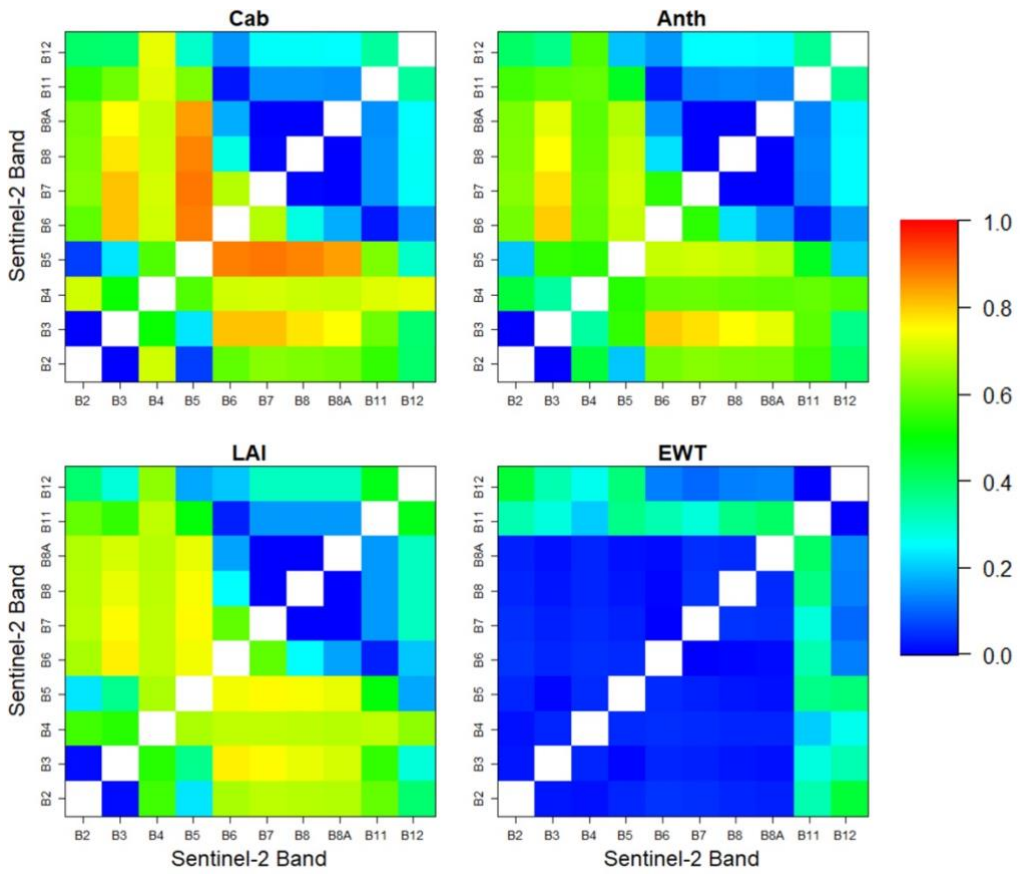

Fig 36. Contour maps calculated with the final look-up table displaying the coefficient of determination (R^2) from the linear relationship between the simulated a) Chlorophyll content (Cab), b) anthocyanin content (Anth), c) leaf area index (LAI) and d) equivalent water thickness (EWT) against all possible normalized difference spectral indices (NDSIs) calculated with the simulated Sentinel-2 bands.

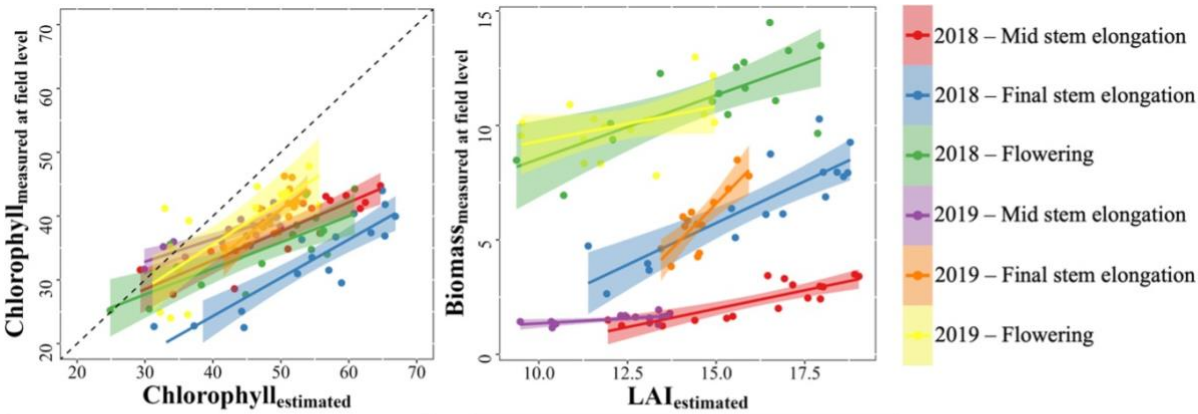

Year	Mid stem elongation	Final stem elongation	Flowering
2018	0.76***	0.80***	0.62***
2019	0.67***	0.56***	0.56***
Both years	0.64***	0.24**	0.44***

All dates = 0.37***

Year	Mid stem elongation	Final stem elongation	Flowering
2018	0.70***	0.73***	0.51**
2019	0.35*	0.66***	0.17
Both years	0.71***	0.66***	0.45***

All dates = 0.02

Fig 37. Linear correlation between a) chlorophyll content measured with Dualex (Cab-D) and chlorophyll content retrieved with the hybrid method (Cab) and b) aboveground biomass measured with crop samples and the leaf area index (LAI) retrieved with the hybrid method. The tables show the coefficient of determination (R^2) between variables measured in the same day, the same growth stage of both years and all dates together from both years dataset. The dotted line indicates 1:1.

The effect of the water levels was noticeable in the EWT values retrieved in 2019 when using the minimum-maximum transformation (Fig 38). The EWT values displayed significant differences between the water levels ($P < 0.001$) in 2019, but not in 2018. The distribution of the EWT values indicated that more water was present in the W2 plots than in the W1 plots of 2019, which is in agreement with the irrigation applied to the W2 plots. Probably, the effect of the irrigation in EWT was more evident in 2019 because the last W2 irrigation was performed two days before Sentinel-2 acquisition this year, while in 2018 the Sentinel-2 acquisition was four days after the W2 irrigation event. In addition, 0.6 mm rainfall was registered in the experimental field between May 8th and 9th; two days before the Sentinel-2 2018 acquisition, which could have mitigated the differences in water content between different water levels. The VIs related to water content (WET and $NDWI_{1640}$) displayed the same pattern; they were significantly different in the two water levels in 2019 but not in 2018 (Supplementary Material S4).

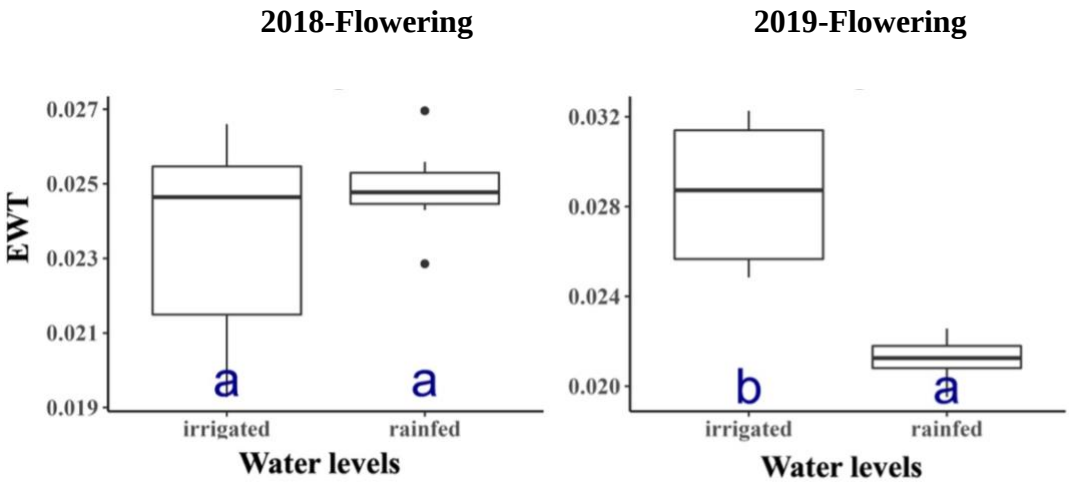

Fig 38. Distribution of the equivalent water thickness (EWT) values retrieved with the hybrid method in each water level at flowering of both years. The centerline of the boxes represents the median and the top and bottom lines show the third and first quartiles. Different letters indicate significant differences between water levels of the same year according to Tukey`s post-hoc test 95%.

4.4.3 N status estimation with the hybrid method and with vegetation indices

Among the 21 VIs tested, OSAVI and GNDVI obtained the strongest correlation with NBI when including all dates and plots (R^2 = 0.34; Supplementary Material S5a). The OSAVI index obtained an R^2 value > 0.34 in all dates, being the strongest correlation at GS65 of 2019 (R^2 = 0.84). The GNDVI presented an R^2 value between 0.84 and 0.61 in all dates, obtaining also the highest value at GS65 2019. The best NNI estimation when including all dates and plots was obtained with CI (R^2 = 0.42), followed by OSAVI (R^2 = 0.41). Overall, all VIs displayed better N status estimation capacity in 2018 than in 2019, especially when estimating NNI.

The performance when estimating winter wheat N status with a single VI was improved when combining the crop parameters retrieved with the hybrid method using as ground-truth measurement of N status NBI or NNI (Fig 39; Supplementary Material S5). The R^2 value when estimating both NBI and NNI using the crop parameters retrieved from all plots and dates was 0.42 (P < 0.001). For NBI estimation, this R^2 value was higher than the maximum R^2 value obtained with the VIs OSAVI and GNDVI (R^2 = 0.34). The highest R^2 value (0.85)

was obtained at GS65 in 2019, and the lowest (R^2 = 0.63) at GS36 in 2019. The correlation between NBI and the combination of Cab and Anth as a new indicator was significant in all dates (R^2 > 0.63; P < 0.001). The prediction capacity of NBI was not reduced in 2019 compared to 2018. The estimation of NNI based on the combination of Cab and LAI retrieved values was highly significant in all dates of 2018 (P < 0.001), however this correlation was weaker in all dates of 2019 (P < 0.05). A good correlation was obtained when analyzing together the plots of the same GS of both years (R^2 = 0.4; P < 0.001).

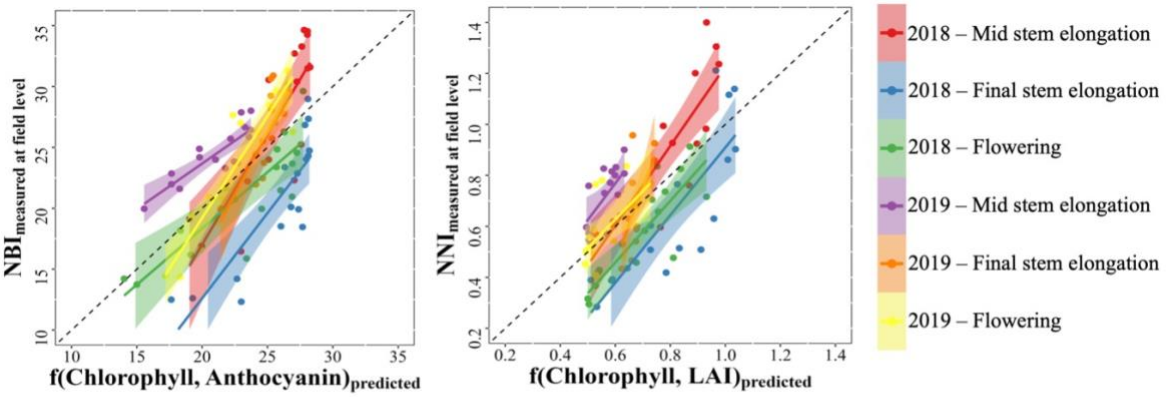

Year	Mid stem elongation	Final stem elongation	Flowering
2018	0.68***	0.71***	0.68***
2019	0.73***	0.63***	0.85***
Both years	0.57***	0.36***	0.64***

All dates = 0.43***

Year	Mid stem elongation	Final stem elongation	Flowering
2018	0.74***	0.68***	0.72***
2019	0.38*	0.42*	0.36*
Both years	0.65***	0.46***	0.40***

All dates = 0.43***

Fig 39. Linear correlation between a) nitrogen balance index (NBI) measured with Dualex and NBI based on chlorophyll (Cab) and anthocyanin (Anth) retrieved with the hybrid method and b) nitrogen nutrition index (NNI) calculated with crop samples and NNI based on Cab and leaf area index (LAI) retrieved with the hybrid method. The tables show the coefficient of determination (R^2) between variables measured in the same day, the same growth stage (GS) and all dates together of both years. The dotted lines indicate 1:1.

4.4.4 Traits prediction with the hybrid method and with vegetation indices

Yield was the winter wheat trait that obtained the most robust correlation with the VIs calculated with the Sentinel-2 bands at flowering, and GPC the weakest (Suplementary material S5). When analyzing the VIs calculated with both dates together, the highest R^2 was achieved when predicting yield with EVI (R^2 = 0.87), followed by the prediction of N output with NDRE (R^2 = 0.78) and GPC with CCCI (R^2 = 0.47). A strong correlation was found between EVI and yield when analyzing the two dates at flowering separated, however, the R^2

was reduced from 0.85 in flowering 2018 to 0.57 in flowering 2019. This behavior was also observed in the correlation of most VIs and yield, probably due to the smaller yield range attained in 2019, due to the lower water availability as discussed in Chapter 4.1 (Fig 18). The CCCI was strongly correlated with GPC (R^2 = 0.80) at flowering 2018, but the R^2 was sharply reduced in 2019 (R^2 = 0.14). After CCCI, the best correlation with GPC when analyzing both years together was attained with NDRE (R^2 = 0.42). The difference in R^2 between years of NDRE was lower; from 0.71 in 2018 to 0.57 in 2019. As observed with yield, the decrease in the accuracy of the estimations in 2019 was also found in GPC and in N output. For N output, the decrease in R^2 with NDRE was from 0.88 in 2018 to 0.67 in 2019. These results highlight the good performance of the VIs based on the Sentinel-2 red edge bands (NDRE and CCCI) for the estimation of winter wheat N-related traits (GPC and N output).

The VIs calculated with Sentinel-2 displayed potential for predicting winter wheat traits, but better results were obtained when combining the crop parameters retrieved with the hybrid method (Fig 40). The prediction capacity when combining the retrieved crop parameters showed more robustness and transferability than the single VIs because the estimation capacity did not display a reduction tendency in 2019. High accuracy was obtained when predicting yield from both years combining the retrieved Cab and LAI (R^2 = 0.84; Fig 40a), however the R^2 value was slightly lower than the value obtained when predicting yield with EVI (R^2 = 0.87). Similar results were observed in 2018 (R^2 = 0.82 and 0.85 with the hybrid method and with EVI, respectively), but the estimation capacity of the hybrid method (R^2 = 0.71) outperformed the capacity of the EVI (R^2 = 0.57) in 2019. The biggest improvement when combining the retrieved crop parameters was observed when estimating GPC. The R^2 value when estimating GPC with the retrieved Cab, LAI and Anth was higher than the value obtained with CCCI when analyzing both years together (R^2 = 0.63 and 0.47 respectively), or the 2019 dataset (R^2 = 0.63 and 0.14; Fig 40b), but not with the 2018 dataset (R^2 = 0.45 and 0.80). The N output prediction capacity when using the retrieved Cab, LAI and Anth was better than the capacity of NDRE because it obtained a $R^2 > 0.78$ in all cases; when analyzing both dates together or separated (Fig 40c).

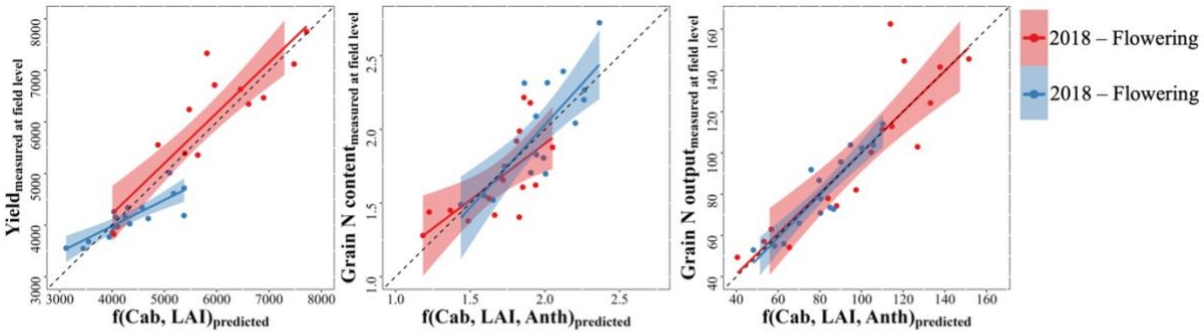

Year	Flowering
2018	0.82***
2019	0.71***
Both years	0.84***

Year	Flowering
2018	0.45**
2019	0.64***
Both years	0.63***

Year	Flowering
2018	0.78***
2019	0.84***
Both years	0.81***

Fig 40. Linear correlation between a) yield measured at harvest with yield based on chlorophyll (Cab) and leaf area index (LAI) retrieved with the hybrid method, b) grain protein concentration (GPC) measured at harvest and GPC based on Cab, LAI and anthocyanin (Anth) retrieved with the hybrid method, and c) N output measured at harvest and N output based on Cab, LAI and Anth retrieved with the hybrid method. The tables show the coefficient of determination (R^2) between variables retrieved with the hybrid method applied to the Sentinel-2 images at flowering of both years, and the winter wheat traits. The dotted line indicates 1:1.

4.4.5 Discussion

This Chapter showed that the hybrid artificial neural network-PROSAIL-PRO applied to the multispectral Sentinel-2 images allows assessing spatio-temporal variability of the crop parameters for accurate N status and traits estimation. This method obtained better results than the traditional VIs, and therefore it is the recommended method for adjusting N fertilization and for predicting traits in winter wheat. The retrieved Cab correctly addressed the temporal changes across the GSs. Typically, the VIs retrieve chlorophyll content based on the relationship between few spectral bands, such as the VIs based on the normalized difference of one band located in the chlorophyll absorption region and another outside (Barnes et al., 2000). However, other crop parameters such as canopy structure or water content influence the reflectance spectrum and can lead to errors in the VIs estimation (Sun et al., 2022; Quemada and Daughtry, 2016). As observed in the results, the hybrid method correctly estimates the water content and the LAI at a given GS. Considering these variables in the hybrid method increases the transferability capabilities. This was observed in the reduction of the accuracy of the VIs under water stress conditions observed in 2019 that did

not affect the hybrid method estimation. Sinha et al., 2020 also obtained better results with PROSAIL-PRO applied to Sentinel-2 bands than with VIs to estimate LAI at different GSs.

The good performance in Cab retrieval can be attributed to the three red edge bands centered at 705 nm, 740 nm and 783 nm that Sentinel-2 provides (Table 4) and are sensitive to chlorophyll content (Xie et al., 2019; Lin et al., 2019). This is an important improvement in Sentinel-2 because previously launched open-access multispectral satellites, such as the Landsat constellation, do not provide red edge bands (Clavarie et al., 2018). Despite Féret et al., 2008 adjusted the coefficients of the PROSPECT model to identify the contribution of the individual plant pigments to hyperspectral spectra, an accurate Anth estimation was not achieved in this study with the multispectral Sentinel-2 bands. As observed in the contour maps, the Anth estimation was poorer than the Cab estimation because the only Sentinel-2 bands that are sensitive to this pigment are B3 (green) and B5 (red edge), which are highly affected by the chlorophyll content (Fig 36) and can mask the Anth signal (Sims and Gamon, 2002). Similarly, de Sá et al., 2021 found that variations in carotenoids concentration do not make changes in the Sentinel-2 reflectance. In addition, satellite imagery usually presents noise in this region because it is sensitive to atmospheric disturbances (Gilabert et al., 1994; Pacifici et al., 2014).

The variables retrieved with the hybrid method accurately described the N status in all GSs, including at early GS, therefore this method allows the adjustment of winter wheat N fertilization rates. In most dates, the NBI was better estimated than the NNI, probably because the NBI was calculated with optical measurements (Dualex). The measurements collected with the leaf clip sensor Dualex were taken in the flag leave, however the Sentinel-2 takes measurements from all observable leaves within the FOV of the sensors. Because the chlorophyll distribution in leaves changes with leaf position and age (Li et al., 2013b), this can be a source of disagreement between leaf clip sensors and remote sensing measurement. Among the winter wheat traits, the GPC estimation was the most challenging, as obtained in Chapter 4.3 combining different indicators, or in other studies (Prey and Schmidhalter, 2019a; Rodrigues et al., 2018). Probably including additional crop parameters retrieved from the hybrid method or weather data could enhance the traits estimation capacity.

One benefit of using satellite imagery with a large footprint is that it allows extracting soil spectra from pure pixels near or within the crop field to feed the PROSAIL-PRO model. This information contributed to compensate by the soil background noise and allowed obtain good

accuracy at the beginning of stem elongation, and therefore, increased the capabilities of the hybrid method for N fertilization recommendation. In addition, Sentinel-2 metadata provides view and illumination angles of each pixel that can be used to reduce uncertainties and increase the transferability capacity of the PROSAIL-PRO model because the angular components highly affect the measured surface reflectance with different intensity and direction depending on the region of the spectrum (Pacifici et al., 2014; Cross et al., 2018). Both, the soil background spectra and view angles are not considered in the VIs calculation and these non-crop components can have an effect that must be compensated to increase model transferability to different locations or dates (Broge and Leblanc, 2001; Verrelst et al., 2008; Breuniga et al., 2015).

Although the PROSAIL-PRO model was originally developed with hyperspectral data (Jacquemoud et al., 2009), its application to multispectral satellite images with a lower number of bands showed accurate results. The RTMs generate simulated spectra dataset using experimental data to calibrate the contribution of each crop component (Féret et al., 2008). Validating the PROSAIL-PRO model with more crop information would improve the estimation capacity and transferability of the model (de Sá et al., 2021). The free availability of the twin Sentinel-2 satellites allows a revisit time of less than five days at near-global scale. This amount of data facilitates the sample acquisition to improve the accuracy of the PROSAIL-PRO method applied to Sentinel-2. The good temporal resolution of the Sentinel-2 would allow detecting changes in crop parameters during crop growth. This capacity should be tested using longer time series throughout the crop cycle. Harmonizing time series of different satellite missions, such as Sentinel-2 and Landsat, allows reducing revisit time and therefore increases the amount of information of the crop growth that could be used for improving N fertilization recommendations (Johansen et al., 2022; Clavarie et al., 2018; Franch et al., 2019).

Chapter 4.5:
Sentinel-2 and WorldView-3 atmospheric correction and signal normalization based on ground-truth spectroradiometric measurements

4.5.1 Specific objectives and application of methods

This Chapter uses the Aranjuez dataset to follow the analysis described in Chapter 3.6 to meet the **Objective 4:** analyze the accuracy of the Sentinel-2 and WorldView-3 satellite imagery for winter wheat monitoring.

a) assess the reliability of the surface reflectance measured by Sentinel-2 and WorldView-3 satellites for winter wheat monitoring after applying different atmospheric correction approaches.

b) to propose and validate an empirical signal normalization procedure for compensating for the off-nadir view angle-induced effects on the surface reflectance of WorldView-3.

Given the benefits of combining information from high- and medium-spatial resolution satellite images when monitoring vegetation status, it is important to compensate the atmospheric and view angle effects to ensure integrating comparable surface reflectance values. This Chapter first compared the values of the atmospheric constituents measured with different sources, and assessed how the atmospheric constituents affect the atmospheric correction results in Sentinel-2 and WorldView-3 surface reflectance. The Sentinel-2 images were corrected with Sen2Cor, MODTRAN and FLAASH atmospheric RTMs, and the WorldView-3 images with MODTRAN and FLAASH. The assessment of the atmospheric corrections was conducted by comparing the derived surface reflectance values with ground-truth reflectance spectra acquired with the FieldSpec hand-held spectroradiometer in a nadir orientation. Finally, an empirical signal normalization procedure using the spectra collected at field level was proposed and validated for reducing the angular induced effect in the WorlView-3 images acquired with different viewing and illumination geometry. This procedure was validated by comparing the values of the resulted WorlView-3 images with the Sentinel-2 to ensure that surface reflectance values extracted from different satellites with different angles can be integrated for use in vegetation monitoring. Therefore, the sensors used in this Chapter are the Sentinel-2 and the WorldView-3 displayed in Table 3, and the FieldSpec spectra acquired at mid stem elongation both years in the Aranjuez experiment.

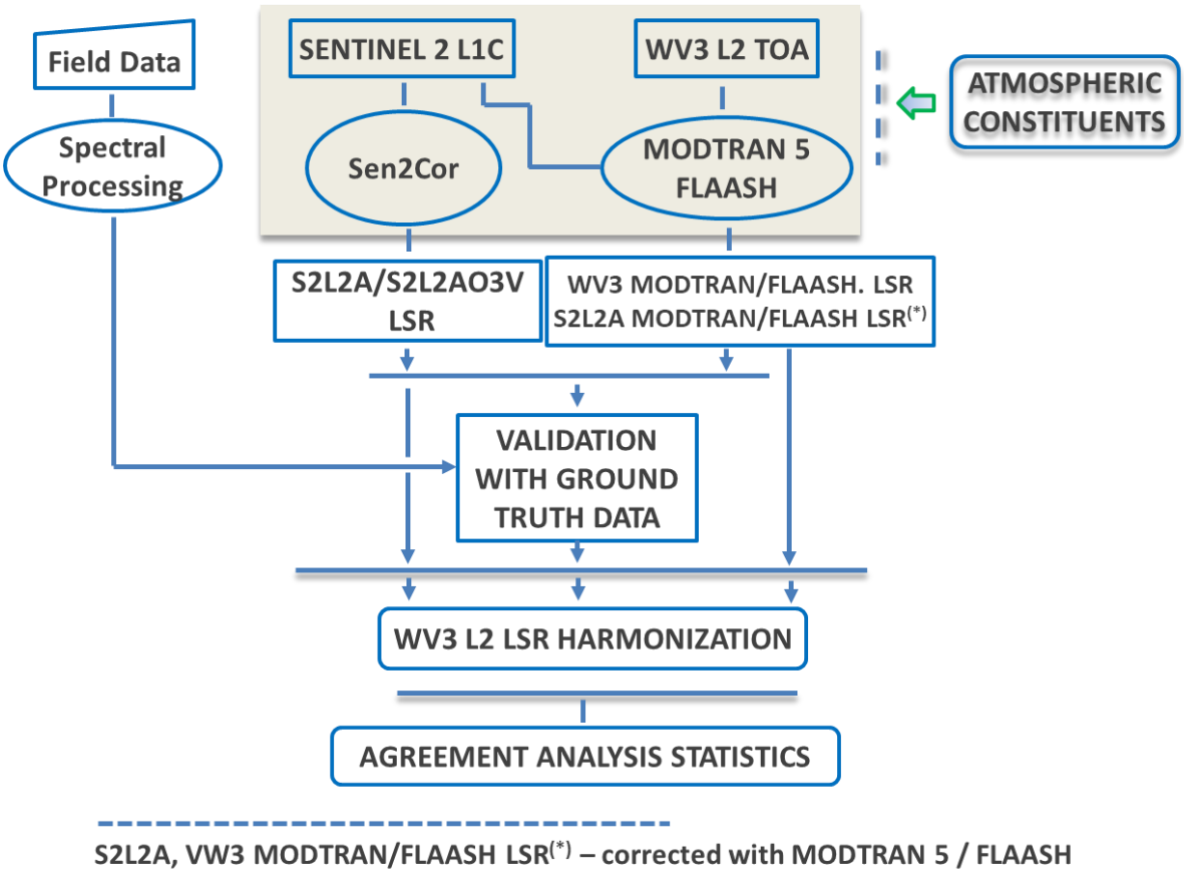

Fig 41. The methodological workflow followed for the atmospheric correction and signal normalization process of Sentinel-2 (S2) and WorldView-3 (WV3). Description of Land Surface Reflectance (LSR) products is in the text.

4.5.2 Gathering of atmospheric constituents and sensitivity analysis

The atmospheric constituents and parameters, referenced to the geodetic coordinates of the center of the Aranjuez experiment, varied with the dates of the images acquisition (Table 12). The WVC obtained from MODIS (1.23 cm in 2018 and 0.715 cm in 2019) were similar to those obtained by Sen2Cor algorithm based on S2L1C imagery (1.28 cm in 2018 and 0.689 cm in 2019). The AOT values obtained from MODIS and Sen2Cor algorithm matched closely in 2019 (0.129 from MODIS and 0.100 from Sen2Cor), however, some differences were found in the 2018 AOT (0.096 from MODIS and 0.197 from Sen2Cor). This disagreement can be attributed to the different Sentinel-2 and MODIS overpass times; while in 2019 the measurements differed only by 9 minutes, in 2018 this time difference was almost one hour (Table 12). In addition to overpass time, differences in the retrieved WVC values could also be due to the different spatial resolution between MCD19A2 (1 km), MOD07 (5

km) and Sentinel-2 (60 m). There are differences between the MCD19A2 and MOD07 products depending on the acquisition time of the corresponding measured constituent values (Table 12). A good correspondence for WVC between Sentinel-2 and MODIS retrieved atmospheric constituent values was obtained when data overpass times were closer. The extent of the difference in values cannot be verified for visibility because the AOT information is lacking in the MOD07 products. In any case, the value closer to the satellite overpass was used in the subsequent atmospheric corrections.

The O_3 values were in the range of the usual concentrations of the area. The monthly range of O_3 over Madrid taken by the National Meteorological Agency (AEMET, 2023) was 307 – 439 DU in April 2018 and 303 – 438 DU in April 2019. The O_3 daily values shown in AEMET (2023) agree with the MODIS data displaying an O_3 concentrations peak at 438 DU around mid-April 2019.

Table 12. Values of the atmospheric constituents (aerosol optical thickness (AOT), water vapor column (WVC), ozone concentration (O_3) and absolute surface temperature (Temp)) extracted from MODIS products information for 17 and 18 April 2018, and for 12 April 2019. The values of the AOT and WVC calculated from the in-scene spectral bands of Sentinel-2 are also shown.

Data source (MODIS product)	Data time for overpasses data sources	Atmospheric Constituents			Temp (ºK)
		AOT	WVC (cm)	O_3 (DU)	
	April 17th, 2018 (Sentinel-2)				
MCD19A2*	*12:05 PM*	0.096	1.692	-	-
MOD07**	*11:31 AM*	-	1.230	335.0	-
MOD11C1***	*12:12 PM*	-	-	-	296.1
Sentinel-2	*11:07 AM*	0.197	1.280	-	-
	April 18th, 2018 (WorldView-3)				
MCD19A2(*)	*11:10 AM*	0.196	1.475	-	-
MOD07(**)	*12:14 PM*	-	1.711	320.3	-
MOD11C1(***)	*11:12 AM*	-	-	-	303.2
	April 12th, 2019 (Sentinel-2 and WorldView-3)				
MCD19A2(*)	*11:15 AM*	0.129	0.715	-	-
MOD07(**)	*12:19 PM*	-	0.576	438.3	-
MOD11C1(***)	*11:24 AM*	-	-	-	302.9
Sentinel-2	*11:06 AM*	0.100	0.689	-	-

*MODIS aerosol and water vapor products
** MODIS water vapor and O_3 products
*** MODIS land surface temperature products

The importance of using accurate values of atmospheric constituents is demonstrated in the sensitivity analysis, which displays the fluctuation of surface reflectance when varying atmospheric constituents. The relative reflectance difference for each band is expressed as a percentage and was calculated as the surface reflectance derived using the atmospheric constituents obtained for each location and date minus the surface reflectance modifying the studied atmospheric constituent, divided by the surface reflectance using the measured atmospheric constituents. The sensitivity analysis for Sen2Cor and MODTRAN showed that both processors exhibited the same directional effect on surface reflectance when modifying O_3 and visibility (calculated from AOT), but with different magnitudes (Fig 42).

The effect of these constituents was more relevant for the visible region than for the red edge and the NIR. Variations in visibility values resulted in changes of surface reflectance up to 100% with Sen2Cor and -800% with MODTRAN, while variations of O_3 changed surface reflectance less than ±5% with Sen2Cor and 20% with MODTRAN (Fig 42). This is contrasted by the WVC changes that had pronounced impacts on the NIR wavelengths in the MODTRAN atmospheric correction, resulting in a maximum fluctuation of 10% of surface reflectance. These findings were expected due to the known effect of O_3 on the reflectance of UV to visible regions (Vermote et al., 2016; Liang and Wang, 2019) and the water vapor absorption feature in the NIR region (Pacifici et al., 2014). Reflectance in all bands increased with higher values of O_3 and WVC, but only visible bands increased with higher visibility values.

Visibility was a critical parameter for atmospheric correction. The effect of visibility on the surface reflectance corrected with Sen2Cor and MODTRAN in the sensitivity analysis was greater than the other atmospheric constituents in all bands. The greatest impact was observed in the blue bands of WorldView-3 and Sentinel-2. The sensitivity analysis showed that if visibility is underestimated, MODTRAN can generate negative surface reflectance in the Coastal and Blue bands.

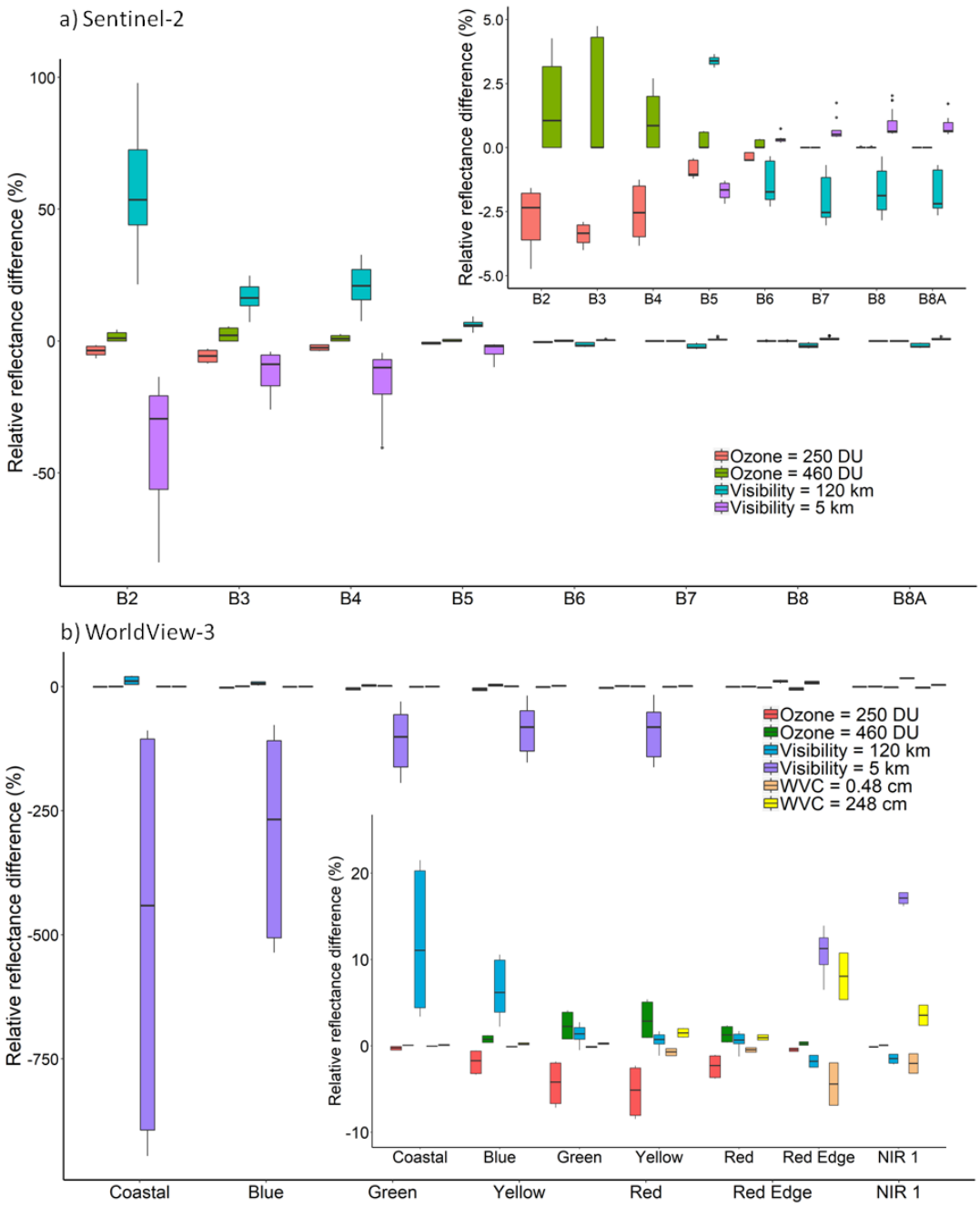

Fig 42. Relative reflectance difference for various a) Sentinel-2 bands corrected with Sen2Cor and b) WorldView-3 bands corrected with MODTRAN of the two studied dates as a result of the sensitivity analysis in which ozone atmospheric concentration and visibility varied between the established ranges. Additionally, the effect of the water vapor column (WVC) variation is shown in b. The smaller graphs in the a and b windows show reflectance on a different scale to better appreciate the atmospheric parameters effect.

4.5.3 Statistical assessment of atmospheric correction procedures

The Sentinel-2 and WorldView-3 surface reflectance imagery derived from the three different atmospheric-RTMs were compared with the ground-truth spectral data (Manakos et al., 2011; Cross et al., 2018). All atmospheric correction processors reduced the reflectance of the visible bands and increased the reflectance of the NIR bands with respect to TOA imagery with both sensors (Fig 43). The atmospheric corrections improved match-ups with ground-truth spectral data, except for the NIR band of WV3 (Fig 43; Table 13). Reflectance from S2L1C was different from the ground-truth data in most visible bands but not in the NIR bands (B8 and B8A) of SV plots, whereas surface reflectance from Sentinel-2 atmospherically corrected was similar for most processors, bands and vegetation types (Table 13). Good performance was demonstrated by the Sentinel-2 red edge bands, especially B6 that did not present significant differences with the field spectra in any case. It should be noted that given the low values registered in the visible region in both vegetation types, slight differences in the surface reflectance make the t-test significant in bands from this region. In the Sentinel-2 visible bands, the actual differences in surface reflectance were small enough for its practical application in studying vegetation properties even if they were significant when compared to the convolved bands.

Overall, the S2L2A diminished the differences with the ground-truth compared to S2L2A_O3V, nevertheless minor differences were found between all processors tested, resulting in coincident values of surface reflectance in many cases. Differences in the derived surface reflectance of Sentinel-2 VNIR bands less than 0.013 between Sen2Cor and FLAASH and less than 0.026 between Sen2Cor and MODTRAN were identified in all cases. These results support the suitability of MODTRAN, FLAASH and Sen2Cor to correct Sentinel-2 imagery using ancillary atmospheric constituent data from MODIS.

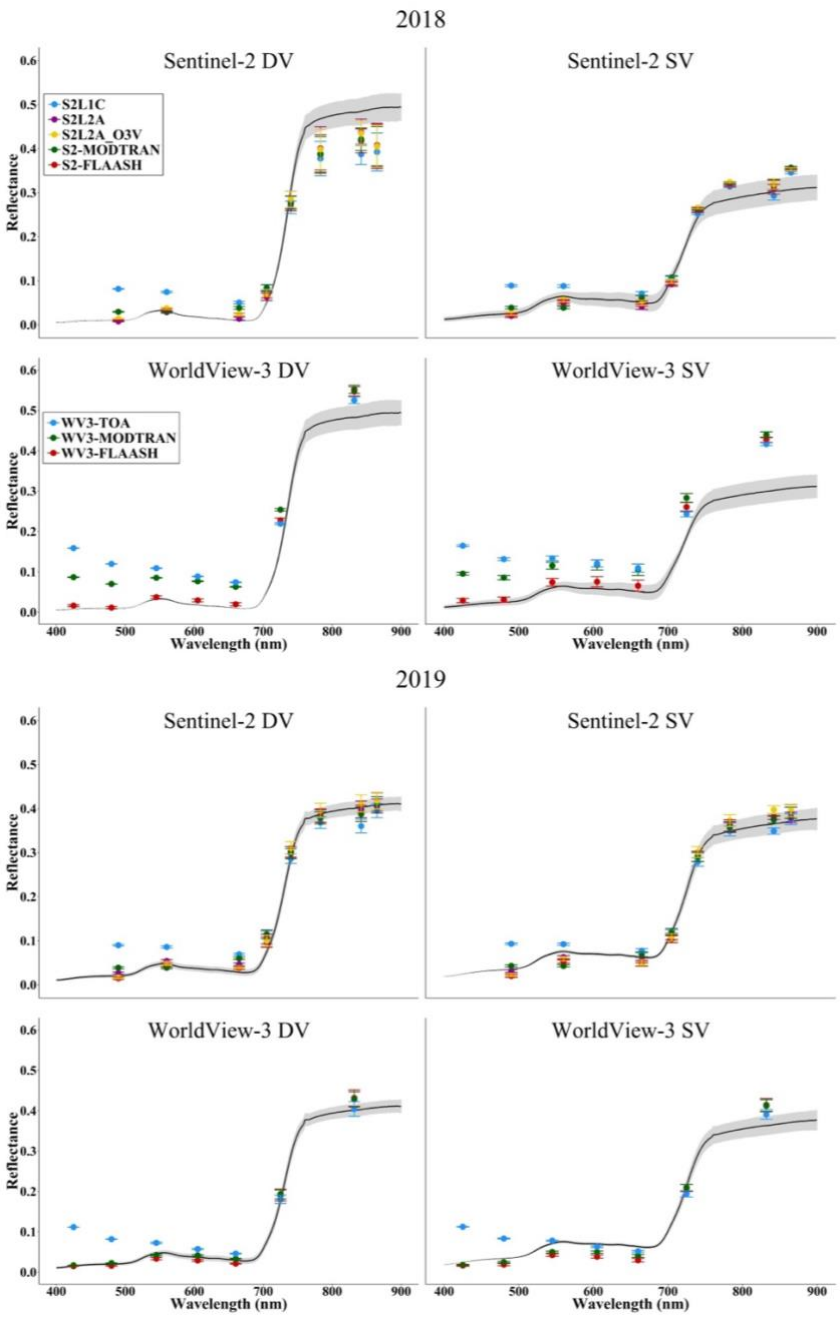

Fig 43. Ground-truth field spectra (continuous line) and Sentinel-2 and WorldView-3 reflectance bands for dense vegetation (DV) and sparse vegetation (SV) plots. Symbols represent reflectance at the top of atmosphere (S2L1C and WV3-TOA), surface reflectance after atmospheric correction with Sen2Cor calculated values (S2L2A), with Sen2Cor customized values for ozone and visibility (S2L2A_O3V) and with MODTRAN (S2-MODTRAN and WV3-MODTRAN) and FLAASH (S2-FLAASH and WV3-FLAASH) using atmospheric constituents values from MODIS for the two experimental years. Spectrum shadow and bars represent standard deviation.

Table 13. *P*-values from the single sample t-test comparing the surface reflectance in the bands from ground-truth spectroradiometer data with that extracted from Sentinel-2 and WorldView-3 imagery atmospherically corrected by the different procedures, for dense vegetation (DV) and sparse vegetation (SV) and years. Values in bold indicate no differences at a significance level $\alpha = 0.05$.

Vegetation type	Reflectance*	Sentinel-2							
		Blue (B2)	Green (B3)	Red (B4)	Red Edge (B5)	Red Edge (B6)	Red Edge (B7)	NIR (B8)	NIR (B8A)
				2018					
DV	S2 L1C	0.000	0.000	0.000	0.001	**0.066**	0.031	0.002	0.030
	S2L2A	0.000	**0.395**	**0.067**	0.046	**0.249**	**0.095**	**0.072**	**0.058**
	S2L2A_O3V	0.004	0.001	0.000	0.008	**0.267**	**0.080**	**0.056**	**0.051**
	S2-MODTRAN	0.000	**0.636**	0.000	0.002	**0.144**	0.045	0.019	0.047
	S2-FLAASH	**0.927**	0.014	0.000	0.014	**0.127**	**0.051**	0.017	**0.055**
SV	S2 L1C	0.000	0.004	**0.076**	**0.990**	**0.558**	**0.233**	**0.696**	**0.150**
	S2L2A	**0.092**	**0.063**	**0.359**	**0.298**	**0.221**	**0.139**	**0.297**	**0.104**
	S2L2A_O3V	**0.388**	**0.331**	**0.934**	**0.582**	**0.188**	**0.133**	**0.229**	**0.102**
	S2-MODTRAN	**0.068**	0.004	**0.308**	**0.899**	**0.261**	**0.157**	**0.264**	**0.083**
	S2-FLAASH	**0.169**	**0.132**	**0.797**	**0.380**	**0.353**	**0.203**	**0.588**	**0.089**
				2019					
DV	S2 L1C	0.000	0.000	0.000	0.010	**0.913**	**0.212**	0.010	**0.394**
	S2L2A	**0.152**	0.049	0.004	0.029	**0.369**	**0.815**	**0.907**	**0.881**
	S2L2A_O3V	0.041	**0.433**	0.031	**0.052**	**0.187**	**0.498**	**0.409**	**0.511**
	S2-MODTRAN	0.000	**0.071**	0.000	0.010	**0.519**	**0.575**	**0.266**	**0.851**
	S2-FLAASH	0.014	**0.467**	**0.055**	**0.070**	**0.418**	**0.862**	**0.361**	**0.534**
SV	S2 L1C	0.000	0.000	0.002	**0.809**	**0.364**	**0.924**	**0.284**	**0.736**
	S2L2A	0.004	0.007	**0.093**	**0.115**	**0.936**	**0.461**	**0.162**	**0.521**
	S2L2A_O3V	0.000	0.002	0.014	**0.081**	**0.301**	**0.096**	0.031	**0.121**
	S2-MODTRAN	0.026	0.000	**0.089**	**0.870**	**0.951**	**0.400**	**0.361**	**0.193**
	S2-FLAASH	0.000	0.000	0.006	0.028	**0.824**	**0.314**	**0.339**	**0.127**

		WorldView-3						
		Coastal	Blue	Green	Yellow	Red	Red Edge	NIR1
				2018				
DV	WV3-TOA	0.000	0.000	0.000	0.000	0.000	0.000	0.028
	WV3-MODTRAN	0.000	0.000	0.000	0.000	0.000	0.000	0.004
	WV3-FLAASH	0.001	**0.425**	0.001	0.000	0.007	0.000	0.006
SV	WV3-TOA	0.000	0.000	0.000	0.000	0.002	**0.141**	0.000
	WV3-MODTRAN	0.000	0.000	0.000	0.001	0.004	**0.161**	0.000
	WV3-FLAASH	0.027	**0.358**	0.041	**0.094**	**0.313**	**0.815**	0.000
				2019				
DV	WV3-TOA	0.000	0.000	0.000	0.001	0.005	0.000	**0.687**
	WV3-MODTRAN	**0.368**	**0.426**	**0.749**	**0.070**	**0.529**	0.000	**0.053**
	WV3-FLAASH	**0.624**	0.039	0.043	**0.228**	0.034	0.000	0.043
SV	WV3-TOA	0.000	0.000	0.001	**0.106**	0.000	0.000	**0.060**
	WV3-MODTRAN	0.000	0.000	0.000	0.000	0.000	0.000	0.009
	WV3-FLAASH	0.000	0.000	0.000	0.000	0.000	0.000	0.009

*Reflectance at the top of atmosphere from Sentinel-2 (S2L1C), surface reflectance corrected with Sen2Cor calculated values (S2L2A) and with Sen2Cor customized values for ozone and visibility (S2L2A_O3V), MODTRAN and FLAASH for the two experimental years. Reflectance at the top of atmosphere from WorldView-3 (TOA) and surface reflectance corrected by MODTRAN and FLAASH.

Both processors, MODTRAN and FLAASH, accounted for the atmospheric effects of the WorldView-3 viewing angle, but only FLAASH was able to substantially reduce the difference in the visible bands relative to ground-truth data in the backward scattering imagery (2018) (Fig 43). In the forward scattering imagery (2019) both processors matched field measurements in the visible bands for DV plots, but not for SV plots (Table 13). The mean value of WorldView-3 visible bands was overestimated in 2018 and underestimated in 2019, and the NIR band was overestimated in all cases. Good agreement between the corrected NIR band of WorldView-3 and the field spectra was only found in DV of 2019 when corrected with MODTRAN (Table 13). These results indicated that, in addition to atmospheric scattering and absorbance, the acquired signal of WorldView-3 was affected by the anisotropy of the non-Lambertian nature of the study field.

4.5.4 WorldView-3/Sentinel-2 signal normalization

Two methods that characterize the impact of the anisotropy reflectance in off-nadir acquisitions were tested in the WorldView-3 imagery. The application of the RPV method to compensate for the two angular components provided results that differed substantially from the ground-truth surface reflectance values and consequently are not reported here. The c-factors of the kernel-driven Ross-Li procedure (Table 14) correctly expressed the corresponding angular components and viewing conditions in visible bands, but were insufficient to compensate for the effect of BRDF on surface reflectance.

It must be indicated that for the RPV model, the values for the corresponding parameters are only available for the visible and NIR spectral regions, without intra-region distinctions. Likewise, the c-factors are computed according to the Ross-Li method (Wanner et al., 1995), for the WorldView-3 bands matching the MODIS blue (B3), green (B4), red (B1) and NIR I (B2) spectral bands. For 2018, the WorldView-3 image was acquired in a backward solar scattering geometry that theoretically leads to an overestimation of the computed surface reflectance. Although the derived c-factors for the visible and NIR would correct the overestimation to some degree, they would do so insufficiently. In contrast, the WorldView-3 image of 2019 was acquired with a forward solar scattering geometry, theoretically leading to an underestimation of the surface reflectance in the visible region and an overestimation in the NIR region. The c-factors would partially compensate for the surface reflectance underestimation, however, the overestimation of NIR reflectance was not corrected.

Subsequently, both methods, i.e., RPV and c-factor, were disregarded for the angular correction of the WorldView-3 datasets.

The calibration coefficients obtained from the empirical normalization approach based on the ground-truth spectra differed for each WorldView-3 band and year of image acquisition (Table 14). The validation procedure extended to a collection of 454 pixels of Sentinel-2 showed a large improvement with respect to non-normalized data (Fig 44a) and a good agreement between the normalized WorldView-3 and the corresponding Sentinel-2 (Fig 44b). The R^2 between the normalized WorldView-3 and the Sentinel-2 datasets was > 0.75 for the four compared bands, and the data points clustered close to the 1:1 line. The largest RMSE was obtained for the NIR bands (B8 from Sentinel-2 versus NIR1 from WorldView-3), which represent about 5% of the average. The correlation between the green and red bands exhibited the best R^2.

Table 14. Coefficients used for the Rahman-Pinty-Verstraete (RPV), c-factor and empirical normalization methods in WorldView-3 imagery both years.

Method	VIS			NIR		
RPV	ρ_0	k	Θ	ρ_0	k	Θ
	0.133	0.851	-0.114	0.211	0.718	0.086

	2018				2019			
	B*	G	R	NIR 1	B	G	R	NIR 1
c-factor	0.937	0.944	0.953	0.953	1.151	1.14	1.125	1.116
Empirical normalization coefficients	0.88	0.74	0.70	0.79	1.64	1.43	1.88	0.89

* B: Blue, G: Green, R: Red, and NIR 1: Near Infrared 1 spectral reflectance bands of WorldView-3.

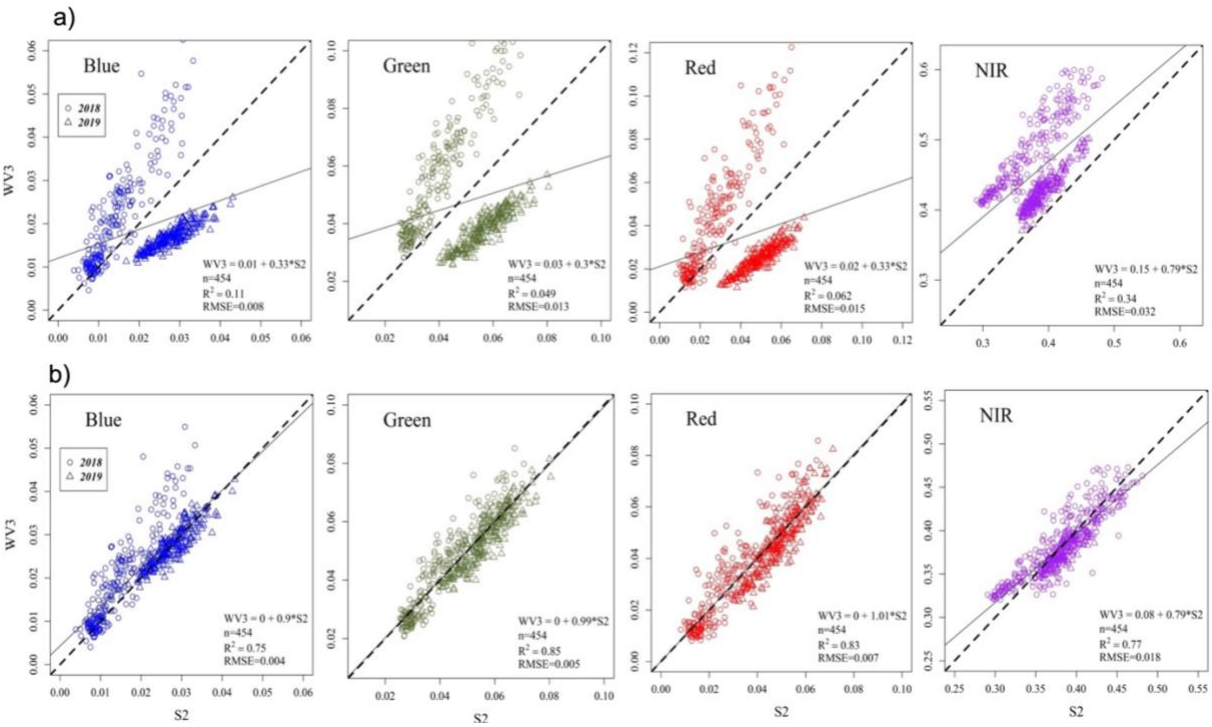

Fig 44. Linear least square regression analysis between Sentinel-2 Level 2A (S2) bands and the corresponding band of WorldView-3 (WV3) a) before and b) after applying the normalization coefficients calculated with the field spectra. Each point represents a pixel of S2 and the mean value of all WV3 pure pixels that lay inside leaving a 1-m buffer in each side of the S2 pixels.

4.5.5 Discussion

The results of this study revealed the utility of using values for atmospheric constituents from ancillary data sources such as the MODIS MCD19A2 and MOD07 atmospheric products for atmospheric corrections of medium and high spatial resolution satellite imagery. This is particularly relevant when working with atmospheric-RTMs such as MODTRAN or FLAASH, which require ancillary input information. These two models performed similarly when working with Sentinel-2 imagery, as the derived surface reflectance that differed less than 0.024 and 0.01 for the visible and NIR bands, respectively. The derived surface reflectance also showed good agreement with the ground-truth spectra (Table 14). Likewise, Sentinel-2 products corrected with Sen2Cor, either with default values (S2L2A) or with MODIS-retrieved atmospheric constituent values (S2L2A_O3V), were similar, with a difference in the corresponding surface reflectance values lower than 0.02 in all bands. This holds when Sentinel-2 and MODIS have near coincident time overpasses. The importance of acquiring reliable values of O_3 atmospheric concentrations, WVC and, especially visibility,

was demonstrated with the sensitivity analysis where it was observed how surface reflectance is affected by these constituents (Liang and Wang, 2019). This analysis verified that the visible region was the most sensitive to atmospheric conditions, since shorter wavelengths are more affected by both Rayleigh scattering by gases (Irwin, 1996), and Mie scattering by aerosols, both of which have a combined impact on visibility (Fig 42). Alternatively, as suggested in Wilson et al. (2015), the Koshmieder formula relating AOT with horizontal visibility might also be tested in future atmospheric correction assessment.

After atmospherically correcting WorldView-3, a difficulty was encountered, i.e., significant differences between the derived surface reflectance and ground-truth spectra were found. The magnitude and sign differed depending on the vegetation type, wavelength, and Sun-surface-sensor geometry. As pointed out in Breuniga et al. (2015) and in Roy et al. (2017), the backscatter direction might be affected by the predominance of sunlit surfaces and exhibit higher surface reflectance than nadir acquisition, as opposed to lower surface reflectance values derived from forward scattering view angles due to a shadow-hiding effect. Differences with nadir acquisition are expected to be more prominent in backscattering than in the forward scattering situation. In 2018, WorldView-3 products were acquired with satellite and Sun azimuth angles of 141.2º and 155.2º, respectively, which correspond to a backscatter situation. This can explain why in 2018, WorldView-3-derived surface reflectance was overestimated in the visible and NIR regions. In contrast, for the 2019 WorldView-3 imagery, satellite and Sun azimuth angles were opposite, with respective angles of 345º and 163.6º. The nearly opposite azimuth directions of the sensor and Sun, means that forward scattering was dominating the surface scattering response observed by the sensor. This forward scattering was probably responsible for the correspondingly underestimated reflectance in the visible regions, as reported by Pacifici et al. (2014) and consequently must be corrected (Cross et al., 2018). The surface reflectance overestimation found in the WorldView-3 NIR band in the backscattering and forward scattering situation is in agreement with other studies that analyzed surface reflectance in winter wheat under different viewing and illumination geometries (He et al., 2016; Roosjen et al., 2016; Chen et al., 2018; He et al., 2019a). These studies indicated that the maximum soil signal acquired by the sensor is at nadir, and it is reduced when the view zenith angle rises, increasing the plant signal and, consequently, the NIR reflectance (Dorigo et al., 2012; Kuester and Spengler, 2018). According to Breunig et al. (2011), anisotropic effects increase from closed to sparse canopies, explaining why in this study the differences with the ground-truth data were greater

in SV than in DV plots. Consequently, off-nadir imagery could lead to inaccurate vegetation index derivation, such as NDVI (Verrelst et al., 2008; Breuniga et al., 2015). In this study the two BRDF correction methods tested (RPV and c-factor) were not capable of compensating for the angular component of the WorldView-3 imagery. Methods such as the RPV or Walthall model were previously applied for correcting the BRDF effects in high spatial resolution datasets, but required an elevated number of multi-view observations (Walthall et al., 1985; Koukal et al., 2014; Liu et al., 2019a). The coefficients required for the c-factor approach were successfully retrieved from low spatial resolution datasets such as MODIS, POLDER (POLarization and Directionality of the Earth's Reflectances) or MISR EOS (Multi-angle Imaging SpectroRadiometer) (Jin et al., 2002; Su et al., 2009; Roy et al., 2017) and implemented in medium-resolution imagery such as Landsat 7 Enhanced Thematic Mapper (ETM+), Landsat 8 Operational Land Imager (OLI) or Sentinel-2 MultiSpectral Imager (MSI) products (Roy et al., 2008; 2017; Franch et al., 2019). According to Roberts (2001), the BRDF effects are dependent on the physical properties of the land use. In MCD43A1 products with 500-m spatial resolution, different land use types are contained within one resolution cell (Fig 7) and therefore their individual anisotropic properties are not properly represented. This explains why the approaches tested in our study (RPV model and c-factor approach) were unable to compensate for the WorldView-3 angular components or the BRDF effects (Zhang and Roy, 2016).

In most cases, the NIR bands of Sentinel-2 (B8 and B8A) exhibited no differences with ground-truth spectra when the images were atmospherically corrected (Table 13). Despite the high variability along the red edge region and its low spatial resolution, the red edge band B6 did not present differences with the ground truth. The empirical normalization procedure of atmospherically corrected WorldView-3 surface reflectance demonstrated good agreement between Sentinel-2 and the normalized WorldView-3. Some displacement from the 1:1 line observed in the NIR bands can be attributed to the slight differences in band centers and spectral response functions (Fig 14). The displacement in the blue bands for the 2018 dataset was probably caused by the difference in time acquisitions, because this displacement was not observed in the 2019 dataset. Therefore, the empirical approach showed the possibility of reducing the angular component dependency in WorldView-3 imagery and coupling information from Sentinel-2 and WorldView-3. The limitation of this approach is that it is highly dependent on temporal and Sun-surface-sensor geometry, and so calibration coefficients should not be extrapolated to other images or land use. The empirical approach

should be tested in other space- or air-borne sensors with different spatial and temporal resolutions. Nevertheless, adaptation of mechanistic methods to correct the angular component in high-resolution satellite imagery deserves complementary investigation in future studies.

Chapter 4.6:
Drought impact on cropland use monitored through multiple endmember spectral mixture analysis using AVIRIS imagery

4.6.1 Specific objectives and application of methods

This Chapter follows the analysis described in Chapter 3.5.4 to validate the use of remote sensing application to regional scale. For this purpose, this Chapter fulfill the **Objective 5:** validate the application of remote sensing imagery for landscape planning at regional scale.

a) assess the reliability of the AVIRIS imagery processed with multiple endmember spectral mixture analysis (MESMA) for cropland use change monitoring by comparing it with official crop reports.

b) determine the agricultural trends and quantify the non-cultivated areas during a multi-year drought period and post-drought period in Central Valley, California.

During 2012 – 2016 California experienced one of the longest and most severe historical droughts it has experienced in the last centuries (Griffin and Anchukaitis, 2014; Warter et al., 2021). The reduction in precipitation and record low snowpack (Sierra Nevada snowpack provides 30% of the California water supply), together with increased temperature, led to a reduction in water storage that did not satisfy the water demands (Belmecheri et al., 2015; Faunt and Sneed, 2015; Hanak et al., 2015; Warter et al., 2021). The agriculture in Central Valley relies on groundwater for irrigation, especially in dry years, causing groundwater level to decline (MacEwan et al., 2017; Liu et al., 2019b; Vasco et al., 2022). At the beginning of the exceptional drought period, two-thirds of surface water was replaced by groundwater pumping, which increased the pumping economic costs by 75% due to a lower elevation of the groundwater level (Howitt et al., 2015; MacEwan et al., 2017). This critical situation led to the state to declare a drought emergency from January 2014 to April 2017 (Office of Governor Edmund G. Brown Jr. 2014; Tortajada et al., 2017). Some of the strategies that farmers followed to reduce economic losses during drought periods were to fallow annual crops, reduce irrigation rates, implement more efficient irrigation systems, plant new orchards, and/or prioritize higher-value crops (Tindula et al., 2013; Sanchez, 2017; Tortajada et al., 2017).

This Chapter analyzes the agricultural trends during 2013 – 2018 in the Central Valley to validate the use of AVIRIS imagery processed with the MESMA approach for crop land use change monitoring at regional scale (Fig 45). Special interest is the identification of non-cultivated areas with remote sensing systems because official crop reports do not provide this

information, and it is important for guiding landscape planning. For this purpose, first, the official crop reports were used to determine the crop land area covered by GV and NPV in June (the peak growth of the summer crops) each year. Second, this information was compared with the GV, NPV and soil area obtained when applying the MESMA approach to the AVIRIS imagery. The agreement between both datasets would support the use of the upcoming NASA SBG mission for crop land use change monitoring.

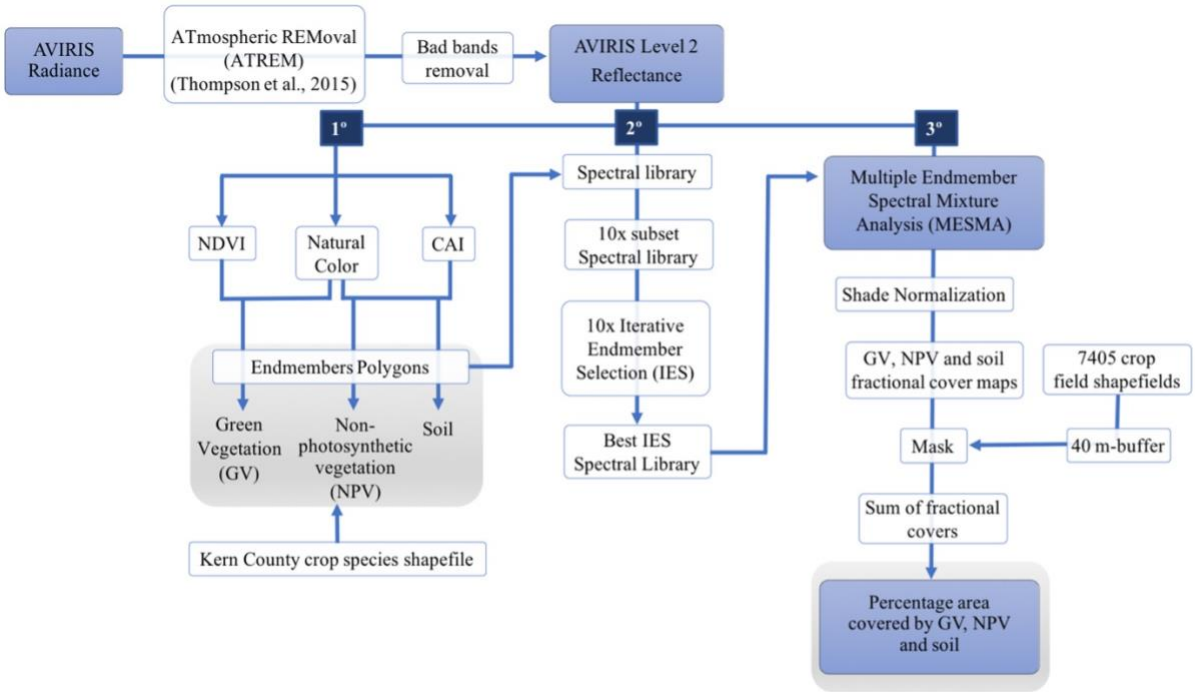

Fig 45. Flow chart showing the process of the AVIRIS imagery to obtain the percentage area of green vegetation (GV), non-photosynthetic vegetation (NPV) and soil within the crop fields of the study area. NDVI refers to the normalized difference vegetation index, and CAI to the cellulose absorption index.

4.6.2 Environmental data and crop reports

According to the United State Drought Monitor (2022a), the drought started in December 2011 and affected all areas in Kern, Kings and Tulare counties (Fig 46). Between 2000 and 2020, exceptional drought intensity was registered only from 2014 to 2017 in the three counties. Approximately 15% of Kern, and 20% of Kings and Tulare counties, were under exceptional drought conditions between January 2014 and January 2017. In addition, ~20% of the area was under extreme drought conditions in the same period. Lower drought intensity

was registered in 2017, as no drought was registered in Tulare County, and only 16% of Kings, and 39% of Kern County was under an abnormally dry climate, and 3.5% of Kern experienced moderate drought conditions. Between February and March 2018, approximately 30% of Kern and Kings, and 20% of Tulare County were under severe drought conditions, and between 35 and 40% were under a moderate drought. The rest of the 2018 year, between 15 and 50% of the area in the counties were under moderate drought, and the remaining area as abnormally dry.

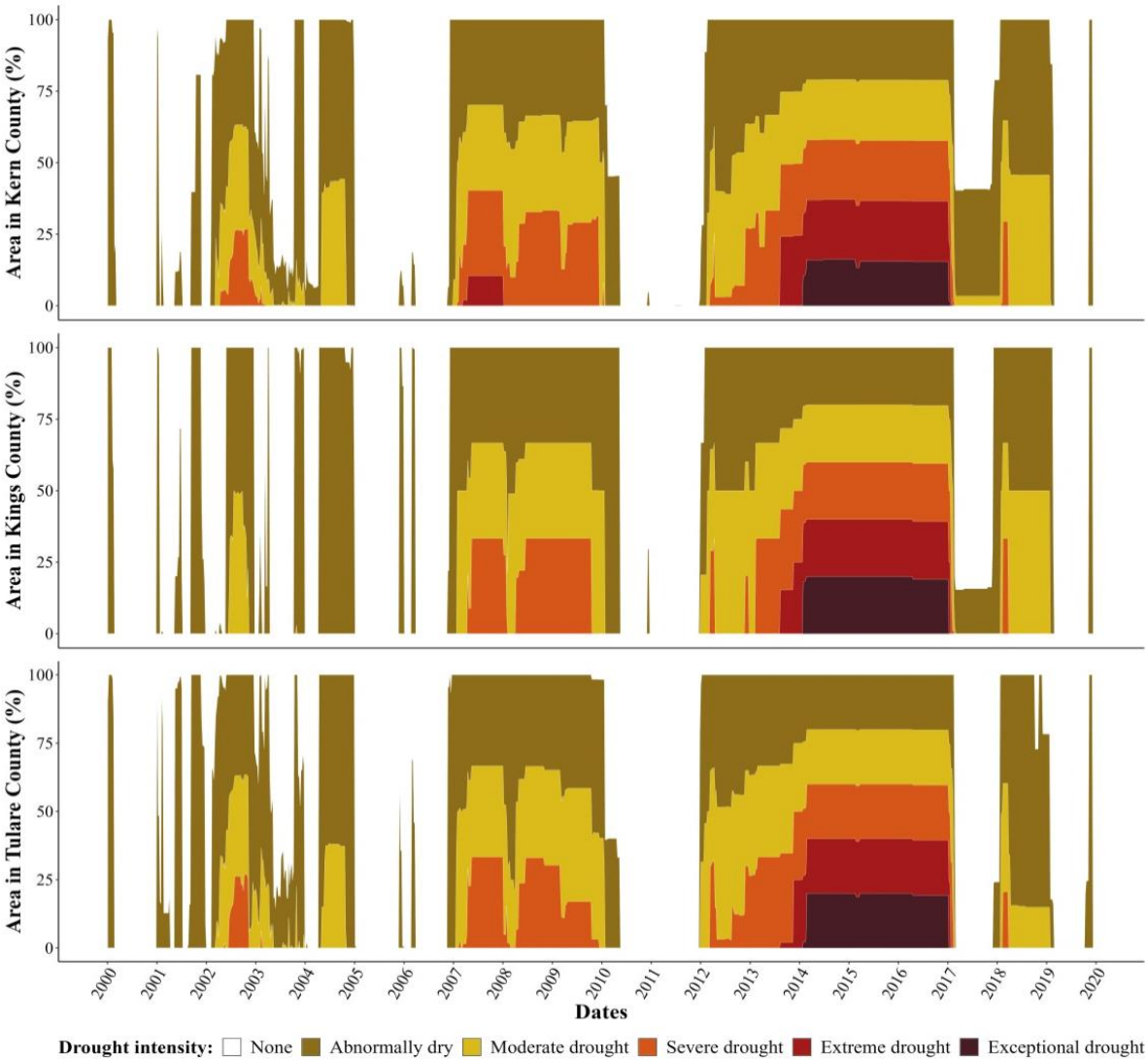

Fig 46. Time series of the percentage area of Kern, Kings and Tulare counties affected by the different drought severity levels. Plot created from information available at the United States Drought Monitor (2022a).

The impact of the drought was observed in the harvested area of each year, as the sum of the harvested area of crops that are photosynthetically active in June (GV) was the lowest during the exceptional drought period (2014, 2015 and 2016) (Fig 48a). The yearly harvested area separated by species and their physiological status in June is shown in Supplementary Material S7. According to crop reports, the greatest effect of the drought was observed in 2015, as this was the year with the smallest GV harvested area ($69.66 \cdot 10^4$ ha), followed by 2014 ($70.05 \cdot 10^4$ ha). A reduction of $2.20 \cdot 10^4$ ha in the GV harvested area was registered in 2014 with respect to 2013, which was the highest reduction in the studied time period and was coincident with the year of the beginning of the exceptional drought period. Despite the exceptional drought condition, an increase of $1.75 \cdot 10^4$ ha in the GV harvested area was recorded in 2016 with respect to 2015. But the harvested area in 2016 did not reach the values of the years when exceptional drought was not detected (2013, 2017 and 2018). The biggest increase in the GV harvested area occurred in 2017 ($75.19 \cdot 10^4$ ha), the wettest year of the studied period, with a difference of $3.89 \cdot 10^4$ ha with respect to 2016. No exceptional drought conditions were registered in 2018, however, the harvested area was reduced by $1.30 \cdot 10^4$ ha with respect to 2017, probably due to the extreme drought conditions registered in February and March 2018, and the moderate drought registered the following months of 2018. The crop reports showed that the sum of the harvested area of crops that are NPV in June followed a similar pattern as the sum of the GV harvested area in the studied period, but NPV values were between 34 and $39 \cdot 10^4$ ha higher than the GV values (Fig 48b). During the exceptional drought period (2014 – 2016), the NPV area was reduced from $111.23 \cdot 10^4$ ha in 2013 to ~$105 \cdot 10^4$ ha. The maximum NPV harvested area was registered in 2017 ($114.12 \cdot 10^4$ ha), followed by 2018 ($112.18 \cdot 10^4$ ha).

Overall, a continuous increase in orchard harvested area was observed throughout the study period (Fig 48c; Supplementary Material S7), whereas the irrigated pasture area was similar in all years (~$4 \cdot 10^4$ ha; Supplementary Material S7). The increase in orchard harvested area between 2013 and 2018 was $9.05 \cdot 10^4$ ha (i.e., 28% compared to 2013), with half of the increase in orchard area occurring in 2014, the first year that exceptional drought was recorded. The orchard represented 45% of the GV harvested area in 2013 and 56% in 2018. On the other hand, the biggest reduction in summer crops area was experienced in 2014 (Fig 48d; Supplementary Material S7). The summer crops harvested area was $35.54 \cdot 10^4$ ha in 2013, and $28.86 \cdot 10^4$ ha in 2014, which is equivalent to a reduction of 19% in the first year of exceptional drought. The following years the summer crops area was similar, with values

between 27.88 and $30.04 \cdot 10^4$ ha, reaching the maximum in 2017, which indicates that the summer crops harvested area did not return to the values obtained before the exceptional drought period started.

4.6.3 Crop patterns with MESMA

The MESMA results showed that the AVIRIS imagery captured changes in the cropland use during the 2013 – 2018 period (Fig 47). The sum of the GV fractional covers within the croplands obtained from MESMA (Fig 49a) followed a similar trend as the sum of the GV harvested area obtained from the crop reports (Fig 48a). Both analyses indicated that the years with the lowest GV area in June were those with exceptional drought (2014 – 2016). According to MESMA, the year with the smallest GV area was 2015 (the sum of the GV fractions in croplands normalized by the total area was 34%), and the year with the highest GV area was 2017 (54%). The MESMA results also indicated that the increase in cropland GV area began in 2016, reaching its highest value in 2017, before experiencing a small reduction in 2018, also in a good agreement with the data from the crop reports.

The MESMA results showed that the cropland soil area steadily increased during the exceptional drought period since 2013 (38%), until reaching the maximum value in 2015 (48%), which was similar to the soil area in 2016 (47%) (Fig 49b). After 2016, the cropland soil area decreased each year, equalling 37% in 2017 and 24% in 2018. Therefore, MESMA results showed that 2015 was the year with the lowest cropland GV and the highest soil in June (Fig 47 and Fig 49). The images acquired in 2015 and 2018 showed that the soil area decreased after the exceptional drought period by 50% with respect to 2015.

The MESMA results were able to explain 90% of the variability observed in the GV total harvested area obtained from the crop reports (Fig 50a). Significant and inverse correlation (R^2 = 0.57; data not shown) was obtained between the total GV harvested area of the crop reports and the soil area obtained with MESMA. This correlation was enhanced when the NPV area of the crop reports was added to the GV (R^2 = 0.60; Fig 50b). Indeed, the longest distance from the regression line was obtained in 2017, when soil was overestimated by MESMA, and in 2014, when soil was underestimated (Fig 50b). No correlation was found between NPV from crop reports and from MESMA; several reasons behind the disagreement of both dataset in NPV values are given in the discussion section.

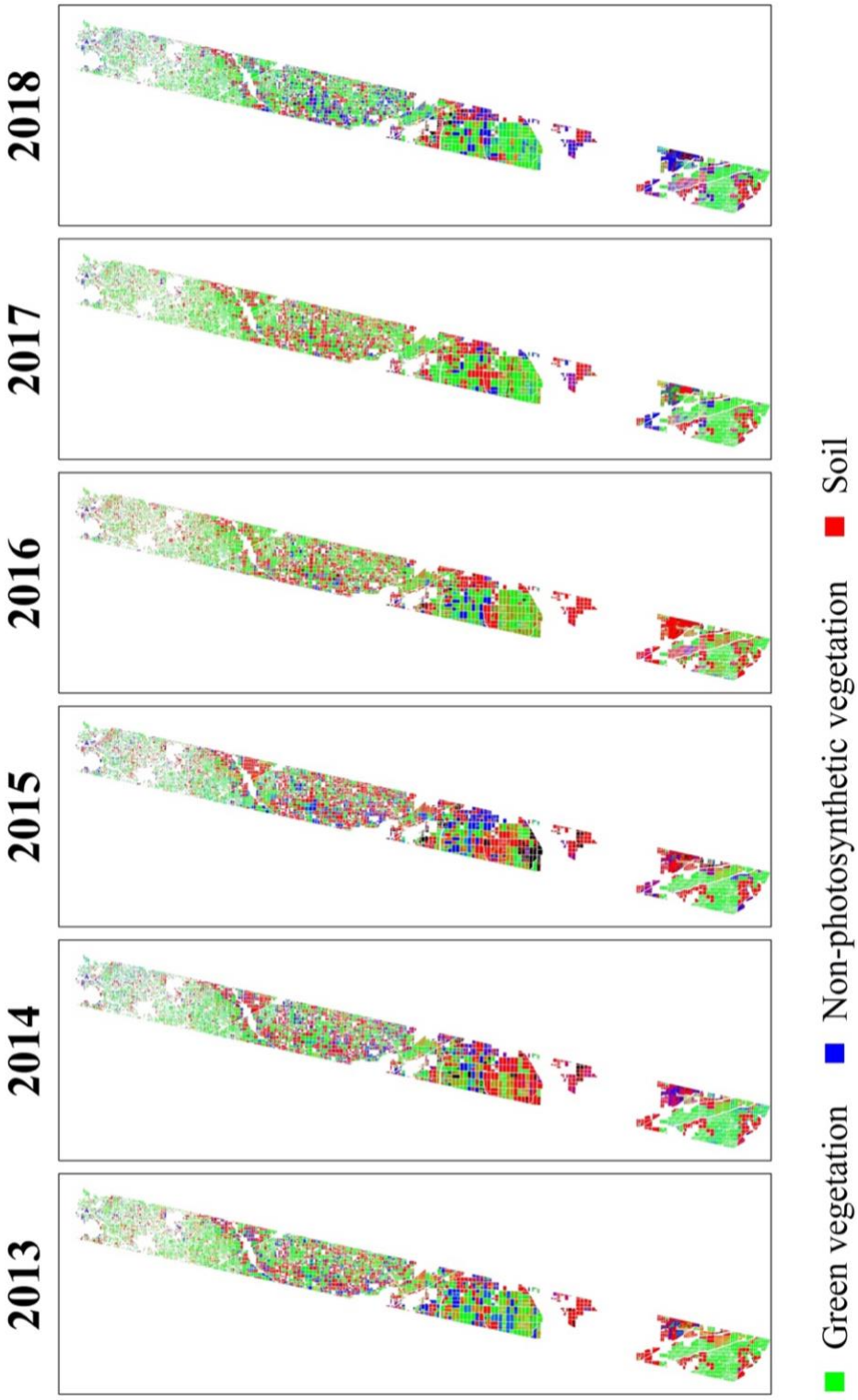

Fig 47. Results from running multiple endmember spectral mixture analysis (MESMA) with the AVIRIS imagery showing the fractional covers of green vegetation (green), non-photosynthetic vegetation (blue) and soil (red) in the cropland of the study area each year in June. The black pixels indicate areas that were not modeled with any of the endmember classes.

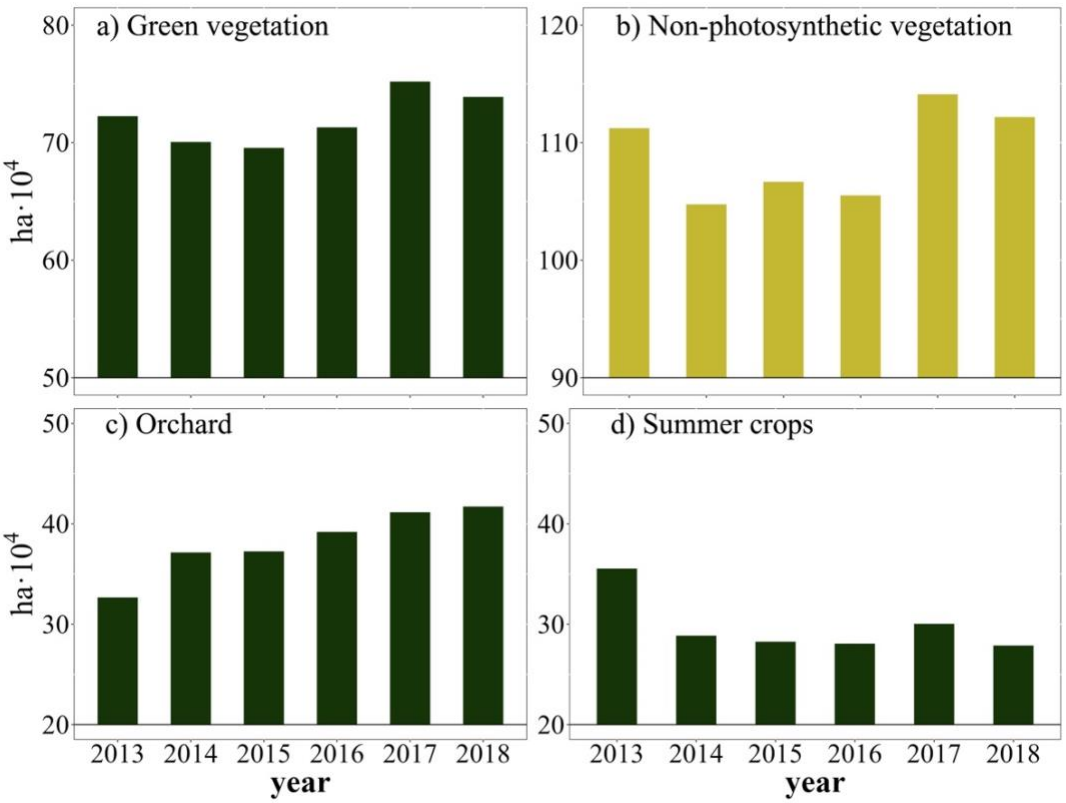

Fig 48. Total harvested area of the crops that are a) green vegetation in June (summer crops, orchards and irrigated pasture), b) non-photosynthetic vegetation in June, c) orchards, and d) summer crops in Kings, Kern and Tulare counties during the 2013 – 2018 period according to the counties crop reports.

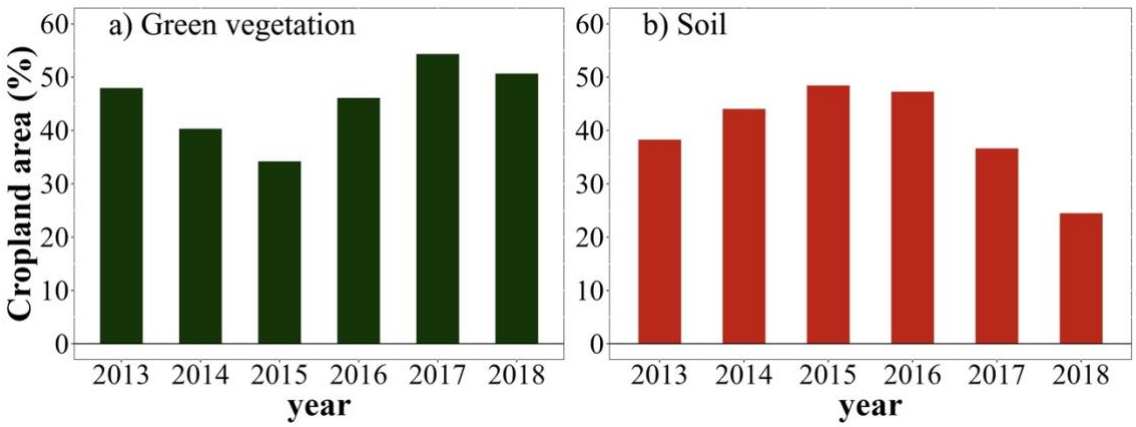

Fig 49. Percentage area within the croplands of the study area covered by a) green vegetation and b) soil extracted from the multiple endmember spectral mixture analysis (MESMA) results using AVIRIS imagery collected in June each year.

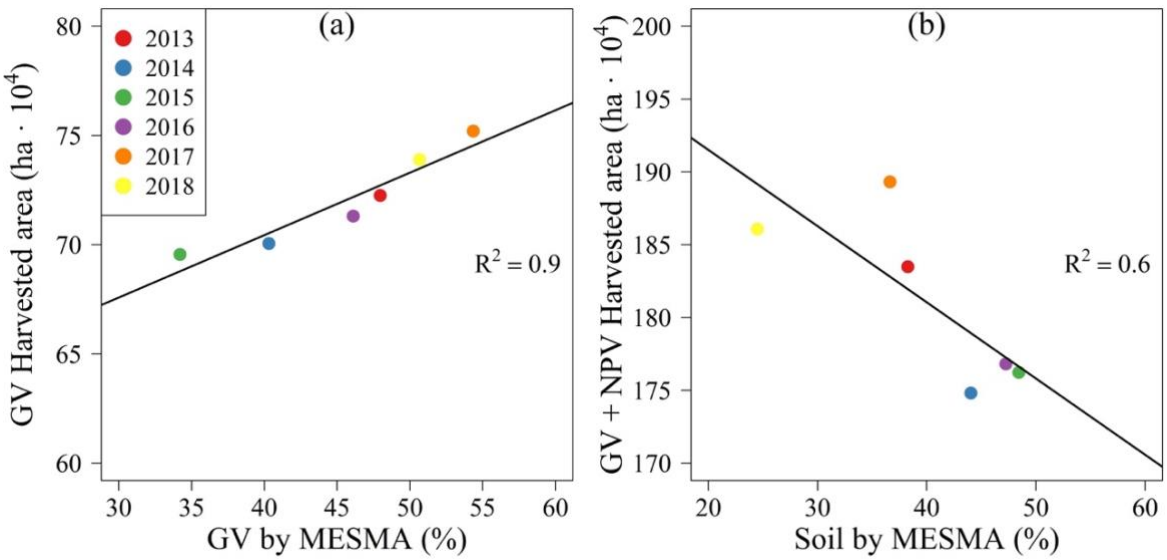

Fig 50. Pairwise relationship between data calculated with the endmember spectral mixture analysis (MESMA) using AVIRIS imagery and obtained from the crop reports in Kings, Kern and Tulare counties during the 2013-2018 period, for a) green vegetation (GV) and GV harvested area, and b) soil and GV plus non-photosynthetic vegetation (NPV) harvested area. The solid line represents the lineal relationship between variables and R^2 is the coefficient of determination.

4.6.4 Discussion

- Cropland use patterns during the 2013 – 2018 period

High accuracy was obtained in this study when MESMA was applied to the AVIRIS imagery to monitor cropland use changes at regional scale. Similarly, Tane et al. (2018a) and Miller et al. (2022) succeed when applying the same methodology for monitoring vegetation changes through time. In this study, the MESMA results and the crop reports described similar trends in cropland use during the exceptional drought period and the post-drought period. During the exceptional drought (2014 – 2016) the cultivated area was the lowest in the study period (2013 – 2018); after the exceptional drought ended it increased, reaching values higher than in 2013. This result agrees with analyses of the drought impact reported by Tortajada et al. (2017) and Lund et al. (2018). The MESMA results also showed an increase in the soil area during the exceptional drought period. According to FAO (2023b), agricultural areas that are uncultivated for less than five years are considered as temporally fallow, rather than

abandoned. Therefore, the current study confirms that fallowing crops was a strategy followed by the farmers during the drought period, and that it can be identified with AVIRIS imagery. This demonstrates that hyperspectral sensors such AVIRIS could be an alternative to combining optical and radar sensors that have already shown great potential for the identification of abandoned land in Central and Eastern Europe (Goga et al., 2019). The crop reports do not offer specific information about the non-cultivated area, for this reason, information derived from remote sensing data can be a useful tool for guiding management decisions related to non-cultivated fields (Milenov et al., 2014). Even more accurate results could be obtained by using several images collected at different dates during the same year (Meerdink et al., 2019).

The crop reports also showed that another strategy followed by the farmers was to switch summer crops into orchard, as reported by Sanchez (2017); Nishikawa et al. (2016) and Alam et al. (2019). The current study showed that in the first year of the exceptional drought period there was an important reduction in summer crop harvested area and an increase in orchards area. Among the orchards, almonds represented >25 % of the area, and the crop reports showed an increase in ~50% of the almond area between 2013 and 2018. This result agrees with Tortajada et al. (2017) and Shivers et al. (2018). California farmers decided to divert the water from less profitable crops to almond trees due to their high economic value (Nishikawa et al., 2016; Alam et al., 2019). The water consumption of almond trees in California has become a controversial topic because almonds can be grown under mild water stress with a reasonable economic profit, whereas additional water applications show low water use efficiency and have been considered excessive (Goldhamer and Fereres, 2017; Gutiérrez-Gordillo et al., 2020; University of California Division of Agriculture and Natural Resources, 2022). Shivers et al. (2019) used paired AVIRIS and thermal imagery to show that nut trees suffered less from water stress than other fruit trees during the California drought period. Future studies with access to ground-reference data should test the ability of remote sensing technology to monitor changes in orchard area during a drought period. The ability of AVIRIS imagery to map plant species distribution was demonstrated by Meerdink et al. (2019) using ground-reference data, however, lower accuracy was obtained in sparse canopies due to contamination by understory species or soils, and the effect of the multiple photon scattering between different land use classes (Somers et al., 2009).

- Performance of hyperspectral imaging when monitoring cropland use

MESMA results were able to adequately assess changes in GV and soil areas. The good performance of the GV assessment (R^2 = 0.90) was attributed to the spectral properties of the photosynthetically active vegetation, clearly different in the visible, SWIR and in the NIR regions from NPV and soil (Dennison et al., 2019; Fig 1). However, spectral distinction between NPV and soil is more complicated, as it relies on specific absorption features of lignin, cellulose and other organic molecules located in the SWIR region (Daughtry, 2001) and is affected by confounded factors such as moisture content (Quemada and Daughtry, 2016). In addition, soil spectra do not have a characteristic absorption feature, and they vary with soil type and color, therefore, soil spatial variability may be a source of uncertainty when mapping land-cover uses (Somers et al., 2011). MESMA has advantages over other classification methods because it uses the entire spectra and allows varying the spectra used in the classification across the image in a per-pixel basin; therefore, it allows broad-scale fractional cover mapping (Roberts et al., 1998).

Due to the inverse correlation between the area covered by GV + NPV observed in the crop reports and the soil area obtained from the MESMA results (R^2 = 0.60), this study validates the use of AVIRIS imagery processed with MESMA approach for quantifying non-cultivated fields. However, some uncertainties could have reduced the accuracy of the assessment:

-When calculating the NPV area with the crop reports, it was considered that all crop fields kept plant residues on the soil. However, there is a variety of tillage management practice that farmers follow in the Central Valley (Mitchel et al., 2016). Therefore, the crop fields where the residue was removed were considered as NPV area in the crop reports and marked as soil in MESMA results. This would lead to a higher estimate of the soil area or non-cultivated fields by MESMA and a lower estimation of NPV area.

-Some crop rotations, such winter cereal-summer crop, are marked as GV in MESMA results, while the area of the winter cereal (NPV) was not considered by MESMA, but it was included when calculating the NPV harvested area with the crop reports.

-The physiological development of the crops can be another source of uncertainty because it varies between years due to the environmental conditions and management

practices (Yang et al., 2004). Therefore, the GV and NPV area observed in the same crop species by MESMA can vary between years.

-Under water scarcity regimes, crops accumulate lower amount of biomass, exposing more soil background to the sensor (Tilling et al., 2007). For this reason, MESMA could produce a higher soil area estimate during the dry years and lower GV area than crop reports that would consider an entire crop field as GV.

-When monitoring orchards, the stems and woody tissues of the crown trees that are exposed to the sensor can lead to a higher estimate of NPV area and lower of GV by MESMA (Asner, 1998).

-The shadow captured by the sensor in orchards is expected to reduce the accuracy due to an overall reduction in reflectance, being this effect more noticeable in old-tree formation (Clark et al., 2005).

-The row spacing in orchards can also reduce the model accuracy (Meerdink et al., 2019) because it can be covered by soil, senesced vegetation or understory species but considered as GV harvested area by the crop reports. In the case the row space is covered by soil or senesced vegetation, it would reduce the GV area captured by MESMA and increase soil or NPV area, which would increase the disagreement with the crop reports. New orchards have more sparse canopies and more space between crowns than older, well-established orchards. For this reason, lower estimates of GV areas by MESMA are expected to be common in new orchards. Due to the increase in new orchards during the beginning of the drought, this effect was more evident in 2014, 2015 and 2016, and therefore, it could contribute to the reduction in GV area and the increase in soil area observed in the MESMA results during the drought.

Due to the specific absorption feature needed to distinguish between NPV and soil, narrow-bands sensors covering the SWIR region are needed for this purpose (Daughtry and Hunt, 2008; Hively et al., 2019). The current results demonstrate the potential of AVIRIS and the upcoming NASA SBG mission to monitor the cropland use change and field abandonment as consequence of the drought at regional scale.

Chapter 5: General discussion

This thesis validated the use of remote sensing data for retrieving crop parameters that can be used to inform management decisions and improve the sustainability of the agricultural systems. Remote sensing information showed potential for field-scale monitoring by assessing the spatial variability of the crop status to adjust water and N rates and to predict harvest parameters. At regional scale, remote sensing techniques allowed assessing crop land use changes and non-cultivated fields to support landscape planning decisions. This thesis proposed and validated different remote sensing modeling approaches to improve the accuracy in crop monitoring.

The results showed that estimating crop status and traits requires considering different crop parameters that can be estimated with remote sensing techniques. For site-specific adjustment of N application according to winter wheat demand, it is required to correctly estimate the crop N status at early GSs, when the first N fertilization is usually applied. The critical %N required for an optimal N status, changes with biomass development, so remote sensing estimation of crop N status must consider both crop parameters (Mistele and Schmidhalter, 2008). To enhance N use efficiency, the water status must be considered before fertilization because the N should be applied in areas where N is a limiting factor and the crop has enough water available to ensure N take up (Zillman et al., 2006; Quemada and Gabriel, 2016). The final winter wheat yield is highly related to biomass (Marti et al., 2007); however, adequate values of biomass under no correct management practices can produce a yield reduction, for example, due to lodging (Berry et al., 2004). Therefore, an accurate yield prediction should consider different crop parameters (Tang et al., 2022). In winter wheat, the N content in leaves and structural organs before flowering that is translocated to the grain will determine the GPC (Kichey et al., 2007). The effectiveness of N translocation to fill the grain is dependent on different factors, such as the water availability (Zhao et al., 2005; Diacono et al., 2013).

The results indicated that the accuracy when estimating some crop parameters with remote sensing can be limited due to the sensor or platform characteristics. In this aspect, acquisitions of crop fields with sensors that have broad spatial resolution can capture an unknown portion of green vegetation, non-photosynthetic vegetation and soil background area within a single pixel that hampers to identify the individual contribution of each

component to the spectral or thermal measurement (Tilling et al., 2007). In addition, the response of the spectral radiation reflected from some plant components such as protein, lignin or cellulose is only found in a small number of narrow wavelengths located in the SWIR region (Curran et al., 1989; Daughtry et al., 2001). For this reason, multispectral sensors with low spectral resolution or sensors that only cover the VNIR region can be limited when estimating some crop components. The viewing and illumination angles are also an important issue that must be addressed because it may lead to strong spectral differences due to BRDF effects that can produce variations in the relative amount of spectral radiation reflected from the soil background or from the vegetation when compared to nadir-looking acquired spectra that should be corrected (Pacifici et al., 2014; Cross et al., 2018). When using spaceborne sensors, in addition to the disturbances due to the angular effect, the spectral radiation reflected from the surface that is finally received by the sensor is highly affected by the atmospheric constituents (Liang and Wang, 2009). Furthermore, the view angle must be considered during the atmospheric correction because the off-nadir view angles lengthen the atmospheric paths of the upwelling radiance signal acquired by the sensor. The atmospheric conditions are continuously changing, and therefore the atmospheric constituents should be measured at the time of the satellite acquisition to perform a correct compensation (Pacifici et al., 2014; Wilson et al., 2015).

This thesis confirmed that the combination of remote sensing indicators related to different crop parameters can improve crop monitoring and management decisions. The confounding effect of crop N and water status in the spectral reflectance was evident, and the results highlighted the difficulty of using only reflectance-based VIs to discriminate between N and water stress. It was observed that the value of most VIs decreased when the crop suffered from N or water stress, making it difficult to identify the stress suffered by the crop using only VIs. This limitation was overcome by combining spectral reflectance with canopy thermal information to simultaneously estimate crop N and water status to adjust N fertilization and irrigation to crop requirements. The reliability of the temperature-based indicator WDI (Moran et al., 1994) in estimating water status was demonstrated because the WDI was correlated with the leaf stomatal conductance and showed robustness in detecting the water levels while reducing the influence of the N levels. The convenience of compensating by the soil background noise using a spectral VI related to ground cover was observed in the better performance of WDI than Tc-Ta. The best VI to assess crop N status and to adjust fertilizer rates was the CCCI (Barnes et al., 2000), which presented a significant

relationship with the NNI in all cases, even at early GS when the CCCI compensated for the soil background noise. The good performance of the CCCI was demonstrated with the measurements collected with the FieldSpec at ground level and with the airborne VNIR sensor at 300 m above the canopy. The CCCI distinguished between the N fertilization levels and was only slightly affected by the crop water status. The effect of water status on the CCCI was mitigated when it was combined with the WDI to provide a robust spectral-thermal indicator (*f*(CCCI, WDI)) that identified N levels regardless of the water regime. Therefore, this thesis demonstrates that simultaneous analysis of CCCI and WDI data derived from remote sensing technology can greatly contribute to site-specific adjustment of N fertilization and irrigation and reduce the environmental impact of agricultural systems.

Similarly, it was found that combining information from different remote sensing indicators related to crop parameters that affect traits improved the traits prediction with multispectral or hyperspectral sensors. Of the three wheat traits evaluated, yield obtained the most accurate estimation, and presented similar results when the indices were retrieved with a hyperspectral sensor or with the multispectral Sentinel-2 bands. Both sensors obtained satisfactory results when SWIR information was included in the GPC prediction. However, an important improvement was obtained with the hyperspectral sensor due to the narrow absorption peak of protein in the SWIR region (Camino et al., 2018). The red edge and SWIR-based indices were important for improving N output prediction with both sensors. Although a more accurate prediction was achieved with the hyperspectral bands, the potential of using the open-access multispectral Sentinel-2 images for wheat trait prediction at field level or at large scales is high.

We can conclude that accurate crop monitoring with remote sensing techniques relies on the correct quantification of the crop parameters that are contained within a pixel or FOV of the sensor. The parameters retrieved can be combined accordingly to the goal, in this case to estimate crop status or to predict harvest. In addition, this thesis validated the application of the hybrid artificial neural network-PROSAIL-PRO and MESMA models to quantify the crop parameters and land cover classes that are contained within a pixel by analyzing all available bands. The main difference is that the hybrid method estimates the plant biochemical and physical parameters and MESMA assesses the fractional cover of the land classes contained in each pixel. Both approaches model the target reflectance spectrum using a reference spectra database called LUT in the hybrid method and spectral library in

MESMA. In this study, the LUT consisted on several spectra simulated with PROSAIL-PRO where each spectrum represents a different combination of crop parameters. The spectral library used by MESMA was constructed with spectra extracted from in-scene pure pixels that completely belong to a single land cover class (endmembers), and therefore, it was not simulated. The spectral library can be constructed with endmembers from images collected on different days, but it is recommended to use the same image that will be analyzed (Meerdink et al., 2019). After this, the IES method was applied to the spectral library to select the most optimal and representative endmembers of each class to be used in the model (Roth et al., 2012). To select the optimal and most representative spectra of the LUT, this thesis tested for the first time a method that used the observed spectra to remove the spectra of the LUT that are substantially different and therefore, represent a set of crop parameters that do not correspond to the observed data. To identify the fractional covers that build the spectrum, MESMA uses a linear mixture model to decompose the spectrum into its fractional components by finding the combination of fractional covers and land classes that produces the lowest RMSE (Shivers et al., 2019). The hybrid method used in this thesis trained an ANN regressor model with the LUT to identify the spectrum of the LUT most similar to the observed spectrum to assess its crop parameters. The main difference in this process is that MESMA tested different combinations of fractional covers that were not previously established, while the hybrid method requires calibrating the model with previous knowledge of the specific characteristic of the crop to establish the range of the crop parameters (Sinha et al., 2020; Camino et al., 2022). The contribution of each crop component to the reflectance spectrum in PROSAIL-PRO was previously established when the model was developed (Féret et al., 2008). This implies that the contributions used by the model do not change between crops with different leaves or canopy structures. Danner et al., 2021 reported good results of the hybrid method for regional-scale monitoring, however the results were sensitive to the crop type. On the other hand, the MESMA approach requires analyzing the image to select pure pixels of each land cover class (Somers et al., 2011), which is one of the most critical steps when applying MESMA. To avoid this, the spectral library used in MESMA can be constructed with spectra simulated with RTMs (Sonnentag et al., 2007). Reducing soil noise in the hybrid method is important to reduce uncertainties in the crop parameters estimation (Camino et al., 2022). This information could be included in the hybrid method using the MESMA results providing the fractional covers that affect the reflectance spectrum. Therefore, future research should test the performance when combining the results from the hybrid and MESMA methods. If the hybrid method is not available, it should be tested the

performance in crop N status monitoring using CCCI but changing the NDVI by the fractional covers of green vegetation (or the inverse of soil background) provided by MESMA. Similarly, the OSAVI can be changed by the MESMA fractional covers when calculating the WDI.

Regarding the transferability capacities of the methods, both models can reduce the background soil noise by using the soil spectra collected from the image and allow compensating for the viewing and illumination angles, which are critical issues that can limit the transferability capacities. The use of in-scene soil spectral data increases the transferability capacities of both methods because soil reflectance can change between locations or dates due to environmental conditions (Somers et al., 2011; Quemada et al., 2018). As observed in this thesis, the angular components was a source of error in WorldView-3 acquisitions. Considering the soil spectra allowed the hybrid method in this thesis to remove soil background noise at early GSs to obtain accurate crop parameters estimation, and the MESMA method to calculate the variations in soil area within the crop fields in different years. The capacity of PROSAIL-PRO to vary the illumination and viewing angles when generating the LUT increases the transferability capacities of the hybrid method (He et al., 2018; 2019b). In the MESMA model, the use of in-scene endmembers allows reducing the induced angular effect. Additionally, to solve illumination issues, the MESMA model embedded in Viper Tools 2.1 includes a shadow normalization process (Dennison and Roberts, 2003; Roberts et al., 2019).

This thesis showed that including PROSAIL-PRO in the hybrid method applied to the multispectral Sentinel-2 imagery allows retrieving several crop parameters that affect the crop N status and final traits. Future versions of the hybrid method should provide crop N status estimation and traits prediction based on the reflectance spectrum. To provide accurate crop status estimation and traits prediction, it is required to train the model with on-ground crop measurements linked to spectral information (Danner et al., 2021). Satellite missions, such as Sentinel-2 with near-global coverage, have the capacity to provide a large number of spectral measurements to calibrate and validate the models. Before assessing crop parameters with satellite data, it is required to measure and remove external disturbances that affect the reflectance spectrum, such as the atmospheric constituents (Pacifici et al., 2014). The atmospherically corrected Sentinel-2 surface reflectance showed good agreement with the *in-situ* collected spectral data in all VNIR bands. The Sen2Cor, MODTRAN and FLAASH

atmospheric-RTM performed similarly and demonstrated the reliability of using atmospheric constituent values from scene-based imagery or from ancillary satellite imagery to provide accurate spectral satellite imagery.

As discussed in this thesis, hyperspectral VSWIR acquisitions allow improving crop monitoring by measuring the protein absorbance to predict GPC and N output, and for distinguishing between crop residue and bare soil in crop fields by measuring absorbance of lignin and cellulose. According to Hively et al., 2021, currently there are no satellite missions that collect hyperspectral SWIR information on a global scale. The upcoming satellite missions will provide new opportunities to improve the sustainability of the agricultural systems by acquiring global imagery with hyperspectral SWIR bands, and they will be suited for its application in PROSAIL-PRO (Berger et al., 2018). The CHIME and Landsat next missions will provide global coverage with hyperspectral VSWIR information, and therefore, these sensors will allow crop N status estimation, traits prediction and identification of bare soil and crop residue. The NASA SBG mission, in addition to provide hyperspectral VSWIR bands with the AVIRIS, it will provide thermal imagery, which is of crucial importance for accurate water status estimation. Therefore, as shown in this thesis, this mission will also allow simultaneous assessment of crop N and water status to adjust N fertilization and irrigation according to crop demand. Monitoring plant health and agricultural areas are some of the priorities identified by the SBG mission (Cawse-Nicholson et al., 2021). This thesis validates the potential of the SBG mission to reduce the environmental impact of agricultural systems and to improve food security by monitoring crop land use change, allowing site-specific adjustment of N fertilization and irrigation rates according to crop demand, and by predicting crop yield, grain protein concentration and N output at global scale.

Chapter 6: Conclusions

1. The cofounding effect of crop N and water status in the spectral reflectance was evident. Combining reflectance with thermal information allows adjusting N fertilization and irrigation to crop requirements. Simultaneous analysis of CCCI and WDI derived from remote sensing technology improved site-specific adjustment of N fertilization and irrigation.

2. The CCCI is a robust indicator of the crop N status because it presented significant relationship with the NNI in all cases, even at early crop growth stages when the CCCI compensated for the soil background noise. The CCCI minimized the effect of the water status.

3. The WDI successfully compensated by the soil background effect to improve the assessment of the water status and to reduce the cofounding effect of the N status.

4. The effect of the water status on the CCCI was mitigated when it was combined with the WDI to provide a robust indicator (*f*(CCCI, WDI)) that identified N levels regardless of the water regime.

5. Combining remote sensing indicators related to different crop parameters improved winter wheat traits prediction. Although a more accurate estimation was achieved with hyperspectral bands, the Sentinel-2 multispectral bands have potential for winter wheat traits prediction at large scales.

6. Yield obtained the most accurate prediction, and presented similar results when the indicators were retrieved with a hyperspectral sensor or with the multispectral Sentinel-2 bands. The SWIR region was important for predicting N-related traits with both sensors; however, more accurate prediction of grain protein concentration was achieved with the hyperspectral sensor.

7. The hybrid artificial neural network-PROSAIL-PRO method accurately estimated the chlorophyll content in all growth stages and described the temporal changes.

8. Combining the crop parameters retrieved with the hybrid method improved the N status estimation and the traits prediction compared with the VIs.

9. The atmospherically corrected Sentinel-2 bands showed good agreement with the ground-truth measurements in all visible-NIR bands. The Sen2Cor, MODTRAN and FLAASH atmospheric RTMs performed similarly when working with Sentinel-2 products and demonstrated the reliability of using atmospheric constituent values from scene-based and from ancillary data sources, such as the MODIS atmospheric products when overpassing synchronously to the multispectral sensor.

10. The reflectance acquired by WorldView-3 was different from the ground-truth spectra due to the steep off-nadir acquisition angles. The proposed empirical signal normalization procedure based on nadir spectra acquisition minimized the angular-induced effect and allowed coupling images from different spaceborne sensors.

11. Applying the MESMA approach to AVIRIS data showed potential for crop land use monitoring because the results agreed with the official crop reports. This approach can be used to identify no-cultivated fields, which are not included in the crop reports.

12. Due to the hyperspectral VSWIR bands covered by the AVIRIS sensor and the simultaneous thermal acquisition, the upcoming NASA SBG mission will be a valuable tool to adjust N and irrigation to crop demand, to predict yield, grain protein concentration and N output and to monitor cropland use changes at global scale.

Chapter 7: References

Adak, Sujan, Adak, Sujan, K. K. Bandyopadhyay, R. N. Sahoo, N. Mridha, M. Shrivastava, and T. J. Purakayastha. 2021. "Prediction of Wheat Yield Using Spectral Reflectance Indices under Different Tillage, Residue and Nitrogen Management Practices." Current Science 121(3):402–13. doi: 10.18520/cs/v121/i3/402-413.

Adams, John B., Milton O. Smith, and Paul E. Johnson. 1986. "Spectral Mixture Modeling: A New Analysis of Rock and Soil Types at the Viking Lander 1 Site." Journal of Geophysical Research 91(B10):10513. doi: 10.1029/jb091ib10p10513.

Adler-Golden, Steven M., Michael W. Matthew, Lawrence S. Bernstein, Robert Y. Levine, Alexander Berk, Steven C. Richtsmeier, Prabhat K. Acharya, Gail P. Anderson, Jerry W. Felde, J. A. Gardner, Michael L. Hoke, Laila S. Jeong, Brian Pukall, Anthony J. Ratkowski, and Hsiao-hua K. Burke. 1999. "Atmospheric Correction for Short-Wave Spectral Imagery Based on MODTRAN4." Imaging Spectrometry V 3753: 61–69. doi: 10.1117/12.366315.

AEMET (State Meteorological Agency). 2023. "Dataset of monthly ozone concentration." Retrieved April 9, 2020 (http://www.aemet.es/es/serviciosclimaticos/vigilancia_clima/radiacion_ozono?w=1).

Aguilera, Eduardo, Luis Lassaletta, Alberto Sanz-Cobena, Josette Garnier, and Antonio Vallejo. 2013. "The Potential of Organic Fertilizers and Water Management to Reduce N2O Emissions in Mediterranean Climate Cropping Systems. A Review." Agriculture, Ecosystems and Environment 164:32–52. doi: 10.1016/j.agee.2012.09.006.

Ainsworth, T. L., J. P. Kelly, and J. S. Lee. 2009. "Classification Comparisons between Dual-Pol, Compact Polarimetric and Quad-Pol SAR Imagery." ISPRS Journal of Photogrammetry and Remote Sensing 64(5):464–71. doi: 10.1016/j.isprsjprs.2008.12.008.

Alam, Sarfaraz, Mekonnen Gebremichael, and Ruopu Li. 2019. “Remote Sensing-Based Assessment of the Crop, Energy and Water Nexus in the Central Valley, California.” Remote Sensing 11(14). doi: 10.3390/rs11141701.

Almeida-Ñauñay, Andrés F., Rosa M. Benito, Miguel Quemada, Juan C. Losada, and Ana M. Tarquis. 2022. “Recurrence Plots for Quantifying the Vegetation Indices Dynamics in a Semi-Arid Grassland.” Geoderma 406. doi: 10.1016/j.geoderma.2021.115488.

Angus, J. F., and R. A. Fischer. 1991. “Grain Protein Responses to Nitrogen Applied to Wheat Growing on a Red Earth.” Australian Journal of Agricultural Research 42(5):735–46. doi: 10.1071/AR9910735.

Aranguren, Marta, Ander Castellón, and Ana Aizpurua. 2020. “Crop Sensor Based Non-Destructive Estimation of Nitrogen Nutritional Status, Yield, and Grain Protein Content in Wheat.” Agriculture 10(5). doi: 10.3390/agriculture10050148.

Ariza, Alexander, Marina Robredo Irizar, and Steven Bayer. 2018. “Empirical Line Model for the Atmospheric Correction of Sentinel-2A MSI Images in the Caribbean Islands.” European Journal of Remote Sensing 51(1):765–76. doi: 10.1080/22797254.2018.1482732.

Arregui, L. M., B. Lasa, A. Lafarga, I. Irañeta, E. Baroja, and M. Quemada. 2006. “Evaluation of Chlorophyll Meters as Tools for N Fertilization in Winter Wheat under Humid Mediterranean Conditions.” European Journal of Agronomy 24(2):140–48. doi: 10.1016/j.eja.2005.05.005.

Arregui, L. M., and M. Quemada. 2008. “Strategies to Improve Nitrogen Use Efficiency in Winter Cereal Crops under Rainfed Conditions.” Agronomy Journal 100(2):277–84. doi: 10.2134/agronj2007.0187.

Asner, Gregory P. 1998. “Biophysical and Biochemical Sources of Variability in Canopy Reflectance.” Remote Sensing of Environment 64(3):234–53. doi: 10.1016/S0034-4257(98)00014-5.

Atzberger, Clement, Martine Guérif, Frédéric Baret, and Willy Werner. 2010. “Comparative Analysis of Three Chemometric Techniques for the Spectroradiometric Assessment of

Canopy Chlorophyll Content in Winter Wheat." Computers and Electronics in Agriculture 73(2):165–73. doi: 10.1016/j.compag.2010.05.006.

Atzberger, Clement, Thomas Jarmer, Martin Schlerf, Benjamin Kotz, and Willy Werner. 2003. "Retrieval of Wheat Bio-Physical Attributes from Hyperspectral Data and SAILH+ PROSPECT Radiative Transfer Model." 3rd EARSeL Workshop on Imaging Spectroscopy: 473–82.

Baker, Neil R. 2008. "Chlorophyll Fluorescence: A Probe of Photosynthesis in Vivo." Annual Review of Plant Biology 59:89–113. doi: 10.1146/annurev.arplant.59.032607.092759.

Bal, Santanu Kumar, Joydeep Mukherjee, Burhan Uddin, Choudhury Ashok, and Kumar Dhawan. 2018. Advances in Crop Environment Interaction. doi: 10.1007/978-981-13-1861-0

Balogh, Jeremiás Máté, and Attila Jámbor. 2020. "The Environmental Impacts of Agricultural Trade: A Systematic Literature Review." Sustainability. 12(3):1–16. doi: 10.3390/su12031152.

Baret, F., M. Weiss, R. Lacaze, F. Camacho, H. Makhmara, P. Pacholcyzk, and B. Smets. 2013. "GEOV1: LAI and FAPAR Essential Climate Variables and FCOVER Global Time Series Capitalizing over Existing Products. Part 1: Principles of Development and Production." Remote Sensing of Environment 137:299–309. doi: 10.1016/j.rse.2012.12.027.

Barnes, E. M., T. R. Clarke, S. E. Richards, P. D. Colaizzi, J. Haberland, M. Kostrzewski, P. Aller, C. Choi, E. Riley, T. Thompson, and R. J. Lascano. 2000. "Coincident Detection of Crop Water Stress, Nitrogen Status and Canopy Density Using Ground Based Multispectral Data." Proceedings of the Fifth International Conference on Precision Agriculture 1619.

Bartholomeus, H. M., M. E. Schaepman, L. Kooistra, A. Stevens, W. B. Hoogmoed, and O. S. P. Spaargaren. 2008. "Spectral Reflectance Based Indices for Soil Organic Carbon Quantification." Geoderma 145(1–2):28–36. doi: 10.1016/j.geoderma.2008.01.010.

Basso, Bruno, and John Antle. 2020. “Digital Agriculture to Design Sustainable Agricultural Systems.” Nature Sustainability 3(4):254–56. doi: 10.1038/s41893-020-0510-0.

Basso, Bruno, Davide Cammarano, Peter R. Grace, Giovanni Cafiero, Luigi Sartori, Michele Pisante, Giuseppe Landi, Sergio de Franchi, and Francesco Basso. 2009. “Criteria for Selecting Optimal Nitrogen Fertilizer Rates for Precision Agriculture.” Italian Journal of Agronomy 4(4):147–58. doi: 10.4081/ija.2009.4.147.

Bastos, Leonardo M., Andre Froes de Borja Reis, Ajay Sharda, Yancy Wright, and Ignacio A. Ciampitti. 2021. “Current Status and Future Opportunities for Grain Protein Prediction Using On-and off-Combine Sensors: A Synthesis-Analysis of the Literature.” Remote Sensing 13(24). doi: 10.3390/rs13245027.

Bei Cui, Qianjun Zhao, Wenjiang Huang, Xiaoyu Song, Huichun Ye, and Xianfeng Zhou. 2019. “A New Integrated Vegetation Index for the Estimationof Winter Wheat Leaf Chlorophyll Content.” Remote Sensing 11(8):1–18.

Belmecheri, Soumaya, Flurin Babst, Eugene R. Wahl, David W. Stahle, and Valerie Trouet. 2015. “Multi-Century Evaluation of Sierra Nevada Snowpack.” Nature Climate Change 6(1):2–3. doi: 10.1038/nclimate2809.

Ben-Dor, E., K. Patkin, A. Banin, and A. Karnieli. 2002. “Mapping of Several Soil Properties Using DAIS-7915 Hyperspectral Scanner Data - A Case Study over Soils in Israel.” International Journal of Remote Sensing 23(6):1043–62. doi: 10.1080/01431160010006962.

Berger, K., A. Halabuk, J. Verrelst, M. Mojses, K. Gerh, G. Tagliabue, M. Wocher, and T. Hank. 2021. “Towards Quantifying Non-Photosynthetic Vegetation for Agriculture Using Spaceborne Imaging Spectroscopy.” International Geoscience and Remote Sensing Symposium (IGARSS) 5822–25.

Berger, Katja, Clement Atzberger, Martin Danner, Guido D’Urso, Wolfram Mauser, Francesco Vuolo, and Tobias Hank. 2018. “Evaluation of the PROSAIL Model Capabilities for Future Hyperspectral Model Environments: A Review Study.” Remote Sensing 10(1). doi: 10.3390/rs10010085.

Berger, Katja, Jochem Verrelst, Jean Baptiste Féret, Tobias Hank, Matthias Wocher, Wolfram Mauser, and Gustau Camps-Valls. 2020. “Retrieval of Aboveground Crop Nitrogen Content with a Hybrid Machine Learning Method.” International Journal of Applied Earth Observation and Geoinformation 92(May). doi: 10.1016/j.jag.2020.102174.

Berk, A., G. P. Anderson, P. K. Acharya, and E. P. Shettle. 2008. “MODTRAN5. 2.0. 0 User’s Manual.” Spectral Sciences Inc., Burlington MA, Air Force Research Laboratory, Hanscom MA.

Berk, Alexander, Lawrence S. Bernstein, and David C. Robertson. 1987. “MODTRAN: A Moderate Resolution Model for LOWTRAN.” 03.

Berry, P. M., M. Sterling, J. H. Spink, C. J. Baker, R. Sylvester-Bradley, S. J. Mooney, A. R. Tams, and A. R. Ennos. 2004. “Understanding and Reducing Lodging in Cereals.” Advances in Agronomy 84(04):217–71. doi: 10.1016/S0065-2113(04)84005-7.

Bhushan, Shashank, David Shean, Oleg Alexandrov, and Scott Henderson. 2021. “Automated Digital Elevation Model (DEM) Generation from Very-High-Resolution Planet SkySat Triplet Stereo and Video Imagery.” ISPRS Journal of Photogrammetry and Remote Sensing 173:151–65. doi: 10.1016/j.isprsjprs.2020.12.012.

Bossung, Christian, Martin Schlerf, and Miriam Machwitz. 2022. “Estimation of Canopy Nitrogen Content in Winter Wheat from Sentinel-2 Images for Operational Agricultural Monitoring.” Precision Agriculture (0123456789). doi: 10.1007/s11119-022-09918-y.

Breiman, Leo. 2001. “Random Forests.” Machine Learning (45):5–32. doi: https://doi.org/10.1023/A:1010933404324.

Breunig, Fábio Marcelo, Lênio Soares Galvão, Antônio Roberto Formaggio, and José Carlos Neves Epiphanio. 2011. “Directional Effects on NDVI and LAI Retrievals from MODIS: A Case Study in Brazil with Soybean.” International Journal of Applied Earth Observation and Geoinformation 13(1):34–42. doi: 10.1016/j.jag.2010.06.004.

Breuniga, Fábio Marcelo, Lênio Soares Galvão, João Roberto Dos Santos, Anatoly A. Gitelson, Yhasmin Mendes De Moura, Thiago Sousa Teles, and William Gaid. 2015.

"Spectral Anisotropy of Subtropical Deciduous Forest Using MISRand MODIS Data Acquired under Large Seasonal Variation in Solarzenith Angle." International Journal of Applied Earth Observation and Geoinformation 35(PB):294–304. doi: 10.1016/j.jag.2014.09.017.

Broge, N. H., and E. Leblanc. 2001. "Comparing Prediction Power and Stability of Broadband and Hyperspectral Vegetation Indices for Estimation of Green Leaf Area Index and Canopy Chlorophyll Density." Remote Sensing of Environment 76(2):156–72. doi: 10.1016/S0034-4257(00)00197-8.

Bronson, Kevin F., Jeffrey W. White, Matthew M. Conley, Doug J. Hunsaker, Kelly R. Thorp, Andrew N. French, Bruce E. Mackey, and Kyle H. Holland. 2017. "Active Optical Sensors in Irrigated Durum Wheat: Nitrogen and Water Effects." Agronomy Journal 109(3):1060–71. doi: 10.2134/agronj2016.07.0390.

California Department of Food and Agriculture. 2016. "California Agricultural Statistics Review 2016." Retrieved June 25, 2022 (https://www.cdfa.ca.gov/statistics/PDFs/2016Report.pdf).

California Department of Water Resources. 2022. "Land Use Maps." Retrieved June 1, 2022 (https://water.ca.gov/programs/water-use-and-efficiency/land-and-water-use/land-use-surveys).

Camino, C., K. Araño, J. A. Berni, H. Dierkes, J. L. Trapero-Casas, G. León-Ropero, M. Montes-Borrego, M. Roman-Écija, M. P. Velasco-Amo, B. B. Landa, J. A. Navas-Cortes, and P. S. A. Beck. 2022. "Detecting Xylella Fastidiosa in a Machine Learning Framework Using Vcmax and Leaf Biochemistry Quantified with Airborne Hyperspectral Imagery." Remote Sensing of Environment 282. doi: 10.1016/j.rse.2022.113281.

Camino, Carlos, Victoria González-Dugo, Pilar Hernández, J. C. Sillero, and Pablo J. Zarco-Tejada. 2018. "Improved Nitrogen Retrievals with Airborne-Derived Fluorescence and Plant Traits Quantified from VNIR-SWIR Hyperspectral Imagery in the Context of Precision Agriculture." International Journal of Applied Earth Observation and Geoinformation 70:105–17. doi: 10.1016/j.jag.2018.04.013.

Campbell, Bruce M., Douglas J. Beare, Elena M. Bennett, Jason M. Hall-Spencer, John S. I. Ingram, Fernando Jaramillo, Rodomiro Ortiz, Navin Ramankutty, Jeffrey A. Sayer, and Drew Shindell. 2017. "Agriculture Production as a Major Driver of the Earth System Exceeding Planetary Boundaries." Ecology and Society 22(4). doi: 10.5751/ES-09595-220408.

Campbell, Elliot J., David B. Lobell, Robert C. Genova, and Christopher B. Field. 2008. "The Global Potential of Bioenergy on Abandoned Agriculture Lands." 5791–94.

Cartelat, A., Z. G. Cerovic, Y. Goulas, S. Meyer, C. Lelarge, J. L. Prioul, A. Barbottin, M. H. Jeuffroy, P. Gate, G. Agati, and I. Moya. 2005. "Optically Assessed Contents of Leaf Polyphenolics and Chlorophyll as Indicators of Nitrogen Deficiency in Wheat (*Triticum aestivum* L.)." Field Crops Research 91(1):35–49. doi: 10.1016/j.fcr.2004.05.002.

Cavalaris, Chris, Sofia Megoudi, Maria Maxouri, Konstantinos Anatolitis, Marios Sifakis, Efi Levizou, and Aris Kyparissis. 2021. "Modeling of Durum Wheat Yield Based on Sentinel-2 Imagery." Agronomy 11(8). doi: 10.3390/agronomy11081486.

Cawse-Nicholson, Kerry, Philip A. Townsend, David Schimel, Ali M. Assiri, Pamela L. Blake, Maria Fabrizia Buongiorno, Petya Campbell, Nimrod Carmon, Kimberly A. Casey, Rosa Elvira Correa-Pabón, Kyla M. Dahlin, Hamid Dashti, Philip E. Dennison, Heidi Dierssen, Adam Erickson, Joshua B. Fisher, Robert Frouin, Charles K. Gatebe, Hamed Gholizadeh, Michelle Gierach, Nancy F. Glenn, James A. Goodman, Daniel M. Griffith, Liane Guild, Christopher R. Hakkenberg, Eric J. Hochberg, Thomas R. H. Holmes, Chuanmin Hu, Glynn Hulley, Karl F. Huemmrich, Raphael M. Kudela, Raymond F. Kokaly, Christine M. Lee, Roberta Martin, Charles E. Miller, Wesley J. Moses, Frank E. Muller-Karger, Joseph D. Ortiz, Daniel B. Otis, Nima Pahlevan, Thomas H. Painter, Ryan Pavlick, Ben Poulter, Yi Qi, Vincent J. Realmuto, Dar Roberts, Michael E. Schaepman, Fabian D. Schneider, Florian M. Schwandner, Shawn P. Serbin, Alexey N. Shiklomanov, E. Natasha Stavros, David R. Thompson, Juan L. Torres-Perez, Kevin R. Turpie, Maria Tzortziou, Susan Ustin, Qian Yu, Yusri Yusup, and Qingyuan Zhang. 2021. "NASA's Surface Biology and Geology Designated Observable: A Perspective on Surface Imaging Algorithms." Remote Sensing of Environment 257. doi: 10.1016/j.rse.2021.112349.

Chaves, M. M., J. S. Pereira, J. Maroco, M. L. Rodrigues, C. P. P. Ricardo, M. L. Osório, I. Carvalho, T. Faria, and C. Pinheiro. 2002. "How Plants Cope with Water Stress in the Field. Photosynthesis and Growth." Annals of Botany 89 (SPEC. ISS.):907–16. doi: 10.1093/aob/mcf105.

Chavez, Pat S. 1988. "An Improved Dark-Object Subtraction Technique for Atmospheric Scattering Correction of Multispectral Data." Remote Sensing of Environment 24(3):459–79. doi: 10.1016/0034-4257(88)90019-3.

Chen, F., D. E. Kissel, L. T. West, D. Rickman, J. C. Luvall, and W. Adkins. 2005. "Mapping Surface Soil Organic Carbon for Crop Fields with Remote Sensing." Journal of Soil and Water Conservation 60(1):51–57.

Chen, Hanyue, Wenjiang Huang, Wang Li, Zheng Niu, Liming Zhang, and Shihe Xing. 2018. "Estimation of LAI in Winter Wheat from Multi-Angular Hyperspectral VNIR Data: Effects of View Angles and Plant Architecture." Remote Sensing 10(10). doi: 10.3390/rs10101630.

Chen, Pengfei, Driss Haboudane, Nicolas Tremblay, Jihua Wang, Philippe Vigneault, and Baoguo Li. 2010. "New Spectral Indicator Assessing the Efficiency of Crop Nitrogen Treatment in Corn and Wheat." Remote Sensing of Environment 114(9):1987–97. doi: 10.1016/j.rse.2010.04.006.

Chen, Xuehong, Zhengfei Guo, Jin Chen, Wei Yang, Yanming Yao, Chishan Zhang, Xihong Cui, and Xin Cao. 2019. "Replacing the Red Band with the Red-SWIR Band (0.74ρred+0.26ρswir) Can Reduce the Sensitivity of Vegetation Indices to Soil Background." Remote Sensing 11(7):1–15. doi: 10.3390/RS11070851.

Cho, Moses Azong, and Andrew K. Skidmore. 2006. "A New Technique for Extracting the Red Edge Position from Hyperspectral Data: The Linear Extrapolation Method." Remote Sensing of Environment 101(2):181–93. doi: 10.1016/j.rse.2005.12.011.

Chollet, F. 2015. "Keras". Retrieved (https://github.com/fchollet/keras).

Cisneros-Araujo, Pablo, Teresa Goicolea, María Cruz Mateo-Sánchez, Juan Ignacio García-Viñás, Miguel Marchamalo, Audrey Mercier, and Aitor Gastón. 2021. "The Role of

Remote Sensing Data in Habitat Suitability and Connectivity Modeling: Insights from the Cantabrian Brown Bear." Remote Sensing 13(6). doi: 10.3390/rs13061138.

Clark, Matthew L., Dar A. Roberts, and David B. Clark. 2005. "Hyperspectral Discrimination of Tropical Rain Forest Tree Species at Leaf to Crown Scales." Remote Sensing of Environment 96(3–4):375–98. doi: 10.1016/j.rse.2005.03.009.

Clarke, T. R., M. S. Moran, E. M. Barnes, P. J. Pinter, and J. Qi. 2001. "Planar Domain Indices: A Method for Measuring a Quality of a Single Component in Two-Component Pixels." International Geoscience and Remote Sensing Symposium (IGARSS) 3:1279–81. doi: 10.1109/igarss.2001.976818.

Clevers, Jan G. P. W., Lammert Kooistra, and Marnix M. M. van den Brande. 2017. "Using Sentinel-2 Data for Retrieving LAI and Leaf and Canopy Chlorophyll Content of a Potato Crop." Remote Sensing 9(5):1–15. doi: 10.3390/rs9050405.

Climatic data in Talure. 2022. "NOAA National Centers for Environmental Information. Climate at a Glance: County Time Series." Retrieved June 16, 2022 (https://www.ncdc.noaa.gov/cag/).

Coates, Austin R., Philip E. Dennison, Dar A. Roberts, and Keely L. Roth. 2015. "Monitoring the Impacts of Severe Drought on Southern California Chaparral Species Using Hyperspectral and Thermal Infrared Imagery." Remote Sensing 7(11):14276–91. doi: 10.3390/rs71114276.

Cohen, Jacob. 1960. "A Coefficient of Agreement for Nominal Scales." Educational and Psychological Measurement XX(1):37–46. doi: DOI: 10.1177/001316446002000104.

Colaço, A. F., and R. G. V. Bramley. 2018. "Do Crop Sensors Promote Improved Nitrogen Management in Grain Crops?" Field Crops Research 218:126–40. doi: 10.1016/j.fcr.2018.01.007.

Constable, GA, and HM Rawson. 1980. "Effect of Leaf Position, Expansion and Age on Photosynthesis, Transpiration and Water Use Efficiency of Cotton." Functional Plant Biology 7(1):89. doi: 10.1071/pp9800089.

Cook, Benjamin I., Toby R. Ault, and Jason E. Smerdon. 2015. "Unprecedented 21st Century Drought Risk in the American Southwest and Central Plains." Science Advances 1(1):1–8. doi: 10.1126/sciadv.1400082.

Cossani, C. Mariano, Gustavo A. Slafer, and Roxana Savin. 2012. "Nitrogen and Water Use Efficiencies of Wheat and Barley under a Mediterranean Environment in Catalonia." Field Crops Research 128:109–18. doi: 10.1016/j.fcr.2012.01.001.

Cossani, Cesar Mariano, and Victor O. Sadras. 2018. Water–Nitrogen Colimitation in Grain Crops. Vol. 150. 1st ed. Elsevier Inc.

Craig Dobson, M., Leland E. Pierce, and Fawwaz T. Ulaby. 1996. "Knowledge-Based Land-Cover Classification Using Ers-1/Jers-1 Sar Composites." IEEE Transactions on Geoscience and Remote Sensing 34(1):83–99. doi: 10.1109/36.481896.

Cross, Matthew D., Ted A. Scambos, Fabio Pacifici, and Wesley E. Marshall. 2018. "Validating the Use of Metre-Scale Multi-Spectral Satellite Image Data for Identifying Tropical Forest Tree Species." International Journal of Remote Sensing 39(11):3723–52. doi: 10.1080/01431161.2018.1448482.

Curran, Paul J. 1989. "Remote Sensing of Foliar Chemistry." Remote Sensing of Environment 30(3):271–78. doi: 10.1016/0034-4257(89)90069-2.

Dai, Jie, Dar Roberts, Philip Dennison, and Douglas Stow. 2018. "Spectral-Radiometric Differentiation of Non-Photosynthetic Vegetation and Soil within Landsat and Sentinel 2 Wavebands." Remote Sensing Letters 9(8):733–42. doi: 10.1080/2150704X.2018.1470697.

Damm, Alexander, André Erler, Walter Hillen, Michele Meroni, Michael E. Schaepman, Wout Verhoef, and Uwe Rascher. 2011. "Modeling the Impact of Spectral Sensor Configurations on the FLD Retrieval Accuracy of Sun-Induced Chlorophyll Fluorescence." Remote Sensing of Environment 115(8):1882–92. doi: 10.1016/j.rse.2011.03.011.

Danner, Martin, Katja Berger, Matthias Wocher, Wolfram Mauser, and Tobias Hank. 2021. "Efficient RTM-Based Training of Machine Learning Regression Algorithms to Quantify Biophysical & Biochemical Traits of Agricultural Crops." ISPRS Journal of

Photogrammetry and Remote Sensing 173:278–96. doi: 10.1016/j.isprsjprs.2021.01.017.

Daughtry, C. S. T., and E. R. Hunt. 2008. "Mitigating the Effects of Soil and Residue Water Contents on Remotely Sensed Estimates of Crop Residue Cover." Remote Sensing of Environment 112(4):1647–57. doi: 10.1016/j.rse.2007.08.006.

Daughtry, C. S. T., C. L. Walthall, M. S. Kim, E. Brown De Colstoun, and J. E. McMurtrey. 2000. "Estimating Corn Leaf Chlorophyll Concentration from Leaf and Canopy Reflectance." Remote Sensing of Environment 74(2):229–39. doi: 10.1016/S0034-4257(00)00113-9.

Daughtry, Craig S. T. 2001. "Discriminating Crop Residues from Soil by Shortwave Infrared Reflectance." Agronomy Journal 93(1):125–31.

De Zan, Francesco, and Andrea Monti Guarnieri. 2006. "TOPSAR: Terrain Observation by Progressive Scans." IEEE Transactions on Geoscience and Remote Sensing 44(9):2352–60. doi: 10.1109/TGRS.2006.873853.

Delgado, Jorge A. 2010. "Crop Residue Is a Key for Sustaining Maximum Food Production and for Conservation of Our Biosphere." Journal of Soil and Water Conservation 65(5):111–16. doi: 10.2489/jswc.65.5.111A.

Dennison, Philip E., Yi Qi, Susan K. Meerdink, Raymond F. Kokaly, David R. Thompson, Craig S. T. Daughtry, Miguel Quemada, Dar A. Roberts, Paul D. Gader, Erin B. Wetherley, Izaya Numata, and Keely L. Roth. 2019. "Comparison of Methods for Modeling Fractional Cover Using Simulated Satellite Hyperspectral Imager Spectra." Remote Sensing, 11(18), 2072. doi: 10.3390/rs11182072

Dennison, Philip E., and D. A. Roberts. 2003. "Endmember Selection for Multiple Endmember Spectral Mixture Analysis Using Endmember Average RMSE." Remote Sensing of Environment 87(2–3):123–35. doi: 10.1016/S0034-4257(03)00135-4.

Diacono, Mariangela, Pietro Rubino, and Francesco Montemurro. 2013. "Precision Nitrogen Management of Wheat. A Review." Agronomy for Sustainable Development 33(1):219–41. doi: 10.1007/s13593-012-0111-z.

Dian, Renwei, Shutao Li, Bin Sun, and Anjing Guo. 2021. “Recent Advances and New Guidelines on Hyperspectral and Multispectral Image Fusion.” Information Fusion 69:40–51. doi: 10.1016/j.inffus.2020.11.001.

DigitalGlobe. 2023. “WorldView-3 Above + Beyond.” Retrieved March 19, 2023 (http://worldview3.digitalglobe.com/).

Dorigo, Wouter A. 2012. “Improving the Robustness of Cotton Status Characterisation by Radiative Transfer Model Inversion of Multi-Angular CHRIS/PROBA Data.” IEEE Journal of Selected Topics in Applied Earth Observations and Remote Sensing 5(1):18–29. doi: 10.1109/JSTARS.2011.2171181.

Dorigo, Wouter, Rudolf Richter, Frédéric Baret, Richard Bamler, and Wolfgang Wagner. 2009. “Enhanced Automated Canopy Characterization from Hyperspectral Data by a Novel Two Step Radiative Transfer Model Inversion Approach.” Remote Sensing 1(4):1139–70. doi: 10.3390/rs1041139.

Doxani, Georgia, Eric Vermote, Jean Claude Roger, Ferran Gascon, Stefan Adriaensen, David Frantz, Olivier Hagolle, André Hollstein, Grit Kirches, Fuqin Li, Jérôme Louis, Antoine Mangin, Nima Pahlevan, Bringfried Pflug, and Quinten Vanhellemont. 2018. “Atmospheric Correction Inter-Comparison Exercise.” Remote Sensing 10(2):1–18. doi: 10.3390/rs10020352.

Dube, Timothy, Santa Pandit, Cletah Shoko, Abel Ramoelo, Dominic Mazvimavi, and Tatenda Dalu. 2019. “Numerical Assessments of Leaf Area Index in Tropical Savanna Rangelands, South Africa Using Landsat 8 OLI Derived Metrics and in-Situ Measurements.” Remote Sensing 11(7). doi: 10.3390/rs11070829.

Eastwood, Michael L., Thomas G. Chrien, Charles M. Sarture, Robert O. Green, and Wallace M. Porter. 1991. “Current Instrument Status of the Airborne Visible/Infrared Imaging Spectrometer (AVIRIS).” Infrared Technology XVII 1540:164.

Ehrler. 1973. “Cotton Leaf Temperatures as Related to Soil Water Depletion and Meteorological Factors.” Agronomy Journal 65(3):404–9.

Eickhout, B., A. F. Bouwman, and H. van Zeijts. 2006. “The Role of Nitrogen in World Food Production and Environmental Sustainability.” Agriculture, Ecosystems and Environment 116(1–2):4–14. doi: 10.1016/j.agee.2006.03.009.

El-Shikha, D. M., P. Waller, D. Hunsaker, T. Clarke, and E. Barnes. 2007. “Ground-Based Remote Sensing for Assessing Water and Nitrogen Status of Broccoli.” Agricultural Water Management 92(3):183–93. doi: 10.1016/j.agwat.2007.05.020.

European Space Agency. 2023a. “Sentinel-2 Overview.” Retrieved March 19, 2023 (https://sentinels.copernicus.eu/web/sentinel/user-guides/sentinel-2-msi/overview).

European Space Agency. 2023b. “Satellite Missions WorldView-3.” Retrieved March 19, 2023 (https://www.eoportal.org/satellite-missions/worldview-3#learning-on-the-job).

European Space Agency. 2023c. “Mission Programmes.” Retrieved March 19, 2023 (https://earth.esa.int/eogateway/missions).

European Space Agency. 2023d. “Sentinel Application Platform (SNAP).” Retrieved April 7, 2020 (https://step.esa.int/main/toolboxes/snap/).

European Space Agency. 2023e. “Copernicus DataHUB Server.” Retrieved April 9, 2022 (https://scihub.copernicus.eu/).

European Space Agency. 2023f. “Sentinel-2 Spectral Response Functions Document Library.” Retrieved April 7, 2020 (https://sentinels.copernicus.eu/web/sentinel/user-guides/sentinel-2-msi/document-library/-/asset_publisher/Wk0TKajiISaR/content/sentinel-2a-spectral-responses).

Farquhar, Graham D., S. Von Caemmerer, and Joseph a. Berry. 1980. “A Biochemical Model of Photosynthesis CO_2 Fixation in Leaves of C3 Species.” Planta 149:78–90.

Faunt, Claudia C. 2009. “Groundwater Availability of the Central Valley Aquifer, California.” United States Geological Survey Professional Paper 1766, 225 P.

Faunt, Claudia C., and Michelle Sneed. 2015. “Water Availability and Subsidence in California’s Central Valley.” San Francisco Estuary and Watershed Science 13(3):0–8. doi: 10.15447/sfews.2015v13iss3art4.

Fawwaz T. Ulaby, Pascale C. Dubois, Jakob van Zyl. 1996. “Radar Mapping of Surface Soil Moisture.” Journal of Hydrology.” 184:57–84. doi: 10.1016/0022-1694(95)02968-0

Féret, J. B., A. A. Gitelson, S. D. Noble, and S. Jacquemoud. 2017. “PROSPECT-D: Towards Modeling Leaf Optical Properties through a Complete Lifecycle.” Remote Sensing of Environment 193:204–15. doi: 10.1016/j.rse.2017.03.004.

Féret, Jean Baptiste, Katja Berger, Florian de Boissieu, and Zbyněk Malenovský. 2021. “PROSPECT-PRO for Estimating Content of Nitrogen-Containing Leaf Proteins and Other Carbon-Based Constituents.” Remote Sensing of Environment 252. doi: 10.1016/j.rse.2020.112173.

Féret, Jean Baptiste, Christophe François, Gregory P. Asner, Anatoly A. Gitelson, Roberta E. Martin, Luc P. R. Bidel, Susan L. Ustin, Guerric le Maire, and Stéphane Jacquemoud. 2008. “PROSPECT-4 and 5: Advances in the Leaf Optical Properties Model Separating Photosynthetic Pigments.” Remote Sensing of Environment 112(6):3030–43. doi: 10.1016/j.rse.2008.02.012.

Ferguson, Richard, and Donald Rundquist. 2018. “Remote Sensing for Site-Specific Crop Management.” Precision Agriculture Basics 103–17. doi: 10.2134/precisionagbasics.2016.0092.

Fitzgerald, G. J., D. Rodriguez, L. K. Christensen, R. Belford, V. O. Sadras, and T. R. Clarke. 2006. “Spectral and Thermal Sensing for Nitrogen and Water Status in Rainfed and Irrigated Wheat Environments.” Precision Agriculture 7(4):233–48. doi: 10.1007/s11119-006-9011-z.

Fitzgerald, Glenn, Daniel Rodriguez, and Garry O’Leary. 2010. “Measuring and Predicting Canopy Nitrogen Nutrition in Wheat Using a Spectral Index-The Canopy Chlorophyll Content Index (CCCI).” Field Crops Research 116(3):318–24. doi: 10.1016/j.fcr.2010.01.010.

Fois, Simonetta, Rosella Motzo, and Francesco Giunta. 2009. “The Effect of Nitrogenous Fertiliser Application on Leaf Traits in Durum Wheat in Relation to Grain Yield and Development.” Field Crops Research 110(1):69–75. doi: 10.1016/j.fcr.2008.07.004.

Food and Agriculture Organization FAOstat. 2022. “Statistics Data: The Food and Agriculture Organization of the United Nations. Official Website.” Retrieved December 1, 2022 (https://www.fao.org/faostat/en/#data).

Food and Agriculture Organization of the United Nations (FAO). 2023. “FAO Term Portal.” Retrieved July 24, 2022 (https://www.fao.org/faoterm/viewentry/en/?entryId=162552).

Franch, Belen, Eric Vermote, Sergii Skakun, Jean Claude Roger, Jeffrey Masek, Junchang Ju, Jose Luis Villaescusa-Nadal, and Andres Santamaria-Artigas. 2019. “A Method for Landsat and Sentinel 2 (HLS) BRDF Normalization.” Remote Sensing 11(6). doi: 10.3390/rs11060632.

Fu, Zhaopeng, Shanshan Yu, Jiayi Zhang, Hui Xi, Yang Gao, Ruhua Lu, Hengbiao Zheng, Yan Zhu, Weixing Cao, and Xiaojun Liu. 2022. “Combining UAV Multispectral Imagery and Ecological Factors to Estimate Leaf Nitrogen and Grain Protein Content of Wheat.” European Journal of Agronomy 132:126405. doi: 10.1016/j.eja.2021.126405.

Gabriel, Jose L., Pablo J. Zarco-Tejada, P. Juan López-Herrera, Enrique Pérez-Martín, Maria Alonso-Ayuso, and Miguel Quemada. 2017. “Airborne and Ground Level Sensors for Monitoring Nitrogen Status in a Maize Crop.” Biosystems Engineering 160:124–33. doi: 10.1016/j.biosystemseng.2017.06.003.

Gabriel, Jose Luis, Miguel Quemada, María Alonso-Ayuso, Jon I. Lizaso, and Diana Martín-Lammerding. 2019. “Predicting n Status in Maize with Clip Sensors: Choosing Sensor, Leaf Sampling Point, and Timing.” Sensors 19(18). doi: 10.3390/s19183881.

Gaju, Oorbessy, Vincent Allard, Pierre Martre, Jacques Le Gouis, Delphine Moreau, Matthieu Bogard, Stella Hubbart, and M. John Foulkes. 2014. “Nitrogen Partitioning and Remobilization in Relation to Leaf Senescence, Grain Yield and Grain Nitrogen Concentration in Wheat Cultivars.” Field Crops Research 155:213–23. doi: 10.1016/j.fcr.2013.09.003.

Gamon, J. A., Josep Penuelas., and C. B. Field. 1992. “A Narrow-Waveband Spectral Index That Tracks Diurnal Changes in Photosynthetic Efficiency.” Remote Sensing of Environment 41(1). doi: https://doi.org /10.1016/0034-4257(92)90059-S.

Gao, B. C. 1996. “NDWI—A Normalized Difference Water Index for Remote Sensing of Vegetation Liquid Water from Space.” Remote Sensing of Environment, 58(3). doi: 10.1016/S0034-4257(96)00067-3.

Gao, Bo Cai, Marcos J. Montes, Curtiss O. Davis, and Alexander F. H. Goetz. 2009. “Atmospheric Correction Algorithms for Hyperspectral Remote Sensing Data of Land and Ocean.” Remote Sensing of Environment 113(SUPPL. 1):S17–24. doi: 10.1016/j.rse.2007.12.015.

Gao, Ying, Jeffrey P. Walker, Mahdi Allahmoradi, Alessandra Monerris, Dongryeol Ryu, and Thomas J. Jackson. 2015. “Optical Sensing of Vegetation Water Content: A Synthesis Study.” IEEE Journal of Selected Topics in Applied Earth Observations and Remote Sensing 8(4):1456–64. doi: 10.1109/JSTARS.2015.2398034.

Garwood, E. A., and T. B. Williams. 1967. “Growth, Water Use and Nutrient Uptake from the Subsoil by Grass Swards.” The Journal of Agricultural Science 69(1):125–30. doi: 10.1017/S002185960001652X.

Gilabert, M. A., C. Conese, and F. Maselli. 1994. “An Atmospheric Correction Method for the Automatic Retrieval of Surface Reflectances from TM Images.” International Journal of Remote Sensing 15(10):2065–86. doi: 10.1080/01431169408954228.

Gitelson, Anatoly A., Yoram J. Kaufman, and Mark N. Merzlyak. 1996. “Use of a Green Channel in Remote Sensing of Global Vegetation from EOS- MODIS.” Remote Sensing of Environment 58(3):289–98. doi: 10.1016/S0034-4257(96)00072-7.

Goga, Tomáš, Ján Feranec, Tomáš Bucha, Miloš Rusnák, Ivan Sačkov, Ivan Barka, Monika Kopecká, Juraj Papčo, Ján Ot’ahel’, Daniel Szatmári, Róbert Pazúr, Maroš Sedliak, Jozef Pajtík, and Jozef Vladovič. 2019. “A Review of the Application of Remote Sensing Data for Abandoned Agricultural Land Identification with Focus on Central and Eastern Europe.” Remote Sensing 11(23). doi: 10.3390/rs11232759.

Gogoi, N. K., B. Deka, and L. C. Bora. 2018. “Remote Sensing and Its Use in Detection and Monitoring Plant Diseases: A Review.” Agricultural Reviews. doi: 10.18805/ag.r-1835.

Goicolea, Teresa, and M. Cruz Mateo-Sánchez. 2022. “Static vs Dynamic Connectivity: How Landscape Changes Affect Connectivity Predictions in the Iberian Peninsula.” Landscape Ecology 37(7):1855–70. doi: 10.1007/s10980-022-01445-5.

Goldhamer, David A., and Elias Fereres. 2017. “Establishing an Almond Water Production Function for California Using Long-Term Yield Response to Variable Irrigation.” Irrigation Science 35(3):169–79. doi: 10.1007/s00271-016-0528-2.

Gómez, Diego, Pablo Salvador, Julia Sanz, and Jose Luis Casanova. 2019. “Potato Yield Prediction Using Machine Learning Techniques and Sentinel 2 Data.” Remote Sensing 11(15). doi: 10.3390/rs11151745.

Gonzalez-Dugo, Victoria, Jean Louis Durand, and François Gastal. 2009. “Water Deficit and Nitrogen Nutrition of Crops.” Sustainable Agriculture 2:557–75. doi: 10.1007/978-94-007-0394-0_25.

Gonzalez-Dugo, Victoria, Jean Louis Durand, François Gastal, and Catherine Picon-Cochard. 2005. “Short-Term Response of the Nitrogen Nutrition Status of Tall Fescue and Italian Ryegrass Swards under Water Deficit.” Australian Journal of Agricultural Research 56(11):1269–76. doi: 10.1071/AR05064.

González, M. C., T. Le Toan, and J. Moreno. 2005. “Multitemporal Analysis of MERIS-FR Data for Crop Monitoring in Two Agricultural Areas: Barrax and Toulouse.” Proc. 2004 Envisat ERS Symp. 572.

Goulas, Yves, Zoran G. Cerovic, Aurélie Cartelat, and Ismaël Moya. 2004. “Dualex: A New Instrument for Field Measurements of Epidermal Ultraviolet Absorbance by Chlorophyll Fluorescence.” Applied Optics 43(23):4488–96. doi: 10.1364/AO.43.004488.

Grainger, Matt. 2010. “World Summit on Food Security (UN FAO, Rome, 16-18 November 2009).” Development in Practice 20(6):740–42. doi: 10.1080/09614524.2010.491540.

Green, R. O., T. G. Chrien, P. J. Nielson, C. M. Sarture, B. T. Eng, C. Chovit, A. T. Murray, M. L. Eastwood, and H. I. Novack. 1993. “Airborne Visible/Infrared Imaging Spectrometer (AVIRIS): Recent Improvements to the Sensor and Data Facility.” Proc. SPIE, Vol. 1937, 1937:180–90.

Green, Robert O., Michael L. Eastwood, Charles M. Sarture, Thomas G. Chrien, Mikael Aronsson, Bruce J. Chippendale, Jessica A. Faust, Betina E. Pavri, Christopher J. Chovit, Manuel Solis, Martin R. Olah, and Orlesa Williams. 1998. “Imaging Spectroscopy and the Airborne Visible/Infrared Imaging Spectrometer (AVIRIS).” Remote Sensing of Environment 65(3):227–48. doi: 10.1016/S0034-4257(98)00064-9.

Greenwood, D. J., G. Lemaire, G. Gosse, P. Cruz, A. Draycott, and J. J. Neeteson. 1990. “Decline in Percentage N of C3 and C4 Crops with Increasing Plant Mass.” Annals of Botany 66(4):425–36. doi: 10.1093/oxfordjournals.aob.a088044.

Griffin, Daniel, and Kevin J. Anchukaitis. 2014. “How Unusual Is the 2012-2014 California Drought?” Geophysical Research Letters 41(24):9017–23. doi: 10.1002/2014GL062433.

Griffin, Michael K., and Hsiao-hua K. Burke. 2003. “Compensation of Hyperspectral Data for Atmospheric Effects.” Lincoln Laboratory Journal 14(1):29–54.

Gueymard, C. A., D. Myers, and K. Emery. 2002. “Proposed Reference Irradiance Spectra for Solar Energy Systems Testing.” Solar Energy 73(6):443–67. doi: 10.1016/S0038-092X(03)00005-7.

Gueymard, Christian. 1989. “A Two-Band Model for the Calculation of Clear Sky Solar Irradiance, Illuminance, and Photosynthetically Active Radiation at the Earth’s Surface.” Solar Energy 43(5):253–65. doi: 10.1016/0038-092X(89)90113-8.

Gutiérrez-Gordillo, Saray, Leontina Lipan, Víctor Hugo Durán Zuazo, Esther Sendra, Francisca Hernández, Martín Samuel Hernández-Zazueta, Ángel A. Carbonell-Barrachina, and Iván Francisco García-Tejero. 2020. “Deficit Irrigation as a Suitable Strategy to Enhance the Nutritional Composition of Hydrosos Almonds.” Water 12(12):1–18. doi: 10.3390/w12123336.

Haboudane, Driss, John R. Miller, Nicolas Tremblay, Pablo J. Zarco-Tejada, and Louise Dextraze. 2002. "Integrated Narrow-Band Vegetation Indices for Prediction of Crop Chlorophyll Content for Application to Precision Agriculture." Remote Sensing of Environment 81(2–3):416–26. doi: 10.1016/S0034-4257(02)00018-4.

Hanak, Ellen, Jeffrey Mount, Caitrin Chappelle, Jay Lund, Josué Medellín-Azuara, Peter Moyle, and Nathaniel Seavy. 2015. "What If California's Drought Continues?" Renewable Resources Journal 29(4):16–23.

Hansen, P. M., and J. K. Schjoerring. 2003. "Reflectance Measurement of Canopy Biomass and Nitrogen Status in Wheat Crops Using Normalized Difference Vegetation Indices and Partial Least Squares Regression." Remote Sensing of Environment 86(4):542–53. doi: 10.1016/S0034-4257(03)00131-7.

Hatfield, J. L., A. A. Gitelson, J. S. Schepers, and C. L. Walthall. 2008. "Application of Spectral Remote Sensing for Agronomic Decisions." Agronomy Journal 100. doi: 10.2134/agronj2006.0370c.

He, Li, Craig A. Coburn, Zhi Jie Wang, Wei Feng, and Tian Cai Guo. 2019a. "Reduced Prediction Saturation and View Effects for Estimating the Leaf Area Index of Winter Wheat." IEEE Transactions on Geoscience and Remote Sensing 57(3):1637–52. doi: 10.1109/TGRS.2018.2868138.

He, Li, Ainong Li, Gaofei Yin, Xi Nan, and Jinhu Bian. 2019b. "Retrieval of Grassland Aboveground Biomass through Inversion of the PROSAIL Model with MODIS Imagery." Remote Sensing 11(13). doi: 10.3390/rs11131597.

He, Li, Hai Yan Zhang, Yuan Shuai Zhang, Xiao Song, Wei Feng, Guo Zhang Kang, Chen Yang Wang, and Tian Cai Guo. 2016. "Estimating Canopy Leaf Nitrogen Concentration in Winter Wheat Based on Multi-Angular Hyperspectral Remote Sensing." European Journal of Agronomy 73:170–85. doi: 10.1016/j.eja.2015.11.017.

Heitholt, J. J., R. C. Johnson, and D. M. Ferris. 1991. "Stomatal Limitation to Carbon Dioxide Assimilation in Nitrogen and Drought-Stressed Wheat." Crop Science 31(1):135–39. doi: 10.2135/cropsci1991.0011183x003100010032x.

Hively, W. Dean, Brian T. Lamb, Craig S. T. Daughtry, Guy Serbin, Philip Dennison, Raymond F. Kokaly, Zhuoting Wu, and Jeffery G. Masek. 2021. "Evaluation of SWIR Crop Residue Bands for the Landsat next Mission." Remote Sensing 13(18). doi: 10.3390/rs13183718.

Hively, W. Dean, Jacob Shermeyer, Brian T. Lamb, Craig T. Daughtry, Miguel Quemada, and Jason Keppler. 2019. "Mapping Crop Residue by Combining Landsat and Worldview-3 Satellite Imagery." Remote Sensing 11(16):1–21. doi: 10.3390/rs11161857.

Hoogmoed, Marianne, and Victor O. Sadras. 2018. "Water Stress Scatters Nitrogen Dilution Curves in Wheat." Frontiers in Plant Science 9:1–11. doi: 10.3389/fpls.2018.00406.

Horler, D. N. H., M. Dockray, and J. Barber. 1983. "The Red Edge of Plant Leaf Reflectance." International Journal of Remote Sensing 4(2):273–88. doi: 10.1080/01431168308948546.

Houlès, Vianney, Martine Guérif, and Bruno Mary. 2007. "Elaboration of a Nitrogen Nutrition Indicator for Winter Wheat Based on Leaf Area Index and Chlorophyll Content for Making Nitrogen Recommendations." European Journal of Agronomy 27(1):1–11. doi: 10.1016/j.eja.2006.10.001.

Howitt, Richard, Josué Medellín-Azuara, Duncan MacEwan, Jay Lund, and Daniel Sumner. 2015. "Economic Analysis of the 2015 Drought For California Agriculture." Center for Watershed Sciences. University of California, Davis, California 20p.

Huete, A., K. Didan, T. Miura, E. P. Rodriguez, X. Gao, and L. G. Ferreira. 2002. "Overview of the Radiometric and Biophysical Performance of the MODIS Vegetation Indices." Remote Sensing of Environment. doi: https://doi.org /10.1016/S0034-4257(02)00096-2.

Huete, A. R. 1988. "A Soil-Adjusted Vegetation Index (SAVI)." Remote Sensing of Environment 25(3):295–309. doi: 10.1016/0034-4257(88)90106-X.

Hunt, E. Raymond, Craig S. T. Daughtry, and Li Li. 2016. "Feasibility of Estimating Leaf Water Content Using Spectral Indices from WorldView-3's near-Infrared and

Shortwave Infrared Bands." International Journal of Remote Sensing 37(2):388–402. doi: 10.1080/01431161.2015.1128575.

Hunt, Merryn L., George Alan Blackburn, Luis Carrasco, John W. Redhead, and Clare S. Rowland. 2019. "High Resolution Wheat Yield Mapping Using Sentinel-2." Remote Sensing of Environment 233:111410. doi: 10.1016/j.rse.2019.111410.

Idso, S. B., R. D. Jackson, P. J. Pinter, R. J. Reginato, and J. L. Hatfield. 1981. "Normalizing the Stress-Degree-Day Parameter for Environmental Variability." Agricultural Meteorology 24:45–55. doi: 10.1016/0002-1571(81)90032-7.

Idso, Sherwood B. 1982. "Non-Water-Stressed Baselines: A Key to Measuring and Interpreting Plant Water Stress." Agricultural Meteorology 27(1–2):59–70. doi: 10.1016/0002-1571(82)90020-6.

Idso, Sherwood B., Ray D. Jackson, and Robert J. Reginato. 1977. "Remote-Sensing of Crop Yields." Science 196(4285):19–25. doi: 10.1126/science.196.4285.19.

Immitzer, Markus, Francesco Vuolo, and Clement Atzberger. 2016. "First Experience with Sentinel-2 Data for Crop and Tree Species Classifications in Central Europe." Remote Sensing 8(3). doi: 10.3390/rs8030166.

Inoue, Yoshio, Martine Guérif, Frédéric Baret, Andrew Skidmore, Anatoly Gitelson, Martin Schlerf, Roshanak Darvishzadeh, and Albert Olioso. 2016. "Simple and Robust Methods for Remote Sensing of Canopy Chlorophyll Content: A Comparative Analysis of Hyperspectral Data for Different Types of Vegetation." Plant Cell and Environment 39(12):2609–23. doi: 10.1111/pce.12815.

Inoue, Yoshio, Eiji Sakaiya, Yan Zhu, and Wataru Takahashi. 2012. "Diagnostic Mapping of Canopy Nitrogen Content in Rice Based on Hyperspectral Measurements." Remote Sensing of Environment 126:210–21. doi: 10.1016/j.rse.2012.08.026.

Irwin, John. 1996. "Full-Spectral Rendering of the Earth's Atmosphere Using a Physical Model of Rayleigh Scattering." Proceedings of the 1996 Eurographics UK Conference 103–15.

Jackson, R. D., S. B. Idso, R. J. Reginato, and P. J. Pinter. 1981. “Canopy Temperature as a Crop Water Stress Indicator.” Water Resources Research 17(4):1133–38. doi: 10.1029/WR017i004p01133.

Jackson, Thomas J., Daoyi Chen, Michael Cosh, Fuqin Li, Martha Anderson, Charles Walthall, Paul Doriaswamy, and E. Ray Hunt. 2004. “Vegetation Water Content Mapping Using Landsat Data Derived Normalized Difference Water Index for Corn and Soybeans.” Remote Sensing of Environment 92(4):475–82. doi: 10.1016/j.rse.2003.10.021.

Jacquemoud, S., and F. Baret. 1990. “PROSPECT: A Model of Leaf Optical Properties Spectra.” Remote Sensing of Environment 34(2):75–91. doi: 10.1016/0034-4257(90)90100-Z.

Jacquemoud, Stéphane, Wout Verhoef, Frédéric Baret, Cédric Bacour, Pablo J. Zarco-Tejada, Gregory P. Asner, Christophe François, and Susan L. Ustin. 2009. “PROSPECT + SAIL Models: A Review of Use for Vegetation Characterization.” Remote Sensing of Environment 113:S56–66. doi: 10.1016/j.rse.2008.01.026.

Jet Propulsion Laboratory. 2023a. “NASA-Led Campaign Studies Hawaii’s Iconic Volcanoes.” Retrieved March 19, 2023 (https://aviris.jpl.nasa.gov/).

Jet Propulsion Laboratory. 2023b. “AVIRIS Overview.” Retrieved March 19, 2023 (https://aviris.jpl.nasa.gov/aviris/index.html).

Jet Propulsion Laboratory. 2023c. “Airborne Visible/Infrared Imaging-Spectrometer Data Portal.” Retrieved October 1, 2022 (https://aviris.jpl.nasa.gov/dataportal/).

Jin, Yufang, Feng Gao, Crystal B. Schaaf, Xiaowen Li, Alan H. Strahler, Carol J. Bruegge, John V Martonchik, and Associate Member. 2002. “Improving MODIS Surface BRDF / Albedo Retrieval.” IEEE Transactions on Geoscience and Remote Sensing 40(7):1593–1604.

Johansen, Kasper, Matteo G. Ziliani, Rasmus Houborg, Trenton E. Franz, and Matthew F. McCabe. 2022. “CubeSat Constellations Provide Enhanced Crop Phenology and Digital Agricultural Insights Using Daily Leaf Area Index Retrievals.” Scientific Reports 12(1):1–12. doi: 10.1038/s41598-022-09376-6.

Jones, H. G. 1999. “Use of Thermography for Quantitative Studies of Spatial and Temporal Variation of Stomatal Conductance over Leaf Surfaces.” Plant, Cell and Environment 22(9):1043–55. doi: 10.1046/j.1365-3040.1999.00468.x.

Justes, E., B. Mary, J. M. Meynard, J. M. Machet, and L. Thelier-Huche. 1994. “Determination of a Critical Nitrogen Dilution Curve for Winter Wheat Crops.” Annals of Botany 74(4):397–407.

Kandil, F. E., M. H. Grace, D. S. Seigler, and J. M. Cheeseman. 2004. “Polyphenolics in Rhizophora Mangle L. Leaves and Their Changes during Leaf Development and Senescence.” Trees - Structure and Function 18(5):518–28. doi: 10.1007/s00468-004-0337-8.

Katkani, Deepak, Anita Babbar, Vipin Kumar Mishra, Ayushi Trivedi, Shweta Tiwari, and Rohit Kumar Kumawat. 2022. “A Review on Applications and Utility of Remote Sensing and Geographic Information Systems in Agriculture and Natural Resource Management.” International Journal of Environment and Climate Change:1–18. doi: 10.9734/ijecc/2022/v12i430651.

Kattge, Jens, Wolfgang Knorr, Thomas Raddatz, and Christian Wirth. 2009. “Quantifying Photosynthetic Capacity and Its Relationship to Leaf Nitrogen Content for Global-Scale Terrestrial Biosphere Models.” Global Change Biology 15(4):976–91. doi: 10.1111/j.1365-2486.2008.01744.x.

Kaufman, Y. J., D. Tanré, L. A. Remer, E. F. Vermote, A. Chu, and B. N. Holben. 1997. “Operational Remote Sensing of Tropospheric Aerosol over Land from EOS Moderate Resolution Imaging Spectroradiometer.” Journal of Geophysical Research Atmospheres 102(14):17051–67. doi: 10.1029/96jd03988.

Keeney, D. R., and D. W. Nelson. 1982. “Nitrogen Inorganic Forms·.” Methods of Soil Analysis 9(9):643–98.

Kerbaol, V., B. Chapron, and P. Vachon. 1998. “Analysis of ERS-1/2 Synthetic Aperture Radar Wave Mode Imagettes.” Journal of Geophysical Research: Oceans 103:7833–46.

Kern County Department of Agriculture and Measurement Standards. 2022a. “Crop Spatial Data.” Retrieved June 1, 2022 (http://www.kernag.com/gis/gis-data.asp).

Kern County Department of Agriculture and Measurement Standards. 2022b. “Planting and Harvesting Dates.” Retrieved June 1, 2022 (http://www.kernag.com/dept/stats/crop-stats.asp).

Kern County Department of Agriculture and Measurement Standards. 2022c. “Kern County Crop Reports.” Retrieved June 1, 2022 (http://www.kernag.com/caap/crop-reports/crop-reports.asp).

Khorchani, Makki, Estela Nadal-Romero, Teodoro Lasanta, and Christina Tague. 2021. “Natural Revegetation and Afforestation in Abandoned Cropland Areas: Hydrological Trends and Changes in Mediterranean Mountains.” Hydrological Processes 35(5):1–18. doi: 10.1002/hyp.14191.

Kichey, Thomas, Bertrand Hirel, Emmanuel Heumez, Frédéric Dubois, and Jacques Le Gouis. 2007. “In Winter Wheat (*Triticum aestivum* L.), Post-Anthesis Nitrogen Uptake and Remobilisation to the Grain Correlates with Agronomic Traits and Nitrogen Physiological Markers.” Field Crops Research 102(1):22–32. doi: 10.1016/j.fcr.2007.01.002.

Kim, Yunjin, and Jakob J. Van Zyl. 2009. “A Time-Series Approach to Estimate Soil Moisture Using Polarimetric Radar Data.” IEEE Transactions on Geoscience and Remote Sensing 47(8):2519–27. doi: 10.1109/TGRS.2009.2014944.

Kings County Department of Agriculture and Measurement Standards. 2022. “Kings County Crop Reports.” Retrieved June 1, 2022 (https://www.countyofkings.com/departments/general-services/agriculture-department-measurement-standards/ag-services/crop-reports-1941-2013/test).

van Klompenburg, Thomas, Ayalew Kassahun, and Cagatay Catal. 2020. “Crop Yield Prediction Using Machine Learning: A Systematic Literature Review.” Computers and Electronics in Agriculture 177:105709. doi: 10.1016/j.compag.2020.105709.

Knipper, Kyle R., William P. Kustas, Martha C. Anderson, Joseph G. Alfieri, John H. Prueger, Christopher R. Hain, Feng Gao, Yun Yang, Lynn G. McKee, Hector Nieto,

Lawrence E. Hipps, Maria Mar Alsina, and Luis Sanchez. 2019. “Evapotranspiration Estimates Derived Using Thermal-Based Satellite Remote Sensing and Data Fusion for Irrigation Management in California Vineyards.” Irrigation Science 37(3):431–49. doi: 10.1007/s00271-018-0591-y.

Kokaly, Raymond F. 2001. “Investigating a Physical Basis for Spectroscopic Estimates of Leaf Nitrogen Concentration.” Remote Sensing of Environment 75(2):153–61. doi: 10.1016/S0034-4257(00)00163-2.

Koukal, Tatjana, Clement Atzberger, and Werner Schneider. 2014. “Evaluation of Semi-Empirical BRDF Models Inverted against Multi-Angle Data from a Digital Airborne Frame Camera for Enhancing Forest Type Classification.” Remote Sensing of Environment 151:27–43. doi: 10.1016/j.rse.2013.12.014.

Kramer, David M., Thomas J. Avenson, and Gerald E. Edwards. 2004. “Dynamic Flexibility in the Light Reactions of Photosynthesis Governed by Both Electron and Proton Transfer Reactions.” Trends in Plant Science 9(7):349–57. doi: 10.1016/j.tplants.2004.05.001.

Kruse, Fred A., William M. Baugh, and Sandra L. Perry. 2015. “Validation of DigitalGlobe WorldView-3 Earth Imaging Satellite Shortwave Infrared Bands for Mineral Mapping.” Journal of Applied Remote Sensing 9(1):096044. doi: 10.1117/1.jrs.9.096044.

Kuester, Michele. 2016. “Radiometric Use of WorldView-3 Imagery.” Technical Note 12.

Kuester, Theres, and Daniel Spengler. 2018. “Structural and Spectral Analysis of Cereal Canopy Reflectance and Reflectance Anisotropy.” Remote Sensing 10(11). doi: 10.3390/rs10111767.

Kusnierek, Krzysztof, and Audun Korsaeth. 2015. “Simultaneous Identification of Spring Wheat Nitrogen and Water Status Using Visible and near Infrared Spectra and Powered Partial Least Squares Regression.” Computers and Electronics in Agriculture 117:200–213. doi: 10.1016/j.compag.2015.08.001.

Ladha, Jagdish K., Himanshu Pathak, Timothy J. Krupnik, J. Six, and Chris van Kessel. 2005. “Efficiency of Fertilizer Nitrogen in Cereal Production: Retrospects and

Prospects." Advances in Agronomy 87(05):85–156. doi: 10.1016/S0065-2113(05)87003-8.

Lanari, Riccardo, Manuela Bonano, Francesco Casu, Claudio De Luca, Michele Manunta, Mariarosaria Manzo, Giovanni Onorato, and Ivana Zinno. 2020. "Automatic Generation of Sentinel-1 Continental Scale DInSAR Deformation Time Series through an Extended P-SBAS Processing Pipeline in a Cloud Computing Environment." Remote Sensing 12(18). doi: 10.3390/RS12182961.

Lassaletta, Luis, Gilles Billen, Bruna Grizzetti, Juliette Anglade, and Josette Garnier. 2014. "50 Year Trends in Nitrogen Use Efficiency of World Cropping Systems: The Relationship between Yield and Nitrogen Input to Cropland." Environmental Research Letters 9(10). doi: 10.1088/1748-9326/9/10/105011.

Lebourgeois, Valentine, Stéphane Dupuy, Élodie Vintrou, Maël Ameline, Suzanne Butler, and Agnès Bégué. 2017. "A Combined Random Forest and OBIA Classification Scheme for Mapping Smallholder Agriculture at Different Nomenclature Levels Using Multisource Data (Simulated Sentinel-2 Time Series, VHRS and DEM)." Remote Sensing 9(3):1–20. doi: 10.3390/rs9030259.

Lehnert, L. W., H. Meyer, and J. Bendix. 2020. "Hsdar: Manage, Analyse and Simulate Hyperspectral Data. R Package Version 1.0.3." Retrieved (https://cran.r-project.org/web/packages/hsdar/index.html).

Lemaire, Gilles, Marie Hélène Jeuffroy, and François Gastal. 2008. "Diagnosis Tool for Plant and Crop N Status in Vegetative Stage. Theory and Practices for Crop N Management." European Journal of Agronomy 28(4):614–24. doi: 10.1016/j.eja.2008.01.005.

Leroux, Louise, Mathieu Castets, Christian Baron, Maria Jose Escorihuela, Agnès Bégué, and Danny Lo Seen. 2019. "Maize Yield Estimation in West Africa from Crop Process-Induced Combinations of Multi-Domain Remote Sensing Indices." European Journal of Agronomy 108:11–26. doi: 10.1016/j.eja.2019.04.007.

Lesk, Corey, Pedram Rowhani, and Navin Ramankutty. 2016. “Influence of Extreme Weather Disasters on Global Crop Production.” Nature 529(7584):84–87. doi: 10.1038/nature16467.

Li, Dong, Xue Wang, Hengbiao Zheng, Kai Zhou, Xia Yao, Yongchao Tian, Yan Zhu, Weixing Cao, and Tao Cheng. 2018. “Estimation of Area- and Mass-Based Leaf Nitrogen Contents of Wheat and Rice Crops from Water-Removed Spectra Using Continuous Wavelet Analysis.” Plant Methods 14(1):1–20. doi: 10.1186/s13007-018-0344-1.

Li, Fei, Dan Li, Salah Elsayed, Yuncai Hu, and Urs Schmidhalter. 2021. “Using Optimized Three-Band Spectral Indices to Assess Canopy N Uptake in Corn and Wheat.” European Journal of Agronomy 127:126286. doi: 10.1016/j.eja.2021.126286.

Li, Fei, Bodo Mistele, Yuncai Hu, Xinping Chen, and Urs Schmidhalter. 2013a. “Comparing Hyperspectral Index Optimization Algorithms to Estimate Aerial n Uptake Using Multi-Temporal Winter Wheat Datasets from Contrasting Climatic and Geographic Zones in China and Germany.” Agricultural and Forest Meteorology 180:44–57. doi: 10.1016/j.agrformet.2013.05.003.

Li, Heli, Chunjiang Zhao, Wenjiang Huang, and Guijun Yang. 2013b. “Non-Uniform Vertical Nitrogen Distribution within Plant Canopy and Its Estimation by Remote Sensing: A Review.” Field Crops Research 142(11):75–84. doi: 10.1016/j.fcr.2012.11.017.

Liang, S., and J. Wang. 2019. Advanced Remote Sensing: Terrestrial Information Extraction And Applications. Academic Press. Elsevier, Amsterdam.

Liang, Shunlin, Hongliang Fang, Jeffrey T. Morisette, Mingzhen Chen, Chad J. Shuey, Charles L. Walthall, and Craig S. T. Daughtry. 2002. “Atmospheric Correction of Landsat ETM+ Land Surface Imagery - Part II: Validation and Applications.” IEEE Transactions on Geoscience and Remote Sensing 40(12):2736–46. doi: 10.1109/TGRS.2002.807579.

Liaw, A., and M. Wiener. 2002. “Classification and Regression by RandomForest.” R News 2(3):18–22.

Lin, Shangrong, Jing Li, Qinhuo Liu, Longhui Li, Jing Zhao, and Wentao Yu. 2019. "Evaluating the Effectiveness of Using Vegetation Indices Based on Red-Edge Reflectance from Sentinel-2 to Estimate Gross Primary Productivity." Remote Sensing 11(11). doi: 10.3390/rs11111303.

Liu, Shuaiqi, Lele Gao, Yu Lei, Miaohui Wang, Qi Hu, and Yu-dong Zhang. 2021. "SAR Speckle Removal Using Hybrid Frequency Modulations." IEEE Transactions on Geoscience and Remote Sensing 59(5):3956–66. doi: 10.1109/TGRS.2020.3014130.

Liu, Tao, Amr Abd-Elrahman, Bon Dewitt, Scot Smith, Jon Morton, and Victor L. Wilhelm. 2019a. "Evaluating the Potential of Multi-View Data Extraction from Small Unmanned Aerial Systems (UASs) for Object-Based Classification for Wetland Land Covers." GIScience and Remote Sensing 56(1):130–59. doi: 10.1080/15481603.2018.1495395.

Liu, Xiang Dong, and Qi Hua Sun. 2016. "Early Assessment of the Yield Loss in Rice Due to the Brown Planthopper Using a Hyperspectral Remote Sensing Method." International Journal of Pest Management 62(3):205–13. doi: 10.1080/09670874.2016.1174791.

Liu, Zhen, Pang Wei Liu, Elias Massoud, Tom G. Farr, Paul Lundgren, and James S. Famiglietti. 2019b. "Monitoring Groundwater Change in California's Central Valley Using Sentinel-1 and Grace Observations." Geosciences 9(10). doi: 10.3390/geosciences9100436.

Lloret, Francisco, Eduard Calvo, Xavier Pons, and Ricardo Díaz-Delgado. 2002. "Wildfires and Landscape Patterns in the Eastern Iberian Peninsula." Landscape Ecology 17(8):745–59. doi: 10.1023/A:1022966930861.

Lobell, David B., Wolfram Schlenker, and Justin Costa-Roberts. 2011. "Climate Trends and Global Crop Production since 1980." Science 333(6042):616–20. doi: 10.1126/science.1204531.

Long, D. S., R. E. Engel, and M. C. Siemens. 2008. "Measuring Grain Protein Concentration with In-Line near Infrared Reflectance Spectroscopy." Agronomy Journal 100(2):247–52. doi: 10.2134/agronj2007.0052.

Longmire, A. R., T. Poblete, J. R. Hunt, D. Chen, and P. J. Zarco-Tejada. 2022. "Assessment of Crop Traits Retrieved from Airborne Hyperspectral and Thermal Remote Sensing Imagery to Predict Wheat Grain Protein Content." ISPRS Journal of Photogrammetry and Remote Sensing 193:284–98. doi: 10.1016/j.isprsjprs.2022.09.015.

Loredana, Pompilio, Boschetti Mirco, Petito Matteo, Pisante Michele, Luigi Ranghetti, and Pepe Monica. 2021. "Mapping Cellulose Absorption Band in Npv Using Prisma Data." International Geoscience and Remote Sensing Symposium (IGARSS) 475–78. doi: 10.1109/IGARSS47720.2021.9554048.

Lucht, W., and J. L. Roujean. 2000. "Considerations in the Parametric Modeling of BRDF and Albedo from Multiangular Satellite Sensor Observations." Remote Sensing Reviews 18(2):343–79. doi: 10.1080/02757250009532395.

Lund, Jay, Josue Medellin-Azuara, John Durand, and Kathleen Stone. 2018. "Lessons from California's 2012–2016 Drought." Journal of Water Resources Planning and Management 144(10):04018067. doi: 10.1061/(asce)wr.1943-5452.0000984.

Ma, Lei, Yu Liu, Xueliang Zhang, Yuanxin Ye, Gaofei Yin, and Brian Alan Johnson. 2019. "Deep Learning in Remote Sensing Applications: A Meta-Analysis and Review." ISPRS Journal of Photogrammetry and Remote Sensing 152:166–77. doi: 10.1016/j.isprsjprs.2019.04.015.

MacEwan, Duncan, Mesut Cayar, Ali Taghavi, David Mitchell, Steve Hatchett, and Richard Howitt. 2017. "Hydroeconomic Modeling of Sustainable Groundwater Management." Journal of the American Water Resources Association 5(3):2–2. doi: 10.1111/j.1752-1688.1969.tb04897.x.

Main-Knorn, Magdalena, Bringfried Pflug, Jerome Louis, Vincent Debaecker, Uwe Müller-Wilm, and Ferran Gascon. 2017. "Sen2Cor for Sentinel-2." doi: 10.1117/12.2278218.

Makino, Amane. 2003. "Rubisco and Nitrogen Relationships in Rice: Leaf Photosynthesis and Plant Growth." Soil Science and Plant Nutrition 49(3):319–27. doi: 10.1080/00380768.2003.10410016.

Makino, Amane, and Barry Osmond. 1991. “Effects of Nitrogen Nutrition on Nitrogen Partitioning between Chloroplasts and Mitochondria in Pea and Wheat.” Plant Physiology 96(2):355–62. doi: 10.1104/pp.96.2.355.

Manakos, I., K. Manevski, C. Kalaitzidis, and D. Edler. 2011. “Comparison between Atmospheric Correction Modules on the Basis of Worldview-2 Imagery and in Situ Spectroradiometric Measurements.” 7th EARSeL SIG Imaging Spectroscopy Workshop 11–13.

Mandal, Dipankar, Vineet Kumar, Debanshu Ratha, Subhadip Dey, Avik Bhattacharya, Juan M. Lopez-Sanchez, Heather McNairn, and Yalamanchili S. Rao. 2020. “Dual Polarimetric Radar Vegetation Index for Crop Growth Monitoring Using Sentinel-1 SAR Data.” Remote Sensing of Environment 247. doi: 10.1016/j.rse.2020.111954.

Manfreda, Salvatore, Matthew F. McCabe, Pauline E. Miller, Richard Lucas, Victor Pajuelo Madrigal, Giorgos Mallinis, Eyal Ben Dor, David Helman, Lyndon Estes, Giuseppe Ciraolo, Jana Müllerová, Flavia Tauro, M. Isabel de Lima, João L. M. P. de Lima, Antonino Maltese, Felix Frances, Kelly Caylor, Marko Kohv, Matthew Perks, Guiomar Ruiz-Pérez, Zhongbo Su, Giulia Vico, and Brigitta Toth. 2018. “On the Use of Unmanned Aerial Systems for Environmental Monitoring.” Remote Sensing 10(4). doi: 10.3390/rs10040641.

MAPA (Ministerio de agricultura, pesca y alimentación). 2023. “Weather Information for Irrigation (SiAR).” Retrieved March 29, 2023 (https://eportal.mapa.gob.es/websiar/SeleccionParametrosMap.aspx?dst=1).

Mariotti, François, Daniel Tomé, and Philippe Patureau Mirand. 2008. “Converting Nitrogen into Protein - Beyond 6.25 and Jones’ Factors.” Critical Reviews in Food Science and Nutrition 48(2):177–84. doi: 10.1080/10408390701279749.

Marti, J., J. Bort, G. A. Slafer, and J. L. Araus. 2007. “Can Wheat Yield Be Assessed by Early Measurements of Normalized Difference Vegetation Index?” Annals of Applied Biology 150(2):253–57. doi: 10.1111/j.1744-7348.2007.00126.x.

Martins, Vitor Souza, Claudio Clemente Faria Barbosa, Lino Augusto Sander de Carvalho, Daniel Schaffer Ferreira Jorge, Felipe de Lucia Lobo, and Evlyn Márcia Leão de

Moraes Novo. 2017. “Assessment of Atmospheric Correction Methods for Sentinel-2 MSI Images Applied to Amazon Floodplain Lakes.” Remote Sensing 9(4). doi: 10.3390/rs9040322.

Masseroni, Daniele, Bianca Ortuani, Martina Corti, Pietro Marino Gallina, Giacomo Cocetta, Antonio Ferrante, and Arianna Facchi. 2017. “Assessing the Reliability of Thermal and Optical Imaging Techniques for Detecting Crop Water Status under Different Nitrogen Levels.” Sustainability 9(9):1–20. doi: 10.3390/su9091548.

Matthew, M. W., S. M. Adler-Golden, A. Berk, S. C. Richtsmeier, R. Y. Levine, L. S. Bernstein, P. K. Acharya, G. P. Anderson, G. W. Felde, M. L. Hoke, and A. J. Ratkowski. 2000. “Status of Atmospheric Correction Using a MODTRAN4-Based Algorithm.” Algorithms for Multispectral, Hyperspectral, and Ultraspectral Imagery VI. SPIE 4049(April).

McAllister, Emma, Andres Payo, Alessandro Novellino, Tony Dolphin, and Encarni Medina-Lopez. 2022. “Multispectral Satellite Imagery and Machine Learning for the Extraction of Shoreline Indicators.” Coastal Engineering 174:104102. doi: 10.1016/j.coastaleng.2022.104102.

McMullan, Patrick M., Peter E. E. McVetty, and Aileen A. Urquhart. 1988. “Dry Matter and Nitrogen Accumulation and Redistribution and Their Relationship To Grain Yield and Grain Protein in Oats.” Canadian Journal of Plant Science 68(4):983–93. doi: 10.4141/cjps88-119.

McNairn, Heather, and Jiali Shang. 2016. “A Review of Multitemporal Synthetic Aperture Radar (SAR) for Crop Monitoring.” Remote Sensing and Digital Image Processing 20:317–40. doi: 10.1007/978-3-319-47037-5_15.

Medrano, H., M. A. J. Parry, X. Socias, and D. W. Lawlor. 1997. “Long Term Water Stress Inactivates Rubisco in Subterranean Clover.” Annals of Applied Biology 131(3):491–501. doi: 10.1111/j.1744-7348.1997.tb05176.x.

Meerdink, Susan K., D. A. Roberts, Keely L. Roth, Jennifer Y. King, Paul D. Gader, and Alexander Koltunov. 2019. “Classifying California Plant Species Temporally Using

Airborne Hyperspectral Imagery." Remote Sensing of Environment 232:111308. doi: 10.1016/j.rse.2019.111308.

Mehdaoui, Rim, and Makram Anane. 2020. "Exploitation of the Red-Edge Bands of Sentinel 2 to Improve the Estimation of Durum Wheat Yield in Grombalia Region (Northeastern Tunisia)." International Journal of Remote Sensing 41(23):8984–9006. doi: 10.1080/01431161.2020.1797217.

Meier, Uwe. 2001. "Growth Stages of Mono-and Dicotyledonous Plants: BBCH Monograph, 2nd Ed." Federal Biological Research Centre for Agriculture and Forestry 49(2):66–70.

Meroni, M., L. Busetto, R. Colombo, L. Guanter, J. Moreno, and W. Verhoef. 2010. "Performance of Spectral Fitting Methods for Vegetation Fluorescence Quantification." Remote Sensing of Environment 114(2):363–74. doi: 10.1016/j.rse.2009.09.010.

Meroni, M., and R. Colombo. 2006. "Leaf Level Detection of Solar Induced Chlorophyll Fluorescence by Means of a Subnanometer Resolution Spectroradiometer." Remote Sensing of Environment 103(4):438–48. doi: 10.1016/j.rse.2006.03.016.

Michaelsen, Anne-Sofie. 2013. "Public Archives and Other Sources for Surveying of Dumpsites and Polluting Enterprises before 1950." The Journal of Transdisciplinary Environmental Studies 12(2):29.

Milenov, Pavel, Vassil Vassilev, Anna Vassileva, Radko Radkov, Vessela Samoungi, Zlatomir Dimitrov, and Nikola Vichev. 2014. "Monitoring of the Risk of Farmland Abandonment as an Efficient Tool to Assess the Environmental and Socio-Economic Impact of the Common Agriculture Policy." International Journal of Applied Earth Observation and Geoinformation 32(1):218–27. doi: 10.1016/j.jag.2014.03.013.

Miller, David L., Erin B. Wetherley, Dar A. Roberts, Christina L. Tague, and Joseph P. Mcfadden. 2022. "Urban Climate Vegetation Cover Change during a Multi-Year Drought in Los Angeles." Urban Climate 43:101157. doi: 10.1016/j.uclim.2022.101157.

Milton, Edward J., Michael E. Schaepman, Karen Anderson, Mathias Kneubühler, and Nigel Fox. 2009. "Progress in Field Spectroscopy." Remote Sensing of Environment 113:S92–109. doi: 10.1016/j.rse.2007.08.001.

Min, M., and W. S. Lee. 2005. "Determination of Significant Wavelengths and Prediction of Nitrogen Content for Citrus." Transactions of the American Society of Agricultural Engineers 48(2):455–61. doi: 10.13031/2013.18308.

Mistele, Bodo, and Urs Schmidhalter. 2008. "Estimating the Nitrogen Nutrition Index Using Spectral Canopy Reflectance Measurements." European Journal of Agronomy 29(4):184–90. doi: 10.1016/j.eja.2008.05.007.

Mitchell, J. P., L. M. Carter, D. C. Reicosky, A. Shrestha, G. S. Pettygrove, K. M. Klonsky, D. B. Marcum, D. Chessman, R. Roy, P. Hogan, and L. Dunning. 2016. "A History of Tillage in California's Central Valley." Soil and Tillage Research 157:52–64. doi: 10.1016/j.still.2015.10.015.

Mohammed, Gina H., Roberto Colombo, Elizabeth M. Middleton, Uwe Rascher, Christiaan van der Tol, Ladislav Nedbal, Yves Goulas, O. Pérez-Priego, Alexander Damm, Michele Meroni, Joanna Joiner, Sergio Cogliati, Wouter Verhoef, Zbyněk Malenovský, Jean Philippe Gastellu-Etchegorry, John R. Miller, Luis Guanter, Jose Moreno, Ismael Moya, Joseph A. Berry, Christian Frankenberg, and Pablo J. Zarco-Tejada. 2019. "Remote Sensing of Solar-Induced Chlorophyll Fluorescence (SIF) in Vegetation: 50 years of Progress." Remote Sensing of Environment 231. doi: 10.1016/j.rse.2019.04.030.

Möller, M., V. Alchanatis, Y. Cohen, M. Meron, J. Tsipris, A. Naor, V. Ostrovsky, M. Sprintsin, and S. Cohen. 2007. "Use of Thermal and Visible Imagery for Estimating Crop Water Status of Irrigated Grapevine." Journal of Experimental Botany 58(4):827–38. doi: 10.1093/jxb/erl115.

Mon, Jarai, K. F. Bronson, D. J. Hunsaker, K. R. Thorp, J. W. White, and A. N. French. 2016. "Interactive Effects of Nitrogen Fertilization and Irrigation on Grain Yield, Canopy Temperature, and Nitrogen Use Efficiency in Overhead Sprinkler-Irrigated Durum Wheat." Field Crops Research 191:54–65. doi: 10.1016/j.fcr.2016.02.011.

Monje, O. A., and B. Bugbee. 1992. “Inherent Limitations of Nondestructive Chlorophyll Meters: A Comparison of Two Types of Meters.” HortScience : A Publication of the American Society for Horticultural Science 27(1):69–71. doi: 10.21273/hortsci.27.1.69.

Moran, M. S., T. R. Clarke, Y. Inoue, and A. Vidal. 1994. “Estimating Crop Water Deficit Using the Relation between Surface-Air Temperature and Spectral Vegetation Index.” Remote Sensing of Environment 49(3):246–63. doi: 10.1016/0034-4257(94)90020-5.

Moreira, Alberto, Pau Prats-Iraola, Marwan Younis, Gerhard Krieger, Irena Hajnsek, and Konstantinos P. Papathanassiou. 2013. “A Tutorial on Synthetic Aperture Radar.” IEEE Geoscience and Remote Sensing Magazine 1(1):6–43. doi: 10.1109/MGRS.2013.2248301.

Mousivand, Alijafar, Wout Verhoef, Massimo Menenti, and Ben Gorte. 2015. “Modeling Top of Atmosphere Radiance over Heterogeneous Non-Lambertian Rugged Terrain.” Remote Sensing 7(6):8019–44. doi: 10.3390/rs70608019.

Moya, I., L. Camenen, S. Evain, Y. Goulas, Z. G. Cerovic, G. Latouche, J. Flexas, and A. Ounis. 2004. “A New Instrument for Passive Remote Sensing: 1. Measurements of Sunlight-Induced Chlorophyll Fluorescence.” Remote Sensing of Environment 91(2):186–97. doi: 10.1016/j.rse.2004.02.012.

Munden, R., P. J. Curran, and J. A. Catt. 1994. “The Relationship between Red Edge and Chlorophyll Concentration in the Broadbalk Winter Wheat Experiment at Rothamsted.” International Journal of Remote Sensing 15(3):705–9. doi: 10.1080/01431169408954110.

Mutanga, Onisimo, Elhadi Adam, and Moses Azong Cho. 2012. “High Density Biomass Estimation for Wetland Vegetation Using Worldview-2 Imagery and Random Forest Regression Algorithm.” International Journal of Applied Earth Observation and Geoinformation 18(1):399–406. doi: 10.1016/j.jag.2012.03.012.

National Academy of Sciences Engineering and Medicine. 2018. “Thriving on Our Changing Planet A Decadal Strategy for Earth Observation from Space (2018).” Retrieved

March 19, 2023 (https://nap.nationalacademies.org/catalog/24938/thriving-on-our-changing-planet-a-decadal-strategy-for-earth).

National Aeronautics and Space Administration. 2023a. "NASA Armstrong Fact Sheet: ER-2 High-Altitude Airborne Science Aircraft." Retrieved March 19, 2023 (https://www.nasa.gov/centers/armstrong/news/FactSheets/FS-046-DFRC.html).

National Aeronautics and Space Administration. 2023b. "Moderate Resolution Imaging Spectroradiometer." Retrieved March 19, 2023 (https://modis.gsfc.nasa.gov/).

National Aeronautics and Space Administration. 2023c. "Atmosphere Discipline Team Imager Products." Retrieved March 19, 2023 (https://atmosphere-imager.gsfc.nasa.gov/).

National Aeronautics and Space Administration. 2023d. "AErosol RObotic NETwork (AERONET)." Retrieved April 7, 2020 (https://aeronet.gsfc.nasa.gov/).

National Aeronautics and Space Administration. 2023e. "Level-1 and Atmosphere Archive and Distribution System (LAADS) Distributed Active Archive Center (DAAC). MOD07 and MOD11C1 Products." Retrieved April 7, 2020 (https://ladsweb.modaps.eosdis.nasa.gov/search/order/1/MODIS:Terra).

National Aeronautics and Space Administration. 2023f. "Level-1 and Atmosphere Archive and Distribution System (LAADS) Distributed Active Archive Center (DAAC). MCD19A2 Products." Retrieved April 7, 2020 (https://ladsweb.modaps.eosdis.nasa.gov/search/order/1/MCD19A2--6).

National Aeronautics and Space Administration. 2023g. "Level-1 and Atmosphere Archive and Distribution System (LAADS) Distributed Active Archive Center (DAAC). MCD43A1 Products." Retrieved April 7, 2020 (https://ladsweb.modaps.eosdis.nasa.gov/missions-and-measurements/products/MCD43A1/).

Neuhaus, Andreas, Marianne Hoogmoed, and Victor Sadras. 2017. "Closing the Yield Gap for Wheat and Canola through an Adjusted Nitrogen Nutrition Index." Better Crops with Plant Food 101(3):16–18.

Nishikawa, Kelly. 2016. “The end of an era: California’s first attempt to manage its groundwater resources through its sustainable groundwater management act and its impact on almond farmers.” Environmental Claims Journal 28(3):206–22. doi: 10.1080/10406026.2016.1129294.

O’Shaughnessy, Susan A., Steven R. Evett, and Paul D. Colaizzi. 2015. “Dynamic Prescription Maps for Site-Specific Variable Rate Irrigation of Cotton.” Agricultural Water Management 159:123–38. doi: 10.1016/j.agwat.2015.06.001.

Office of Governor Edmund G. Brown Jr. 2014. “Governor of California Declares Drought State of Emergency.” Retrieved August 3, 2022 (https://www.ca.gov/archive/gov39/2014/01/17/news18368/index.html).

Osborne, S. L., J. S. Schepers, D. D. Francis, and M. R. Schlemmer. 2002. “Detection of Phosphorus and Nitrogen Deficiencies in Corn Using Spectral Radiance Measurements.” Agronomy Journal 94(6):1215–21. doi: 10.2134/agronj2002.1215.

Otero, Iago, Martí Boada, Anna Badia, Eduard Pla, Jordi Vayreda, Santi Sabaté, Carles A. Gracia, and Josep Peñuelas. 2011. “Loss of Water Availability and Stream Biodiversity under Land Abandonment and Climate Change in a Mediterranean Catchment (Olzinelles, NE Spain).” Land Use Policy 28(1):207–18. doi: 10.1016/j.landusepol.2010.06.002.

Ottman, M. J., T. A. Doerge, and E. C. Martin. 2000. “Durum Grain Quality as Affected by Nitrogen Fertilization near Anthesis and Irrigation during Grain Fill.” Agronomy Journal 92(5):1035–41. doi: 10.2134/agronj2000.9251035x.

Pacifici, Fabio, Nathan Longbotham, and William J. Emery. 2014. “The Importance of Physical Quantities for the Analysis of Multitemporal and Multiangular Optical Very High Spatial Resolution Images.” IEEE Transactions on Geoscience and Remote Sensing 52(10):6241–56. doi: 10.1109/TGRS.2013.2295819.

Paek, Sung Wook, Sivagaminathan Balasubramanian, Sangtae Kim, and Olivier de Weck. 2020. “Small-Satellite Synthetic Aperture Radar for Continuous Global Biospheric Monitoring: A Review.” Remote Sensing 12(16). doi: 10.3390/RS12162546.

Palombi, Lorenzo, Giovanna Cecchi, David Lognoli, Valentina Raimondi, Guido Toci, and Giovanni Agati. 2011. “A Retrieval Algorithm to Evaluate the Photosystem I and Photosystem II Spectral Contributions to Leaf Chlorophyll Fluorescence at Physiological Temperatures.” Photosynthesis Research 108(2–3):225–39. doi: 10.1007/s11120-011-9678-5.

Patel, Raj. 2013. “The Long Green Revolution.” Journal of Peasant Studies 40(1):1–63. doi: 10.1080/03066150.2012.719224.

Pietragalla, J., and A. Pask. 2019. “Stomatal Conductance. Physiological Breeding II: A Field Guide to Wheat Phenotyping. A. Pask, J. Pietragalla, D. Mullan & M. Reynolds (Eds.).” México, CIMMYT, pp.15-17. doi: 10.1017/9781107339217.013.

Pingali, Prabhu L. 2012. “Green Revolution: Impacts, Limits, Andthe Path Ahead.” Proceedings of the National Academy of Sciences of the United States of America 109(31):12302–8. doi: 10.1073/pnas.0912953109.

Plascyk, James A., and Fred C. Gabriel. 1975. “The Fraunhofer Line Discriminator MKII-An Airborne Instrument for Precise and Standardized Ecological Luminescence Measurement.” IEEE Transactions on Instrumentation and Measurement 24(4):306–13. doi: 10.1109/TIM.1975.4314448.

Prey, Lukas, and Urs Schmidhalter. 2019a. “Simulation of Satellite Reflectance Data Using High-Frequency Ground Based Hyperspectral Canopy Measurements for in-Season Estimation of Grain Yield and Grain Nitrogen Status in Winter Wheat.” ISPRS Journal of Photogrammetry and Remote Sensing 149:176–87. doi: 10.1016/j.isprsjprs.2019.01.023.

Prey, Lukas, and Urs Schmidhalter. 2019b. “Temporal and Spectral Optimization of Vegetation Indices for Estimating Grain Nitrogen Uptake and Late-Seasonal Nitrogen Traits in Wheat.” Sensors 19(21):1–27. doi: 10.3390/s19214640.

Qian, Shen En. 2021. “Hyperspectral Satellites, Evolution, and Development History.” IEEE Journal of Selected Topics in Applied Earth Observations and Remote Sensing 14:7032–56. doi: 10.1109/JSTARS.2021.3090256.

Qiu, Ruicheng, Shuang Wei, Man Zhang, Han Li, Hong Sun, Gang Liu, and Minzan Li. 2018. “Sensors for Measuring Plant Phenotyping: A Review.” International Journal of Agricultural and Biological Engineering 11(2):1–17. doi: 10.25165/j.ijabe.20181102.2696.

Qiu, Shi, Yukun Lin, Rong Shang, Junxue Zhang, Lei Ma, and Zhe Zhu. 2019. “Making Landsat Time Series Consistent: Evaluating and Improving Landsat Analysis Ready Data.” Remote Sensing 11(1). doi: 10.3390/rs11010051.

Quemada, M., W. D. Hively, C. S. T. Daughtry, B. T. Lamb, and J. Shermeyer. 2018. “Improved Crop Residue Cover Estimates Obtained by Coupling Spectral Indices for Residue and Moisture.” Remote Sensing of Environment 206:33–44. doi: 10.1016/j.rse.2017.12.012.

Quemada, Miguel, and Craig S. T. Daughtry. 2016. “Spectral Indices to Improve Crop Residue Cover Estimation under Varying Moisture Conditions.” Remote Sensing 8(8). doi: 10.3390/rs8080660.

Quemada, Miguel, and Jose L. Gabriel. 2016. “Approaches for Increasing Nitrogen and Water Use Efficiency Simultaneously.” Global Food Security 9:29–35. doi: 10.1016/j.gfs.2016.05.004.

Quemada, Miguel, Jose Luis Gabriel, and Pablo Zarco-Tejada. 2014. “Airborne Hyperspectral Images and Ground-Level Optical Sensors as Assessment Tools for Maize Nitrogen Fertilization.” Remote Sensing 6(4):2940–62. doi: 10.3390/rs6042940.

R Core Team. 2021. “R: A Language and Environment for Statistical Computing.” Retrieved (https://www.r-project.org/).

Rahman, Hafizur, Bernard Pinty, and Michel M. Verstraete. 1993. “Coupled Surface-Atmosphere Reflectance (CSAR) Model Very High Resolution Radiometer Data.” Journal of Geophysical Research 98(93):20,791-20,801. doi: 10.1029/93JD02072

Rahman, Muhammad Moshiur, Andrew Robson, and Mila Bristow. 2018. “Exploring the Potential of High Resolution Worldview-3 Imagery for Estimating Yield of Mango.” Remote Sensing 10(12). doi: 10.3390/rs10121866.

Raun, W. R., J. B. Solie, M. L. Stone, K. L. Martin, K. W. Freeman, R. W. Mullen, H. Zhang, J. S. Schepers, and G. V. Johnson. 2005. "Optical Sensor-Based Algorithm for Crop Nitrogen Fertilization." Communications in Soil Science and Plant Analysis 36(19–20):2759–81. doi: 10.1080/00103620500303988.

Ravier, Clémence, Miguel Quemada, and Marie Hélène Jeuffroy. 2017. "Use of a chlorophyll meter to assess nitrogen nutrition index during the growth cycle in winter wheat." Field Crops Research 214:73–82. doi: 10.1016/j.fcr.2017.08.023.

Raya-Sereno, M.D., J. I. Ortiz-Monasterio, M. Alonso-Ayuso, Jr. Rodrigues, F.A., A. A. Rodríguez, L. González-Perez, and M. Quemada. 2021a. "High-Resolution Airborne Hyperspectral Imagery for Assessing." Remote Sensing 13(1317). doi: doi.org/10.3390/rs13071373.

Raya-Sereno, Maria D., Maria Alonso-Ayuso, Jose L. Pancorbo, Jose L. Gabriel, Carlos Camino, Pablo J. Zarco-Tejada, and Miguel Quemada. 2021b. "Residual Effect and N Fertilizer Rate Detection by High-Resolution VNIR-SWIR Hyperspectral Imagery and Solar-Induced Chlorophyll Fluorescence in Wheat." IEEE Transactions on Geoscience and Remote Sensing 1–17. doi: 10.1109/TGRS.2021.3099624.

Reyniers, Mieke, and E. Vrindts. 2006. "Measuring Wheat Nitrogen Status from Space and Ground-Based Platform." International Journal of Remote Sensing 27(3):549–67. doi: 10.1080/01431160500117907.

Richter, Rudolf. 1996. "Atmospheric Correction of Satellite Data with Haze Removal Including a Haze/Clear Transition Region." Computers and Geosciences 22(6):675–81. doi: 10.1016/0098-3004(96)00010-6.

Roberts, D. A., M. Gardner, R. Church, S. Ustin, G. Scheer, and R. O. Green. 1998. "Mapping Chaparral in the Santa Monica Mountains Using Multiple Endmember Spectral Mixture Models." Remote Sensing of Environment 65(3):267–79. doi: 10.1016/S0034-4257(98)00037-6.

Roberts, D. A., Margaret E. Gardner, Rick Church, Susan L. Ustin, and Robert O. Green. 1997. "Optimum Strategies for Mapping Vegetation Using Multiple-Endmember

Spectral Mixture Models." Imaging Spectrometry III 3118:108–19. doi: 10.1117/12.278930.

Roberts, D. A., K. Halligan, P. Dennison, K. Dudley, B. Somers, and A. Crabbe. 2019. "Viper Tools User Manual, Version 2.1." 1–92.

Roberts, Dar A., Philip E. Dennison, Keely L. Roth, Kenneth Dudley, and Glynn Hulley. 2015. "Relationships between Dominant Plant Species, Fractional Cover and Land Surface Temperature in a Mediterranean Ecosystem." Remote Sensing of Environment 167:152–67. doi: 10.1016/j.rse.2015.01.026.

Roberts, Dar, Michael Alonzo, Erin B. Wetherley, Kenneth L. Dudley, and Phillip E. Dennison. 2017. "Multiscale Analysis of Urban Areas Using Mixing Models." Integrating Scale in Remote Sensing and GIS 247–82. doi: 10.1201/9781315373720-19.

Roberts, Gareth. 2001. "A Review of the Application of BRDF Models to Infer Land Cover Parameters at Regional and Global Scales." Progress in Physical Geography: Earth and Environment 25(4):483–511. doi: 10.1177/030913330102500402.

Rodrigues, Francelino A., Gerald Blasch, Pierre Defourny, J. Ivan Ortiz-Monasterio, Urs Schulthess, Pablo J. Zarco-Tejada, James A. Taylor, and Bruno Gérard. 2018. "Multi-Temporal and Spectral Analysis of High-Resolution Hyperspectral Airborne Imagery for Precision Agriculture: Assessment of Wheat Grain Yield and Grain Protein Content." Remote Sensing 10(6). doi: 10.3390/rs10060930.

Rodriguez, D., V. O. Sadras, L. K. Christensen, and R. Belford. 2005. "Spatial Assessment of the Physiological Status of Wheat Crops as Affected by Water and Nitrogen Supply Using Infrared Thermal Imagery." Australian Journal of Agricultural Research 56(9):983–93. doi: 10.1071/AR05035.

Rondeaux, Geneviève, Michael Steven, and Frédéric Baret. 1996. "Optimization of Soil-Adjusted Vegetation Indices." Remote Sensing of Environment 55(2):95–107. doi: 10.1016/0034-4257(95)00186-7.

Roosjen, Peter P. J., Juha M. Suomalainen, Harm M. Bartholomeus, and Jan G. P. W. Clevers. 2016. "Hyperspectral Reflectance Anisotropy Measurements Using a

Pushbroom Spectrometer on an Unmanned Aerial Vehicle-Results for Barley, Winter Wheat, and Potato." Remote Sensing 8(11):1–16. doi: 10.3390/rs8110909.

Rossi, Christian, Mathias Kneubühler, Martin Schütz, Michael E. Schaepman, Rudolf M. Haller, and Anita C. Risch. 2022. "Spatial Resolution, Spectral Metrics and Biomass Are Key Aspects in Estimating Plant Species Richness from Spectral Diversity in Species-Rich Grasslands." Remote Sensing in Ecology and Conservation 8(3):297–314. doi: 10.1002/rse2.244.

Roth, Keely L., Philip E. Dennison, and Dar A. Roberts. 2012. "Comparing Endmember Selection Techniques for Accurate Mapping of Plant Species and Land Cover Using Imaging Spectrometer Data." Remote Sensing of Environment 127:139–52. doi: 10.1016/j.rse.2012.08.030.

Rouse, J. W., R. H. Haas, J. A. Schell, and D. W. Deering. 1973. "Monitoring the vernal advancement and retrogradation (green wave effect) of natural vegetation." Progress Report RSC 1978-1.

Roy, David P., Junchang Ju, Philip Lewis, Crystal Schaaf, Feng Gao, Matt Hansen, and Erik Lindquist. 2008. "Multi-Temporal MODIS-Landsat Data Fusion for Relative Radiometric Normalization, Gap Filling, and Prediction of Landsat Data." Remote Sensing of Environment 112(6):3112–30. doi: 10.1016/j.rse.2008.03.009.

Roy, David P., Jian Li, Hankui K. Zhang, Lin Yan, Haiyan Huang, and Zhongbin Li. 2017. "Examination of Sentinel-2A Multi-Spectral Instrument (MSI) Reflectance Anisotropy and the Suitability of a General Method to Normalize MSI Reflectance to Nadir BRDF Adjusted Reflectance." Remote Sensing of Environment 199:25–38. doi: 10.1016/j.rse.2017.06.019.

Rud, Ronit, Y. Cohen, V. Alchanatis, A. Levi, R. Brikman, C. Shenderey, B. Heuer, T. Markovitch, Z. Dar, C. Rosen, D. Mulla, and T. Nigon. 2014. "Crop Water Stress Index Derived from Multi-Year Ground and Aerial Thermal Images as an Indicator of Potato Water Status." Precision Agriculture 15(3):273–89. doi: 10.1007/s11119-014-9351-z.

Rumelhart, D. E., G. E. Hinton, and R. J. Williams. 1986. “Learning Representations by Back-Propagating Errors.” Nature 323(2):533–536. doi: 10.7551/mitpress/1888.003.0013.

de Sá, Nuno César, Mitra Baratchi, Leon T. Hauser, and Peter van Bodegom. 2021. “Exploring the Impact of Noise on Hybrid Inversion of Prosail RTM on Sentinel-2 Data.” Remote Sensing 13(4):1–20. doi: 10.3390/rs13040648.

Sadras, Víctor O. 2004. “Yield and Water-Use Efficiency of Water- and Nitrogen-Stressed Wheat Crops Increase with Degree of Co-Limitation.” European Journal of Agronomy 21(4):455–64. doi: 10.1016/j.eja.2004.07.007.

Sadras, Victor O., and Gilles Lemaire. 2014. “Quantifying Crop Nitrogen Status for Comparisons of Agronomic Practices and Genotypes.” Field Crops Research 164(1):54–64. doi: 10.1016/j.fcr.2014.05.006.

Salarieh, Bamdad, Jeewantha De Silva, and Behzad Kordi. 2020. “High Frequency Response of Grounding Electrodes: Effect of Soil Dielectric Constant.” IET Generation, Transmission and Distribution 14(15):2915–21. doi: 10.1049/iet-gtd.2019.1554.

Sanad, Marwa N. M. E., Andrei Smertenko, and Kimberley A. Garland-Campbell. 2019. “Differential Dynamic Changes of Reduced Trait Model for Analyzing the Plastic Response to Drought Phases: A Case Study in Spring Wheat.” Frontiers in Plant Science 10(April):1–19. doi: 10.3389/fpls.2019.00504.

Sanchez, Nadya. 2017. “Changes in Evapotranspiration of Agricultural Crops in Kern County during the 2014-2015 Drought Years.” MS Rep. Davis, CA: Univ. of California.

Satellite image corporation. 2017. “WorldView-3 Satellite Sensor Specifications.” Retrieved March 28, 2020 (https://sentinels.copernicus.eu/web/sentinel/user-guides/sentinel-2-msi/document-library/-/asset_publisher/Wk0TKajiISaR/content/sentinel-2a-spectral-responses).

Schaaf, Abigail, Philip Dennison, Gregory Fryer, Keely Roth, and D. A. Roberts. 2011. “Mapping Plant Functional Types at Multiple Spatial Resolutions Using Imaging Spectrometer Data.” GIScience and Remote Sensing 48(3):324–44. doi: 10.2747/1548-1603.48.3.324.

Schepers, J. S., T. M. Blackmer, W. W. Wilhelm, and M. Resende. 1996. “Transmittance and Reflectance Measurements of Corn Leaves from Plants with Different Nitrogen and Water Supply.” Journal of Plant Physiology 148(5):523–29. doi: 10.1016/S0176-1617(96)80071-X.

Schierhorn, Florian, Daniel Müller, Alexander V. Prishchepov, Monireh Faramarzi, and Alfons Balmann. 2014. “The Potential of Russia to Increase Its Wheat Production through Cropland Expansion and Intensification.” Global Food Security 3(3–4):133–41. doi: 10.1016/j.gfs.2014.10.007.

Schodlok, Martin C., Michaela Frei, and Karl Segl. 2022. “Implications of New Hyperspectral Satellites for Raw Materials Exploration.” Mineral Economics (0123456789). doi: 10.1007/s13563-022-00327-1.

Schulz, Christian, Ann Kathrin Holtgrave, and Birgit Kleinschmit. 2021a. “Large-Scale Winter Catch Crop Monitoring with Sentinel-2 Time Series and Machine Learning–An Alternative to on-Site Controls?” Computers and Electronics in Agriculture 186(May):106173. doi: 10.1016/j.compag.2021.106173.

Schulz, Dario, He Yin, Bernhard Tischbein, Sarah Verleysdonk, Rabani Adamou, and Navneet Kumar. 2021b. “Land Use Mapping Using Sentinel-1 and Sentinel-2 Time Series in a Heterogeneous Landscape in Niger, Sahel.” ISPRS Journal of Photogrammetry and Remote Sensing 178:97–111. doi: 10.1016/j.isprsjprs.2021.06.005.

Segarra, Joel, Maria Luisa Buchaillot, Jose Luis Araus, and Shawn C. Kefauver. 2020. “Remote Sensing for Precision Agriculture: Sentinel-2 Improved Features and Applications.” Agronomy 10(5):1–18. doi: 10.3390/agronomy10050641.

Seligman, N. G., R. S. Loomis, J. Burke, and A. Abshahi. 1983. “Nitrogen Nutrition and Canopy Temperature in Field-Grown Spring Wheat.” The Journal of Agricultural Science 101(3):691–97. doi: 10.1017/S0021859600038727.

Sellam, V., and E. Poovammal. 2016. “Prediction of Crop Yield Using Regression Analysis.” Indian Journal of Science and Technology 9(38). doi: 10.17485/ijst/2016/v9i38/91714.

Serrano, Lydia, Josep Peñuelas, and Susan L. Ustin. 2002. “Remote Sensing of Nitrogen and Lignin in Mediterranean Vegetation from AVIRIS Data.” Remote Sensing of Environment 81(2–3):355–64. doi: 10.1016/s0034-4257(02)00011-1.

Shang, Jiali, Xianfeng Jiao, Heather McNairn, John Kovacs, Dan Walters, Baoluo Ma, and Xiaoyuan Geng. 2013. “Tracking Crop Phenological Development of Spring Wheat Using Synthetic Aperture Radar (SAR) in Northern Ontario, Canada.” 2013 2nd International Conference on Agro-Geoinformatics: Information for Sustainable Agriculture, Agro-Geoinformatics 2013 517–21. doi: 10.1109/Argo-Geoinformatics.2013.6621975.

Shang, Rong, and Zhe Zhu. 2019. “Harmonizing Landsat 8 and Sentinel-2: A Time-Series-Based Reflectance Adjustment Approach.” Remote Sensing of Environment 235(September):111439. doi: 10.1016/j.rse.2019.111439.

Shiferaw, Bekele, Melinda Smale, Hans Joachim Braun, Etienne Duveiller, Mathew Reynolds, and Geoffrey Muricho. 2013. “Crops That Feed the World 10. Past Successes and Future Challenges to the Role Played by Wheat in Global Food Security.” Food Security 5(3):291–317. doi: 10.1007/s12571-013-0263-y.

Shivers, Sarah W., D. A. Roberts, Joseph P. McFadden, and Christina Tague. 2018. “Using Imaging Spectrometry to Study Changes in Crop Area in California’s Central Valley during Drought.” Remote Sensing 10(10). doi: 10.3390/rs10101556.

Shivers, Sarah W., Dar A. Roberts, and Joseph P. Mcfadden. 2019. “Using Paired Thermal and Hyperspectral Aerial Imagery to Quantify Land Surface Temperature Variability and Assess Crop Stress within California Orchards.” Remote Sensing of Environment 222:215–31. doi: 10.1016/j.rse.2018.12.030.

Sims, Daniel A., and John A. Gamon. 2002. “Relationships between Leaf Pigment Content and Spectral Reflectance across a Wide Range of Species, Leaf Structures and Developmental Stages.” Remote Sensing of Environment 81(2–3):337–54. doi: 10.1016/S0034-4257(02)00010-X.

Sims, Daniel A., and John A. Gamon. 2003. “Estimation of Vegetation Water Content and Photosynthetic Tissue Area from Spectral Reflectance: A Comparison of Indices

Based on Liquid Water and Chlorophyll Absorption Features." Remote Sensing of Environment 84(4):526–37. doi: 10.1016/S0034-4257(02)00151-7.

Singh, I. D., and N. C. Stoskopf. 1971. " Harvest Index in Cereals 1 ." Agronomy Journal 63(2):224–26. doi: 10.2134/agronj1971.00021962006300020008x.

Sinha, S., C. Jeganathan, L. K. Sharma, and M. S. Nathawat. 2015. "A Review of Radar Remote Sensing for Biomass Estimation." International Journal of Environmental Science and Technology 12(5):1779–92. doi: 10.1007/s13762-015-0750-0.

Sinha, Sanjiv K., Hitendra Padalia, Anindita Dasgupta, Jochem Verrelst, and Juan Pablo Rivera. 2020. "Estimation of Leaf Area Index Using PROSAIL Based LUT Inversion, MLRA-GPR and Empirical Models: Case Study of Tropical Deciduous Forest Plantation, North India." International Journal of Applied Earth Observation and Geoinformation 86:102027. doi: 10.1016/j.jag.2019.102027.

Sishodia, Rajendra P., Ram L. Ray, and Sudhir K. Singh. 2020. "Applications of Remote Sensing in Precision Agriculture: A Review." Remote Sensing 12(19):1–31. doi: 10.3390/rs12193136.

Skakun, S., E. Vermote, JC Roger, and Franch B. 2017. "Combined Use of Landsat-8 and Sentinel-2A Images for Winter Crop Mapping and Winter Wheat Yield Assessment at Regional Scale." NASA AIMS Geosciences. 3(2):1–21. doi: 10.3934/geosci.2017.2.163.

Snyder, C. S., T. W. Bruulsema, T. L. Jensen, and P. E. Fixen. 2009. "Review of Greenhouse Gas Emissions from Crop Production Systems and Fertilizer Management Effects." Agriculture, Ecosystems and Environment 133(3–4):247–66. doi: 10.1016/j.agee.2009.04.021.

Söderström, Mats, Thomas Börjesson, Carl Göran Pettersson, Knud Nissen, and Olle Hagner. 2010. "Prediction of Protein Content in Malting Barley Using Proximal and Remote Sensing." Precision Agriculture 11(6):587–99. doi: 10.1007/s11119-010-9181-6.

Sola, Ion, Alberto García-Martín, Leire Sandonís-Pozo, Jesús Álvarez-Mozos, Fernando Pérez-Cabello, María González-Audícana, and Raquel Montorio Llovería. 2018. "Assessment of Atmospheric Correction Methods for Sentinel-2 Images in

Mediterranean Landscapes." International Journal of Applied Earth Observation and Geoinformation 73:63–76. doi: 10.1016/j.jag.2018.05.020.

Somers, Ben, Gregory P. Asner, Laurent Tits, and Pol Coppin. 2011. "Endmember Variability in Spectral Mixture Analysis: A Review." Remote Sensing of Environment 115(7):1603–16. doi: 10.1016/j.rse.2011.03.003.

Somers, Ben, Kenneth Cools, Stephanie Delalieux, Jan Stuckens, Dimitry Van der Zande, Willem W. Verstraeten, and Pol Coppin. 2009. "Nonlinear Hyperspectral Mixture Analysis for Tree Cover Estimates in Orchards." Remote Sensing of Environment 113(6):1183–93. doi: 10.1016/j.rse.2009.02.003.

Sonnentag, O., J. M. Chen, D. A. Roberts, J. Talbot, K. Q. Halligan, and A. Govind. 2007. "Mapping Tree and Shrub Leaf Area Indices in an Ombrotrophic Peatland through Multiple Endmember Spectral Unmixing." Remote Sensing of Environment 109(3):342–60. doi: 10.1016/j.rse.2007.01.010.

Sticksel, E., F. X. Maidl, F. Retzer, and G. Fischbeck. 1999. "Nitrogen Uptake and Utilization in Winter Wheat under Different Fertilization Regimes, with Particular Reference to Main Stems and Tillers." Journal of Agronomy and Crop Science 183(1):47–52. doi: 10.1046/j.1439-037X.1999.00320.x.

Su, Lihong, Yuxia Huang, M. J. Chopping, A. Rango, and J. V. Martonchik. 2009. "An Empirical Study on the Utility of BRDF Model Parameters and Topographic Parameters for Mapping Vegetation in a Semi-Arid Region with MISR Imagery." International Journal of Remote Sensing 30(13):3463–83. doi: 10.1080/01431160802562230.

Sun, Jia, Lunche Wang, Shuo Shi, Zhenhai Li, Jian Yang, Wei Gong, Shaoqiang Wang, and Torbern Tagesson. 2022. "Leaf Pigment Retrieval Using the PROSAIL Model: Influence of Uncertainty in Prior Canopy-Structure Information." Crop Journal 10(5):1251–63. doi: 10.1016/j.cj.2022.04.003.

Swatantran, Anu, Ralph Dubayah, Dar A. Roberts, Michelle Hofton, and J. Bryan Blair. 2011. "Mapping Biomass and Stress in the Sierra Nevada Using Lidar and

Hyperspectral Data Fusion." Remote Sensing of Environment 115(11):2917–30. doi: 10.1016/j.rse.2010.08.027.

Tanaka, Yoshikazu, Nobuhiro Sasaki, and Akemi Ohmiya. 2008. "Biosynthesis of Plant Pigments: Anthocyanins, Betalains and Carotenoids." Plant Journal 54(4):733–49. doi: 10.1111/j.1365-313X.2008.03447.x.

Tane, Zachary, Dar Roberts, Alexander Koltunov, Stuart Sweeney, and Carlos Ramirez. 2018a. "A Framework for Detecting Conifer Mortality across an Ecoregion Using High Spatial Resolution Spaceborne Imaging Spectroscopy." Remote Sensing of Environment 209:195–210. doi: 10.1016/j.rse.2018.02.073.

Tane, Zachary, Dar Roberts, Sander Veraverbeke, Ángeles Casas, Carlos Ramirez, and Susan Ustin. 2018b. "Evaluating Endmember and Band Selection Techniques for Multiple Endmember Spectral Mixture Analysis Using Post-Fire Imaging Spectroscopy." Remote Sensing 10(3):1–21. doi: 10.3390/rs10030389.

Tang, Xiaopei, Haijun Liu, Dongxue Feng, Wenjie Zhang, Jie Chang, Lun Li, and Li Yang. 2022. "Prediction of Field Winter Wheat Yield Using Fewer Parameters at Middle Growth Stage by Linear Regression and the BP Neural Network Method." European Journal of Agronomy 141(19):126621. doi: 10.1016/j.eja.2022.126621.

Tanner, C. B. 1963. " Plant Temperatures 1 ." Agronomy Journal 55(2):210–11. doi: 10.2134/agronj1963.00021962005500020043x.

Tanner, C. B., and Thomas R. Sinclair. 1983. "Efficient Water Use in Crop Production: Research or Re-Search?" Limitations to Efficient Water Use in Crop Production 1–27. doi: 10.2134/1983.limitationstoefficientwateruse.c1.

Taylor, James, Brett Whelan, Lars Thylén, Mikael Gilbertsson, and James Hassall. 2005. "Monitoring Wheat Protein Content On-Harvester - Australian Experiences." Precision Agriculture 2005, ECPA 2005:369–75.

Tester, M., and P. Langridge. 2010. "Breeding Technologies to Increase Crop Production in a Changing World." Science 818(5967):818–22.

Thenkabail, Prasad S., Isabella Mariotto, Murali Krishna Gumma, Elizabeth M. Middleton, David R. Landis, and K. Fred Huemmrich. 2013. "Selection of Hyperspectral Narrowbands (Hnbs) and Composition of Hyperspectral Twoband Vegetation Indices (HVIS) for Biophysical Characterization and Discrimination of Crop Types Using Field Reflectance and Hyperion/EO-1 Data." IEEE Journal of Selected Topics in Applied Earth Observations and Remote Sensing 6(2):427–39. doi: 10.1109/JSTARS.2013.2252601.

Thompson, D., B. Gao, R. Green, D. A. Roberts, P. Dennison, and S. Lundeen. 2015. "Atmospheric Correction for Global Mapping Spectroscopy: ATREM Advances for the HyspIRI Preparatory Campaign." Remote Sensing of Environment 167:64–77. doi: 10.1016/j.rse.2015.02.010.

Tian, Jia, Shanshan Su, Qingjiu Tian, Wenfeng Zhan, Yanbiao Xi, and Ning Wang. 2021. "A Novel Spectral Index for Estimating Fractional Cover of Non-Photosynthetic Vegetation Using near-Infrared Bands of Sentinel Satellite." International Journal of Applied Earth Observation and Geoinformation 101:102361. doi: 10.1016/j.jag.2021.102361.

Tilling, Adam K., Garry J. O'Leary, Jelle G. Ferwerda, Simon D. Jones, Glenn J. Fitzgerald, Daniel Rodriguez, and Robert Belford. 2007. "Remote Sensing of Nitrogen and Water Stress in Wheat." Field Crops Research 104(1–3):77–85. doi: 10.1016/j.fcr.2007.03.023.

Tindula, Gwen N., Morteza N. Orang, and Richard L. Snyder. 2013. "Survey of Irrigation Methods in California in 2010." Journal of Irrigation and Drainage Engineering 139(3):233–38. doi: 10.1061/(asce)ir.1943-4774.0000538.

Toro, Guillermo, Jaume Flexas, and José Mariano Escalona. 2019. "Contrasting Leaf Porometer and Infra-Red Gas Analyser Methodologies: An Old Paradigm about the Stomatal Conductance Measurement." Theoretical and Experimental Plant Physiology 31(4):483–92. doi: 10.1007/s40626-019-00161-x.

Tortajada, Cecilia, Matthew J. Kastner, Joost Buurman, and Asit K. Biswas. 2017. "The California Drought: Coping Responses and Resilience Building." Environmental Science and Policy 78:97–113. doi: 10.1016/j.envsci.2017.09.012.

Tremblay, Nicolas, Edith Fallon, and Noura Ziadi. 2011. “Sensing of Crop Nitrogen Status: Opportunities, Tools, Limitations, and Supporting Information Requirements.” HortTechnology 21(3):274–81. doi: 10.21273/horttech.21.3.274.

Tremblay, Nicolas, Zhijie Wang, and Carl Belec. 2010. “Performance of Dualex in Spring Wheat for Crop Nitrogen Status Assessment, Yield Prediction and Estimation of Soil Nitrate Content.” Journal of Plant Nutrition 33(1):57–70. doi: 10.1080/01904160903391081.

Tremblay, Nicolas, Zhijie Wang, and Carl Bélec. 2007. “Evaluation of the Dualex for the Assessment of Corn Nitrogen Status.” Journal of Plant Nutrition 30(9):1355–69. doi: 10.1080/01904160701555689.

Tremblay, Nicolas, Zhijie Wang, and Zoran G. Cerovic. 2012. “Sensing Crop Nitrogen Status with Fluorescence Indicators. A Review.” Agronomy for Sustainable Development 32(2):451–64. doi: 10.1007/s13593-011-0041-1.

Trudel, Melanie, François Charbonneau, and Robert Leconte. 2012. “Using RADARSAT-2 Polarimetric and ENVISAT-ASAR Dual-Polarization Data for Estimating Soil Moisture over Agricultural Fields.” Canadian Journal of Remote Sensing 38(4):514–27. doi: 10.5589/m12-043.

Tsouros, Dimosthenis C., Stamatia Bibi, and Panagiotis G. Sarigiannidis. 2019. “A Review on UAV-Based Applications for Precision Agriculture.” Information 10(11). doi: 10.3390/info10110349.

Tulare County Agricultural Commissioner/Sealer. 2022. “Tulare County Crop Reports.” Retrieved June 1, 2022 (https://agcomm.co.tulare.ca.us/standards-and-exclusion/crop-reports1/crop-reports-2011-2020/).

United States Drought Monitor. 2022a. “Historical Drought Conditions.” Retrieved June 26, 2022 (https://www.drought.gov/states/california).

United States Drought Monitor. 2022b. “Drought Classification.” Retrieved October 5, 2022 (https://droughtmonitor.unl.edu/About/AbouttheData/DroughtClassification.aspx).

United States Geological Survey. 2022. “Alluvial Boundary of California’s Central Valley.” Retrieved October 10, 2022 (https://water.usgs.gov/GIS/metadata/usgswrd/XML/pp1766_Alluvial_Bnd.xml#stdorder).

United States Geological Survey. 2023a. “Landsat 9 Missions.” Retrieved March 19, 2023 (https://www.usgs.gov/landsat-missions/landsat-9).

United States Geological Survey. 2023b. “Landsat 8 Program for Estimating Land Surface Reflectance.” Retrieved December 23, 2020 (https://www.usgs.gov/centers/eros/science/usgs-eros-archive-landsat-archives-landsat-8-olitirs-level-2-data-products?qt-science_center_objects=0#qt-science_center_objects/).

University of California Division of Agriculture and Natural Resources. 2022. “Crop Irrigation Strategies.” Retrieved July 23, 2022 (http://ucmanagedrought.ucdavis.edu/Agriculture/Crop_Irrigation_Strategies/).

Upreti, Deepak, Wenjiang Huang, Weiping Kong, Simone Pascucci, Stefano Pignatti, Xianfeng Zhou, Huichun Ye, and Raffaele Casa. 2019. “A Comparison of Hybrid Machine Learning Algorithms for the Retrieval of Wheat Biophysical Variables from Sentinel-2.” Remote Sensing 11(5). doi: 10.3390/rs11050481.

Vasco, Donald W., Kyra H. Kim, Tom G. Farr, J. T. Reager, David Bekaert, Simran S. Sangha, Jonny Rutqvist, and Hiroko K. Beaudoing. 2022. “Using Sentinel-1 and GRACE Satellite Data to Monitor the Hydrological Variations within the Tulare Basin, California.” Scientific Reports 12(1):1–14. doi: 10.1038/s41598-022-07650-1.

Verhoef, W. 1984. “Light Scattering by Leaf Layers with Application to Canopy Reflectance Modeling: The SAIL Model.” Remote Sensing of Environment 16(2):125–41. doi: 10.1016/0034-4257(84)90057-9.

Verhoef, W. 1985. “Earth Observation Modeling Based on Layer Scattering Matrices.” Remote Sensing of Environment 17(2):165–78. doi: 10.1016/0034-4257(85)90072-0.

Verhoef, Wout, and Heike Bach. 2007. “Coupled Soil-Leaf-Canopy and Atmosphere Radiative Transfer Modeling to Simulate Hyperspectral Multi-Angular Surface

Reflectance and TOA Radiance Data." Remote Sensing of Environment 109(2):166–82. doi: 10.1016/j.rse.2006.12.013.

Vermote, Eric F., Didier Tanré, Jean Luc Deuzé, Maurice Herman, and Jean Jacques Morcrette. 1997. "Second Simulation of the Satellite Signal in the Solar Spectrum, 6s: An Overview." IEEE Transactions on Geoscience and Remote Sensing 35(3):675–86. doi: 10.1109/36.581987.

Vermote, Eric, Chris Justice, Martin Claverie, and Belen Franch. 2016. "Preliminary Analysis of the Performance of the Landsat 8/OLI Land Surface Reflectance Product." Remote Sensing of Environment 185:46–56. doi: 10.1016/j.rse.2016.04.008.

Verrelst, J., M. E. Schaepman, B. Koetz, and M. Kneubühler. 2008. "Angular Sensitivity Analysis of Vegetation Indices Derived from CHRIS/PROBA Data." Remote Sensing of Environment 112(5):2341–53. doi: 10.1016/j.rse.2007.11.001.

Verrelst, Jochem, Zbyněk Malenovský, Christiaan Van der Tol, Gustau Camps-Valls, Jean Philippe Gastellu-Etchegorry, Philip Lewis, Peter North, and Jose Moreno. 2019. "Quantifying Vegetation Biophysical Variables from Imaging Spectroscopy Data: A Review on Retrieval Methods." Surveys in Geophysics 40(3):589–629. doi: 10.1007/s10712-018-9478-y.

Vogelmann, J. E., B. N. Rock, and D. M. Moss. 1993. "Red Edge Spectral Measurements from Sugar Maple Leaves." International Journal of Remote Sensing 14(8):1563–75. doi: 10.1080/01431169308953986.

Walker, Anthony P., Tristan Quaife, Peter M. van Bodegom, Martin G. De Kauwe, Trevor F. Keenan, Joanna Joiner, Mark R. Lomas, Natasha MacBean, Chongang Xu, Xiaojuan Yang, and F. Ian Woodward. 2017. "The Impact of Alternative Trait-Scaling Hypotheses for the Maximum Photosynthetic Carboxylation Rate (Vcmax) on Global Gross Primary Production." New Phytologist 215(4):1370–86. doi: 10.1111/nph.14623.

Walthall, C. L., J. M. Norman, J. M. Welles, G. Campbell, and B. L. Blad. 1985. “Simple Equation to Approximate the Bidirectional Reflectance from Vegetative Canopies and Bare Soil Surfaces.” Applied Optics 24(3):383. doi: 10.1364/ao.24.000383.

Wang, Dian, Ronghua Ma, Kun Xue, and Steven Arthur Loiselle. 2019a. “The Assessment of Landsat-8 OLI Atmospheric Correction Algorithms for Inland Waters.” Remote Sensing 11(2). doi: 10.3390/rs11020169.

Wang, Ku, David R. Huggins, and Haiying Tao. 2019b. “Rapid Mapping of Winter Wheat Yield, Protein, and Nitrogen Uptake Using Remote and Proximal Sensing.” International Journal of Applied Earth Observation and Geoinformation 82:101921. doi: 10.1016/j.jag.2019.101921.

Wang, Z. J., J. H. Wang, L. Y. Liu, W. J. Huang, C. J. Zhao, and C. Z. Wang. 2004. “Prediction of Grain Protein Content in Winter Wheat (*Triticum aestivum* L.) Using Plant Pigment Ratio (PPR).” Field Crops Research 90(2–3):311–21. doi: 10.1016/j.fcr.2004.04.004.

Wanner, W., X. Li, and a H. Strahler. 1995. “Kernel-Driven Models for the Bidirectional Reflectance Dis- Contain Only Geometric Terms but No Physical Parameters . Function Land Surfaces Attempt The Complete Model Then Is Linear Be Scaled to Ar- to Describe the BRDF as a Linear Superposition of a Set.” Journal of Geophysical Research 100(D10):21077–89. doi: 10.1029/95JD02371

Warren, M. A., S. G. H. Simis, V. Martinez-Vicente, K. Poser, M. Bresciani, K. Alikas, E. Spyrakos, C. Giardino, and A. Ansper. 2019. “Assessment of Atmospheric Correction Algorithms for the Sentinel-2A MultiSpectral Imager over Coastal and Inland Waters.” Remote Sensing of Environment 225:267–89. doi: 10.1016/j.rse.2019.03.018.

Warter, M. M., M. B. Singer, M. O. Cuthbert, D. A. Roberts, K. K. Caylor, R. Sabathier, and J. Stella. 2021. “Drought Onset and Propagation into Soil Moisture and Grassland Vegetation Responses during the 2012-2019 Major Drought in Southern California.” Hydrology and Earth System Sciences 25(6):3713–29. doi: 10.5194/hess-25-3713-2021.

Weiss, M., F. Jacob, and G. Duveiller. 2020. "Remote Sensing for Agricultural Applications: A Meta-Review." Remote Sensing of Environment 236:111402. doi: 10.1016/j.rse.2019.111402.

Wik, Mette, Prabhu Pingali, and Sumiter Broca. 2008. "Global Agricultural Performance: Past Trends and Future Prospects." Background Paper for the World Development Report (2008):1–39.

Wilson, R. T., E. J. Milton, and J. M. Nield. 2015. "Are Visibility-Derived AOT Estimates Suitable for Parameterizing Satellite Data Atmospheric Correction Algorithms?" International Journal of Remote Sensing 36(6):1675–88. doi: 10.1080/01431161.2015.1023558.

Wiseman, Grant, Heather McNairn, Saeid Homayouni, and Jiali Shang. 2014. "RADARSAT-2 Polarimetric SAR Response to Crop Biomass for Agricultural Production Monitoring." IEEE Journal of Selected Topics in Applied Earth Observations and Remote Sensing 7(11):4461–71. doi: 10.1109/JSTARS.2014.2322311.

Wolfe, W. L. 1998. Introduction to Radiometry. 29th ed. SPIE press.

Wood, C. W., D. W. Reeves, and D. G. Himelrick. 1993. "Relationships between Chlorophyll Meter Readings and Leaf Chlorophyll Concentration, N Status, and Crop Yield: A Review." Proceedings of the Agronomy Society of New Zealand 23:1–9.

World maps of Köppen-Geiger climate classification. 2023. "Köppen-Geiger Climate Classification." Retrieved March 19, 2023 (https://koeppen-geiger.vu-wien.ac.at/).

World Meteorological Organisation Global Ozone Research and Monitoring Project-Report No. 59. 2018. Scientific Assessment of Ozone Depletion: 2018.

World Reference Base for Soil Resources. 2014. "International Soil Classification Systems for Naming Soils and Creating Legends for Soil Maps." World Soil Resources Reports No. 106. FAO, Rome.

Xie, Qiaoyun, Jadu Dash, Alfredo Huete, Aihui Jiang, Gaofei Yin, Yanling Ding, Dailiang Peng, Christopher C. Hall, Luke Brown, Yue Shi, Huichun Ye, Yingying Dong, and Wenjiang Huang. 2019. "Retrieval of Crop Biophysical Parameters from Sentinel-2

Remote Sensing Imagery." International Journal of Applied Earth Observation and Geoinformation 80:187–95. doi: 10.1016/j.jag.2019.04.019.

Xu, Yang, Lian Feng, Dan Zhao, and Jianzhong Lu. 2020. "Assessment of Landsat Atmospheric Correction Methods for Water Color Applications Using Global AERONET-OC Data." International Journal of Applied Earth Observation and Geoinformation 93:102192. doi: 10.1016/j.jag.2020.102192.

Yadava, Umedi L. 1986. "A Rapid and Nondestructive Method to Determine Chlorophyll in Intact Leaves." HortScience 21(6):1449–50. doi: 10.21273/hortsci.21.6.1449.

Yan, Yan, Xiao Zhang, Dong Li, Hengbiao Zheng, Xia Yao, Yan Zhu, Weixing Cao, and Tao Cheng. 2021. "Laboratory Shortwave Infrared Reflectance Spectroscopy for Estimating Grain Protein Content in Rice and Wheat." International Journal of Remote Sensing 42(12):4467–92. doi: 10.1080/01431161.2021.1895450.

Yang, H. S., A. Dobermann, J. L. Lindquist, D. T. Walters, T. J. Arkebauer, and K. G. Cassman. 2004. "Hybrid-Maize - A Maize Simulation Model That Combines Two Crop Modeling Approaches." Field Crops Research 87(2–3):131–54. doi: 10.1016/j.fcr.2003.10.003.

Yang, Yi, Sarah E. Hobbie, Rebecca R. Hernandez, Joseph Fargione, Steven M. Grodsky, David Tilman, Yong Guan Zhu, Yu Luo, Timothy M. Smith, Jacob M. Jungers, Ming Yang, and Wei Qiang Chen. 2020. "Restoring Abandoned Farmland to Mitigate Climate Change on a Full Earth." One Earth 3(2):176–86. doi: 10.1016/j.oneear.2020.07.019.

YARA. 2023. "Wheat Nutrient Application Timing." Retrieved March 19, 2023 (https://www.yara.co.uk/crop-nutrition/wheat/wheat-nutrient-application-timing/).

Yuzugullu, Onur, Frank Lorenz, Peter Fröhlich, and Frank Liebisch. 2020. "Understanding Fields by Remote Sensing: Soil Zoning and Property Mapping." Remote Sensing 12(7):1–20. doi: 10.3390/rs12071116.

Zarco-Tejada, P. J., A. Berjón, R. López-Lozano, J. R. Miller, P. Martín, V. Cachorro, M. R. González, and A. De Frutos. 2005. "Assessing Vineyard Condition with Hyperspectral Indices: Leaf and Canopy Reflectance Simulation in a Row-Structured

Discontinuous Canopy." Remote Sensing of Environment 99(3):271–87. doi: 10.1016/j.rse.2005.09.002.

Zarco-Tejada, P. J., V. González-Dugo, and J. A. J. Berni. 2012. "Fluorescence, Temperature and Narrow-Band Indices Acquired from a UAV Platform for Water Stress Detection Using a Micro-Hyperspectral Imager and a Thermal Camera." Remote Sensing of Environment 117:322–37. doi: 10.1016/j.rse.2011.10.007.

Zarco-Tejada, Pablo J., John R. Miller, Thomas L. Noland, Gina H. Mohammed, and Paul H. Sampson. 2001. "Scaling-up and Model Inversion Methods with Narrowband Optical Indices for Chlorophyll Content Estimation in Closed Forest Canopies with Hyperspectral Data." IEEE Transactions on Geoscience and Remote Sensing 39(7):1491–1507. doi: 10.1109/36.934080.

Zhang, H. K., and D. P. Roy. 2016. "Landsat 5 Thematic Mapper Reflectance and NDVI 27-Year Time Series Inconsistencies Due to Satellite Orbit Change." Remote Sensing of Environment 186:217–33. doi: 10.1016/j.rse.2016.08.022.

Zhao, Chunjiang, Liangyun Liu, Jihua Wang, Wenjiang Huang, Xiaoyu Song, and Cunjun Li. 2005. "Predicting Grain Protein Content of Winter Wheat Using Remote Sensing Data Based on Nitrogen Status and Water Stress." International Journal of Applied Earth Observation and Geoinformation 7(1):1–9. doi: 10.1016/j.jag.2004.10.002.

Zhao, Haitao, Xiaoyu Song, Guijun Yang, Zhenhai Li, Dongyan Zhang, and Haikuan Feng. 2019. "Monitoring of Nitrogen and Grain Protein Content in Winter Wheat Based on Sentinel-2A Data." Remote Sensing 11(14). doi: 10.3390/rs11141724.

Zhao, Tiejun, and Akimasa Nakano. 2018. "Agricultural Product Authenticity and Geographical Origin Traceability - Use of Nondestructive Measurement -." Japan Agricultural Research Quarterly 52(2):115–22. doi: 10.6090/jarq.52.115.

Zhu, Xiaolin, Fangyi Cai, Jiaqi Tian, and Trecia Kay Ann Williams. 2018. "Spatiotemporal Fusion of Multisource Remote Sensing Data: Literature Survey, Taxonomy, Principles, Applications, and Future Directions." Remote Sensing 10(4). doi: 10.3390/rs10040527.

Ziadi, Noura, Gilles Bélanger, Annie Claessens, Louis Lefebvre, Athyna N. Cambouris, Nicolas Tremblay, Michel C. Nolin, and Léon Étienne Parent. 2010. “Determination of a Critical Nitrogen Dilution Curve for Spring Wheat.” Agronomy Journal 102(1):241–50. doi: 10.2134/agronj2009.0266.

Zillmann, E., M. Schönert, H. Lilienthal, B. Siegmann, T. Jarmer, P. Rosso, and H. Weichelt. 2015. “Crop Ground Cover Fraction and Canopy Chlorophyll Content Mapping Using Rapideye Imagery.” International Archives of the Photogrammetry, Remote Sensing and Spatial Information Sciences - ISPRS Archives 40(7W3):149–55. doi: 10.5194/isprsarchives-XL-7-W3-149-2015.

Zillmann, Erik, Simone Graeff, Johanna Link, William David Batchelor, and Wilhelm Claupein. 2006. “Assessment of Cereal Nitrogen Requirements Derived by Optical On-the-Go Sensors on Heterogeneous Soils.” Agronomy Journal 98(3):682–90. doi: 10.2134/agronj2005.0253.

Chapter 8: Supplementary material

Chapter 4. 2: Simultaneous assessment of nitrogen and water status in winter wheat through planar-domain vegetation indices using hyperspectral and thermal sensors

S1. Root mean square error (RMSE) of the linear relationship between nitrogen nutrition index (NNI) and different spectral vegetation indices extracted from the airborne imagery (Aircraft) and the ground-level FieldSpec instrument (FS).

Vegetation indices	Mid stem elongation			Final stem elongation				Flowering			
	2018	2019			2018	2019			2018	2019	
	FS	Aircraft	FS	Aircraft	FS	Aircraft	FS	Aircraft	FS	Aircraft	FS
NDVI	0.254	0.149	0.140	0.284	0.314	0.162	0.180	0.203	0.200	0.154	0.163
GNDVI	0.255	0.15	0.132	0.269	0.275	0.159	0.161	0.196	0.221	0.138	0.154
OSAVI	0.247	0.148	0.139	0.261	0.279	0.156	0.177	0.190	0.223	0.156	0.163
EVI	0.246	0.148	0.139	0.245	0.26	0.154	0.174	0.180	0.245	0.157	0.166
PRI	0.252	0.149	0.136	0.266	0.254	0.2	0.162	0.194	0.197	0.171	0.178
CI	0.263	0.15	0.131	0.265	0.234	0.151	0.159	0.189	0.195	0.154	0.163
TCARI	0.304	0.129	0.145	0.356	0.3	0.19	0.194	0.276	0.27	0.183	0.17
DCNI	0.269	0.117	0.137	0.35	0.225	0.173	0.163	0.239	0.204	0.152	0.164
mND_{705}	0.249	0.149	0.13	0.273	0.264	0.145	0.146	0.193	0.193	0.156	0.162
mSR_{705}	0.262	0.149	0.13	0.265	0.225	0.145	0.157	0.19	0.196	0.156	0.166
NDRE	0.254	0.145	0.125	0.269	0.244	0.152	0.140	0.191	0.188	0.14	0.152
$N_{850, 1510}$	-	-	-	-	-	0.196	-	0.227	-	0.181	-
TCARI/OSAVI	0.265	0.118	0.133	0.304	0.266	0.161	0.153	0.213	0.219	0.128	0.149
CCCI	0.258	0.102	0.112	0.28	0.231	0.161	0.135	0.193	0.193	0.123	0.145

S2. Two-way ANOVA for N level, water level and NxWater interaction on ground-based crop parameters, spectral vegetation indices and temperature-based indicators from airborne imagery in the two years at flowering.

*Significant at the 0.05 probability level, ** at the 0.01 probability level, *** at the 0.001 probability level or ns not significant.

	2018			2019		
Indices	N Level	Water Level	NxWater	N Level	Water Level	NxWater
NNI	***	ns	ns	***	ns	*
Conductance	NA	NA	NA	ns	***	ns
NDVI	***	ns	ns	***	***	ns
GNDVI	***	ns	ns	***	***	ns
OSAVI	***	ns	ns	***	***	ns
EVI	***	ns	ns	***	***	ns
PRI	***	ns	ns	***	***	ns
CI	***	ns	ns	***	***	ns
TCARI	*	ns	ns	*	*	ns
DCNI	***	ns	ns	***	***	ns
mND705	***	ns	ns	***	***	ns
mSR705	***	ns	ns	***	***	ns
N850,1510	***	ns	ns	***	***	ns
NDRE	***	ns	ns	***	***	ns
TCARI/OSAVI	***	ns	ns	***	***	ns
CCCI	***	ns	ns	***	**	ns
Tc-Tair	***	***	***	*	***	ns
WDI	***	***	***	ns	***	ns
NDWI1240	***	ns	ns	***	***	ns
NDWI1640	***	ns	ns	***	***	ns
f(CCCI, WDI)	***	ns	ns	***	ns	ns

S3. Hyperspectral and thermal vegetation indices used for estimating crop nitrogen or water status for each N and water level extracted from the airborne imagery at flowering of both experimental years. Capital letters above the error bars indicate differences among N levels and lower-case letters next to the mean value indicate differences between water levels in each N level according to Tukey test 95%. Symbols are mean values and bars standard errors.

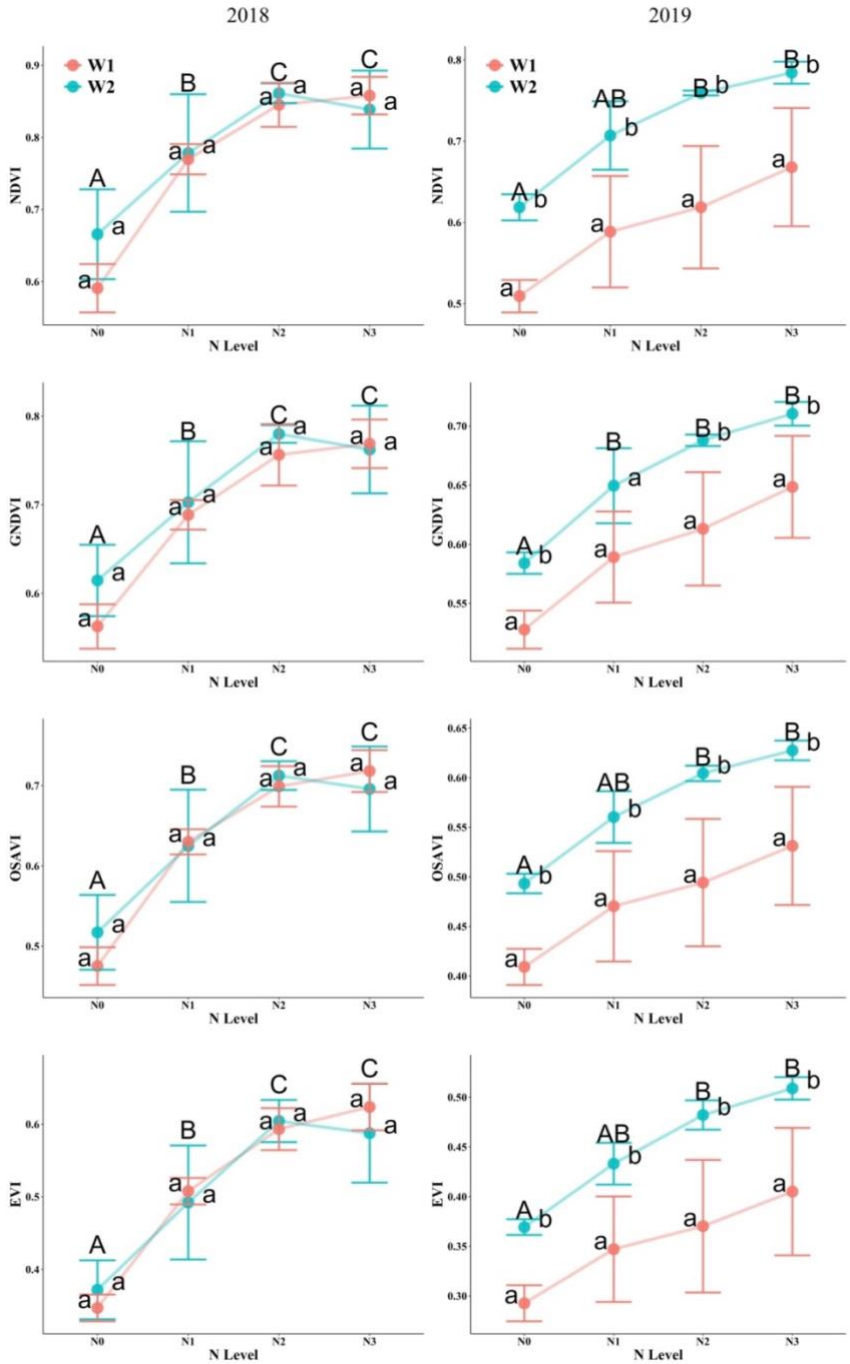

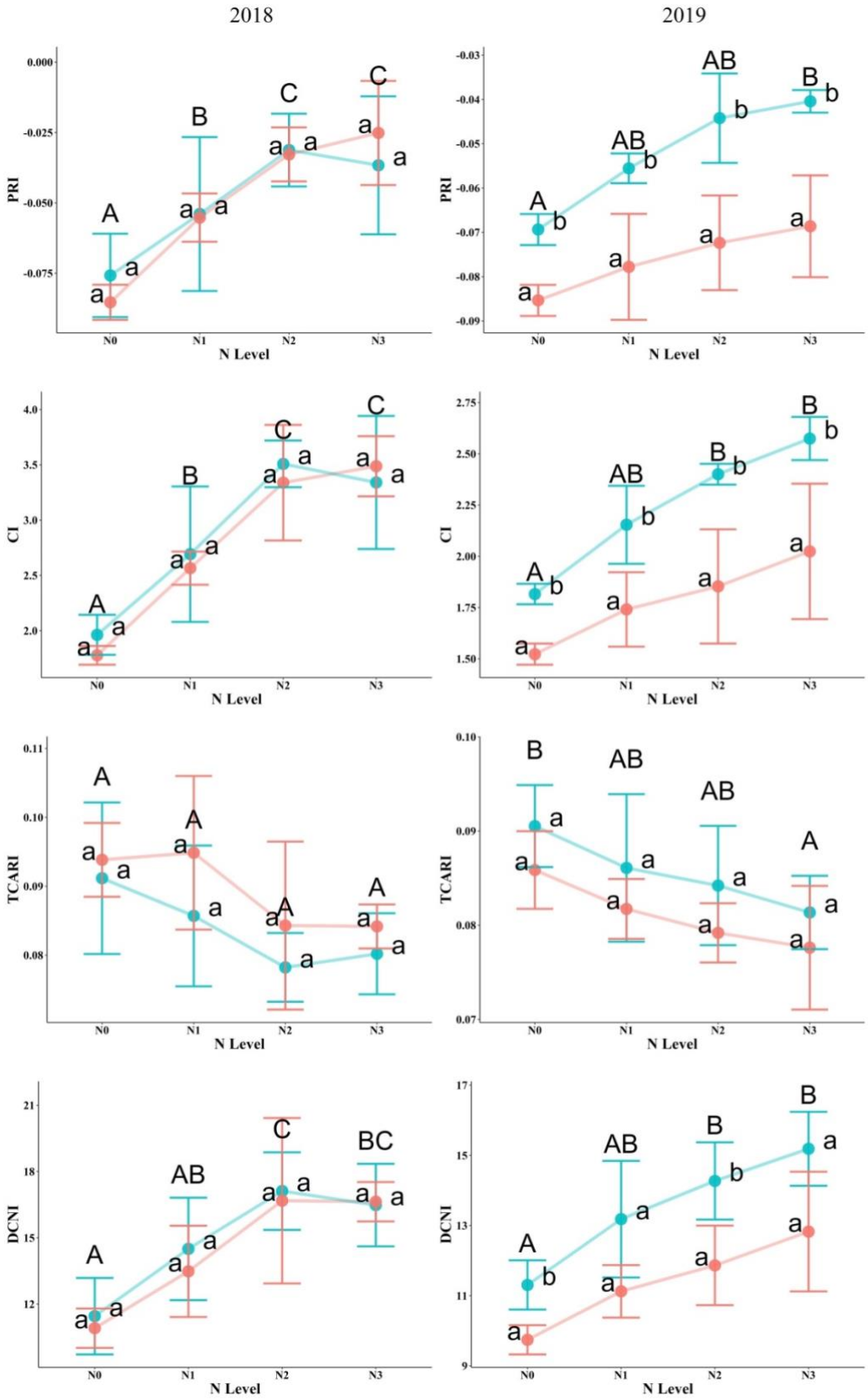
2018
2019
PRI
CI
TCARI
DCNI
N Level
N0
N1
N2
N3

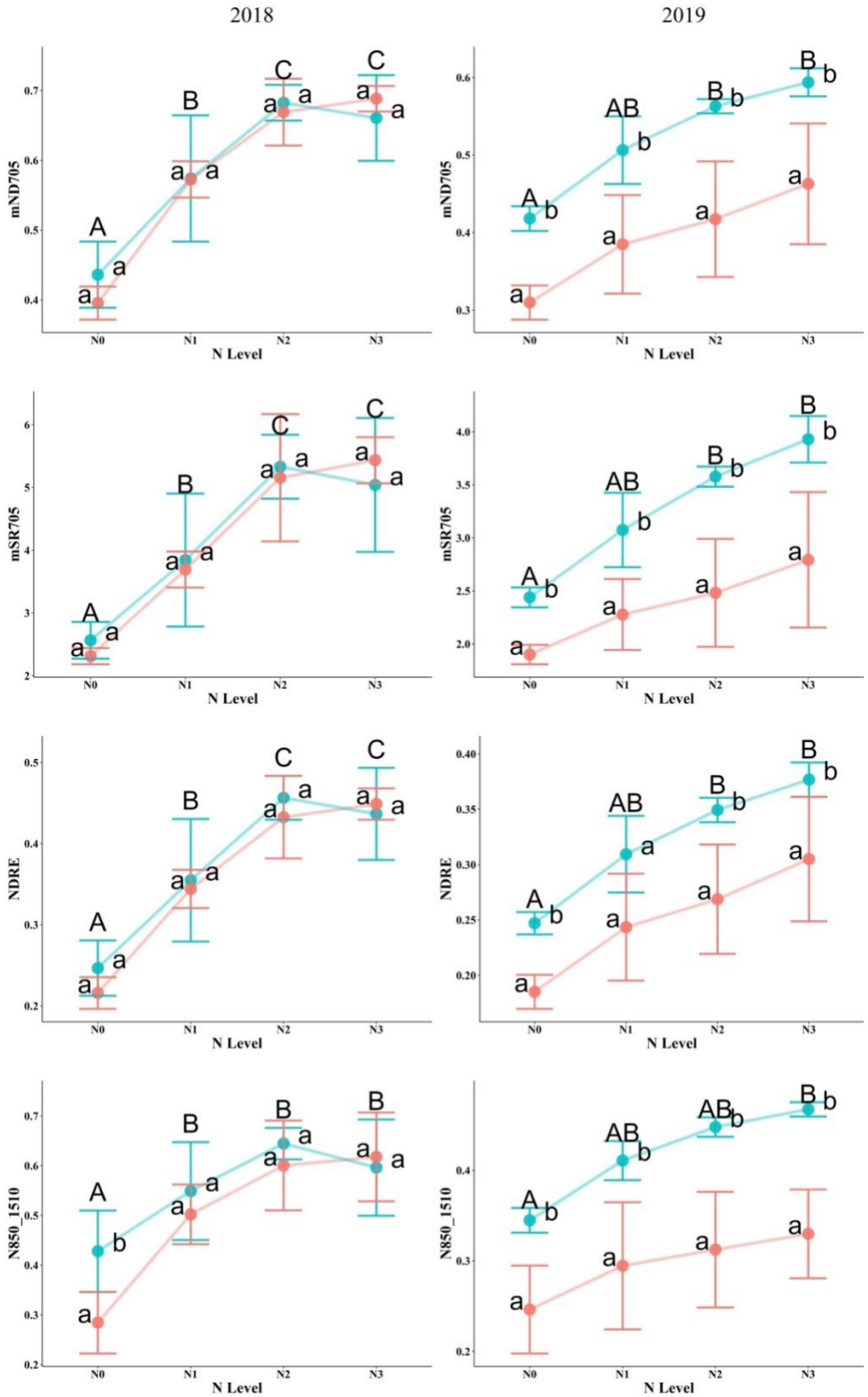
2018
2019
mND705
mSR705
NDRE
N850_1510
N0
N1
N2
N3
N Level

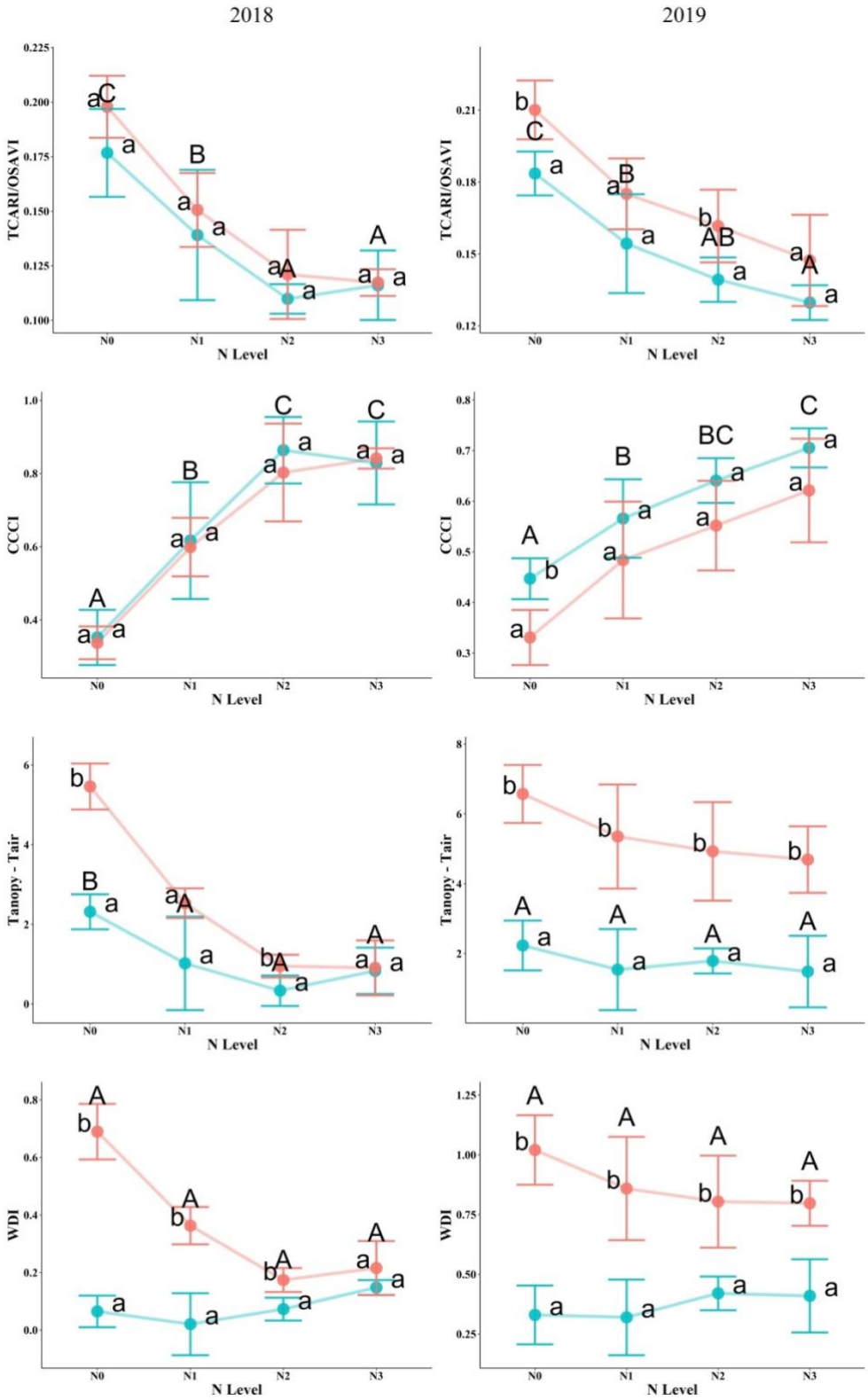
2018
2019
TCARI/OSAVI
CCCI
Tanopy - Tair
WDI
N Level
N0
N1
N2
N3

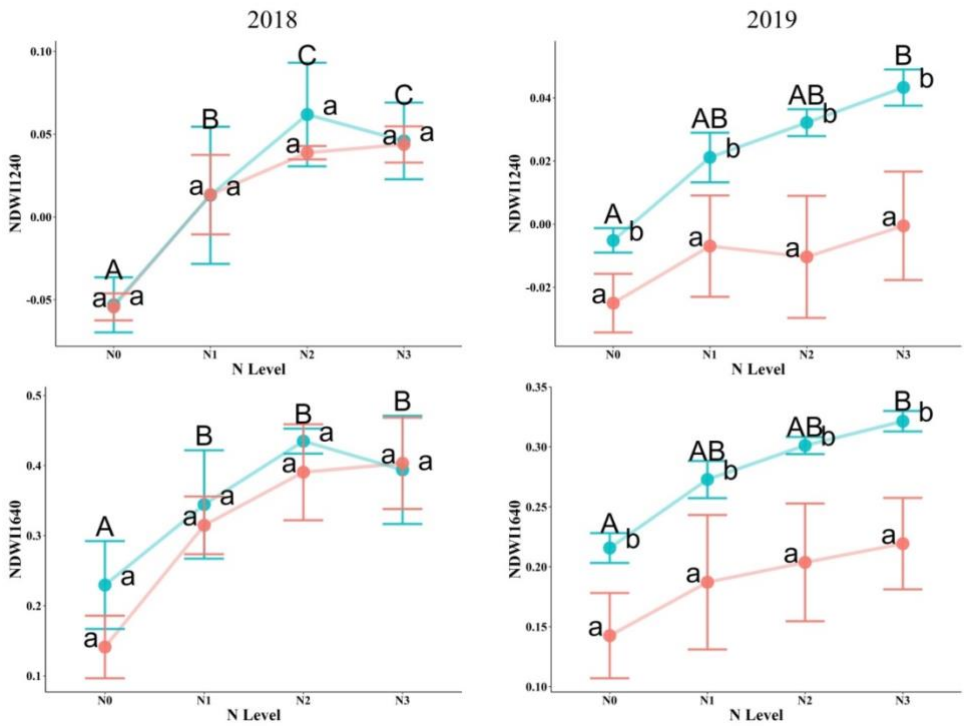
2018
2019
NDWI1240
NDWI1640
N Level
N0
N1
N2
N3

Chapter 4.4: Quantification of winter wheat nitrogen status through radiative transfer models using Sentinel-2 imagery

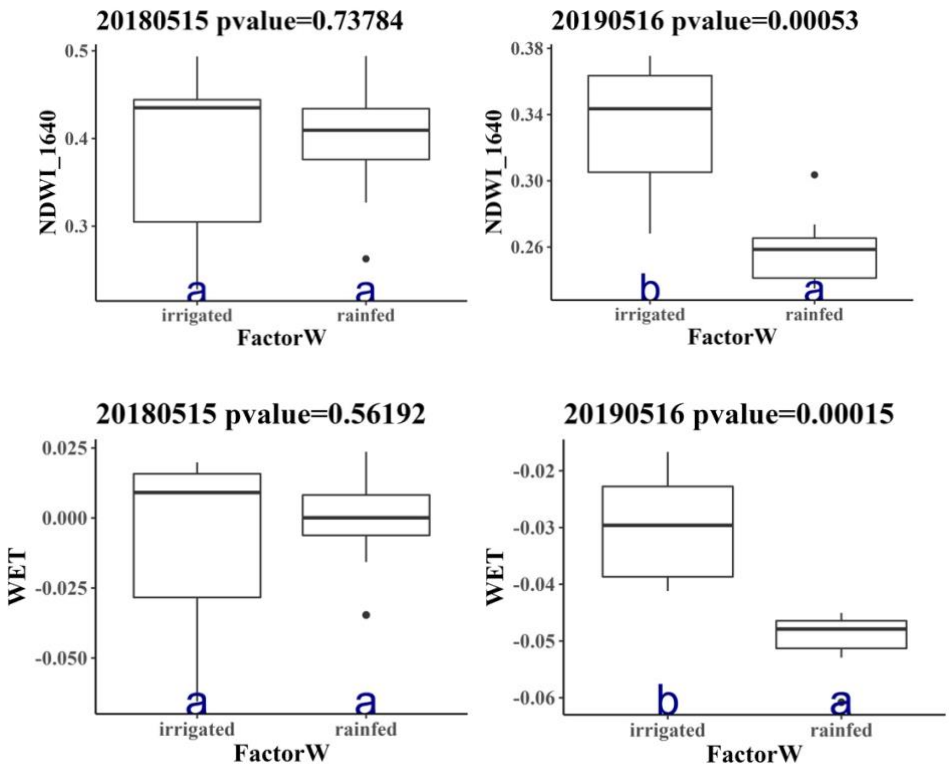

S4. Distribution of the a) normalized difference water index-1510 (NDWI-1510) and b) WET values in each water level at flowering of both years. The centerline of the boxes represents the median while and the top and bottom lines show the third and first quartiles. Different letters indicate significant differences between water levels of the same year according to Tukey`s post-hoc test 95%.

S5. Values of the coefficient of determination (R^2) obtained between different vegetation indices and nitrogen balance index (NBI) or nitrogen nutrition index (NNI) in each date of both experimental years and analyzing all dates together. For each crop parameter, the vegetation indices are ordered according to the R^2 value when analyzing all dates together.

Index	2018			2019			All dates
	GS34 28/3/2018	GS37 17/04/2018	GS65 12/05/2018	GS32 10/03/2019	GS39 12/04/2019	GS65 12/05/2019	
NBI							
OSAVI	0.69	0.79	0.62	0.67	0.34	0.84	0.34
GNDVI	0.65	0.76	0.72	0.64	0.61	0.84	0.34
EVI	0.68	0.81	0.59	0.65	0.15	0.78	0.29
CI	0.65	0.77	0.60	0.68	0.59	0.51	0.29
NDVI	0.63	0.74	0.59	0.63	0.53	0.84	0.29
TCARI/OSAVI	0.35	0.64	0.71	0.66	0.60	0.33	0.25
mSR-705	0.63	0.76	0.56	0.63	0.53	0.40	0.25
mND-705	0.60	0.60	0.41	0.64	0.47	0.77	0.25
NDRE	0.65	0.81	0.81	0.55	0.46	0.60	0.22
PRI	0.62	0.61	0.04	0.07	0.09	0.60	0.19
TCARI	0.28	0.54	0.75	0.50	0.42	0.01	0.18
NR	0.26	0.63	0.55	0.59	0.48	0.71	0.17
OSAVI-1510	0.62	0.75	0.56	0.53	0.04	0.65	0.16
NDWI-2190	0.58	0.66	0.48	0.55	0.03	0.60	0.16
N870	0.60	0.73	0.55	0.54	0.04	0.65	0.14
NDWI-1640	0.60	0.73	0.55	0.54	0.04	0.65	0.14
DCNI	0.43	0.61	0.52	0.40	0.14	0.01	0.10
CCCI	0.54	0.78	0.82	0.06	0.32	0.00	0.05
WET	0.46	0.57	0.37	0.42	0.00	0.23	0.04
TCARI-1510	0.05	0.47	0.02	0.06	0.16	0.00	0.03
TCARI/OSAVI-1510	0.34	0.46	0.28	0.41	0.01	0.53	0.01
NNI							
CI	0.60	0.64	0.66	0.34	0.29	0.15	0.42
OSAVI	0.60	0.59	0.67	0.46	0.32	0.54	0.41
EVI	0.63	0.66	0.72	0.45	0.24	0.61	0.39
GNDVI	0.56	0.53	0.65	0.46	0.44	0.55	0.36
mSR-705	0.58	0.65	0.67	0.27	0.24	0.07	0.34
NDVI	0.53	0.52	0.61	0.46	0.35	0.46	0.32
TCARI/OSAVI	0.30	0.47	0.66	0.25	0.28	0.08	0.28
PRI	0.55	0.45	0.03	0.01	0.07	0.20	0.27
NR	0.21	0.60	0.61	0.46	0.36	0.49	0.26
OSAVI-1510	0.60	0.61	0.70	0.22	0.06	0.27	0.24

TCARI	0.24	0.43	0.64	0.11	0.11	0.01	0.22
NDWI-2190	0.56	0.55	0.60	0.27	0.05	0.15	0.21
N870	0.58	0.59	0.68	0.23	0.05	0.23	0.21
NDWI-1640	0.58	0.59	0.68	0.23	0.05	0.23	0.21
mND-705	0.43	0.35	0.37	0.35	0.15	0.25	0.21
NDRE	0.70	0.68	0.76	0.15	0.60	0.65	0.19
WET	0.49	0.56	0.56	0.18	0.00	0.00	0.09
DCNI	0.43	0.50	0.50	0.05	0.01	0.16	0.07
CCCI	0.72	0.69	0.72	0.03	0.49	0.13	0.03
TCARI/OSAVI-1510	0.37	0.39	0.44	0.18	0.01	0.11	0.01
TCARI-1510	0.02	0.28	0.01	0.02	0.08	0.19	0.01
Yield							
EVI	-	-	0.85	-	-	0.57	0.87
OSAVI-1510	-	-	0.77	-	-	0.31	0.79
OSAVI	-	-	0.84	-	-	0.61	0.78
N870	-	-	0.76	-	-	0.30	0.76
NDWI_1640	-	-	0.70	-	-	0.25	0.76
NR	-	-	0.76	-	-	0.58	0.72
mSR-705	-	-	0.81	-	-	0.12	0.71
NDWI-2190	-	-	0.68	-	-	0.24	0.70
WET	-	-	0.55	-	-	0.03	0.65
NDVI	-	-	0.81	-	-	0.60	0.65
CI	-	-	0.82	-	-	0.22	0.60
TCARI/OSAVI-1510	-	-	0.43	-	-	0.20	0.58
GNDVI	-	-	0.89	-	-	0.66	0.53
NDRE	-	-	0.89	-	-	0.40	0.46
PRI	-	-	0.02	-	-	0.43	0.20
mND-705	-	-	0.51	-	-	0.48	0.18
TCARI-1510	-	-	0.00	-	-	0.03	0.17
TCARI/OSAVI	-	-	0.85	-	-	0.12	0.16
CCCI	-	-	0.78	-	-	0.00	0.05
DCNI	-	-	0.59	-	-	0.16	0.01
TCARI	-	-	0.82	-	-	0.00	0.00
Grain protein concentration							
CCCI	-	-	0.80	-	-	0.14	0.47
NDRE	-	-	0.71	-	-	0.57	0.42
GNDVI	-	-	0.52	-	-	0.48	0.28
TCARI/OSAVI	-	-	0.53	-	-	0.05	0.28
TCARI	-	-	0.57	-	-	0.02	0.25
PRI	-	-	0.00	-	-	0.12	0.25
mND-705	-	-	0.22	-	-	0.24	0.20

TCARI-510	-	-	0.00	-	-	0.19	0.17
NDVI	-	-	0.42	-	-	0.36	0.10
CI	-	-	0.51	-	-	0.15	0.08
NR	-	-	0.43	-	-	0.35	0.07
OSAVI	-	-	0.49	-	-	0.44	0.06
DCNI	-	-	0.50	-	-	0.11	0.05
N870	-	-	0.53	-	-	0.22	0.03
mSR_705	-	-	0.52	-	-	0.09	0.02
OSAVI-1510	-	-	0.55	-	-	0.25	0.02
NDWI-2190	-	-	0.47	-	-	0.16	0.02
NDWI-1640	-	-	0.51	-	-	0.16	0.01
EVI	-	-	0.54	-	-	0.52	0.01
TCARI/OSAVI-1510	-	-	0.33	-	-	0.10	0.00
WET	-	-	0.46	-	-	0.01	0.00
N output							
NDRE	-	-	0.88	-	-	0.67	0.78
GNDVI	-	-	0.74	-	-	0.69	0.70
OSAVI	-	-	0.70	-	-	0.64	0.65
NR	-	-	0.63	-	-	0.55	0.63
NDVI	-	-	0.64	-	-	0.57	0.60
OSAVI-1510	-	-	0.71	-	-	0.36	0.60
N870	-	-	0.69	-	-	0.32	0.59
EVI	-	-	0.73	-	-	0.69	0.58
CI	-	-	0.71	-	-	0.23	0.56
mSR_705	-	-	0.72	-	-	0.13	0.55
NDWI_1640	-	-	0.65	-	-	0.25	0.53
NDWI_2190	-	-	0.62	-	-	0.25	0.53
WET	-	-	0.55	-	-	0.02	0.41
TCARI/OSAVI-1510	-	-	0.41	-	-	0.17	0.36
TCARI/OSAVI	-	-	0.74	-	-	0.10	0.35
CCCI	-	-	0.88	-	-	0.08	0.32
mND_705	-	-	0.37	-	-	0.40	0.29
TCARI	-	-	0.75	-	-	0.01	0.06
TCARI-1510	-	-	0.00	-	-	0.14	0.01
PRI	-	-	0.01	-	-	0.28	0.01
DCNI	-	-	0.60	-	-	0.15	0.00

Chapter 4.6: Drought impact on cropland use monitored through multiple endmember spectral mixture analysis using AVIRIS imagery in Central Valley, California

S6. Possible impacts and range of different indicators for the different drought severity levels developed by United States Drought Monitor (2022b). Information regarding Palmer Drought Severity Index, CPC Soil Moisture Model, USGS Weekly Streamflow, Standardized Precipitation Index and Objective Drought Indicator Blends can be found at Integrated Drought Management Programme (2022a); National Oceanic and Atmospheric Administration (2022a); United States Geological Survey (2022b); Integrated Drought Management Programme (2022b) and National Oceanic and Atmospheric Administration (2022b), respectively.

Drought severity level	Possible Impacts	Palmer Drought Severity Index (PDSI)	CPC Soil Moisture Model (Percentiles)	USGS Weekly Streamflow (Percentiles)	Standardized Precipitation Index (SPI)	Objective Drought Indicator Blends (Percentiles)
Abnormally Dry	- Coming into drought: short-term dryness slowing planting, growth of crops or pastures - Coming out of drought: some lingering water deficits pastures or crops not fully recovered	-1.0 to -1.9	21 to 30	21 to 30	-0.5 to -0.7	21 to 30
Moderate Drought	Some damage to crops, pastures Streams, reservoirs, or wells low, some water shortages developing or imminent Voluntary water-use restrictions requested	-2.0 to -2.9	11 to 20	11 to 20	-0.8 to -1.2	11 to 20
Severe Drought	Crop or pasture losses likely Water shortages common Water restrictions imposed	-3.0 to -3.9	6 to 10	6 to 10	-1.3 to -1.5	6 to 10
Extreme Drought	Major crop/pasture losses Widespread water shortages or restrictions	-4.0 to -4.9	3 to 5	3 to 5	-1.6 to -1.9	3 to 5
Exceptional Drought	Exceptional and widespread crop/pasture losses Shortages of water in reservoirs, streams, and wells creating water emergencies	-5.0 or less	0 to 2	0 to 2	-2.0 or less	0 to 2

S7. Yearly harvested area (ha) of each crop indicated in the crop reports. Crops are separated according to their physiological status in June as green vegetation (GV) or non-photosynthetic vegetation (NPV). The main GV crops that the crop reports included in "others" classification are carrot, cilantro, eggplant, beet and zucchini. The NPV crops included in the "others" classification are winter cereals and legumes used for seed.

Crop type		Crop Name	Harvested area (ha)					
			2013	2014	2015	2016	2017	2018
GV	**Summer crop**	Alfalfa	104903.1	90287.47	86197.71	69876.32	59885.43	55249.35
		Blueberries	795.21	816.66	841.34	936.85	979.34	1521.62
		Broccoli	424.92	477.53	349.24	225.01	207.60	167.14
		Cantaloupe	226.62	0.00	0.00	0.00	0.00	0.00
		Cherries	3842.09	3635.70	3718.25	3456.42	3582.69	3291.31
		Corn	94579.57	68446.97	83371.79	84437.33	82260.52	69600.33
		Cotton	74021.93	54233.59	40741.76	51148.26	66321.97	57514.78
		Cucumbers	67.58	28.73	33.59	26.71	20.64	16.19
		Garlic	1116.93	1460.92	1643.03	2237.91	2250.05	2165.07
		Lettuce	0.00	129.50	137.59	237.96	0.00	0.00
		Onions	3099.89	3184.88	2998.72	3083.71	3427.69	2589.99
		Peppers	1072.42	890.31	700.11	829.61	777.00	829.61
		Potatoes Spring	4564.86	4738.87	4738.87	5010.01	5010.01	4479.87
		Sorghum	5094.19	5286.82	6195.74	5022.96	6837.98	5320.41
		Tomatoes	18921.90	19766.08	18732.51	17664.54	14438.79	15519.71
		Triticale	1515.55	1229.03	1232.27	889.50	718.72	1603.77
		Watermelons	898.40	963.15	785.09	724.39	1129.07	829.61
		Others	40285.68	33047.87	30150.32	34854.80	52548.07	58264.67
	Orchard	Almonds	81953.77	107169.76	111998.87	121823.03	124991.32	129562.65
		Apples	0.00	0.00	0.00	416.83	0.00	273.16
		Apricots	687.56	547.54	739.36	648.71	579.51	556.44
		Grapes	71528.66	71480.90	67160.07	69496.73	73787.21	68845.18
		Kiwifruit	991.48	963.15	760.81	748.67	777.00	744.62
		Lemons	2804.47	2917.79	3176.79	2909.69	3601.71	3808.10
		Nectarines	5578.60	4562.43	4379.92	4353.21	4491.61	4108.78
		Olives	4977.64	4734.83	3658.36	4330.14	4289.67	3957.83
		Oranges	37757.20	38768.92	35207.68	37919.08	38283.30	36421.74
		Peaches	7241.05	6175.91	6066.24	6115.61	6478.21	5961.83
		Pears	80.53	59.89	118.98	82.96	79.72	9.31
		Pecans	346.41	428.97	403.47	361.79	363.81	354.91
		Persimmons	983.39	327.80	378.79	360.98	348.03	387.69
		Pistachios	54868.95	67779.64	72994.43	77966.40	85864.25	92131.22
		Plums	5110.37	4592.78	4454.78	4323.67	4299.79	4242.73
		Pomegranates	1707.77	2286.48	1962.73	1197.87	1157.40	1141.21
		Prunes	1396.17	1392.12	1323.32	1254.53	1205.96	1210.01
		Quince	51.80	34.80	39.66	44.52	47.35	39.25
		Tangerines	5584.67	8781.69	9995.74	8943.56	10440.90	11533.55
		Walnuts	20749.47	22465.74	21320.07	23488.78	24347.93	24921.37
		Other Citrus	22264.61	25994.60	26392.41	25160.54	26086.06	27000.65
	Pasture	Irrigated Pasture	40468.60	40468.60	40468.60	40468.60	40063.91	42775.31
NPV		Barley	4419.17	1181.68	6027.80	4467.73	6943.60	5155.70
		Beans	4427.67	3928.69	3919.38	5761.92	4065.48	2264.22
		Oat	1104.79	679.06	865.22	360.98	420.47	879.79
		Pasture	994789.41	980719.69	987162.70	984931.26	994835.95	986491.33
		Wheat	62568.91	38040.08	50555.80	44608.54	44400.53	46169.82
		Others	45015.65	22982.52	18182.54	14993.62	90487.79	80856.26

Chapter 9: Annex

Related publications

This Ph.D. thesis was funded by the Ministerio de Economía y Competitividad (Spain; AGL2017-83283-C2-1-R; PRE2018-084215), Ministerio de Educación (Spain; FPU17/01251), Comunidad de Madrid, Spain (AGRISOST-CM S2018/BAA-4330 project) and Structural Funds 2014-2020 (ERDF and ESF) and was developed at the CEIGRAM (Research Centre for the Management of agricultural and Environmental Risks).

As a result of this work, four research articles were published in high impact Q1 scientific journals, and one more is currently under review.

Scientific publications:

Pancorbo, J. L., Lamb, B. T., Quemada, M., Hively, W. D., Gonzalez-Fernandez, I., and Molina, I. (2021). Sentinel-2 and WorldView-3 atmospheric correction and signal normalization based on ground-truth spectroradiometric measurements. ISPRS Journal of Photogrammetry and Remote Sensing, 173, 166-180.
DOI: https://doi.org/10.1016/j.isprsjprs.2021.01.009

Pancorbo, J. L., Camino, C., Alonso-Ayuso, M., Raya-Sereno, M. D., Gonzalez-Fernandez, I., Gabriel, J. L., Pablo J. Zarco-Tejada and Quemada, M. (2021). Simultaneous assessment of nitrogen and water status in winter wheat using hyperspectral and thermal sensors. European Journal of Agronomy, 127, 126287.
DOI: https://doi.org/10.1016/j.eja.2021.126287

Pancorbo, J. L., Quemada, M., and Roberts, D. A. (2023). Drought impact on cropland use monitored with AVIRIS imagery in Central Valley, California. Science of The Total Environment, 859, 160198.
DOI: https://doi.org/10.1016/j.scitotenv.2022.160198

Pancorbo, J. L., Alonso-Ayuso, M., Camino, C., Raya-Sereno, M. D., Zarco-Tejada, P. J., Molina, I., Gabriel, J. L. and Quemada, M. (2023). Airborne hyperspectral and Sentinel imagery to quantify winter wheat traits through ensemble modeling approaches. Precision Agriculture, 1-24.

DOI: https://doi.org/10.1007/s11119-023-09990-y

Pancorbo, J. L., Quemada, M., Raya-Sereno, M. D., and Camino, C. (2023). Hybrid artificial neural network-PROSAIL-PRO method applied to Sentinel-2 to estimate winter wheat nitrogen status and traits.
DOI: In progress.

Dataset availability:

Quemada, M., Camino, C., **Pancorbo**, **J. L.,** Raya-Sereno, M. D., Zarco-Tejada, P., Alonso-Ayuso, M., and Gabriel, J.L. (2023). Data from airborne hyperspectral and Sentinel imagery to quantify winter wheat traits through ensemble modeling approaches: figshare, doi:10.6084/m9.figshare.21865410.v1.

Oral presentations in scientific congresses:

Quemada, M., **Pancorbo, J. L**., Alonso- Ayuso, M., Gabriel, J.L., López-Herrera, J. and Pérez-Martín E. Vegetation indices from remote sensing imagery as proxies for yield and grain N in wheat. 12th European Conference on Precision Agriculture (ECPA). Montpellier, France, July - 2019. https://doi.org/10.3920/978-90-8686-888-9

Pancorbo, J. L., Camino, C., Alonso-Ayuso, M., Raya-Sereno, M. D., Gabriel, J. L., Pablo J. Zarco-Tejada and Quemada, M. Hyperspectral and thermal imagery to assess nitrogen and water status in winter wheat. XVI European Society for Agronomy Congress. Smart Agriculture for great human challenges. Sevilla, Spain, September - 2020

Pancorbo, J. L., Alonso-Ayuso, M., Raya- Sereno, M. D., Gabriel, J. L., Gonzalez-Fernandez, I. and Quemada, M. Sensitivity of hyperspectral bands to N concentration at different growth stages in winter wheat. INI 2021 - 8th Global Nitrogen Conference. Berlin, Germany, May, June - 2021. ISSN 2199-6571.

Pancorbo, J. L., Lamb, B. T., Quemada, M., Hively, W. D., Gonzalez-Fernandez, I., and Molina, I. Atmospheric correction assessment and normalization procedure for coupling Sentinel-2 and WorldView-3 imagery. 2021 IEEE International Geoscience and Remote Sensing Symposium. July 2021, Brussels, Belgium. https://doi.org/10.1109/IGARSS47720.2021.9553527

Pancorbo, J. L., Camino, C., Alonso-Ayuso, M., Raya-Sereno, M. D., Gonzalez-Fernandez, I., Gabriel, J. L., Pablo J. Zarco-Tejada and Quemada, M. Identificación del estado hídrico y nutricional del cultivo con sensores espectrales y térmicos. 17o Reunión Red de uso eficiente del Nitrógeno en agricultura. Emisiones de N_2O en la agricultura. Vitoria-Gasteiz, Spain, June-2022

Pancorbo, J. L., Camino, C., Alonso-Ayuso, M., Raya-Sereno, M. D., Gonzalez-Fernandez, I., Gabriel, J. L., Pablo J. Zarco-Tejada and Quemada, M. Hyperspectral and thermal sensors for distinguishing between nitrogen and water stress in winter wheat. Proceedings of the XXI International Nitrogen Workshop. Halving nitrogen waste by 2030. Madrid, Spain, October - 2022.

Poster presentations in scientific congresses:

Pancorbo, J. L., Alonso-Ayuso, M., Camino, C., Raya-Sereno, M. D., Zarco-Tejada, P. J., Molina, I., Gabriel, J. L. and Quemada, M. Winter wheat traits prediction through ensemble modeling approaches using hyperspectral and Sentinel-2 imagery. Proceedings of the XXI International Nitrogen Workshop. Halving nitrogen waste by 2030. Madrid, Spain, October - 2022. ISBN 978-84-122114-6-7

Pancorbo, J. L., Quemada, M., and Roberts, D. A. Monitoring agricultural patterns in Central Valley, California during a multi-year drought with AVIRIS imagery. Proceedings of the XXI International Nitrogen Workshop. Halving nitrogen waste by 2030. Madrid, Spain, October - 2022. ISBN 978-84-122114-6-7